UNIVERSITÀ DEGLI STUDI DI PISA

DIPARTIMENTO DI FISICA E. Fermi

Corso di Dottorato di Ricerca in Fisica -

XXXVII Ciclo

The X17 search with the MEG II apparatus

Candidate

Hicham Benmansour

Supervisor

Prof. Angela Papa

ANNO ACCADEMICO 2024/2025

The X17 search with the MEG II apparatus

by

Hicham BENMANSOUR

A thesis submitted to the
Department of Physics
in conformity with the requirements for
the Ph.D. degree

University of Pisa, Italy
February 2025

Abstract

Based in Debrecen, Hungary, the Atomki group observed in 2015 an anomalous excess in the angular distribution of electron-positron pairs from the $^7\mathrm{Li}(\mathrm{p}, \mathrm{e}^+\mathrm{e}^-)^8\mathrm{Be}$ reaction. This excess, which could not be explained by the monotonous decline of the Internal Pair Conversion background, was interpreted as evidence for a new light neutral boson with a mass of approximately 17 MeV/c^2, nicknamed X17. Additionally, several excesses observed in the decays of excited states of ^{4}He and ^{12}C were found to be kinematically consistent with X17, further thickening the plot.

The MEG-II apparatus, originally designed to search for the charged lepton flavour-violating decay $\mu^+ \to \mathrm{e}^+\gamma$, can be adapted to investigate X17's existence and properties, offering improved resolution and broader angular acceptance with respect to Atomki. Utilizing a Cockcroft-Walton generator that accelerates protons up to 1.1 MeV, MEG-II employs a specially designed lithium target along with a magnetic spectrometer consisting of a cylindrical drift chamber and two fast scintillator arrays immersed in a gradient magnetic field. This setup allows MEG-II to study the $^7\mathrm{Li}(\mathrm{p}, \mathrm{e}^+\mathrm{e}^-)^8\mathrm{Be}$ reaction and analyze its Angular Opening and energy sum ($E_{sum} = E_{\mathrm{e}^+} + E_{\mathrm{e}^-}$) spectra.

Here, we present the analysis of data collected over four weeks in 2023, with proton energies ranging from 500 keV to 1080 keV, resulting in the excitation of two different resonances with Q-values of 17.6 MeV and 18.1 MeV. No significant excess was found, and limits at 90% C.L. were set on the X17 branching ratios relative to γ emission from the two resonances: $R_{\mathrm{X17}/\gamma,17.6} < 1.8 \times 10^{-6}$ and $R_{\mathrm{X17}/\gamma,18.1} < 1.2 \times 10^{-5}$. The X17 hypothesis, based on Atomki results, is incompatible at 94% confidence with our best fit.

Sommario

Con sede a Debrecen, Ungheria, il gruppo Atomki ha osservato nel 2015 un eccesso anomalo nella distribuzione angolare delle coppie di elettroni-positroni provenienti dalla reazione $^{7}\mathrm{Li}(\mathrm{p},\mathrm{e}^{+}\mathrm{e}^{-})^{8}\mathrm{Be}$. Questo eccesso, che non può essere spiegato dall' andamento monotono del fondo dalla Conversione Interna di Coppie, è stato interpretato come evidenza dell'esistenza di un nuovo bosone neutro leggero con una massa di circa 17 MeV/c^2, soprannominato X17. Inoltre, sono stati osservati diversi eccessi nei decadimenti degli stati eccitati di ^{4}He e ^{12}C, che sono risultati cinematicamente coerenti con X17.

L'apparato MEG-II è stato disegnato per cercare il decadimento che viola la conservazione del sapore leptonico nel settore carico $\mu^{+} \to \mathrm{e}^{+}\gamma$. Può essere adattato per indagare l'esistenza e le proprietà di X17, offrendo un rivelatore con risoluzioni migliori ed un' accettanza angolare maggiore rispetto all' apparato di Atomki. MEG-II utilizza un acceleratore Cockcroft-Walton che rilascia protoni con energia fino a 1.1 MeV e impiega un bersaglio di litio progettato specificamente. Inoltre, è dotato di uno spettrometro magnetico composto da una camera a deriva cilindrica e due array di scintillatori veloci, immersi in un gradiente di campo magnetico. Questa configurazione consente a MEG-II di studiare la reazione $^{7}\mathrm{Li}(\mathrm{p},\mathrm{e}^{+}\mathrm{e}^{-})^{8}\mathrm{Be}$ e analizzare gli spettri di apertura angolare (Angular Opening) e di somma di energia ($E_{sum} = E_{\mathrm{e}^{+}} + E_{\mathrm{e}^{-}}$).

Qui presentiamo l'analisi dei dati raccolti nel corso di quattro settimane nel 2023, con l'energia dei protoni che varia da 500 keV a 1080 keV, portando all'eccitazione di due diverse risonanze con valori di Q di 17.6 MeV e 18.1 MeV. Non è stato trovato alcun eccesso significativo e sono stati stabiliti limiti al 90% C.L. sui rapporti di ramificazione del X17 rispetto all'emissione di γ delle due risonanze: $R_{\mathrm{X17}/\gamma,17.6} < 1.8 \times 10^{-6}$ e $R_{\mathrm{X17}/\gamma,18.1} < 1.2 \times 10^{-5}$. L'ipotesi X17, basata

sui risultati Atomki, è incompatibile al 94% di confidenza con il nostro best fit.

Contents

List of Tables

List of Figures

The X17 search with the MEG II apparatus

Hicham BENMANSOUR

February 14, 2025

Introduction

This work aims to probe the existence of the so-called X17 particle, suggested to explain an anomalous excess observed in $^{7}\mathrm{Li}(\mathrm{p}, \mathrm{e}^{+}\mathrm{e}^{-})^{8}\mathrm{Be}$ by the Hungarian Atomki group [1]. In 2016, impinging $E_{\mathrm{p}} = 1.1$ MeV protons onto a thin $\mathrm{Li_2O}$ target and exciting the 1030 keV Li resonance, they measured the angular opening of the resulting $\mathrm{e}^{+}\mathrm{e}^{-}$ pair. Though well explained at low angles by the monotonously decreasing Internal Pair Conversion (IPC) process, the distribution showed a bump-like excess at angles close to 140°. Difficult to explain through Standard Model processes, a new light neutral boson with mass circa 17 MeV/c^2, nicknamed X17 and quickly decaying to an $\mathrm{e}^{+}\mathrm{e}^{-}$ pair was proposed to interpret the anomaly. In the next years, the group observed similar anomalies in $^{3}\mathrm{H}(\mathrm{p}, \mathrm{e}^{+}\mathrm{e}^{-})^{4}\mathrm{He}$ and $^{11}\mathrm{B}(\mathrm{p}, \mathrm{e}^{+}\mathrm{e}^{-})^{12}\mathrm{C}$ reactions. Though the mentioned transitions have various energies, the excesses were all found to be kinematically consistent with a 17 MeV/c^2 boson, triggering a strong interest of the theoretical and experimental communities. Indirect searches have put strong constraints on the boson properties. To date, no experiment has independently confirmed or refuted Atomki's observation through the $^{7}\mathrm{Li}(\mathrm{p}, \mathrm{e}^{+}\mathrm{e}^{-})^{8}\mathrm{Be}$ channel. The MEG-II experiment, designed to search for the charged lepton flavour violating decay $\mu^{+} \to \mathrm{e}^{+}\gamma$, features its own Cockcroft-Walton accelerator, delivering protons up to 1.1 MeV. It also employs a next-generation magnetic spectrometer, comprising an ultra-light cylindrical drift chamber (CDCH) and two arrays of ultra-fast scintillating counters (pTC), all immersed in the COBRA gradient magnetic field. With some adaptations of the apparatus and a specially designed Li target region, MEG-II can perform the X17 search. Additionally, its liquid xenon and bismuth germanate calorimeters offer high-resolution photon reconstruction and monitoring capabilities. Here, we present the first independent results from the X17 search. With enhanced resolution and broader angular acceptance, MEG-II has the potential to provide new insights into the existence and properties of the particle.

Chapter 1 introduces the Internal Pair Conversion theory, reviews Atomki's experiments and results for $^{8}\mathrm{Be}$, $^{4}\mathrm{He}$ and $^{12}\mathrm{C}$, and highlights the observed anomalous excesses for each nucleus. Chapter 2 discusses theories that aim to explain these excesses, both within and beyond the Standard Model. It also highlights X17's potential nature and properties. Chapter 3 outlines the motivation behind

the $\mu^+ \to e^+\gamma$ search and describes the MEG-II experiment, including the design and operation of its various subsystems: the liquid xenon calorimeter, the COBRA magnetic field, the cylindrical drift chamber and the pixelated timing counters.

The focus of Chapter 4 is two-fold: first, it details the changes needed to adapt MEG-II's apparatus and trigger and data acquisition (TDAQ) strategy for the X17 search. Next, it describes the Monte Carlo (MC) simulations of the detectors, the Internal Pair Conversion (IPC) and other background processes, as well as the X17 signal, incorporating a recent and comprehensive IPC model developed by Zhang and Miller.

The $\mu^+ \to e^+\gamma$ search relies solely on positron reconstruction. Chapter 5 explains the procedure for reconstructing e^- tracks and e^+e^- pairs and discusses the advanced selection criteria used to accurately extract pair kinematics. Chapter 6 presents the main dataset for the X17 search, acquired in 2023, and compares it with MC simulations to characterize the dataset's content: a mix of 440 keV and 1030 keV resonances. Finally, Chapter 7 employs a blinded analysis strategy and a maximum likelihood fit to extract the X17 signal yield from the 2023 dataset. The results are presented as a function of the X17 branching ratio with respect to the $^7\mathrm{Li}(\mathrm{p},\gamma)^8\mathrm{Be}$ photon production.

My contributions focused on several crucial aspects of the X17 search:

- Simulating and understanding the Internal Pair Conversion (IPC) and other background processes
- Developing the e^+e^- pair reconstruction and selection procedure
- Designing the trigger and data acquisition (TDAQ) strategy, commissioning the apparatus, and monitoring the DAQ and detectors
- Comparing data and simulations to characterize the dataset content
- Developing the analysis strategy, fit procedure and parameterization

Chapter 1

Anomalies in the Internal Pair Creation of ^{8}Be, ^{4}He, ^{12}C

In 2016, Attila Krasznahorkay's experimental nuclear physics group at the Atomki laboratory, part of the Hungarian Academy of Sciences Institute for Nuclear Research, investigated the $^{7}\mathrm{Li}(\mathrm{p}, \mathrm{e}^{+}\mathrm{e}^{-})^{8}\mathrm{Be}$ reaction. They observed an anomalous excess in the angular distribution of the lepton pair that surpassed predictions from Internal Pair Conversion (IPC) and known backgrounds. One intriguing explanation proposed for this anomaly was the emission of a 17 MeV/c^2 neutral boson, hypothetically emitted by the excited ^{8}Be nucleus during proton capture. This particle, unaccounted for by the Standard Model, was nicknamed X17. After further measurements with improved setups and analyses, this anomaly started puzzling the community.

Interest in X17 intensified when the Atomki group extended their study to other nuclei in 2019 and 2022, observing similar anomalies in the angular distributions from the $^{3}\mathrm{H}(\mathrm{p}, \mathrm{e}^{+}\mathrm{e}^{-})^{4}\mathrm{He}$ and $^{11}\mathrm{B}(\mathrm{p}, \mathrm{e}^{+}\mathrm{e}^{-})^{12}\mathrm{C}$ reactions. The observed angular opening spectra were once again consistent with the production of a 17 MeV/c^2 neutral boson, making X17 a promising candidate in the search for New Physics.

This chapter will begin by introducing the $^{7}\mathrm{Li}(\mathrm{p}, \gamma)^{8}\mathrm{Be}$ reaction, its associated excited states, and the Internal Pair Conversion (IPC) theory based on Rose's precursor model. It will then explore the Atomki experiments and results from the decays of $^{8}\mathrm{Be}^{*}$, $^{4}\mathrm{He}^{*}$, and $^{12}\mathrm{C}^{*}$ excited states.

Authors use various notations to refer to the electron-positron angular opening, including Θ, θ_{+-}, θ_{ee}, $\theta_{\mathrm{e^+e^-}}$, Angle between Particles, and Angular Opening. Despite the different labels, they all represent the same observable. This work will most often use Angular Opening. It should not be confused with θ, which represents the polar angle in MEG-II's cylindrical coordinate system.

1.1 The ^{7}Li(p, γ)^{8}Be reaction

Several energy levels from the ^{8}Be nucleus are introduced in Fig. 1.1 based on [2] and extracted from [3]. The ground state, lying 0.1 MeV above the $\alpha\alpha$ breakup threshold, has spin-parity $J^P = 0^+$ and isospin $T = 0$. The two lowest excitations are 2^+ and 4^+ rotational states with respective excitation energies 3.03 MeV and 11.35 MeV. This first excited state will be referred to later on. Above these lie the 2^+ states with energies between 16 MeV and 17 MeV and whose only decay channel is the $\alpha\alpha$ final state. Above the 17.26 MeV p+^{7}Li dissociation threshold lie the 1^+ 17.6 MeV and 18.1 MeV ^{8}Be* excited states with isospin 1 and 0 respectively. They are respectively referred to as ^{8}Be*(17.6) and ^{8}Be*(18.1) hereinafter. The Atomki anomaly was observed in the de-excitation of the latter, the ^{8}Be*(18.1) state.

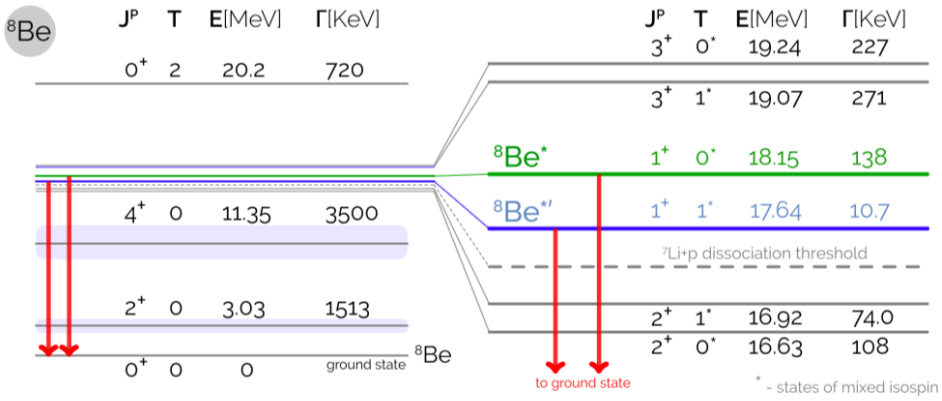

Figure 1.1: ^{8}Be most relevant energy states with associated spin-parity J^P, isospin T and decay width Γ based on [2] and extracted from [3]. Two states are of particular importance for this work, ^{8}Be*(17.6) and ^{8}Be*(18.1).

While the 2^+ excited states are obtained through the β decay of ^{8}B, the ^{8}Be*(17.6) and ^{8}Be*(18.1) states are populated through proton impinging on a lithium target. These states decay almost always ($\approx 100\%$) back to p+^{7}Li but electromagnetic transitions are allowed with a reduced branching ratio. The Branching Ratio ($\mathcal{BR}$) for the gamma emission was estimated to be $\mathcal{BR}(^{8}\text{Be}^*(18.1) \rightarrow {}^{8}\text{Be} + \gamma) \approx 1.4 \times 10^{-5}$ [4]. The ^{7}Li(p, γ)^{8}Be reaction was studied in depth by [5]. The excitation curve as a function of the proton kinetic energy for the reaction is shown in Fig. 1.2. The figure clearly shows two resonances. One, very sharp, at E_{p}= 0.441 MeV populates the ^{8}Be*(17.6) state while the other, smoother, at E_{p}= 1.030 MeV populates the ^{8}Be*(18.1) state. At these proton energies, an excited state is created before photon emission (see Fig. 1.3 (left)) and the process is called

resonant proton capture. Below the resonances, a non-resonant yield is associated with the direct proton capture process [6] (see Fig. 1.3 (right)).

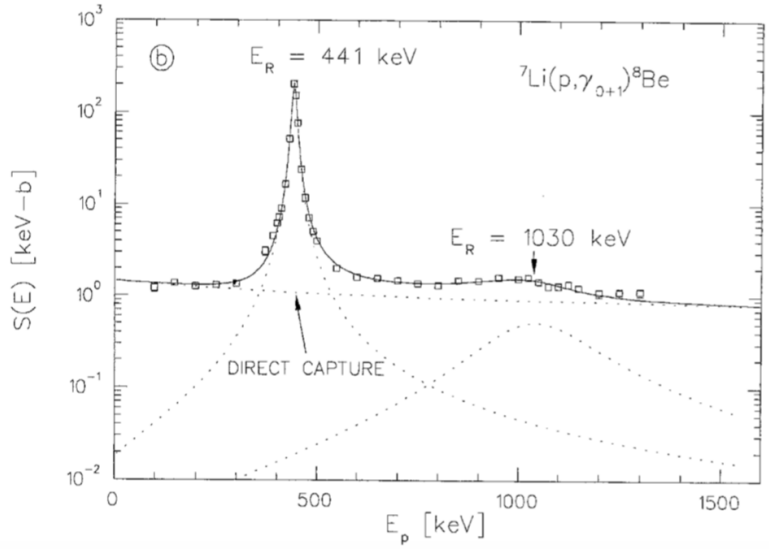

Figure 1.2: Excitation curve of the ^{7}Li(p, γ)^{8}Be reaction, presented as the astrophysical S factor S(E) in keV$\times$barn as a function of the proton kinetic energy in keV. The solid line is a fit to the square data points and the dotted lines represent the individual contributions of each resonance as well as the direct capture process. Figure from [5].

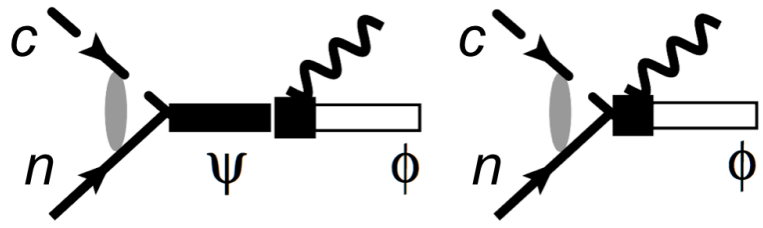

Figure 1.3: Feynman diagrams for the resonant (left) and non-resonant (right) proton capture process. c, n, ϕ and ψ represent the proton, ^{7}Li, ^{8}Be ground state and ^{8}Be excited state respectively. The resonant process enables the creation of an excited state ψ before photon emission. Figure from [7].

A nuclear transition occurs when a nucleus passes from an excited state to a lower-energy state, allowed by the emission of a photon. The order of multipole

expansion of the electromagnetic field, also called multipolarity of the emitted radiation, can be used to classify the transition. Writing l the order of the multipole expansion, the electric and magnetic multipole transitions are labelled El and Ml. A dipole, multipole of order 1, has $2^l = 2$ poles while an octupole, multipole of order 3, has $2^l = 8$ poles. El and Ml radiations carry the same angular momentum l (in units of $\hbar$) but differ in parity. The electric multipoles have parity $P = (-1)^l$ while magnetic multipoles have parity $P = (-1)^{l+1}$. The multipole parity should match the parity change from the initial to the final state: $P(\mathrm{M}l) = P_i P_f = (-1)^{l+1}$ or $P(\mathrm{E}l) = P_i P_f = (-1)^l$. The conservation of angular momentum also imposes: $\mid J_i - J_f \mid \leq l \leq J_i + J_f$. The transition from the 1^+ ^{8}Be*(17.6) or 1^+ ^{8}Be*(18.1) states to the 0^+ ground state imposes $l = 1$ and conserves parity. They both correspond to M1 transitions. The electric monopole E0 is forbidden for these ^{8}Be* transitions to ground state. Because E0 transfer zero angular momentum, the single photon emission is forbidden, while conversion electrons, conversion pairs or two-photon emission can occur. Magnetic monopoles M0 were never observed experimentally.

Using the No-Core Shell Model with Continuum (NCSMC), Gysbers et al. [8] have estimated the different multipole contributions of the ^{7}Li(p, γ)^{8}Be reaction cross-section as a function of the proton kinetic energy in the center of mass (see Fig. 1.4). The model is consistent with the blue data points from [5]. As expected, the sharp and smooth resonances populating respectively the ^{8}Be*(17.6) and ^{8}Be*(18.1) states correspond to an M1 multipolarity. It can be noticed that the E1 contribution, corresponding to non-resonant direct proton capture, is not negligible, especially in between the resonances. E2 transitions are three orders of magnitude weaker than E1 transitions.

1.2 Internal Pair Creation

The photon emission is not the only process allowed by nuclear transitions. If the atom is not fully ionized, the excited nucleus can interact electromagnetically with one of the atom's orbital electrons. An electron with energy equal to the ΔE between the initial and final states is then ejected from the atom in the Internal Conversion (IC) process [9]. If $\Delta \mathrm{E} \geq 2m_e c^2$, with m_e the electron rest mass, the Internal Pair Creation (IPC) [9] process becomes a competing mechanism. The excited nucleus decays through the emission of an electron-positron pair. Its probability can be estimated through the conversion coefficient, defined as the number of IPC (or IC) events per emitted photon for a given nuclear transition. The IPC and IC processes are largely reduced with respect to the gamma emission. The IPC branching ratio for the ^{8}Be*(18.1) transition to ground state based on Rose [10] is:

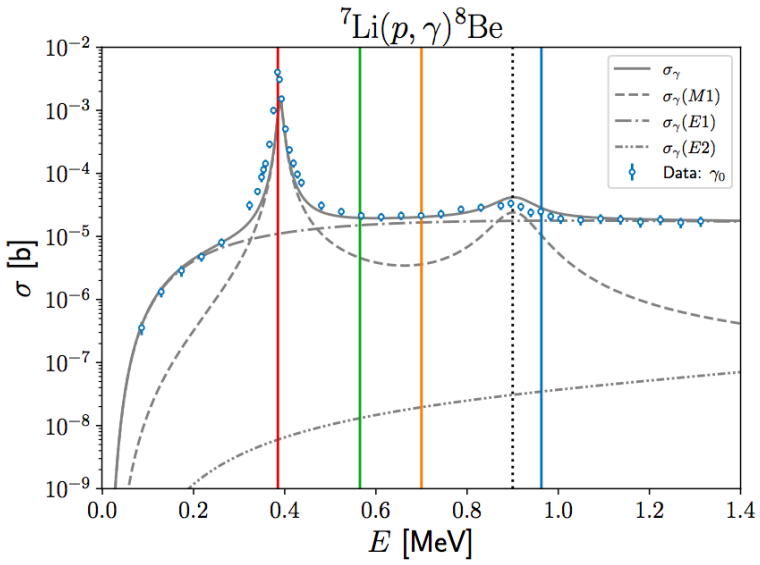

Figure 1.4: ^{7}Li(p, γ)^{8}Be reaction cross-section estimate as a function of the center of mass proton kinetic energy. The individual subcontributions from M1, E1 and E2 multipoles are shown in a dashed, dash-dotted and dash-dot-dotted manner respectively. Figure from [8]. The estimate is compared to the blue data points extracted from [5].

$$\begin{aligned}\mathcal{BR}(^8\mathrm{Be}^* \to {}^8\mathrm{Be} + \mathrm{e}^+\mathrm{e}^-) &\approx 3.9 \times 10^{-3} \times \mathcal{BR}(^8\mathrm{Be}^* \to {}^8\mathrm{Be} + \gamma) \\ &\approx 5.5 \times 10^{-8}\end{aligned} \tag{1.1}$$

In [10] and [11], Rose has modelled the IC and IPC processes respectively and estimated their dependence on the atomic number Z and the photon energy k in units of the electron rest mass (m_e). On the one hand, the IC coefficients tend to increase with Z while IPC coefficients slightly decrease. On the other hand, IPC coefficients increase with k while IC coefficients decrease quickly. At $Z \approx 40$ and $k = 5.0$, both decay modes are estimated to have equal probability. The IPC process is also dependent on the multipolarity of the nuclear transition.

Rose has developed a model for these decays based on the Born approximation where the scattering process is treated as a first-order perturbation of the free field. This approximation holds at small scattering fields and low atomic numbers. For a given set of p_+, p_-, W_+ and W_- the momenta and energies of the positron and electron and a given multipolarity l, Rose has determined a formulation of the number of IPC events as a function of the electron-positron opening angle Θ:

$$\begin{aligned}\gamma_l(\Theta) = & \frac{2\alpha}{\pi(l+1)}\left(\frac{p_+p_-}{q}\right)\frac{(q/k)^{2l-1}}{(k^2-q^2)^2} \\ & \times\left\{(2l+1)\left(W_+W_- + 1 - \frac{1}{3}p_+p_-\cos\Theta\right)\right. \\ & + l\left[\left(\frac{q^2}{k^2}\right) - 2\right](W_+W_- - 1 + p_+p_-\cos\Theta) \\ & + \frac{1}{3}(l-1)p_+p_-\left[\left(\frac{3}{q^2}\right)(p_- + p_+\cos\Theta)\right. \\ & \left.\left.\times(p_+ + p_-\cos\Theta) - \cos\Theta\right]\right\}\end{aligned} \tag{1.2}$$

for electric multipoles

$$\begin{aligned}\gamma_l(\Theta) = & \frac{2\alpha}{\pi}\left(\frac{p_+p_-}{q}\right)\frac{(q/k)^{2l+1}}{(k^2-q^2)^2}\left\{1 + W_+W_-\right. \\ & \left. - \frac{p_+p_-}{q^2}(p_- + p_+\cos\Theta)(p_+ + p_-\cos\Theta)\right\}\end{aligned} \tag{1.3}$$

for magnetic multipoles

α represents the fine structure constant and $\vec{q} = \vec{p}_+ + \vec{p}_-$. These distributions peak at 0° then quickly and monotonously decrease. One precursor idea of Rose was to use these angular distribution shapes in order to determine the multipolarity of a nuclear transition. To probe the feasibility, he calculated in Fig. 1.5 the ratio between the IPC yields at 0° and 90° as a function of the photon energy for $l \in [1, 5]$ for both electric and magnetic multipoles. The results point at a steeper and steeper angular opening distribution as the multipole order increases.

Writing $x_1 = (p_+ - p_-)^2/k^2$, $x_2 = (p_+ + p_-)^2/k^2$ and $J_l = \int_{x_1}^{x_2} x^l(1-x)^{-2}dx$, Rose also extracted the positron energy distribution by integrating Eq. 1.2 and Eq. 1.3 over the positron-electron opening angle:

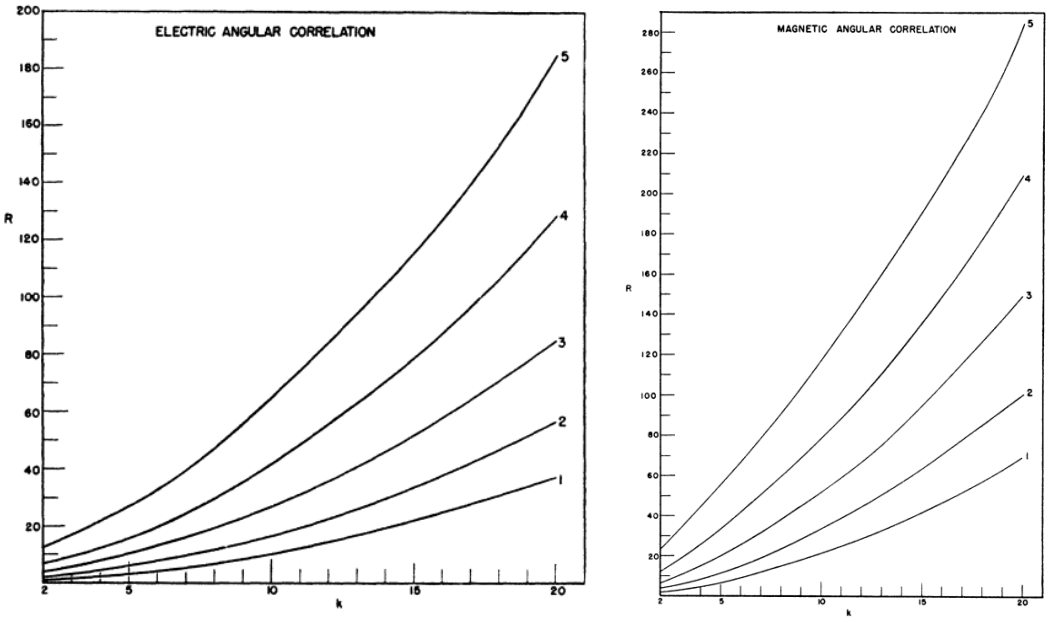

Figure 1.5: Ratio R of $\gamma_l(0°)$ and $\gamma_l(90°)$ as a function of the photon energy k for several values of multipole order l (besides the curve) for electric (left) and magnetic (right) multipoles. Figures from [10].

$$\begin{aligned}\Gamma_l\left(W_+\right) = \frac{\alpha}{\pi(l+1)k^3}\Bigg\{ & \frac{l}{2}k^2 J_{l+1} \\ & + \left[2lW_+W_- - \frac{1}{4(7l+1)}k^2\right] J_l \\ & + \left[l\left(W_+^2 + W_-^2 + 1\right) + 1 - W_+W_-\right] J_{l-1} \\ & - \frac{1}{4(l-1)}\left(W_+ - W_-\right)^2 J_{l-2}\Bigg\}\end{aligned} \tag{1.4}$$

for electric multipoles

$$\begin{aligned}\Gamma_l\left(W_+\right) = \frac{\alpha}{\pi k^3}\Bigg\{ & \left(1 + W_+W_-\right) J_l \\ & - \frac{k^2}{4}\left(J_{l+1} - x_1x_2J_{l-1}\right)\Bigg\}\end{aligned} \tag{1.5}$$

for magnetic multipoles

Finally, Rose calculated the IPC coefficients by integrating Eq. 1.2 and Eq. 1.3 over the positron energy. These coefficients and their dependence on the photon energy k are presented in Fig. 1.6 for a set of multipole order values and for both electric and magnetic multipoles. An increased transition energy favours the IPC process. The decays of ^{8}Be*(18.1) and ^{8}Be*(17.6) excited states, with $\Delta E > 17$ MeV are among the most energetic known nuclear transitions and are preferred channels to study the IPC process. The IPC coefficients are also well separated for different multipole orders, allowing IPC rates to be of help to determine the multipolarity of a nuclear transition. Rose reports an error of 15-20% on its numerical calculations based on the comparison with results from [12] at $Z = 84$, though the Born approximation is expected to be less reliable at such high Z.

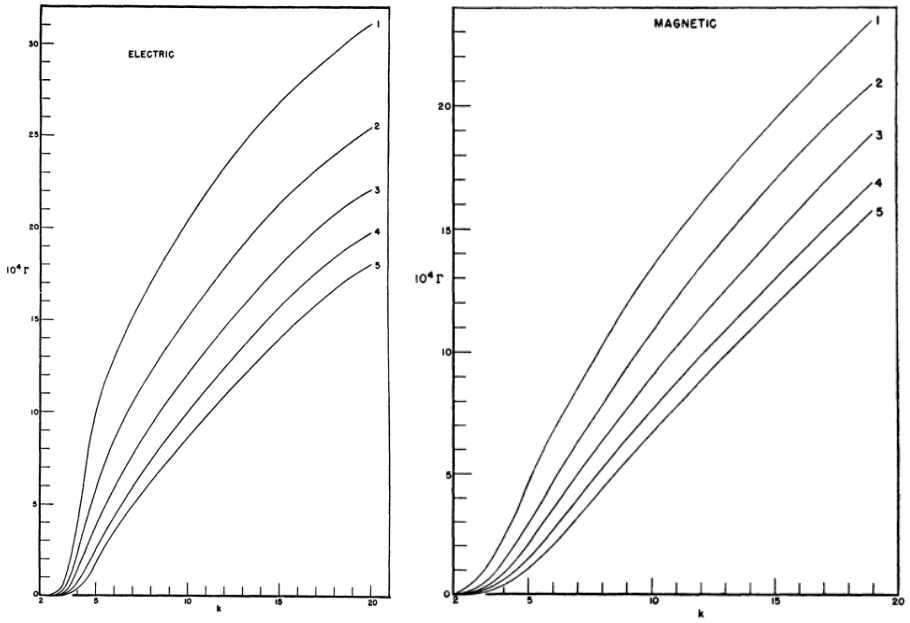

Figure 1.6: Total number of internal pairs produced as a function of the photon energy k for several values of multipole order l (besides the curve) for electric (left) and magnetic (right) multipoles. Figures from [10].

More recently, the Atomki group made use of Rose's model to generate the angular opening models expected from E0, E1, E2, M1 and M2 transitions. The rapid monotonous drop with increasing opening angle is observed in Fig. 1.7.

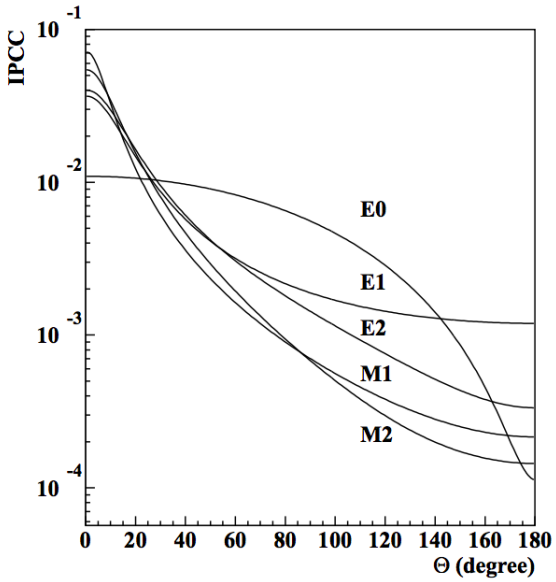

Figure 1.7: Simulated angular opening models for E0, E1, E2, M1 and M2 transitions from the Atomki group based on Rose's IPC model. Curves normalized to the same area. Figure from [13].

1.3 Atomki anomalies in Internal Pair Conversion of ^{8}Be, ^{4}He and ^{12}C excited nuclei

Internal Pair Conversion (IPC) measurements have long been used as a probe of nuclear transition multipolarities. In recent decades, along with advancements in detector technologies and improvements in kinematic resolutions, IPC processes have been studied as a probe for new light particles beyond the Standard Model. Anomalies or excesses over the well-known monotonously and rapidly decreasing shape of the IPC electron-positron angular opening distribution would indeed be hints for such New Physics. Such distributions and potential anomalies were studied and discussed in [14, 15, 16, 17, 18]. In 2016 [1], the Atomki group, led by A. Krasznahorkay and located in Debrecen, Hungary investigated such an anomaly in the ^{7}Li(p, e^{+}e^{-})^{8}Be reaction and observed a significant deviation from the expected distributions, a striking peak-like excess above the shapes simulated based on Rose's model on Fig. 1.7. One of the potential explanations for the anomaly is the creation of a 17 MeV/c^{2} light boson emitted during proton capture by the excited nucleus. In the next years, the group studied the IPC distributions from two other reactions, ^{3}H(p, e^{+}e^{-})^{4}He [19, 20] and ^{11}B(p, e^{+}e^{-})^{12}C [21], where significant anomalies were observed once again. The deviations were found to be consistent with the hypothesis of a 17 MeV/c^{2} boson, nicknamed X17 and triggered a strong

interest in the community.

1.3.1 Experimental apparatus

For their first measurement of the Internal Pair Conversion process [1], the Atomki group was interested in studying the electron-positron angular opening (Θ), energy sum ($E_{sum} = E_{e^+} + E_{e^-}$) and invariant mass ($M$) from the ^{7}Li(p, e$^+e^-$)^{8}Be reaction. They excited both the ^{8}Be*(17.6) state with protons at kinetic energy $E_p = 441$ keV and the ^{8}Be*(18.1) state with protons at $E_p = 1100$ keV. Thanks to a 2 MV Van de Graaff accelerator, a proton beam with a typical current of 1.0 μA was sent towards the lithium target. To excite the sharp 441 keV resonance, a thin 15 μg/cm^2 ($\approx$ 50 nm thickness) lithium fluoride LiF was evaporated onto a 10 μm Al backing. The relative flatness and lower amplitude of the 1030 keV resonance requires a thicker target to produce charged particles with a reasonable rate: a 700 μg/cm^2 ($\approx$ 2.1 μm thickness) lithium oxide Li_2O was evaporated onto another 10 μm Al backing. One crucial point of the measurement is to reduce the material around the target in order to mitigate the background coming from the conversion of photons in matter, called External Pair Conversion (EPC). The targets were therefore supported with two thin 3-mm diameter 12-cm long Plexiglas rods, 25 mm from and parallel to the beam. The target state was continuously monitored by measuring the gamma rate and spectrum from the ^{7}Li(p, γ)^{8}Be reactions with a 470 cm^3 High Purity Germanium (HPGe) detector, placed 50 cm from the target. With this 10 keV resolution HPGe, the line broadening due to the target thickness and the associated proton energy loss in the target was precisely followed throughout the run. Due to deterioration, the target was changed every few hours. The target region was held in vacuum within a 24 cm long 800 μm thick, 3.5 cm radius carbon fibre tube. 15 cm behind the target, a Tantalum Faraday-cup absorbed the remainder of the beam.

The spectrometer for measuring the energy and direction of the electron and positron is inspired from [22]. Five plastic scintillators ΔE-E telescopes are placed in the plane orthogonal to the beam. The thin ΔE detectors (52×52×1 mm^3) provide good γ suppression. The 80×60×70 mm^3 E detectors and their positioning provide charged particle energy measurement and good angular coverage. The telescopes are positioned at relative angles of 0°, 60°, 120°, 180°, 270°. In front of each telescope, a multi-wire proportional counter (MWPC), built at ATOMKI based on [23], measures the hit position of the charged particle. The angular opening from an electron-positrion pair is computed combining the position of two hits in two different MWPCs with the position of the beam spot on target. The MWPCs hit position estimate leads to an angular resolution of 2° (FWHM). However, multiple scattering in the target holder, the carbon fibre vacuum chamber and the MWPC windows causes a spread in the angular opening resolution evaluated with

Monte-Carlo simulations to be $\Delta\Theta \approx 7°$ (FWHM). The detection of an electron-positron pair corresponds to a quadruple coincidence in two plastic scintillators and two MWPCs. A layout of the setup is shown in Fig. 1.8 (left). The detector response based on simulations is displayed in Fig. 1.8 (right). It represents the pair detection efficiency as a function of the electron-positron angular opening Θ. An ideal 4π acceptance detector would give a sine function as detector response. Variations of the response correspond to favoured or unfavoured angular opening regions based on the telescopes' geometrical arrangement. 60° is here favoured due to 4 of the 5 telescopes being positioned at 60° relatively to one another. The simulated detector response can be compared to an experimental detector response making use of the event mixing method introduced in [24]. It consists of uncorrelated pairs from single particle events (one MWPC hit) whose angular opening is computed as in the case of a coincident pair. Both responses show reasonably good agreement. More details on the setup can be found in [13].

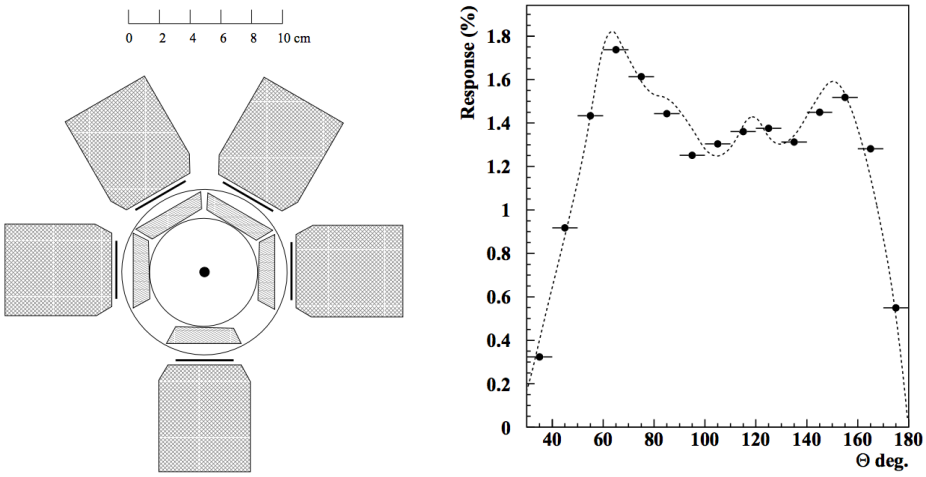

Figure 1.8: (Left) Layout of Atomki's first e^+e^- spectrometer: five ΔE-E telescopes (black-dark gray) and five MWPCs (clear gray). The target is a black dot at the center. (Right) Spectrometer response of the five-telescope setup as a function of the angular opening based on Monte-Carlo simulations (dashed line) and on experimental data (black dots). Figures from [25].

For a second measurement in 2017 [25], the ATOMKI group explored further the ^{7}Li(p, e^+e^-)^{8}Be from the ^{8}Be*(17.6) state and replaced the MWPCs with five double-sided silicon strip detectors (DSSSDs) made of 3 mm thick strips. For a third measurement in 2018 [26], they re-investigated the anomaly observed in the ^{8}Be*(18.1) state decay with an improved setup. The Al backing was replaced by

a 20 μg/cm^2 thick carbon foil. The number of telescopes was increased from 5 to 6 leading to the setup pictured in Fig. 1.9.

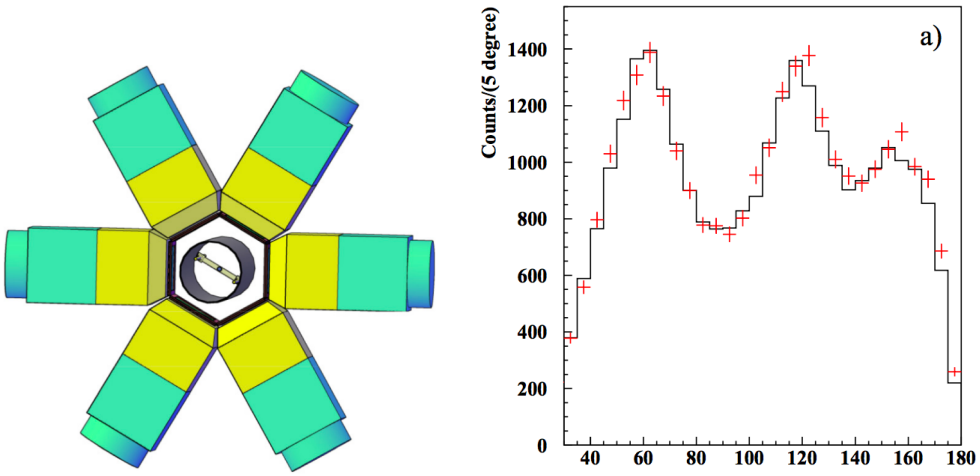

Figure 1.9: (Left) CAD layout of Atomki's six-telescope e^+e^- spectrometer: 6 ΔE-E telescopes (yellow) and their light guides (blue) and 6 DSSSDs. The blue target at the center is held by two rods parallel to the beam and is surrounded by a cylindrical carbon fibre chamber. Figure from [20]. (Right) Spectrometer response of the six-telescope setup as a function of the angular opening based on Monte-Carlo simulations (black line) and on experimental data (red crosses). Figure from [21].

In 2021, they investigated the Internal Pair Conversion process from the ^{3}H(p, e^+e^-)^{4}He reaction bombarding ^{3}H absorbed in a 4.2 mg/cm^2 thick Ti layer evaporated onto a 400 μm-thick molybdenum disk. The density of ^{3}H was $\approx 2.7 \times 10^{20}$ atoms/cm^2. To prevent ^{3}H evaporation, the target was cooled making use of the cooling system presented in Fig. 1.10. The six-telescope spectrometer previously introduced was used for this measurement. The target was shifted 25 mm backward along the beam axis with respect to the spectrometer center in order to prevent screening by the target holder. Thanks to this shift, the e^+e^- pairs with angular openings of up to 140° can be detected by the spectrometer.

In 2022 [21], they investigated the Internal Pair Conversion from the ^{11}B(p, e^+e^-)^{12}C reaction making use of the same setup. A 2 mg/cm^2 thick ^{11}B target was evaporated onto a 5 μm thick Ta foil.

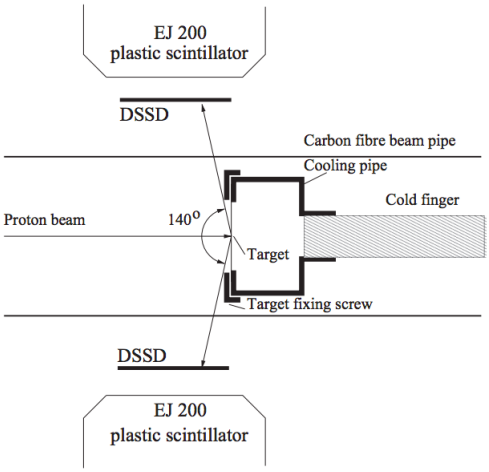

Figure 1.10: Scheme of the ^{3}H target cooling system. Figure from [20].

1.3.2 The Atomki Anomaly in ^{7}Li(p, e^{+}e^{-})^{8}Be

First results

The Atomki group triggered the interest of the community for the first time with their results on the study of the Internal Pair Conversion process from ^{8}Be. In [1], the Atomki group studied the angular opening, invariant mass and energy sum spectra from the IPC of the ^{7}Li(p, e^{+}e^{-})^{8}Be making use of the setup described in Sec. 1.3.1 and a proton beam at $E_{\mathrm{p}} = 440$ keV and $E_{\mathrm{p}} = 1100$ keV. They studied both 441 keV and 1030 keV resonances leading to the population of the ^{8}Be*(17.6) and ^{8}Be*(18.1) states respectively. Gamma spectra measurements from the ^{8}Be*(17.6) and ^{8}Be*(18.1) decays are shown in Fig. 1.11. The gamma peaks at 17.6 MeV and 18.1 MeV lines are clearly visible along with the first and second escape peaks due to the finite size of the detector. The transition to first excited state with energies close to 15 MeV can also be seen.

By summing the energies of the coincident electron and positron from the ^{7}Li(p, e^{+}e^{-})^{8}Be reaction one can build the E_{sum} distribution and therefore reconstruct the energies of the involved transitions. See Fig. 1.12. The spectra are shown for pairs with symmetric energies, requesting $|y| < 0.5$ with y the energy asymmetry: $y = \frac{E_{\mathrm{e}^-} - E_{\mathrm{e}^+}}{E_{\mathrm{e}^-} + E_{\mathrm{e}^+}}$. The energy asymmetry absolute value $|y|$ ranges between 0 (symmetric energies: $E_{\mathrm{e}^-} = E_{\mathrm{e}^+}$) and 1 ($E_{\mathrm{e}^-} \gg E_{\mathrm{e}^+}$ or $E_{\mathrm{e}^+} \gg E_{\mathrm{e}^-}$). Again, the transition to ground state and to first excited state are clearly visible for both resonances. At both $E_{\mathrm{p}} = 440$ keV and $E_{\mathrm{p}} = 1100$ keV, a 6 MeV contribution from ^{19}F(p, αe^{+}e^{-})^{16}O is observed. At $E_{\mathrm{p}} = 1100$ keV, an additional 11 MeV contribution from ^{27}Al(p, e^{+}e^{-})^{28}Si can be seen.

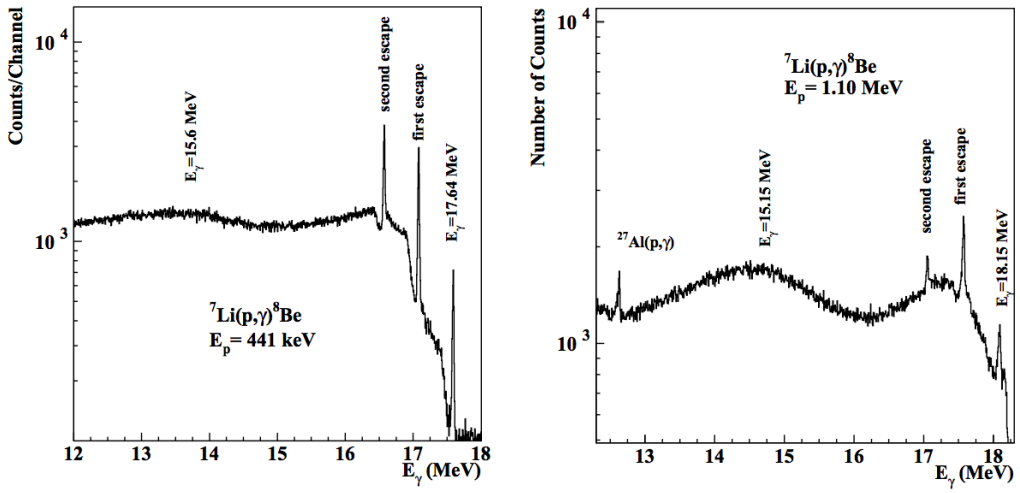

Figure 1.11: Typical gamma-ray spectrum measured with a 470 cm^3 HPGe detector from ^{7}Li(p, γ)^{8}Be at E_p = 440 keV (left) and at E_p = 1100 keV (right). Figures from [25].

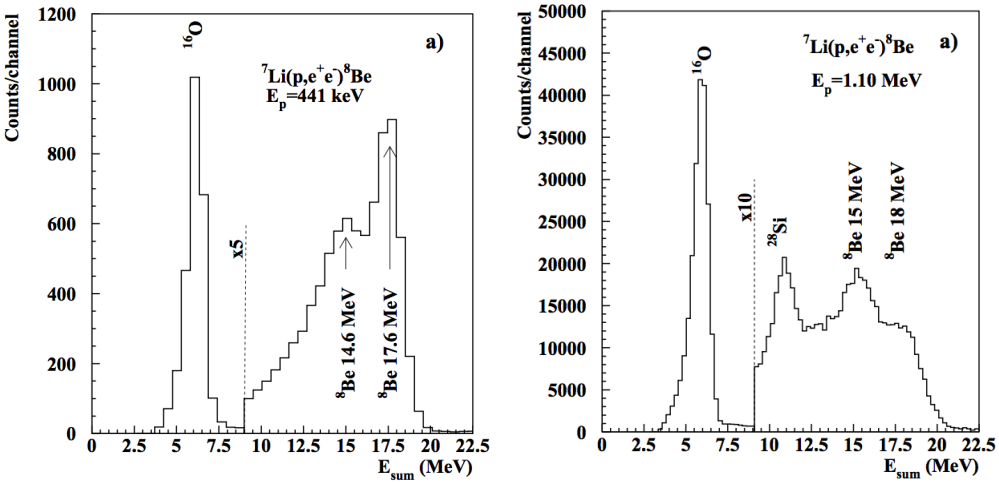

Figure 1.12: Typical E_{sum} spectrum extracted from spectrometer data from ^{7}Li(p, e$^+$e$^-$)^{8}Be at E_p = 440 keV (left) and at E_p = 1100 keV (right). Figures from [1].

The Atomki spectrometer was designed to reconstruct the angular opening of coincident electron-positron pairs. The angular opening spectrum from $^{7}\mathrm{Li}(\mathrm{p},\mathrm{e}^{+}\mathrm{e}^{-})^{8}\mathrm{Be}$ at $E_{\mathrm{p}} = 440$ keV and at $E_{\mathrm{p}} = 1100$ keV are shown in Fig. 1.13 for $|y| < 0.5$.

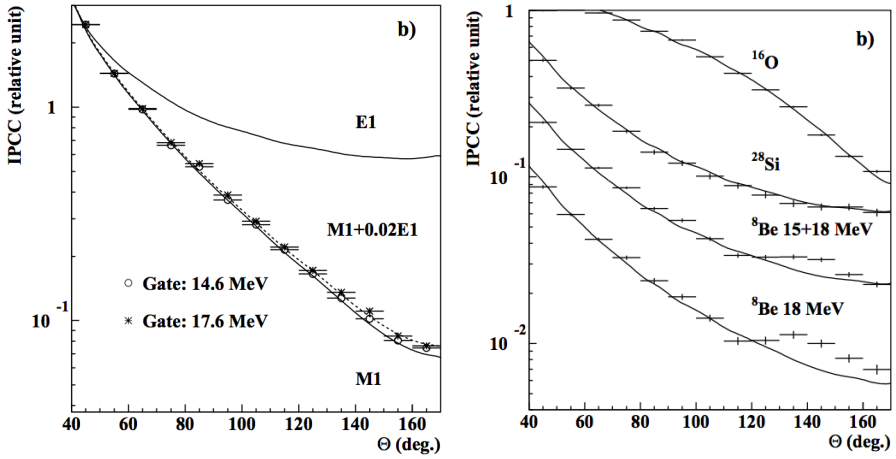

Figure 1.13: (Left) Experimental angular opening spectrum extracted from spectrometer $\mathrm{e}^{+}\mathrm{e}^{-}$ data from $^{7}\mathrm{Li}(\mathrm{p},\mathrm{e}^{+}\mathrm{e}^{-})^{8}\mathrm{Be}$ at $E_{\mathrm{p}} = 440$ keV for transition to first excited state (14.6 MeV gate) or to ground state (17.6 MeV gate). The data points are compared with a simulation assuming a pure M1 (full line), a pure E1 (full line) or a mixed M1+E1 transition (dashed line). (Right) Experimental angular opening spectrum extracted from spectrometer $\mathrm{e}^{+}\mathrm{e}^{-}$ data from $^{7}\mathrm{Li}(\mathrm{p},\mathrm{e}^{+}\mathrm{e}^{-})^{8}\mathrm{Be}$ at $E_{\mathrm{p}} = 1100$ keV (right) for transition to first excited state (15 MeV gate) or to ground state (18 MeV gate). The ^{8}Be data points are compared with a simulation assuming an M1+E1 transition. Figures from [1].

The raw spectra are corrected for the detector response shown in Fig. 1.8. The distributions can be shown separately for the transition to ground state and to first excited state making a selection of the E_{sum}, called 14.6 MeV (or 15 MeV) gate and 17.6 MeV (or 18 MeV) gate. The data points are fitted with a Monte-Carlo simulation of the angular opening distribution assuming a mix of a pure M1 (resonant) and a pure E1 (non-resonant) transition introduced in Fig. 1.7. The amplitudes of each multipole are left free in the fit. At $E_{\mathrm{p}} = 440$ keV, the data points are well interpreted by a mix (dashed line) of M1 and E1 transition, E1 representing 2% of the total number of pairs. A pure M1 transition is not able to fully explain the data, a small deviation above 110° is observed. However, adding a small contribution from the flatter simulated E1 angular opening shape

accounts well for the shape of the data points at large angles. The fit is consistent with the theory, the ^{8}Be*(17.6) transition to ground state being dominated by an M1 contribution along with a small contribution from non-resonant E1 (see Fig. 1.4). The ^{16}O and ^{28}Si are also well described by the model (full line). For ^{8}Be at $E_{\mathrm{p}} = 1100$ keV, the IPC shape was again fitted assuming an M1+E1 mixed transition and estimated to be M1+23%E1. As expected from Fig. 1.4, the non-resonant contribution is increased in the 18.1 MeV transition with respect to the 17.6 MeV transition. However, the data at $E_{\mathrm{p}} = 1100$ keV at 18 MeV cannot be explained by the IPC model used by Atomki. An excess of events at angles close to 140° is observed above the expected monotonously decreasing IPC shape. The anomaly is mitigated when including the 15 MeV energy sum pairs, pointing towards an anomaly occurring in the transition of ^{8}Be*(18.1) to ground state. No M1+E1 mixed transition was able to explain the excess.

The group also performed a proton energy scan, measuring the angular opening shape from ^{7}Li(p, e^{+}e^{-})^{8}Be at various proton energies: $E_{\mathrm{p}} = 1.20$ MeV, $E_{\mathrm{p}} = 1.10$ MeV, $E_{\mathrm{p}} = 1.04$ MeV and $E_{\mathrm{p}} = 0.8$ MeV. It is clear that the anomaly disappears when E_{p} is above or below the resonance (center at $E_{\mathrm{p}} = 1.03$ MeV). Moreover, the excess appears more significant at $E_{\mathrm{p}} = 1.10$ MeV than at $E_{\mathrm{p}} = 1.04$ MeV. This was interpreted by accounting for an estimated O(100 keV) proton energy loss in the target, allowing the 1.10 MeV proton beam to reach the center of the resonance at 1.03 MeV. These datasets highlight an anomaly associated with the 1.03 MeV resonance.

The event excess measured at $E_{\mathrm{p}} = 1.10$ MeV has a significance of 6.8σ. The Atomki group tried to explain such an anomaly by the emission of a neutral massive boson by the excited ^{8}Be*(18.1) nucleus, the boson subsequently decaying to an electron-positron pair.

$$\mathrm{p} + {}^{7}\mathrm{Li} \rightarrow {}^{8}\mathrm{Be}^{*} \rightarrow {}^{8}\mathrm{Be} + X, X \rightarrow \mathrm{e}^{+}\mathrm{e}^{-} \tag{1.6}$$

In the boson reference frame, the electron-positron pair is emitted back-to-back. Due to the boost of the boson with respect to the lab frame, the electron-positron pair will be reconstructed with $\Theta < 180°$ in the lab frame. The higher the boson boost, the lower its associated Θ. The isotropic emission of such a hypothetical boson was simulated for a range of boson masses. The data were fitted summing the IPC M1+E1 background and the boson electron-positron decay in Fig. 1.15 and minimizing the χ^2. A strikingly good fit, with reduced $\chi^2_{red} = 1.07$, was found with such a model and assuming a boson mass of 16.7 MeV/c^2.

Assuming the 18.1 MeV M1 IPC coefficient [10] to be 3.9×10^{-3} and $\mathcal{BR}(X \rightarrow \mathrm{e}^{+}\mathrm{e}^{-}) = 100\%$, the group estimated the boson to γ branching ratio from the best χ^2 fit to be 5.8×10^{-6}. The boson mass was determined to be $m_0 = 16.70 \pm 0.35$(stat) MeV/c^2. On top of the quoted statistical uncertainty on the mass, an

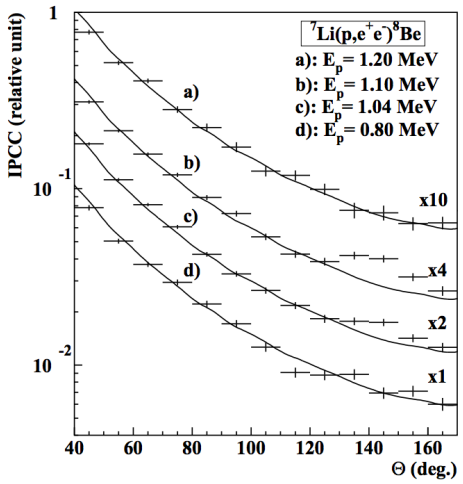

Figure 1.14: Experimental angular opening spectrum extracted from spectrometer e^+e^- data from ^{7}Li(p, e^+e^-)^{8}Be at $E_p = 1.20$ MeV, $E_p = 1.10$ MeV, $E_p = 1.04$ MeV and $E_p = 0.8$ MeV. The data points are compared with a simulation assuming a mixed M1+E1 transition (full line). Figure from [1].

additional 0.5 MeV/c^2 systematic uncertainty stems from a $\Delta\Theta = 6°$ uncertainty on the position of the spectrometer. A boson decay is expected to have a negligible contribution at $|y| \geq 0.5$. The absence of an anomaly for this dataset supports the boson decay hypothesis. Finally, the analysis and simulation were reproduced looking into the electron-positron invariant mass (see Fig. 1.15). Again, an event excess close to 17 MeV/c^2 is observed leading to the "X17" nickname for the hypothetical boson.

Updated results

In 2017 [25], the Atomki group re-investigated the anomaly observed previously in ^{7}Li(p,e^+e^-)^{8}Be after replacing the MWPCs by DSSSDs. The electron-positron angular opening spectra from the decay of both the ^{8}Be*(17.6) and the ^{8}Be*(18.1) states were studied. The experimental data are shown in Fig. 1.16. While not observed in the previous study, an anomalous excess of events is observed in the ^{8}Be*(17.6) state decay, at $E_p = 441$ keV. According to the group, this difference is due to the improvement of the apparatus. The fit method was updated and now uses a probability density function (PDF) defined as:

$$PDF(e^+e^-) = N_{bkg}PDF(IPC) + N_{sig}PDF(signal) \tag{1.7}$$

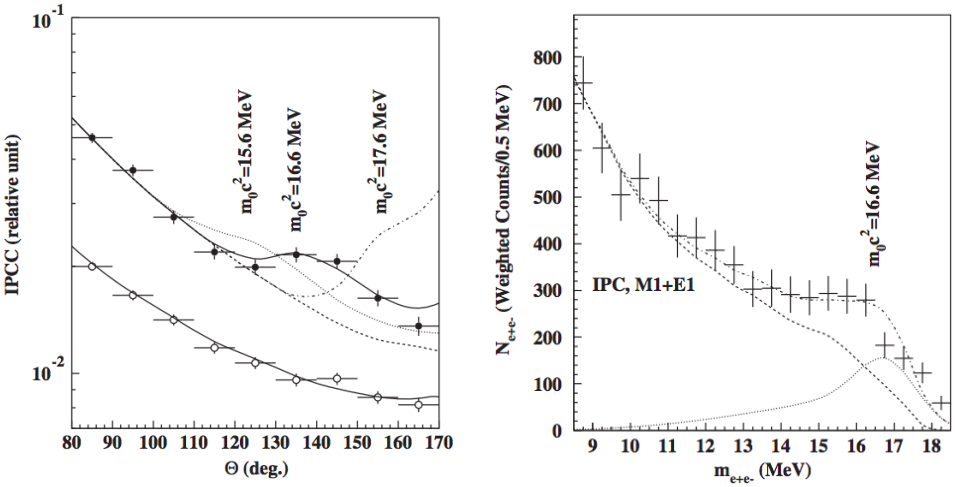

Figure 1.15: (Left) Experimental angular opening spectrum at $E_{\mathrm{p}} = 1.1$ MeV for $|y| < 0.5$ (closed circles) and $|y| \geq 0.5$ (open circles). The $|y| < 0.5$ data points are compared with a simulation assuming a mixed M1+E1 IPC only (dashed line) or the sum of a mixed M1+E1 IPC background and a neutral boson e^+e^- decay. Three hypotheses for the boson mass are shown: 15.6 MeV/c^2 (dotted line), 16.6 MeV/c^2 (full line) or 17.6 MeV/c^2 (dash-dotted line). (Right) Experimental invariant mass spectrum at $E_{\mathrm{p}} = 1.1$ MeV for $|y| < 0.5$ (closed circles). The data points are compared with a simulation assuming a mixed M1+E1 IPC (dashed line), a 16.6 MeV/c^2 neutral boson e^+e^- decay (dotted line) and the sum of both (dash-dotted line). Figures from [1].

.

with N_{bkg} and N_{sig} the fitted number of background and signal events respectively.

The data were fitted with a mixed M1+E1 IPC background and an additional boson decay. The signal PDF is two-dimensional, introducing the dependence between the simulated boson mass and the electron-positron angular opening. The best fit gives $m_0 = 17.0 \pm 0.2$ MeV/c^2, consistent with the boson mass extracted previously. The boson to γ branching ratio from the best fit is 4.0×10^{-6}.

The anomaly in the decay of the ^{8}Be*(18.1) state was also re-investigated making use of the improved spectrometer and a proton beam energy of 1100 keV. Fig. 1.16 shows the electron-positron angular opening spectrum for 13 MeV $\leq E_{sum} \leq$ 20 MeV, therefore including both the transitions to ground state and to first excited state. The branching ratio was found to be 6.8×10^{-6} and the boson mass is consistent with the X17 hypothesis.

In 2018, the Atomki group repeated the measurement at 18.1 MeV. They used

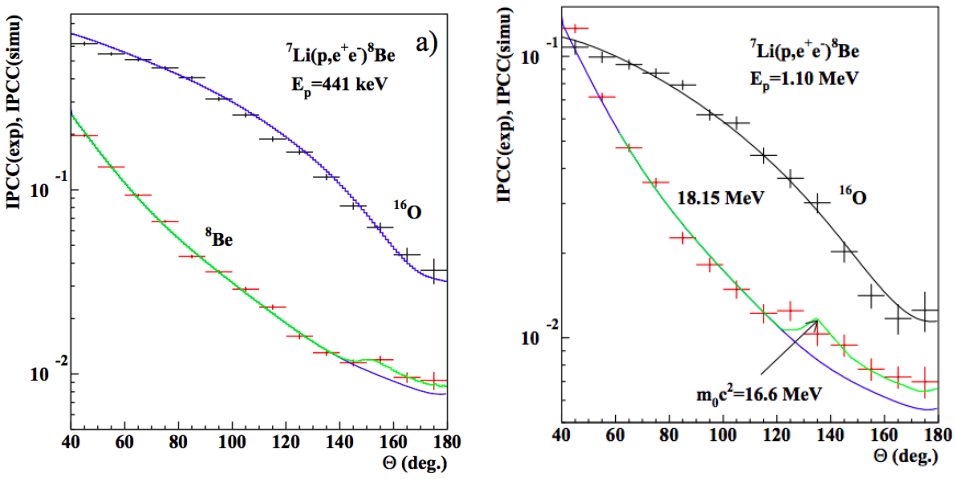

Figure 1.16: Experimental angular opening spectrum extracted from spectrometer e^+e^- data from $^{7}\mathrm{Li}(\mathrm{p},\mathrm{e}^+\mathrm{e}^-)^{8}\mathrm{Be}$ and $^{19}\mathrm{F}(\mathrm{p},\alpha\mathrm{e}^+\mathrm{e}^-)^{16}\mathrm{O}$ at E_p = 440 keV (left) and E_p = 1.10 MeV (right). The ^{8}Be data points (red) are compared with a simulation (green) assuming a mixed M1+E1 IPC background and a 16.6 MeV/c^2 boson electron-positron decay. Figures from [25].

.

an improved spectrometer (see Sec. 1.3.1) with one additional telescope and developed a cosmic-ray background suppression method. The new data is shown in Fig. 1.17 along with data from Fig. 1.13 [1]. Both datasets are in good agreement. The anomalous excess of events is still present and the data is fitted using Eq. 1.7.

The results of the fit are shown in Tab. 1.1. Previous results refers to 2016 dataset [1] with the old χ^2 fit. Exp1 refers to the same dataset fitted with the new PDF fit based on Eq. 1.7. Exp2 refers to 2018 dataset [26] shown in Fig. 1.17 with the PDF fit. The best-fit mass differs by 0.3 MeV/c^2 and could be due to an unstable beam position in Exp1. Indeed, a mm order variation of the beam spot leads to a non-negligible systematic uncertainty.

	Previous res.	Exp1	Exp2	Average
m_0c^2(MeV)	16.7(51)	16.86(6)	17.17(7)	17.01(16)
B_X	5.8×10^{-6}	$6.8(10) \times 10^{-6}$	$4.7(21) \times 10^{-6}$	$6(1) \times 10^{-6}$
Significance	6.8σ	7.37σ	4.90σ	

Table 1.1: Summary of Atomki's fit results (rest mass m_0, branching ratio wrt. γ B_X and significance) on $^{7}\mathrm{Li}(\mathrm{p},\mathrm{e}^+\mathrm{e}^-)^{8}\mathrm{Be}$ at $E_\mathrm{p} = 1.1$ MeV with neutral boson decay hypothesis. Reproduced from [26].

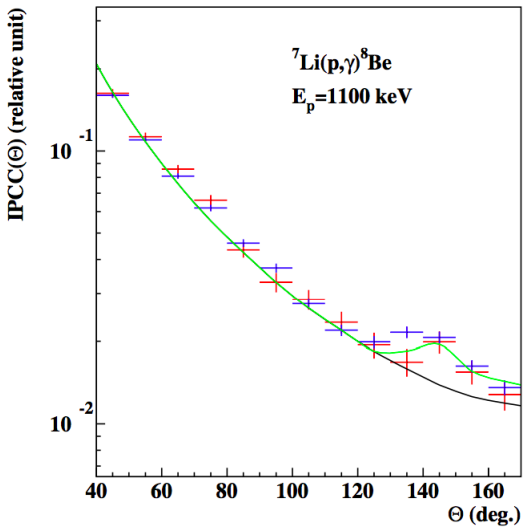

Figure 1.17: Experimental angular opening spectrum extracted from spectrometer e^+e^- data from $^{7}\mathrm{Li}(p, e^+e^-)^{8}\mathrm{Be}$ at $E_p = 1.10$ MeV for old (blue) and new (red) data. The ^{8}Be data points (red) are compared with a simulation (green) assuming a mixed M1+E1 and a boson electron-positron decay. The black curve shows the simulation for IPC only. Figure from [26].

.

The average of Exp1 and Exp2 gives a rest mass $m_0 = 17.01(16)$ MeV/c^2 and a boson to γ branching ratio of $B_X = 6(1) \times 10^{-6}$, corresponding to a partial width $\Gamma_X = 1.2 \times 10^{-5}$ eV. The results obtained with several datasets using two different apparatus give strength to the existence of an anomaly in Internal Pair Conversion from the $^{7}\mathrm{Li}(p, e^+e^-)^{8}\mathrm{Be}$ reaction. The X17 hypothesis, a 17 MeV/c^2 neutral boson emitted by the excited ^{8}Be nucleus and subsequently decaying to an electron-positron pair, provides one potential explanation for the anomaly.

1.3.3 Anomalies in $^{3}\mathrm{H}(p, e^+e^-)^{4}\mathrm{He}$ and $^{11}\mathrm{B}(p, e^+e^-)^{12}\mathrm{C}$

Anomaly in ^{4}He

In 2019, the Atomki group made use of the previous apparatus to study the $^{3}\mathrm{H}(p, e^+e^-)^{4}\mathrm{He}$ reaction [19, 20], shooting protons at a tritium target and reconstructing the coincident electron-positron pairs with a six-telescope spectrometer (see Sec. 1.3.1). In [27], Tilley et. al. introduce the energy levels of the ^{4}He nucleus. Its low-energy spectrum is represented in Fig. 1.18.

The group studied the electron-positron spectra of the transition from the 21.01 MeV 0^- state to the 0^+ ground state. They used protons at $E_p = 900$ keV

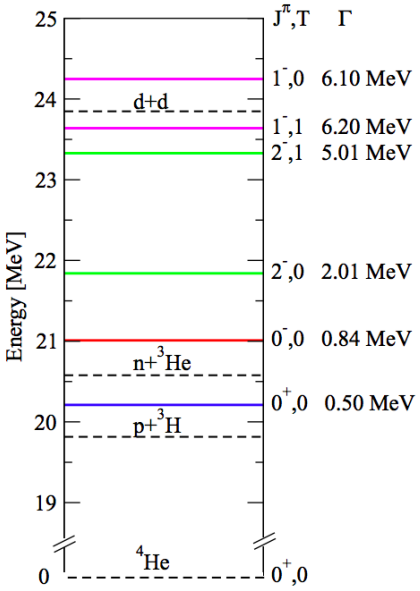

Figure 1.18: ^{4}He most relevant energy states with associated spin-parity J^P, isospin T and decay width Γ based on [27]. Resonance energies and energy thresholds for specific ^{4}He decay channels are indicated with full and dashed lines respectively. Two states are of particular importance for this work, the 20.21 and 21.01 MeV energy states (full blue and red lines respectively). Figure from [28].

to populate the wide ($\Gamma = 0.84$ MeV) 21.01 MeV. It should be noted that due to the close energies and the large widths of the 20.21 and 21.01 MeV excited states, they are both populated at such proton energies. Both contributions were not disentangled by Atomki. The proton energy was set to be below the 1018 keV energy threshold for the ^{3}H(p,n)^{3}He reaction and the reaction is therefore forbidden. This proton energy leads to an effective ^{4}He* nucleus energy of $E = 20.49$ MeV. In Fig. 1.19, the electron-positron energy sum spectrum after background subtraction shows a clear enhancement above 20 MeV, representing the excited ^{4}He* state energy.

A signal and a background region were defined based on E_{sum} with 19.5 MeV $\leq E_{sum} \leq$ 22.0 MeV and 5.0 MeV $\leq E_{sum} \leq$ 19.0 MeV respectively. Pairs with $|y| \leq 0.5$ from both these regions were selected to build the angular opening and invariant mass spectrum in Fig. 1.20. The background angular opening spectrum was fitted with a fourth-order exponential polynomial background and is monotonously decreasing. Due to the large amount of material related to the target cooling system, the gamma conversion in matter or EPC is the dominant background contribution. Another background comes from the IPC E0 transition $0^{+}(fes) \rightarrow 0^{+}(gs)$,

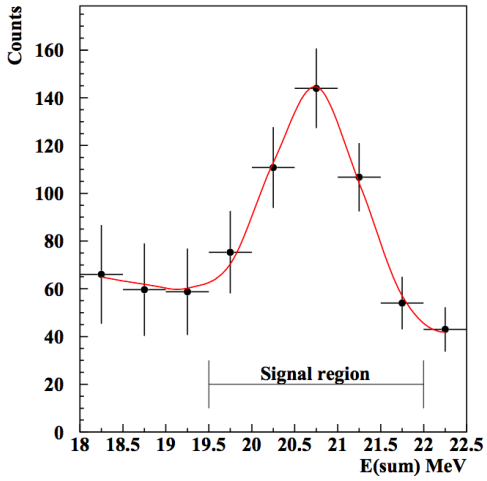

Figure 1.19: Electron-positron energy sum spectrum from ^{3}H(p, e^{+}e^{-})^{4}He at E_{p} = 900 keV after background subtraction. Details on the procedure can be found in [19]. Figure from [19].

fes and *gs* being the first excited state and ground state respectively. The cosmic ray background was subtracted. The fitted curve in the background region is matched to the data in the signal region for $40° \leq \Theta \leq 90°$. The background is not able to match the data at larger angles and a 7.2σ significant excess of events is observed at angles above 100°, the structure being similar to the one observed in ^{8}Be. The excess was again interpreted as the electron-positron decay of a neutral boson whose mass was left free in the fit (procedure introduced in 1.3.2). The best fit resulted in a boson mass $m_X = 16.84 \pm 0.16(\mathrm{stat}) \pm 0.20(\mathrm{syst})$ MeV/c^2 and a partial width $\Gamma_X = 3.9 \times 10^{-5}$ eV. In the invariant mass spectrum, the excess of events around 17 MeV/c^2 is again present. These anomalies are in striking agreement with the X17 hypothesis.

In [20], the study was repeated at $E_{\mathrm{p}} = 510$, 610 and 900 keV. The anomalous excess is observed at all three energies. Due to the large widths of the 20.21 and 21.01 MeV ^{4}He* states, it is unclear whether the anomaly arises from one of the two resonant states or from direct proton capture. The results are again consistent with the creation and subsequent decay of a light neutral boson of ≈ 17 MeV/c^2.

Anomaly in ^{12}C

With the same apparatus, the Atomki group also studied the electron-positron angular opening spectrum from the ^{11}B(p, e^{+}e^{-})^{12}C reaction at proton energies E_{p} = 1.50, 1.70, 1.88, 2.10 and 2.50 MeV. The excited levels of ^{12}C are introduced in [29]. The group studied the E1 transition from the 17.23 MeV 1^{-}

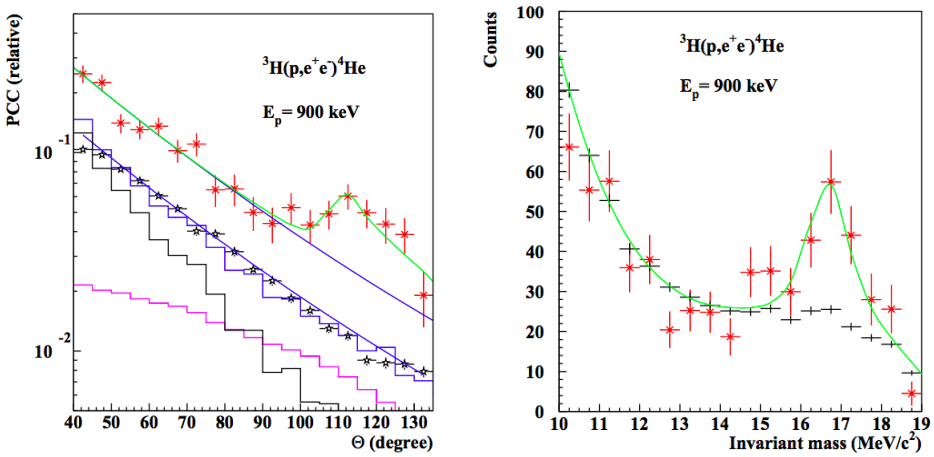

Figure 1.20: Experimental angular opening (left) and invariant mass (right) spectrum from ^{3}H(p, e$^+$e$^-$)^{4}He at $E_{\mathrm{p}} = 900$ keV with 19.5 MeV $\leq E_{sum} \leq$ 22.0 MeV (red crosses) and 5.0 MeV $\leq E_{sum} \leq$ 19.0 MeV (black crosses). The datasets are fitted with a fourth-order exponential polynomial background (blue curve). The background can be explained by two contributions: EPC (black histogram) and IPC E0 (magenta histogram). The red dataset is compared with the sum of the background and a simulated electron-positron decay from a 17 MeV/c^2 boson (green curve). Figures from [19].

.

^{12}C* state to the 0$^+$ ^{12}C ground state. The associated resonant proton energy is $E_{\mathrm{p}} = 1.388$ MeV. Due to its large cross-section, the transition is widely used in particle and nuclear physics for detector calibration. Making use of the wide resonance associated with ^{12}C*, the Atomki group manufactured a relatively thick (2 mg/cm^2)^{11}B target with an estimated 300 keV energy loss. The 17.23 MeV ^{12}C* state can also decay to an intermediate 4.44 MeV 2$^+$ state leading to an $E = 12.76$ MeV transition. The group built the electron-positron energy sum spectrum at $E_{\mathrm{p}} = 1.70$ MeV. It is shown in Fig. 1.21. The 17.23 MeV transition as well as the 12.76 MeV transition are both observed as clear peaks. A few hundreds of keV shift with respect to the mentioned transition energy is observed and is due to the additional energy provided at $E_{\mathrm{p}} = 1.70$ MeV with respect to the resonant proton energy $E_{\mathrm{p}} = 1.388$ MeV.

The electron-positron spectra from the 17.23 MeV transition at the investigated E_{p} are shown in Fig. 1.22. The monotonously decreasing shape of the background is broken at angles above 140° due to a bump-like excess of events. While the region below 140° can be well fitted by including an E1-M1 mixed IPC contribution and

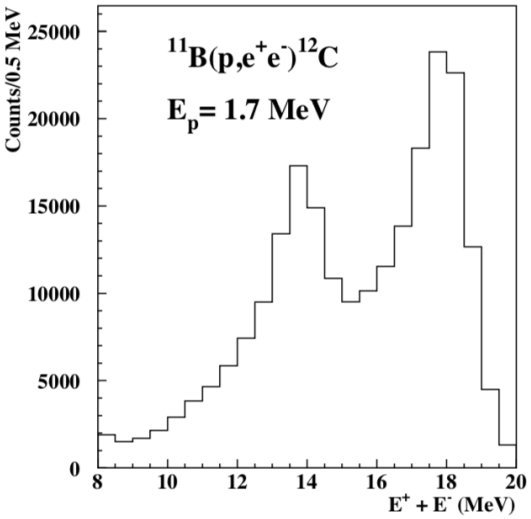

Figure 1.21: Electron-positron energy sum spectrum from $^{11}\mathrm{B}(\mathrm{p}, \mathrm{e}^{+}\mathrm{e}^{-})^{12}\mathrm{C}$ at $E_{\mathrm{p}} = 1.70$ MeV. Figure from [19].

an EPC one, it doesn't explain the larger angles.

Including in the model the electron-positron decay of a boson whose mass is close to 17 MeV/c^2 provides, once again, good compatibility with the datasets. A summary of the fitted mass and branching ratio is provided in Tab. 1.2. The table quotes the statistical uncertainties while an additional systematic uncertainty of $\Delta m_0 = \pm 0.20$ MeV/c^2 was estimated due to uncertainty on the beam spot position.

E_{p}	B_X	m_0c^2	Significance
(MeV)	$\times 10^{-6}$	(MeV/c^2)	
1.50	1.1(6)	16.81(15)	3σ
1.70	3.3(7)	16.93(8)	7σ
1.88	3.9(7)	17.13(10)	8σ
2.10	4.9(21)	17.06(10)	3σ
Averages	3.6(3)	17.03(11)	

Table 1.2: Summary of Atomki's fit results (rest mass m_0, branching ratio wrt. γ, B_X and significance) on $^{11}\mathrm{B}(\mathrm{p}, \mathrm{e}^{+}\mathrm{e}^{-})^{12}\mathrm{C}$ for various proton energies E_{p} with neutral boson decay hypothesis. Reproduced from [21].

All anomalies in the electron-positron angular opening spectra emitted by ^{8}Be, ^{4}He and ^{12}C excited states can be interpreted by the electron-positron decay of a massive neutral boson and are consistent with a boson rest mass close to 17 MeV/c^2, a new particle beyond the Standard Model. We will see next whether

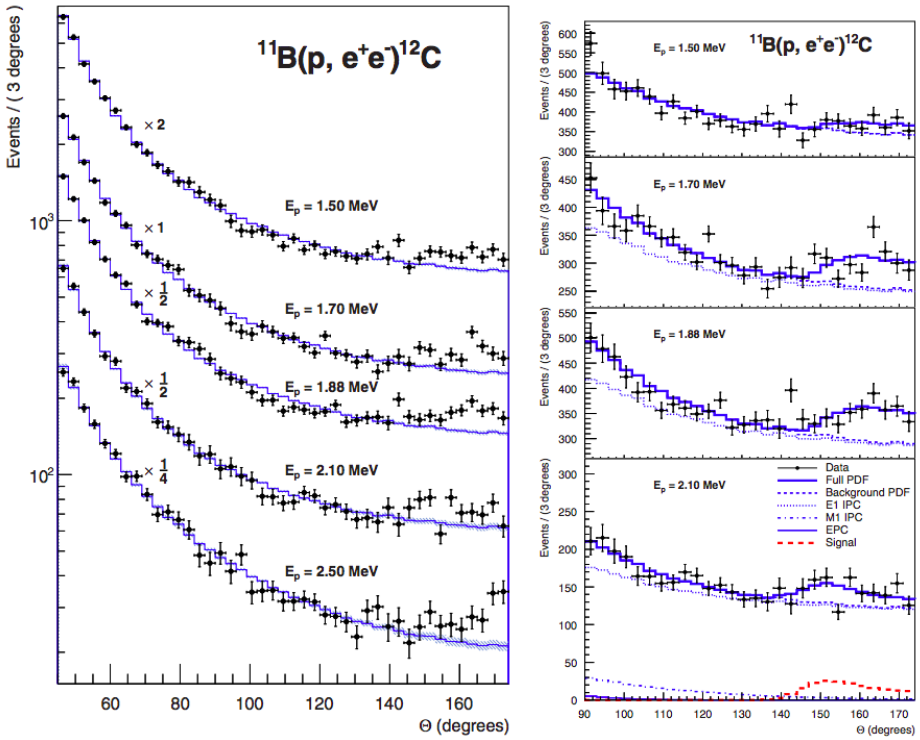

Figure 1.22: Experimental angular opening spectrum from ^{11}B(p, e$^+$e$^-$)^{12}C and associated best fit without (left) and with the electron-positron decay hypothesis. The full background (dashed blue histogram) can be divided into three contributions, E1 IPC (dotted blue histogram), M1 IPC (dash-dotted blue histogram) and EPC (thin blue histogram). The signal shape is indicated with a red histogram. The full PDF, sum of signal and background, is shown as a thick blue histogram. Figures from [19].

.

other interpretations within the Standard Model are viable. We will also combine Atomki results with other experiments' published results in order to determine the possible nature of an X17 particle.

Chapter 2

Theoretical interpretations of the X17 anomaly and experimental efforts

The Atomki group reported striking anomalies in the electron-positron angular distributions from several excited nuclei, sparking considerable interest among nuclear and particle physics theorists who try and uncover the physics underlying these observations. Various explanations were proposed within the Standard Model framework, including an improved IPC background model and higher-order QED corrections for the ^{8}Be*(18.1) decay, explored in the first section of this chapter. Not fully satisfactory, these interpretations led to suggesting the existence of a massive neutral boson, vector of a fifth fundamental force of nature. This hypothesis is examined in the second part of the chapter. We will see how the Atomki anomalies, alongside null results from other experiments using complementary channels, can shed light on the nature of a possible X17 particle. Tab. 2.1 summarizes possible interpretations of the anomaly and assesses their viability. Finally, ongoing experimental efforts aimed at further investigating the Atomki anomaly will be reviewed.

Authors use various notations to refer to the electron-positron angular opening, including Θ, θ_{+-}, θ_{ee}, $\theta_{e^+e^-}$, Angle between Particles, and Angular Opening. Despite the different labels, they all represent the same observable. This work will most often use Angular Opening. It should not be confused with θ, which represents the polar angle in MEG-II's cylindrical coordinate system.

2.1 Standard Model interpretation of the Atomki anomalies

2.1.1 Refined IPC models: Zhang-Miller and Gysbers

In [7], Zhang and Miller advanced the idea that the IPC simulations used by Atomki, relying on Rose's precursor model, were incomplete. The latter indeed neglected both the anisotropy of the photon emission and the interferences between the multipoles. As a remedy, Zhang and Miller included both these effects

Model	Process	Result
Within the Standard Model		
Improved IPC models [7, 8, 28]	$^{7}\mathrm{Li}\,(\mathrm{p}, \mathrm{e}^{+}\mathrm{e}^{-})\,^{8}\mathrm{Be}$ $^{3}\mathrm{H}\,(\mathrm{p}, \mathrm{e}^{+}\mathrm{e}^{-})\,^{4}\mathrm{He}$	Cannot explain a bump-like structure.
NLO QED [30]	$^{7}\mathrm{Li}\,(\mathrm{p}, \mathrm{e}^{+}\mathrm{e}^{-})\,^{8}\mathrm{Be}$	Bump compatible with the anomaly.
Hard $\gamma\gamma$ process [31]	$^{7}\mathrm{Li}\,(\mathrm{p}, \mathrm{e}^{+}\mathrm{e}^{-})\,^{8}\mathrm{Be}$	Bump compatible with the anomaly. Cannot explain the absence of excess at 440 keV.
Beyond the Standard Model		
New vector particle	$^{7}\mathrm{Li}\,(\mathrm{p}, \mathrm{e}^{+}\mathrm{e}^{-})\,^{8}\mathrm{Be}$ $^{3}\mathrm{H}\,(\mathrm{p}, \mathrm{e}^{+}\mathrm{e}^{-})\,^{4}\mathrm{He}$ $^{11}\mathrm{B}\,(\mathrm{p}, \mathrm{e}^{+}\mathrm{e}^{-})\,^{12}\mathrm{C}$	Strong constraints from existing results leads to protophobic property. Disfavoured by absence of anomaly at lower E_{p} In good agreement with measured decay widths. Disfavoured by $^{12}\mathrm{C}$ anomaly observation.
New axial vector particle	$^{7}\mathrm{Li}\,(\mathrm{p}, \mathrm{e}^{+}\mathrm{e}^{-})\,^{8}\mathrm{Be}$ $^{3}\mathrm{H}\,(\mathrm{p}, \mathrm{e}^{+}\mathrm{e}^{-})\,^{4}\mathrm{He}$ $^{11}\mathrm{B}\,(\mathrm{p}, \mathrm{e}^{+}\mathrm{e}^{-})\,^{12}\mathrm{C}$	No constraints from π^{0} decay. Can explain the absence of anomaly at 440 keV. In rough agreement with measured decay widths. Most promising solution.
New pseudoscalar particle	$^{7}\mathrm{Li}\,(\mathrm{p}, \mathrm{e}^{+}\mathrm{e}^{-})\,^{8}\mathrm{Be}$ $^{3}\mathrm{H}\,(\mathrm{p}, \mathrm{e}^{+}\mathrm{e}^{-})\,^{4}\mathrm{He}$ $^{11}\mathrm{B}\,(\mathrm{p}, \mathrm{e}^{+}\mathrm{e}^{-})\,^{12}\mathrm{C}$	Contradicts measured decay widths. Observation of excess in $^{12}\mathrm{C}$ incompatible with pseudoscalar hypothesis.
New scalar particle	$^{7}\mathrm{Li}\,(\mathrm{p}, \mathrm{e}^{+}\mathrm{e}^{-})\,^{8}\mathrm{Be}$	Violates parity conservation.

Table 2.1: Summary of possible interpretations of the Atomki anomalies. Adapted from [32].

in an IPC model adapted from the Halo Effective Field Theory (EFT) [33]. The schematic Feynman representation of the $^{7}\mathrm{Li}\,(\mathrm{p},\gamma)\,^{8}\mathrm{Be}$ and $^{7}\mathrm{Li}\,(\mathrm{p},\mathrm{e}^{+}\mathrm{e}^{-})\,^{8}\mathrm{Be}$ processes are shown in Fig. 2.1, with θ the angle between the incoming proton and the outgoing photon and θ_{+-} the electron-positron angular opening.

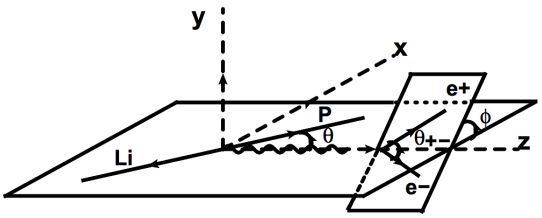

Figure 2.1: Feynman schematic representation of the IPC process from $^{7}\mathrm{Li}\,(\mathrm{p},\mathrm{e}^{+}\mathrm{e}^{-})\,^{8}\mathrm{Be}$. Figure from [7].

.

The astrophysical S factor, proportional to the photon production cross section was written:

$$S = e^{2\pi\eta} E \times \frac{\mathrm{d}\sigma_\gamma}{\mathrm{d}\cos\theta}, \quad \frac{\mathrm{d}\sigma_\gamma}{\mathrm{d}\cos\theta} = \frac{M}{4\pi}\frac{\omega}{p}\frac{1}{8}\sum_{a,\sigma,\lambda}|\mathcal{M}_\gamma|^2 \tag{2.1}$$

$$\sum_{a,\sigma,\lambda}|\mathcal{M}_\gamma|^2 = T_0 + T_1 P_1(\cos\theta) + T_2 P_2(\cos\theta) \tag{2.2}$$

with $M = \frac{M_n M_c}{(M_n+M_c)}$, M_n and M_c the proton and Li masses, ω and E are the photon and proton energy respectively, p is the proton momentum, $\eta = \frac{k_c}{p}$ with $k_c = Z_{\mathrm{Li}} Z_p \alpha_{em} M$, P_i is the i^{th} Legendre polynomial. Each T_i coefficient includes M1, E1, E2 contributions and their interferences. On the contrary of Atomki, E2 contribution was included in order to estimate its weight on the total cross-section. This formulation puts forward the dependence on the photon direction θ. The model parameters were extracted from a fit of published datasets studying $^{7}\mathrm{Li}\,(\mathrm{p},\gamma)\,^{8}\mathrm{Be}$ astrophysical S factor [5] and anisotropy [34, 35]. The best fit is shown in Fig. 2.2. All variables are shown as a function of lab proton energy E_{lab}. The top plot shows the astrophysical S factor and E1 and E2 contributions. E2's is found to be negligible compared to E1 and M1's. The second plot compares the cross-section of the photon production at $\theta = 0°$ and $\theta = 150°$. The photon emission is clearly anisotropic at the $^{8}\mathrm{Be}^{*}(17.6)$ resonance close to $E_{lab} = 1.0$ MeV. The last two plots correspond to $a_1 = T_1/T_0$ and $a_2 = T_2/T_0$. The full model (in red) agrees well with the data (in black) for all datasets, except for a_2 at $E_{lab} \geq 1$ MeV, though the data suffers large error bars in this region.

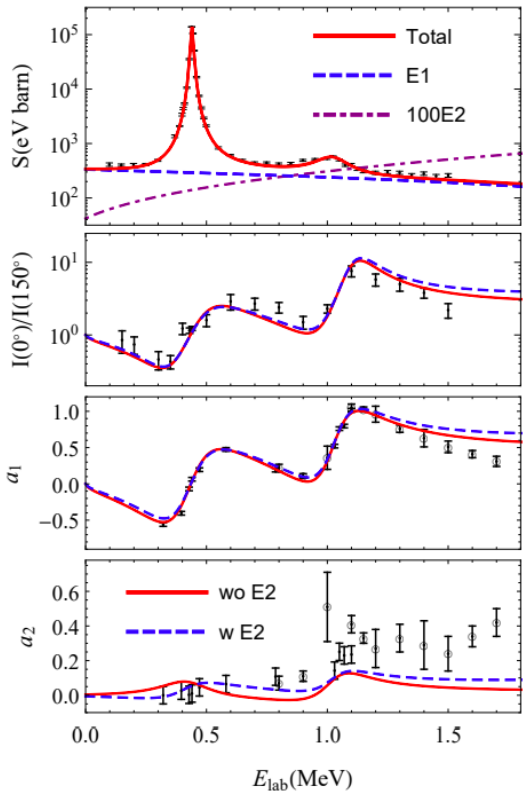

Figure 2.2: Astrophysical S factor, anisotropy and a_i coefficients of the $^7\mathrm{Li}\,(\mathrm{p},\gamma)\,^8\mathrm{Be}$ reaction as a function of lab proton energy E_{lab}. The full model in red is compared to the datasets in black from [5, 35, 34]. The E1 and 100×E2 multipole contributions are shown as blue and purple dashed lines respectively. The red full line includes M1, E1 and E2 contributions altogether. Figure from [7].

.

Adding the lepton line to the photon line, the electron-positron pair cross-section can be computed:

$$M_{+-}^4 \sum |\mathcal{M}_{e^+e^-}|^2 /2 = T_{0,0} + T_{0,2}\cos 2\phi + T_{1,0}P_1 + T_{2,0}P_2 + T_{2,2}P_2\cos 2\phi \quad (2.3)$$
$$+ T_{3,1}\sin\theta\cos\phi + T_{4,1}\sin 2\phi\cos\phi$$

The $T_{0,0}$ contribution to the cross-section and its E1, M1 and E2 subcontributions are plotted in Fig. 2.3. The curves are shown at $^8\mathrm{Be}^*(18.1)$ resonant proton energy and for two values of the electron-positron energy asymmetry y, $y = 0$ or $y = 0.8$. All eight curves are monotonously decreasing as a function of θ_{+-}.

These subcontributions are equivalent to Rose's model for each multipole. The angular-dependent terms from Eq. 2.3 were neglected by Rose.

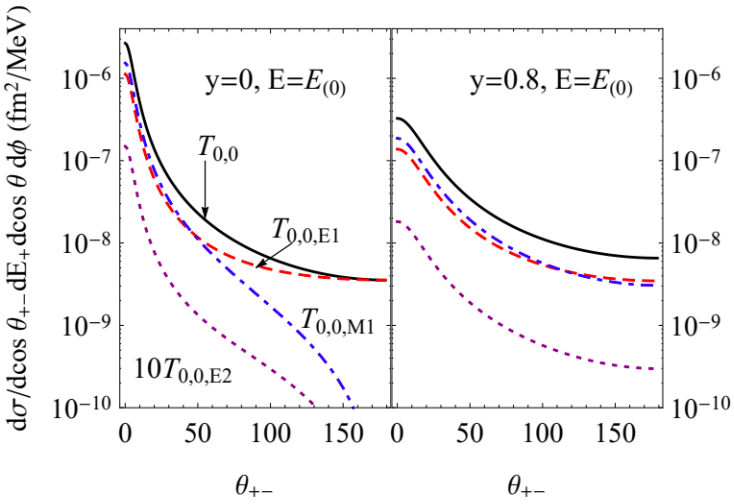

Figure 2.3: $T_{0,0}$ contribution to the ^{7}Li (p, e$^+$e$^-$) ^{8}Be Zhang-Miller cross-section as a function of the angular opening θ_{+-} and the E1, M1 and E2 subcontributions at the ^{8}Be*(18.1) resonant proton energy (center-of-momentum proton energy $E = E_{(0)} = 0.895$ MeV) at $y = 0$ (left) and $y = 0.8$ (right). Figure from [7].

.

By including the other $T_{i,j}$ terms, one can draw the total cross-section as a function of the invariant mass M_{+-} and angular opening θ_{+-}. These are shown in Fig. 2.4 along with the Atomki datasets and background simulations. The Zhang-Miller model is in good agreement with Atomki's IPC simulations in invariant mass but differs in the angular opening. They suggest detector efficiency variations as a possible explanation. Nonetheless, this first version of the model used by Zhang-Miller is monotonously decreasing and unable to explain a bump-like structure at large angles. The anisotropy effect, estimated by comparing the differential cross-section for various values of cos θ, as well as the multipole interferences should be included as it can impact the IPC cross-section shape and was found to reduce the significance of the excess by one standard deviation. However, these effects cannot lead to a bump-like structure like the one observed by Atomki.

They also have tried introducing a form factor (FF) to the resonance's electromagnetic coupling vertex with a polynomial parametrization $f(M_{+-}^2) = 1 + f_1 r + f_2 r^2 + f_3 r^3$, with $r = M_{+-}^2/\widetilde{\Lambda}^2$ and $\widetilde{\Lambda} = 20$ MeV/c^2. The bump-like structure in invariant mass can be explained with such a form factor (see Fig. 2.5), with a χ^2 per degrees of freedom, χ^2_{red} equal to 0.5 and 1.1 respectively for FF1 and FF2,

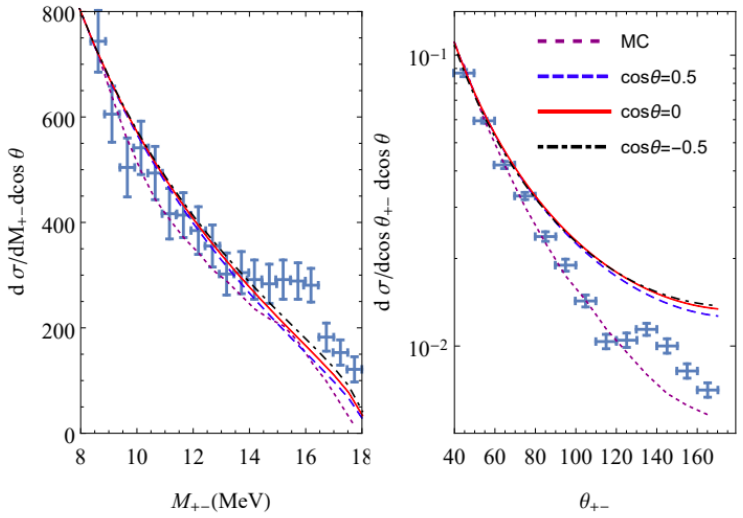

Figure 2.4: Differential Zhang-Miller cross-sections as a function of invariant mass M_{+-} (left) and angular opening θ_{+-} (right) for $\cos\,\theta = -0.5, 0, 0.5$ calculated in [7]. The model is compared to Atomki's data points (blue) and Atomki's Monte-Carlo background (dashed purple). Figure from [7].

.

corresponding to two sets of FF parameters. An excess of events can also be seen at large θ_{+-}, largely decreasing the significance of the excess observed by Atomki. However, the set of parameters required by such a FF to explain the anomaly is in contradiction with results from previous calculations.

In conclusion, Zhang and Miller have included anisotropy, multipole interferences and form factors in the Internal Pair Conversion model. Still, none of these effects can explain fully the anomaly observed experimentally by the Atomki group.

Recently, Gysbers et al. [8] developed a model from the Internal Pair Conversion background based on an ab initio No-Core Shell Model with Continuum (NCSMC) adapted from [36] and applied to the proton capture on ^{7}Li. The No-Core Shell Model is a structure technique suited for characterizing bound states and approximating narrow resonances. It treats nuclei as groups of non-relativistic point-like nucleons with internucleon interactions.

They use it and start by deriving the photon production $^7\mathrm{Li}(\mathrm{p},\gamma)^8\mathrm{Be}$ cross-section. In Fig. 2.6, they compare their calculated S-factor vs p+^{7}Li center-of-mass proton energy with data from [5] for both the transition to ground state γ_0 and the sum of transition to ground state γ_0 and to first excited state γ_1. The agreement between model and data is good, validating the NCSMC method.

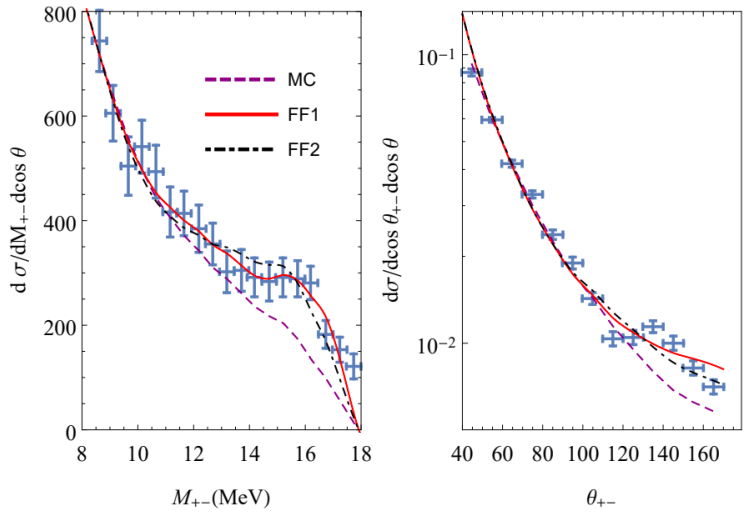

Figure 2.5: Differential Zhang-Miller cross-sections as a function of invariant mass M_{+-} (left) and angular opening θ_{+-} (right) for $\cos\,\theta = 0$ calculated in [7] after introduction of a form factor FF1 (full red) or FF2 (dash-dotted black). The model is compared to Atomki's data points (blue) and Atomki's Monte-Carlo background (dashed purple). Figure from [7].

.

They also calculated the IPC differential cross-section. They find it is dominated by E1 and M1 contributions while E2 is largely suppressed. The calculated differential cross-section at the ^{8}Be*(18.1) resonance is displayed in Fig. 2.7 along with its various subcontributions and the Atomki data from [1] (blue data points) and [37] (red data points). The model is matched with the data at angular opening $\Theta = 65°$ (upper panels) and $\Theta = 105°$ (middle panels). The model is shown for $|y| < 0.5$ (left panels) and $|y| < y_{max}$ (right panels), y_{max} corresponding to the full kinematic-allowed region. The various multipole contributions are shown for M1 (dashed line), E1 (dash-dotted) and E2 (dash-dot-dotted). The leading-order contributions ($K = 0$) are shown in gray and other colors correspond to next-order contributions. The sum of all contributions is a full black line while the sum of leading-order contributions is a dotted black line. The calculated shapes are all monotonously decreasing, E1's flattening out at large angles while M1's are steeper. The next-order contributions have a negligible effect. E1 and M1 have comparable contributions. When matched at 65° the total cross-section overestimates the data at larger angles, while when matched at 105° underestimates the data at lower angles. This could be due to the energy loss in the target neglected

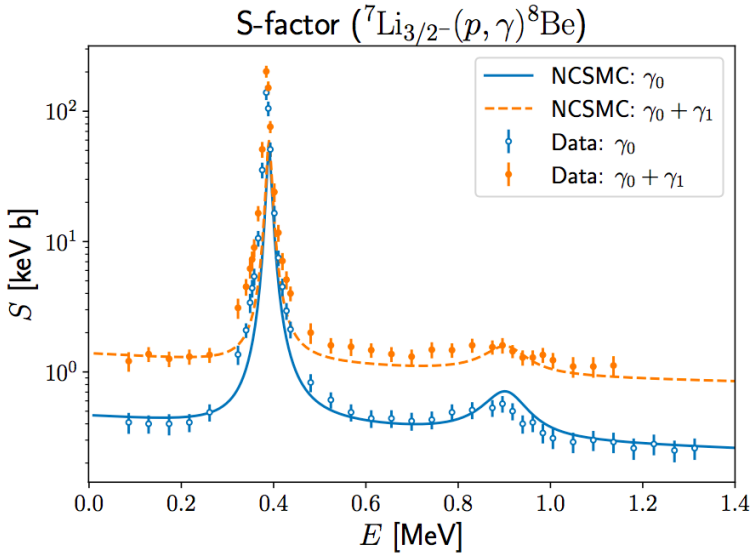

Figure 2.6: Astrophysical S factor as a function of p+^{7}Li center-of-mass proton energy E for the transition to ground state γ_0 (blue) and the sum of transition to ground state and to first excited state $\gamma_0 + \gamma_1$ (orange). The model with full or dashed lines is compared to the data points taken from [5]. Figure from [8].

.

by the theoreticians. Nonetheless, the shapes cannot explain any bump-like structure at $\approx 140°$ and their results are largely in line with Atomki's Standard Model background.

The last two studies in [7] and [8] are unable to explain the Atomki anomaly in ^{8}Be through any nuclear physics effect.

In [28], Viviani et al. have carried out ab initio calculations for the ^{3}H(p, e$^+$e$^-$)^{4}He cross-sections using exact hyperspherical-harmonics methods. They concluded that the predicted cross-sections are monotonically decreasing as a function of the electron-positron opening angle. The Standard Model can explain no bump-like structure similar to the ^{4}He Atomki anomaly.

2.1.2 Higher-order processes: Aleksejevs

In [30], Aleksejevs et al. calculated the full set of second-order corrections and the interference terms to the Born approximation used by the Atomki group. They studied whether an interference between the Born-level IPC amplitude and a Next-to-Leading-Order (NLO) non-resonant component could give rise to a bump-like shape in the IPC angular opening distribution in order to try and explain the Atomki anomaly with Standard Model considerations. To do so, they computed

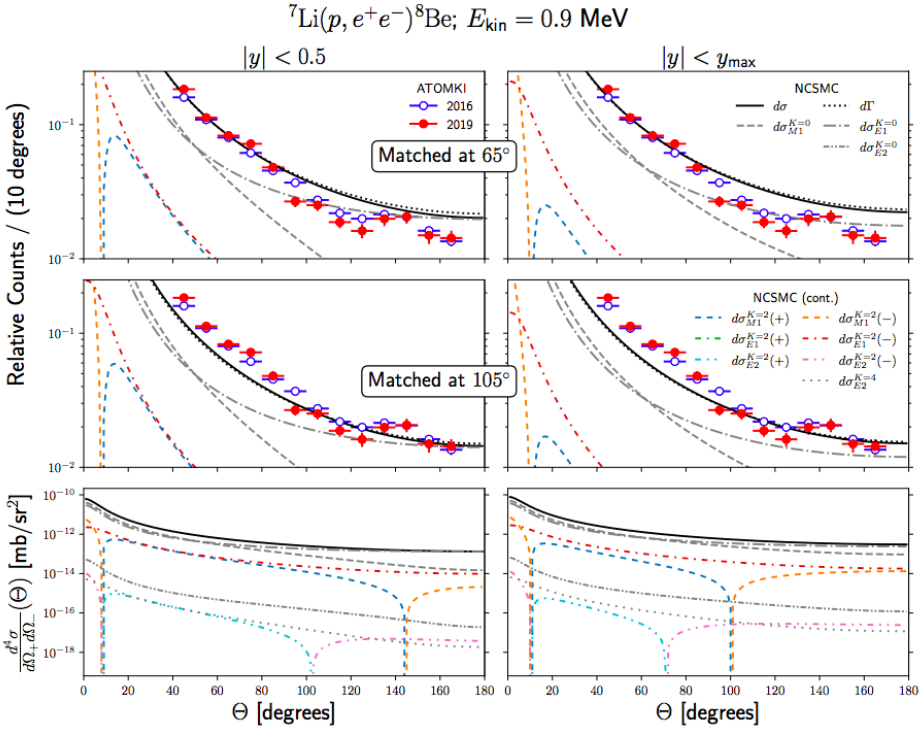

Figure 2.7: Differential cross-section of the IPC ^{7}Li(p, e$^+$e$^-$)^{8}Be process at p+^{7}Li center-of-mass proton energy $E = 0.9$ MeV as a function of angular opening Θ. Calculated in [8] and matched to Atomki data at 65° (top panels) and 105° (middle panels). The cross-sections are integrated over the electron-positron energy asymmetry for $|y| < 0.5$ (left) and for all kinematic-allowed values (right). The model is compared to Atomki's data points from [1] (blue) and from [37] (red). More details in the text. Figure from [8].

.

the doubly differential decay rate of ^{8}Be$^* \to {}^8$Be e$^+$e$^-$ from Eq. 2.4 (writing M_{LO} and M_{NLO} the Leading-Order (LO) and Next-to-Leading-Order (NLO) matrix elements and Φ the phase space element) and included the higher-order QED contributions of the decays shown in Fig. 2.8.

$$\frac{d^2\Gamma}{d\theta_+ d\theta_-} = \left(|M_{LO}|^2 + 2\Re\left[M_{LO}M^*_{NLO}\right]\right)\Phi \tag{2.4}$$

They also implemented a Monte-Carlo simulation of the Atomki pair spectrometer and a smearing function in order to include acceptance and resolutions effects into their calculations. They then calculated the expected angular opening

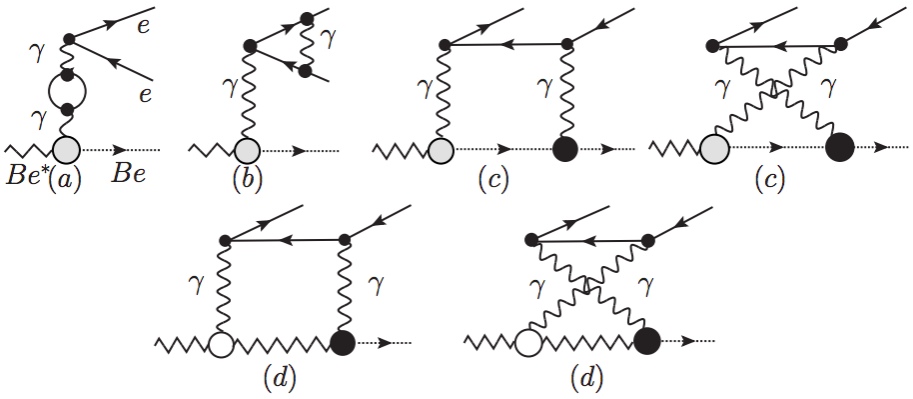

Figure 2.8: Higher-order QED Feynman diagrams of the ^{8}Be* $\rightarrow$ ^{8}Be + e^+e^- transition. Black, gray and white circles represent $0 \rightarrow 0$, $1 \rightarrow 0$ and $1 \rightarrow 1$ spin transitions respectively. Figure from [30].

.

and invariant mass distributions and fitted these to the Atomki data by leaving freedom to the overall normalization of the Born contribution and the coefficient of the interference term between the Born and the second-order diagrams. The results of the best fit is shown in Fig. 2.9.

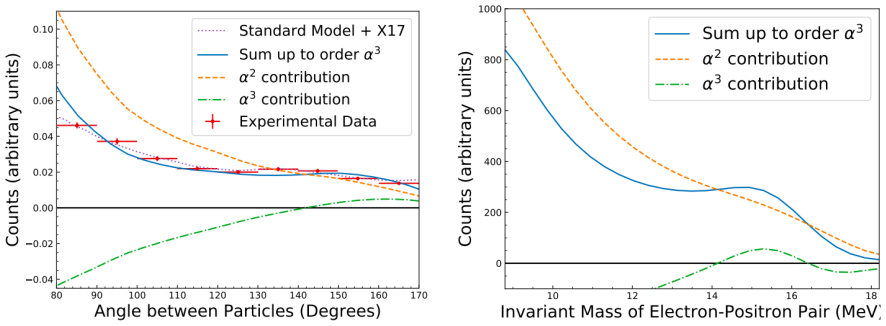

Figure 2.9: IPC angular opening (left) and invariant mass (right) distribution as the sum (blue full line) of QED LO (yellow dashed line) and NLO (green dash-dotted line) contributions calculated in [30]. The Atomki data (red points) and their IPC+X17 simulation (purple dotted line) are shown for comparison. Figure from [30].

.

Though the LO contribution is monotonously decreasing, the NLO one gives rise to a bump-like structure both in angular opening above 140° and in invariant mass above 15 MeV/c^2, close to the observed Atomki anomaly. The angular

opening fit gives $\chi^2_{red} = 38/7$. The fit is worse than the fit assuming the X17 boson decay but it goes to show that higher-order Standard Model effects can lead to an excess over a LO background. The authors also found that this effect is largely amplified due to the non-uniformities in Atomki's angular acceptance. An independent measurement with a varied or more uniform acceptance detector could discriminate between the X17 hypothesis and NLO effects.

2.1.3 Modified Bethe-Heitler: Koch

In [31], Koch studied the likelihood of a Modified Bethe-Heitler process to explain the Atomki anomaly. In this nuclear decay chain, he proposes that the excited ^{8}Be nucleus undergoes a transition to an intermediary state before the decay to ground state. The two high-energy γs emitted in the two successive transitions then convert to an e^+e^- pair through a Bethe-Heitler process. The process is shown in Fig. 2.10 and relies on three main items:

- a broad intermediary state
- orientation of the nuclear multipole coefficients due to one the γ's emission
- energy and momentum conservation

A broad intermediary state is required to have the two photons emitted within a short Δt. A favored candidate is the ^{8}Be 4^+ state at 11.35 MeV with a 3.5 MeV width. The successive decay chain is shown in Eq. 2.5 and Eq. 2.6 for the ^{8}Be*(17.6) and ^{8}Be*(18.1) respectively with energy difference ΔM_{ij}, multipole order of the transition ΔN and isospin difference ΔT.

$$\mathbf{1}^+ \xrightarrow[\Delta N=3,\Delta T=0]{\Delta M_{12}=6.8\text{MeV}} \mathbf{4}^+ \xrightarrow[\Delta N=4,\Delta T=0]{\Delta M_{23}=11.35\text{MeV}} \mathbf{0}^+ \tag{2.5}$$

$$\mathbf{1}^+ \xrightarrow[\Delta N=3,\Delta T=1]{\Delta M_{12}=6.3\text{MeV}} \mathbf{4}^+ \xrightarrow[\Delta N=4,\Delta T=0]{\Delta M_{23}=11.35\text{MeV}} \mathbf{0}^+ \tag{2.6}$$

Koch has found the γs are emitted with a favored relative angle θ_{rel} depending on the transition multipole order N:

$$\theta_{\text{rel}} \pm \delta\theta_{\text{rel}} = \begin{cases} (144 \pm 14)^\circ & \text{for } N = 3 \\ (152 \pm 11)^\circ & \text{for } N = 4 \\ \cdots \end{cases} \tag{2.7}$$

The position of the expected MBH excess is compatible with the Atomki anomaly. He also calculated the expected invariant mass m_X and opening angle of the electron-positron pair from the MBH process. The result is shown in

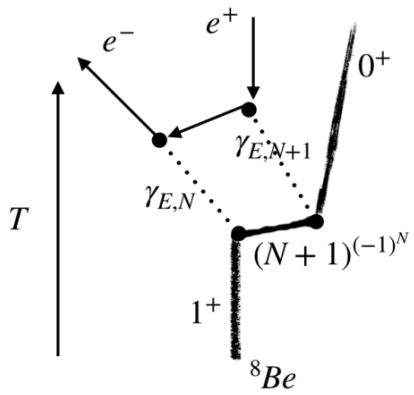

Figure 2.10: Modified Bethe-Heitler diagram for the ^{8}Be*(18.1) transition to ground state. Figure from [31].

.

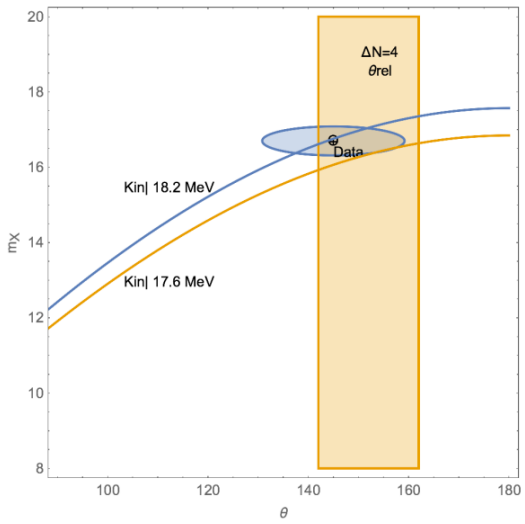

Figure 2.11: Invariant mass m_X of the electron-positron pair as a function of the opening angle for ^{8}Be*(18.1) (blue curve) and ^{8}Be*(17.6) (orange curve) initial states. The Atomki anomaly from [1] and its experimental uncertainties are shown in a blue elliptic contour. The orange rectangle represents the region in angular opening where an excess from the MBH process is expected for the $\Delta N = 4$ transition. Figure from [31].

.

Fig. 2.11. It shows such a process would be observed with an invariant mass excess close to 17 MeV/c^2, as observed by Atomki.

It was also found that the conversion rates are in reasonable agreement with the Atomki observation. However, even though the kinematic agreement is good, the MBH model cannot explain why the Atomki anomaly was mostly observed in the ^{8}Be*(18.1) decay rather than in the ^{8}Be*(17.6) decay. A measurement of the ^{7}Li(p, $\gamma\gamma$)^{8}Be angular spectrum would provide an answer to the MBH process as the Atomki anomaly origin.

2.2 Beyond the Standard Model interpretation of the Atomki anomalies: the X17 particle

Though several explanations within the Standard Model were put forward to try and explain the Atomki anomaly, they only agree partially with Atomki's observations. The X17 hypothesis, the electron-positron decay of a new massive neutral boson beyond the Standard Model, vector of a fifth force of nature, has triggered lots of interest and work within the community. The hypothesis on the nature of this boson and the properties accommodating Atomki's observations and constraints from other experiments will be discussed here.

2.2.1 Kinematic consistency

It was already shown that a massive boson emitted in the transition of the excited ^{8}Be*, ^{4}He* or ^{12}C* to ground state and subsequently decaying to an electron-positron pair could provide a credible explanation for the Atomki anomaly. The electron-positron opening angle θ_{ee} is dependent on the mass of the boson m_X and on the energy of the transition from excited state to ground state $m_{N^*} - m_N$ following:

$$\theta_{ee}^{min} = 2 \arcsin(\frac{m_X}{m_{N^*} - m_N}) \tag{2.8}$$

In [38], Denton et al. put together all results from Atomki on ^{8}Be*, ^{4}He* or ^{12}C* and showed that all the excesses in angle are compatible with a boson mass close to 17 MeV/c^2 (see Fig. 2.12).

A priori, the X17 particle can be a scalar or pseudoscalar boson (spin 0), an axial vector or vector boson (spin 1) depending on its spin-parity assignment. We review here the forbidding, favouring and disfavouring arguments and other constraints on its properties.

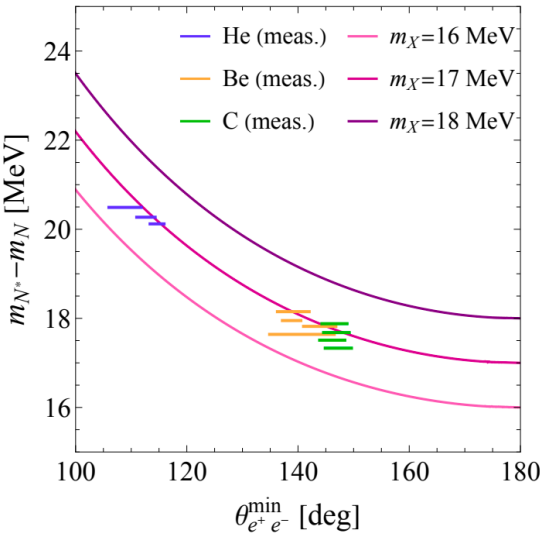

Figure 2.12: Opening angle measured by Atomki in ^{8}Be*, ^{4}He* or ^{12}C* (in yellow, purple and green respectively) along with the boson contours for masses $m_X = 16, 17, 18$ MeV (purple, red and pink lines respectively) based on Eq. 2.8. Figure from [38].

.

2.2.2 Scalar boson hypothesis

Let's assume the X17 particle is a scalar boson: it has spin-parity 0^+. ^{8}Be(18.15)$\rightarrow$ ^{8}Be is a $1^+ \rightarrow 0^+$ transition. The X17 boson must carry an angular momentum $L = 1$. Parity conservation imposes X17 has a parity $P = (-1)^L = -1$, which contradicts the scalar particle parity. The scalar hypothesis is therefore forbidden. Tab. 2.2 summarizes the forbidden and allowed transitions in which X17 can be produced based on its nature. It should be noted that the ^{4}He*(21.01) and ^{4}He*(20.21) partially overlay due to their widths and positions. It is therefore unclear whether the Atomki anomaly observed in ^{3}H(p, e$^+$e$^-$)^{4}He stems from the ^{4}He*(21.01) or ^{4}He*(20.21) transition to ground state. Due to their opposite parities, both states cannot simultaneously produce a pure vector or pure axial vector X17.

2.2.3 Pseudoscalar boson hypothesis

According to Ellwanger et al. [40], a pseudoscalar X17 could explain the ^{8}Be anomaly if the boson Yukawa couplings to electron and quarks are of the order of the ones to the Standard Model Higgs boson. In [39], Feng. et al searched for dynamical evidence of the X17 boson and in particular whether experimentally observed decay rates of the ^{8}Be and ^{4}He anomalies can be described by a single

State	J^P	Scalar X	Pseudoscalar X	Vector X	Axial Vector X
^{8}Be*(18.15)	1^+	forbidden	allowed	allowed	allowed
^{12}C*(17.23)	1^-	allowed	forbidden	allowed	allowed
^{4}He*(21.01)	0^-	forbidden	allowed	forbidden	allowed
^{4}He*(20.21)	0^+	allowed	forbidden	allowed	forbidden

Table 2.2: Allowed and forbidden transitions based on X17 nature hypothesis. Adapted from [39].

hypothesis on the X17's nature. Using EFT, they found out that the ratio of the decay widths in the pseudoscalar hypothesis should be: $\Gamma_P^{^8\mathrm{Be}}/\Gamma_P^{^4\mathrm{He}} \approx 10^{-6}$. Including the theoretical and experimental uncertainties cannot reconcile the expected ratio from the experimental values: $\Gamma_X^{^8\mathrm{Be}} = (1.2 \pm 0.2) \times 10^{-5}$ eV and $\Gamma_X^{^4\mathrm{He}} = (4.0 \pm 1.2) \times 10^{-5}$ eV. The pseudoscalar hypothesis here is strongly disfavored. Studying the $^4\mathrm{He}^* \to {}^4\mathrm{He} + \gamma\gamma$ reaction would further probe the hypothesis as a pseudoscalar decay to two photons is allowed while it is forbidden for a vector boson. Finally, the confirmation of the anomaly observation in ^{12}C killed off any hope of a simultaneous pseudoscalar explanation. As seen in Tab. 2.2, the pseudoscalar hypothesis is forbidden in a $1^- \to 0^+$ transition.

2.2.4 Vector boson hypothesis

In [39], Feng et al. calculated the theoretical decay width from ^{4}He assuming a vector X17 boson that can explain the ^{8}Be anomaly:

$$\Gamma\left(^4\mathrm{He}^*(20.21) \to {}^4\mathrm{He}\ \mathrm{X}\right) = (0.3 - 3.6) \times 10^{-5}\ \mathrm{eV} \tag{2.9}$$

This result is in very good agreement with the Atomki measurement: $\Gamma_X^{^4\mathrm{He}} = (4.0 \pm 1.2) \times 10^{-5}$ eV. We write ε_p, ε_n, ε_u and ε_d the X17 coupling with protons, neutrons, up and down quarks respectively. In [4], they give

$$\frac{\mathcal{BR}\left(^8\mathrm{Be}^* \to {}^8\mathrm{Be}X\right)}{\mathcal{BR}\left(^8\mathrm{Be}^* \to {}^8\mathrm{Be}\gamma\right)} = (\varepsilon_p + \varepsilon_n)^2 \frac{|\vec{p}_X|^3}{|\vec{p}_\gamma|^3} \approx 5.8 \times 10^{-6} \tag{2.10}$$

leading to:

$$|\varepsilon_p + \varepsilon_n| \approx 0.011 \text{ or } |\varepsilon_u + \varepsilon_d| \approx 3.7 \times 10^{-3} \tag{2.11}$$

In the dark photon hypothesis, fermion charges are proportional to their Standard Model charges $\varepsilon_f = q_f \varepsilon$ with ε the kinetic mixing parameter. Eq. 2.11 would therefore give $\varepsilon \approx 0.011$. This value is ruled out by the NA48/2 experiment [41], which set the following limit on this parameter: $\varepsilon < \varepsilon_{max} = 8 \times 10^{-4}$ at 90% CL. The NA48/2 result forbids the dark photon solution but not the general vector

boson one if Eq. 2.12 is verified,

$$|2\varepsilon_u + \varepsilon_d| < 8 \times 10^{-4} \tag{2.12}$$

leading to

$$-2.3 < \frac{\varepsilon_d}{\varepsilon_u} < -1.8 \text{ or } -0.067 < \frac{\varepsilon_p}{\varepsilon_n} < 0.078 \tag{2.13}$$

The latter condition gave rise to the "protophobic" designation for the vector boson solution, due to the low coupling with proton compared to neutron. The boson decay length and the KLOE-2 [42] experiment also impose:

$$|\varepsilon_e| \gtrsim 1.3 \times 10^{-5} \text{ and } |\varepsilon_e| < 2 \times 10^{-3} \tag{2.14}$$

The various constraints on a vector boson solution from experimental observations are summarized in Fig. 2.13.

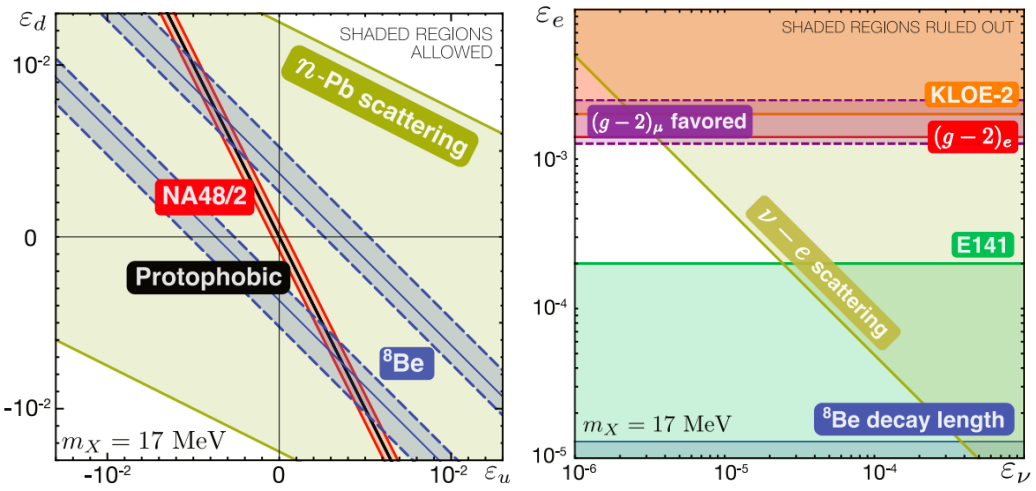

Figure 2.13: Required charges to explain the ^{8}Be anomaly and regions ruled out by other experiments in the (ε_u, ε_d) (left) and (ε_ν, ε_e) (right) parameter space. Figure from [4].

.

The NA64 experiment also put strong constraints on the kinetic mixing parameter of a hypothetical vector boson [43], as seen in Fig. 2.14. Though the vector boson solution is strongly constrained, some region remains unexplored for boson masses close to 17 MeV/c^2.

Zhang and Miller [44] studied the protophobic vector boson hypothesis and computed an isospin relation between photon and boson couplings to nucleons. The cross-section of such a boson is shown in Fig. 2.15 and is found to be dominated

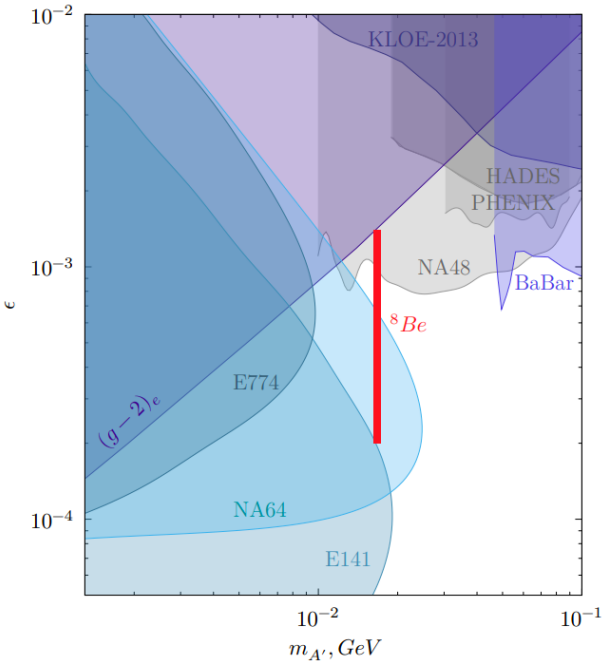

Figure 2.14: (Kinetic mixing ε, mass $m_{A'}$) parameter space excluded at 90% C.L. by NA64 2017-2018 data (blue area) and by other experiments. The region allowed to explain the ^{8}Be anomaly is shown in red. Figure from [43].

.

by the E1 contribution, almost independent from the proton energy. The shaded region covers the four proton energies investigated by Atomki in [1]: 0.8, 1.04, 1.1, 1.2 MeV. According to this hypothesis, the anomaly should have been observed at all four energies which contradicts Atomki's results. The protophobic vector boson as a solution to the ^{8}Be anomaly is invalidated.

In [45], it was pointed out that the observation of the X17 anomaly in ^{12}C is in tension with a combined protophobic vector boson explanation of the anomalies.

2.2.5 Axial vector boson hypothesis

The axial vector hypothesis could simultaneously reconcile all three anomalies. This solution also avoids the strong constraints already mentioned on the coupling to proton [38] from π^0 decay experiments such as NA48/2. The axial vector case was found to be allowed if its coupling is of the order of $g' \approx 10^{-4}$ [46, 47]. An axial vector hypothesis can explain simultaneously the anomaly in ^{8}Be*(18.15) and the absence of significant anomaly in ^{8}Be*(17.64). Feng et al. [39] calculated the decay width ratio in the axial vector hypothesis. It was estimated to be $\Gamma_A^{^8\mathrm{Be}}/\Gamma_A^{^4\mathrm{He}} \approx 10^{-2}$.

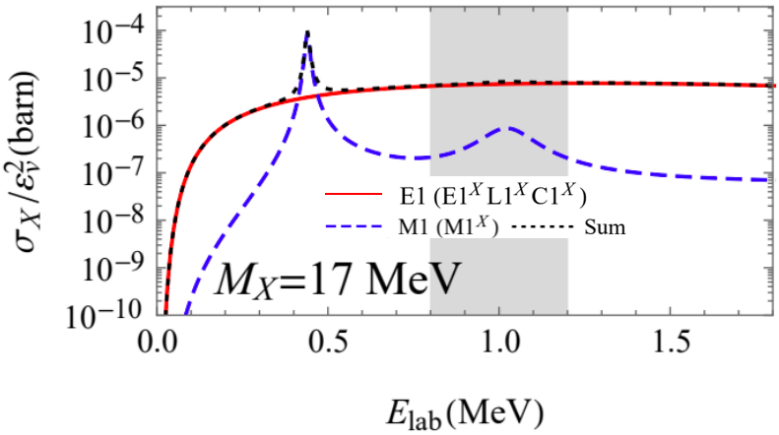

Figure 2.15: X17 boson cross-section (black dashed line) as a function of the lab proton energy assuming a vector boson hypothesis with mass $M_X = 17$ MeV/c^2. The E1 and M1 contributions are shown in red full and blue dashed lines respectively. Figure from [44].

.

Large theoretical uncertainties on the nuclear matrix elements still make it hard to get precise results on this hypothesis and make Atomki's ^{8}Be and ^{4}He results consistent with this order of magnitude. An axial vector boson could explain both the ^{8}Be and ^{4}He anomalies. Finally, with a multipole expansion method, Barducci and Toni [45] have estimated the range of boson-nucleon couplings to simultaneously match the experimental observations on ^{8}Be, ^{4}He and ^{12}C. They found the axial vector solution to be the most promising candidate and other spin-parity assignments to be disfavored. They also point out that such a candidate could explain the KTeV anomaly in $\pi^0 \to e^+e^-$ decay [48] while being compatible with $(g-2)_e$ measurements.

2.3 Experimental efforts

The results from Atomki require experimental confirmation. The theoretical interpretations of the anomaly require additional and complementary results in order to settle for an SM or BSM interpretation of the anomaly and to understand the nature and properties of the hypothetical new particle. This has triggered a lot of work from the experimental community, most of it still unpublished.

2.3.1 Published results

The X17 boson could be produced in $e^- Z \to e^- ZX$ studied by impinging a high-energy electron beam on an active target. The NA64 collaboration performed

the measurement and observed no evidence for the X17 existence [43]. It could also be observed in the neutral pion decay $\pi^0 \rightarrow \gamma X, X \rightarrow e^+e^-$. The NA48/2 collaboration looked for such a decay in the X17 mass range and again, no evidence for X17 was found [41]. Both experiments set strong constraints on X17 couplings to quarks as seen in Sec. 2.2.4.

In [49], Anh et al. have reproduced the Atomki measurement impinging a proton beam at $E_p = 1225$ keV at a Li_2O target and observed an excess at an angular opening close to 140°, consistent with Atomki's results (see Fig. 2.16). The result is not totally independent from Atomki as the article was signed by several Atomki collaborators.

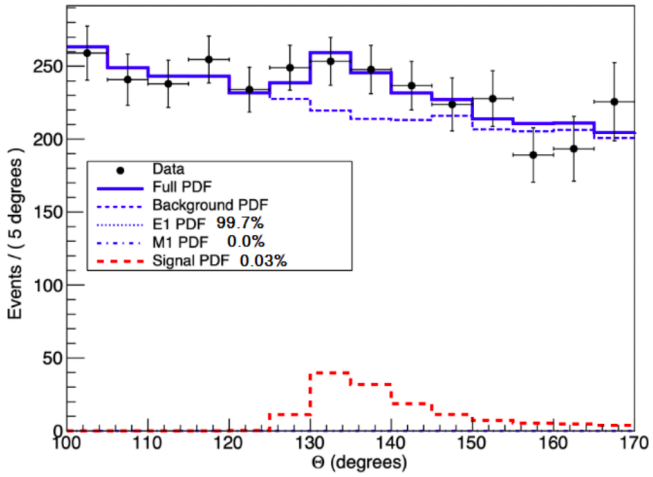

Figure 2.16: Angular opening spectrum from $^7Li(p, e^+e^-)^8Be$ at $E_p = 1225$ keV from Anh et al. [49]. Figure from [49].

.

In [50], Abraamyan et al. studied the invariant mass spectra of photon pairs produced in dC, pC and dCu at momenta of 2.75, 5.5 and 3.83 GeV/c per nucleon respectively. A significant excess of events was observed at a 17 MeV/c^2 invariant and tests point to a particle explanation for the excess which could be consistent with X17.

2.3.2 Ongoing experiments

Several experiments have the capabilities to search for a new light boson. Some reproduce the experiments carried out by Atomki in ^8Be and ^4He, others go through complementary channels. All these experiments, their channel of study and their prospects are summarized in Tab. 2.3 and Tab. 2.4 for non-IPC and IPC experiments respectively.

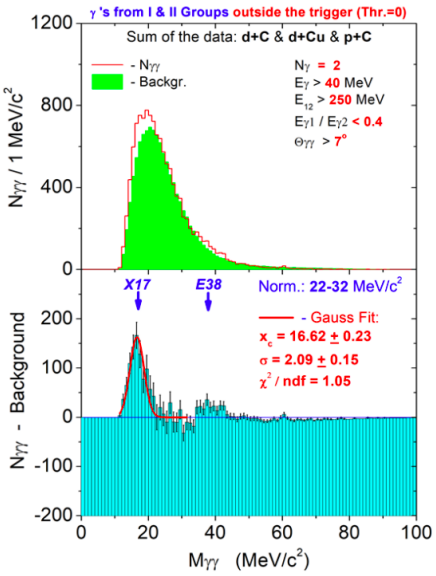

Figure 2.17: Sum of $\gamma\gamma$ invariant spectra from dC, pC and dCu from Abraamyan et al. [50]. Figure from [50].

.

Experiment	Process	Note
NA64 [43]	$e^- Z \to e^- Z X$	$\varepsilon^2 \lesssim 5 \times 10^{-7}$ excluded
N48/2 [41]	$\pi^0 \to \gamma X$	$\varepsilon^2 \gtrsim 2 \times 10^{-7}$ excluded
PHOTON-2 @JINR [50]	dC, pC and dCu $\to \gamma\gamma$	Observed 17 MeV/c^2 $\gamma\gamma$ invariant mass excess
FASER [51]	pp collisions	$\varepsilon^2 \lesssim 10^{-8}$ excluded
BESIII [52]	$J/\Psi \to \eta_c X$	Obj.: $\lvert\varepsilon_c\rvert \gtrsim 3 \times 10^{-3}$
Belle II [52]	$J/\Psi\,(\eta_c + X) + l\bar{l}$ $J/\Psi + X$	Obj.: $\lvert\varepsilon_c\rvert \gtrsim 1.8 \times 10^{-2}$ $2.0 \times 10^{-4} \leq \lvert\varepsilon_e\rvert \leq 8.0 \times 10^{-4}$
PADME [53]	Resonant production	Obj.: $\varepsilon^2 \sim 1 \times 10^{-6}$
DarkLight [54]	$e^- + p \to e^- + p + e^+e^-$	Obj.: Search $m_X = 10 - 100$ MeV/c^2
Mu3e [55]	$\mu^+ \to e^+ \nu_e \bar{\nu}_\mu A'$	Obj.: Search $m_X = 10 - 80$ MeV/c^2
LHCb [56]	$D^*(2007)^0 \to D^0 A'$	Obj.: Search $m_X < 100$ MeV/c^2
VEPP-3 [57]	$e^+e^- \to \gamma A'$	Obj.: $\varepsilon^2 = 5 \times 10^{-8}$
MESA [58]	e^- target	Obj.: Search $m_X = 10 - 40$MeV/c^2
HPS [59]	e^- target	Obj.: $\varepsilon^2 < 1 \times 10^{-6}$
JLab [60]	e^- Bremsstrahlung	Obj.: $7.2 \times 10^{-8} < \varepsilon^2 < 5.9 \times 10^{-9}$

Table 2.3: Summary of all non-IPC experiments which could provide hints on the X17 search. Their results or objective is quoted in the last column.

Experiment	Nuclei of study	Note
HUS [49]	^{8}Be, ^{12}C	excess in e^+e^- angular correlation from ^{8}Be at $E_p = 1225$ keV observed with 4σ significance
LNL [61]	^{8}Be	data acquired, no results yet
New JEDI [62]	^{8}Be	data acquired, no results yet
COPE [63]	^{8}Be, ^{4}He	setup development, no results yet
CCPAC [64]	^{8}Be, ^{10}B	setup development, no results yet
nTOF [65]	^{4}He	setup development, no results yet
LUNA [66]	^{4}He	setup development, no results yet
U. Melbourne [67]	^{8}Be, ^{4}He, ^{12}C	setup development, no results yet
MEG-II [68]	^{8}Be	results in this work

Table 2.4: Summary of all IPC experiments which could provide hints on the X17 search.

Chapter 3

The MEG-II experiment and apparatus

The results obtained by Atomki require independent experimental confirmation. The MEG-II apparatus is able to perform the measurement and search for the X17 particle. The search relies on the subdetectors originally developed for the MEG-II experiment, which looks for the charged lepton flavour violating decay $\mu^+ \to e^+\gamma$. We will first discuss the motivation for MEG-II, grounded in the theory of charged Lepton Flavour Violation (cLFV), followed by an overview of the $\mu^+ \to e^+\gamma$ decay signature and backgrounds. Finally, we will present the MEG-II apparatus, detailing the LXe calorimeter, positron spectrometer and TDAQ architecture and operation.

3.1 Standard Model and cLFV

Describing the fundamental constituents of matter and their interactions, the Standard Model (SM) of particle physics is a fundamental theory in our understanding of the Universe and one of the most successful models in the history of physics. However, the Standard Model is thought to be an approximation below O(100 GeV) energies of a more comprehensive model. Despite its successes, several experimental observations have no explanation within the Standard Model. Four of these can be mentioned.

- The dark matter and dark energy are estimated to represent 26% and 69% of the energy content of the Universe respectively. The SM includes no description of these.
- The gravitational interaction cannot be modelled by the SM.
- The hierarchy problem: the SM cannot naturally explain the 125 GeV measured Higgs boson mass which lies at electroweak scales well below the $O(10^{19}$ GeV) Planck scale

- The observation of neutrino oscillation implies a non-zero neutrino mass and is in conflict with the SM massless prediction.

In order to provide descriptions for these observations, extensions of the SM or Beyond the Standard Model (BSM) theories were developed, including SUSY, GUT or see-saw mechanism.

3.1.1 Beyond the Standard Model (BSM) theories

The SUperSYmmetric models (SUSY) provide a solution to the hierarchy problem by associating each SM fermion with a superpartner boson and to each SM boson a superpartner fermion (see Tab. 3.1). Exact SUSY predicts the SM particle and its superpartner masses to be equal, contradicting the non-observation of superpartners at electroweak scales (O(100 GeV)). However, SUSY breaking could explain such results while enabling sizeable BSM effects experimentally observable today. SUSY models also have the advantage to put forward the lightest superpartner, a light, stable, electrically neutral and weakly interactive particle, as an interesting dark matter candidate.

SM particle	SUSY superpartner
charged leptons (e, μ, τ)	sleptons $\left(\tilde{\ell}_i\right)$
neutrinos $(\nu_\mathrm{e}, \nu_\mu, \nu_\tau)$	sneutrinos $(\tilde{\nu}_i)$
charged gauge bosons $(\mathrm{W}^\pm)$	charginos $\left(\tilde{\chi}_i^\pm\right)$

Table 3.1: A few SM particles and their SUSY associated superpartner.

The Seesaw mechanism could explain the small non-zero mass of the neutrinos. In this scenario, the neutrino is assumed to be a Majorana particle and heavy right-handed neutrinos with mass m_R are introduced. Left-handed neutrino masses can be expressed as m_D^2/m_R and can therefore get tiny masses.

The Grand Unified Theories (GUT) propose that the three gauge groups $\mathrm{SU}(3)_C \times \mathrm{SU}(2)_L \times \mathrm{U}(1)_Y$ can be unified at high energy scales, leading to the electromagnetic, weak and strong forces to be one and only force. The measurement of the running coupling constants for these three forces at low energies shows a unifying trend towards high energies and GUT models could provide complete unification at scales of $\mathrm{O}(10^{16}$ GeV).

3.1.2 $\mu \to e\gamma$ in the Standard Model with massive neutrinos

In the Standard Model, the lepton flavour is a conserved quantity and the $\mu \to e\gamma$ decay is therefore forbidden. However, the observation of neutrino oscillations

proved the conservation of neutral lepton flavour doesn't hold and opened a channel to the $\mu \to e\gamma$ decay through the process in Fig. 3.1.

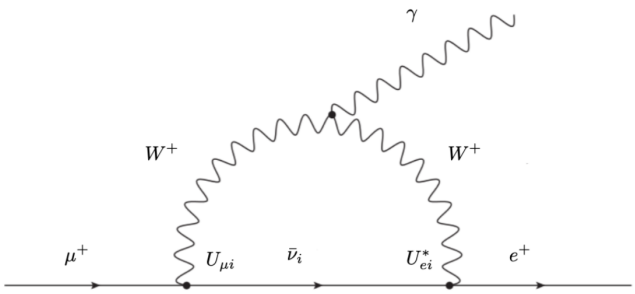

Figure 3.1: One Feynman schematic representation of the $\mu \to e\gamma$ process within the Standard Model extended with massive neutrinos.

.

Extending the SM with massive neutrinos enables the $\mu \to e\gamma$ with a branching ratio $\mathcal{BR}$ [69]:

$$\mathcal{BR}(\mu \to e\gamma) = \frac{3\alpha}{32\pi} \sum_i \left| U_{\mu i} U_{ei} \frac{\Delta m_i^2}{M_W^2} \right|^2 \approx 10^{-54} \tag{3.1}$$

Such a low value cannot be probed experimentally. Therefore, any observation of the $\mu \to e\gamma$ decay today would be a clear sign of charged Lepton Flavour Violation (cLFV) and could hint at BSM physics.

3.1.3 $\mu \to e\gamma$ beyond the Standard Model

SUSY models with supersymmetry breaking provide at electroweak scales a non-zero flavour mixing of the lepton superpartners, the sleptons. GUTs and the Seesaw mechanism could also open a channel for cLFV. An example of a $\mu \to e\gamma$ diagram in a SUSY framework is shown in Fig. 3.2.

Theoretical calculations of $\mathcal{BR}(\mu \to e\gamma)$ expected values in SUSY-GUT frameworks showed that $\mu \to e\gamma$ decay channel is opened with $\mathcal{BR} > 10^{-15}$, regions which can be probed experimentally today. The $\mathcal{BR}$ in a SM extended with massive neutrinos being largely suppressed, the $\mu \to e\gamma$ search provides a clean channel to study new physics at scales above O(TeV). If unobserved, strong constraints on BSM models can be set.

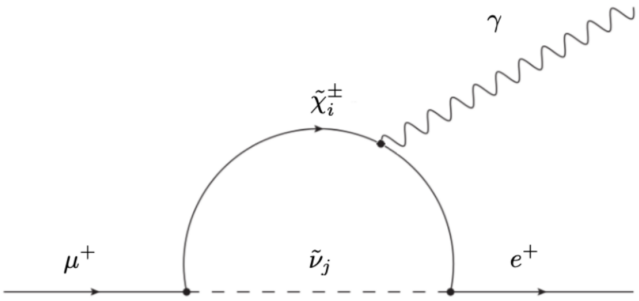

Figure 3.2: One Feynman schematic representation of the $\mu \to e\gamma$ process within a SUSY framework.

.

3.2 The $\mu \to e\gamma$ search

Due to its relatively long lifetime and its availability at accelerators around the world, muons have become an attractive probe for new physics. Its main measured properties are summarized in Tab. 3.2.

Parameter	Value
Half-life	$(2.1969811 \pm 0.0000022) \times 10^{-6}$ s
Mass	$105.6583745 \pm 0.0000024$ MeV/c^2
Spin	1/2
Magnetic moment anomaly $\left(\frac{g_\mu - 2}{2}\right)$	116 592 059(22) $\times 10^{-11}$ (0.19 ppm) [70]

Table 3.2: Main muon properties

Its interactions with the photon, the $W^{\pm}$ bosons, the Z boson and the Higgs boson are well understood through the Lagrangian:

$$\begin{aligned}\mathcal{L} &= e\bar{\mu}\gamma^\mu \mu A_\mu \\ &- \frac{g}{\sqrt{2}}\left(\bar{v}_{\mu_L}\gamma^\mu \mu_L W_\mu^+ + \bar{\mu}_L \gamma^\mu v_{\mu_L} W_\mu^-\right) \\ &- \sqrt{g^2 + g'^2}\left(\bar{\mu}_L\gamma^\mu\left(-\frac{1}{2} + \sin^2\theta_W\right)\mu_L + \bar{\mu}_R\gamma^\mu \sin^2\theta_W \mu_R\right) Z_\mu^0 \\ &- \frac{m_\mu}{v}\bar{\mu}\mu H\end{aligned} \tag{3.2}$$

The main muon decay channel is the Michel decay $\mu^+ \to e^+\nu_e\overline{\nu_\mu}$ with a branching ratio close to 100%. Two other decays are allowed with reduced branching

ratio: $\mu^+ \to e^+\nu_e\overline{\nu_\mu}e^+e^-$ and the Radiative Muon Decay (RMD) $\mu^+ \to e^+\nu_e\overline{\nu_\mu}\gamma$. Their branching ratios are summarized in Tab. 3.3.

Decay channel	Branching ratio
$\mu^+ \to e^+\nu_\mu\overline{\nu_e}$	≈ 1
$\mu^+ \to e^+\nu_\mu\overline{\nu_e}\gamma$	$(6.0 \pm 0.5) \times 10^{-8}$ when $E_\gamma > 40$ MeV and $E_{e^+} > 45$ MeV
$\mu^+ \to e^+\nu_\mu\overline{\nu_e}e^+e^-$	$(3.4 \pm 0.4) \times 10^{-5}$

Table 3.3: Main muon decay channels

3.2.1 The $\mu \to e\gamma$ signature

The $\mu \to e\gamma$ experimental search is performed with positive muons μ^+ instead of negative muons μ^- not to suffer from the μ^- capture by the nuclei from the experiment material. In the muon rest frame, the $\mu \to e\gamma$ decay can be identified through its unique two-body decay features:

- simultaneous positron-gamma emission: $t_{e\gamma} = 0$
- back-to-back emission: $\Theta_{e\gamma} = 180°$
- monochromatic emission at half the muon mass energies: $E_e = E_\gamma = m_\mu/2 \approx 52.8$ MeV

In a $\mu \to e\gamma$ search experiment, the number of expected signal events can be written as:

$$N_{sig} = R_\mu \times T \times \Omega \times \epsilon_e \times \epsilon_\gamma \times \epsilon_s \times \mathcal{BR}(\mu \to e\gamma) \tag{3.3}$$

R_μ represents the stopped muon rate, T the data taking duration, Ω the geometrical acceptance, ϵ_e and ϵ_γ the positron and γ detector efficiency and ϵ_s the efficiency of the analysis and associated selection. $R_\mu \times T$ is the total number of stopped muons and $R_\mu \times T \times \Omega \times \epsilon_e \times \epsilon_\gamma \times \epsilon_s$ the total number of measured muon decays. An optimized sensitivity on the branching ratio requires simultaneously a high muon rate and high detector efficiencies, an experimentally challenging combination.

3.2.2 The $\mu \to e\gamma$ backgrounds

The $\mu \to e\gamma$ search suffers two different backgrounds:

- the main one: an accidental background from the coincidence of a Michel positron and a γ from RMD, bremsstrahlung or annihilation-in-flight.

- the Radiative Muon Decay $\mu^+ \to e^+\nu_e\overline{\nu_\mu}\gamma$

The number of accidental background events N_{acc} is proportional to:

$$N_{acc} \propto R_\mu^2 \times \left(\sigma_{E_\gamma}\right)^2 \times \sigma_{E_e} \times \left(\sigma_{\Theta_{e\gamma}}\right)^2 \times \sigma_{t_{e\gamma}} \times T \tag{3.4}$$

σ_i represents the resolution on the observable i. It is clear that the accidental background is reduced when the resolutions on the observables are improved. γ energy and angular resolutions are particularly important as they contribute quadratically to the background. Eq. 3.4 also shows that continuous muon beams are the favoured choice for the $\mu \to e\gamma$ search as pulsed beams have a higher instantaneous rate which leads to a larger accidental background, keeping in mind that N_{acc} scales quadratically with the beam rate.

The effective RMD branching ratio is highly dependent on the considered positron and γ energies as seen in Fig. 3.3. Due to its four-body decay kinematics, the RMD background is largely reduced at $E_e \approx m_\mu/2, E_e \approx m_\mu/2$. Again, the background can be reduced with improved resolutions. The RMD effective branching ratio was estimated to be below 10^{-15} when considering $\sigma_{E_e} \approx 100$ keV and $\sigma_{E_\gamma} \approx 1$ MeV. This value leads to the RMD background being significantly lower than the accidental background.

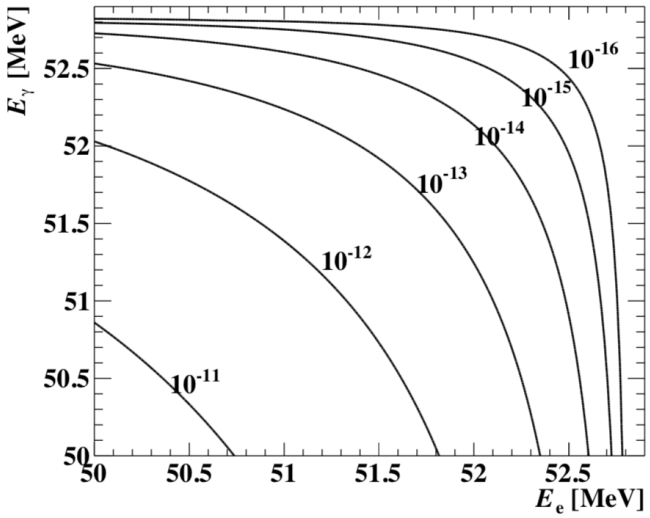

Figure 3.3: Effective branching ratio of the Radiative Muon Decay (RMD) integrated above the photon and positron energies E_γ and E_{e^+}.

.

The first limit on the $\mu \to e\gamma$ branching ratio was set making use of cosmic rays. After 70 years of improvement, the best limit at 90% confidence level was set by the MEG collaboration in 2016 [71]: $\mathcal{BR}(\mu \to e\gamma) < 4.3 \times 10^{-13}$. After upgrading the

MEG detector, the MEG-II collaboration hopes to achieve an order-of-magnitude sensitivity improvement.

3.3 The MEG-II experiment

With 60 researchers from Italy, Japan, Russia, the United States and Switzerland, the MEG-II experiment aims at searching for the charged lepton flavour violating decay $\mu^+ \to e^+\gamma$ with a sensitivity below 10^{-13}. Located at the Paul Scherrer Institute (PSI) in Switzerland, its apparatus results from an intense upgrade program of the MEG setup. The final design [68] is presented in this section. A first outlook is shown in Fig. 3.4. Detailed operation of the apparatus is presented in [72].

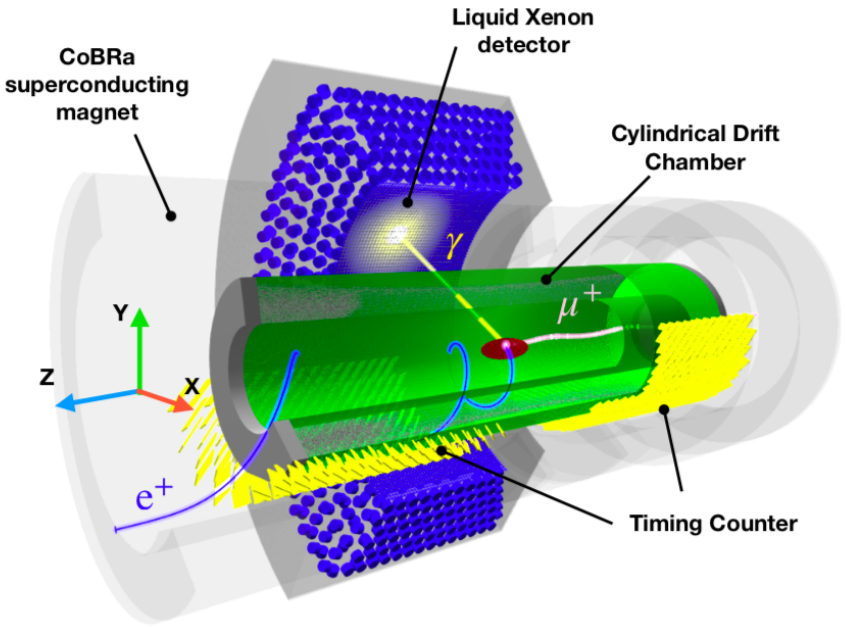

Figure 3.4: Design of the MEG-II apparatus.

.

The experiment makes use of the known kinematics of the muon-at-rest two-body decay. The muon beam available at the πE5 beamline at PSI is stopped into a plastic scintillator target. The decay photon is absorbed into the liquid XEnon Calorimeter (XEC) and the resulting scintillation light is measured by surrounding photomultiplier tubes (PMTs) and silicon photomultipliers (SiPMs). The decay positron is curved into the COnstant Bending RAdius (COBRA) magnetic field where hits on the Cylindrical Drift CHamber (CDCH) wires provide the starting

point for the trajectory reconstruction. A pixelated Timing Counter (pTC) provides positron timing measurement. A Radiative Decay Counter (RDC) mitigates the RMD background through detection of low-energy positrons. The MEG-II global coordinate system is defined as a right-handed system with the z-axis following the muon beam axis pointing downstream, the x-axis pointing opposite to the XEC and the y-axis the vertical $-\vec{g}$ axis. A polar coordinate system (r,θ,ϕ) is also used and defined as ($\sqrt{x^2+y^2+z^2}$,$\cos^{-1}\frac{z}{\sqrt{(x^2+y^2+z^2)}}$,$\tan^{-1}\frac{y}{x}$). The coodinate systems' center is taken at COBRA center.

3.3.1 Muon beamline

The Paul Scherrer Institute provides the most intense continuous positive muon beam in the world. A proton beam from a Cockcroft-Walton accelerator is accelerated at 590 MeV by a ring cyclotron. The proton beam with a current up to 2.2 mA is sent towards a graphite target producing pions subsequently decaying following $\pi^+ \rightarrow \mu^+\nu_\mu$. The muons from pions decaying within a few μm from the target, also called surface muons, are extracted and sent towards the πE5 beamline at a momentum of $\approx$ 28 MeV/c. An alternance of quadrupole and sextupole magnets brings the beam toward the experimental area. There, two quadrupole triplets along with a Wien filter (also called separator) mitigate the positron background coming from the muon decay in flight to less than 1% with respect to the number of muons. Finally, a Beam Transport Solenoid (BTS) focuses the beam before entering the MEG-II apparatus. It contains a 300 μm Mylar degrader film which slows down the muons to ensure maximal stopping efficiency in the muon-stopping target. A scheme of the beamline from the graphite target to the experimental apparatus is presented in Fig. 3.5.

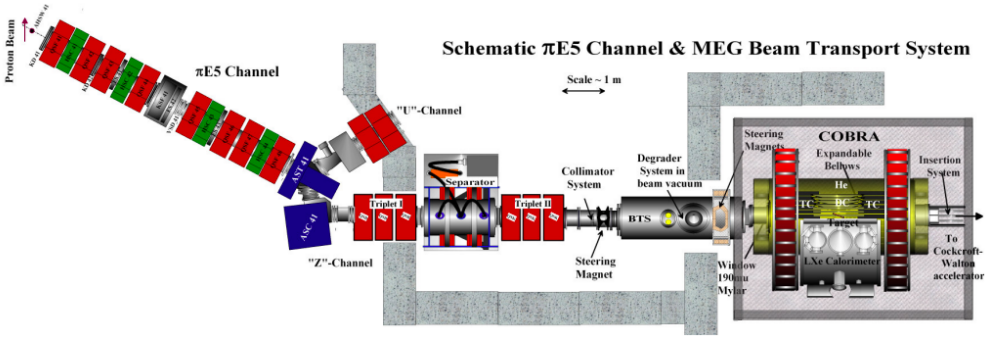

Figure 3.5: Drawing of the πE5 beamline at PSI.

.

3.3.2 Muon stopping target

After reaching the center of the MEG-II volume (corresponding to COBRA center), the muons are stopped into the MEG-II target (see Fig. 3.6), a 175 μm sheet of polyvinyltoluene-based scintillator. The target thickness and tilt angle are a compromise between a high muon-stopping efficiency and a reduced thickness to mitigate positron multiple scattering inside the target. A 15° tilt angle provides a long stopping length for muons while a short path is seen by the decay positrons emitted perpendicularly to the muon beam. To mitigate the systematic uncertainty from the target position and deformation, two CCD cameras continuously monitor the position of reference dots on the target surface.

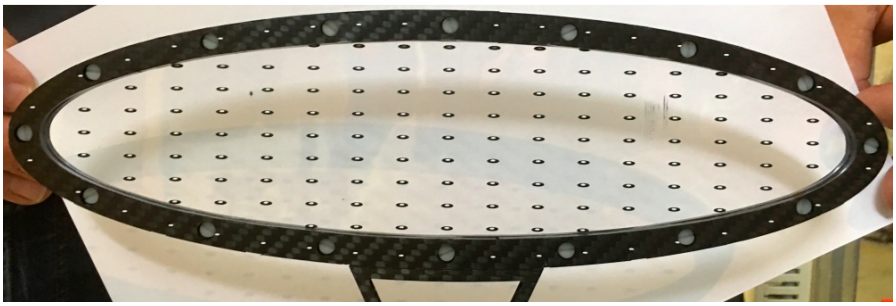

Figure 3.6: Photograph of the MEG-II target and its printed reference dots.

.

3.3.3 The LXe calorimeter

Design

The MEG-II calorimeter is a C-shaped cryostat filled with 900L of xenon and covered on the front face by 4092 Hamamatsu S10943-4372 Multi Pixel Photon Counters (MPPCs) and on the other faces by 668 Hamamatsu R9869 photomultipliers (see Fig. 3.7). The MPPCs on the front face of the detector provide high segmentation and therefore good spatial resolution of the gamma conversion point in the volume. Liquid Xenon (LXe) as a gamma detector medium can simultaneously measure the kinematical variables of the gamma with high energy resolution, high time resolution, and good position resolutions. Its high Z and density (2.98 g/cm^3) provide short radiation length and Moliere radius, good containment of the shower and compact detector size. Its high light yield (46 000 photons/MeV) enables high energy resolution and its short decay time (45 ns) provides high timing resolution and pile-up rejection capabilities in a high rate environment. On top of that, a high photosensor coverage and granularity, along with photosensors directly immersed in the LXe enables effective reconstruction of gamma scintillation

light. The recombination process of the gamma-ionized xenon leads to Vacuum UltraViolet (VUV) scintillation light at a wavelength of 175 nm. The MEG-II collaboration met and solved several technical challenges imposed by the use of LXe as a gamma detector. The entire Xe volume has to remain at a stable temperature between 161 K and 169 K, the liquid state range. A high purity of the Xe needs to be achieved to prevent scintillation light absorption by contaminants. Finally, the photosensors should be operated at 165 K while being sensitive to VUV-light, requiring specifically designed photosensors [68].

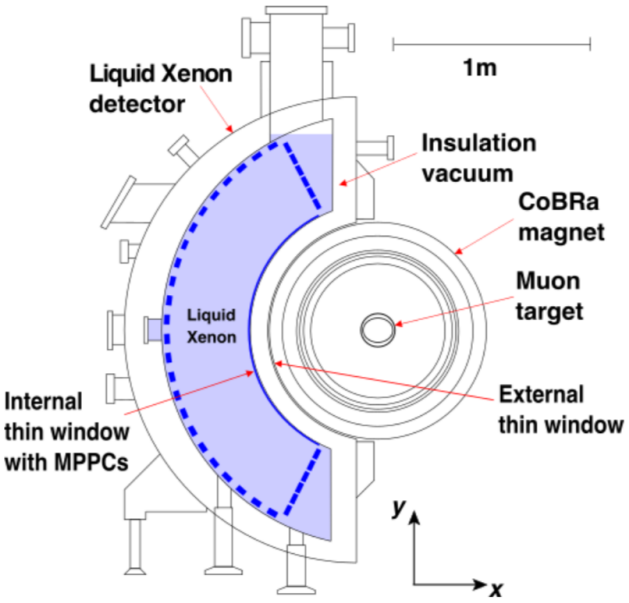

Figure 3.7: The MEG-II xenon calorimeter design and structure.

.

Event reconstruction

The pulse timing t_{pulse} is estimated by the constant fraction method applied to the waveform extracted from the sensor. The waveform is also integrated over a 150 ns window in order to estimate the pulse charge Q. The number of scintillation photons N_{ph} seen by each photon sensor is evaluated following Eq. 3.5:

$$N_{ph} = \frac{N_{pe}}{\epsilon_{QE(PDE)}} = \frac{Q}{G \times F_{EC} \times \epsilon_{QE(PDE)}} \tag{3.5}$$

N_{pe} represents the number of detected photoelectrons, ϵ_{QE} and ϵ_{PDE} the quantum efficiency of the PMTs and the photon detection efficiency of the MPPCs respectively, G the photosensor gain and F_{EC} the excess charge factor.

The pulse timing t_{pulse} extracted from the waveform can be converted to a scintillation light arrival time t_{pm} by accounting for time walk t_{walk} and time offset t_{offset} of individual sensors: $t_{pm} = t_{pulse} - t_{walk} - t_{offset}$

The gamma conversion position $\vec{x}$ is estimated making use of the number of scintillation photons seen by surrounding MPPCs. The $\chi^2_{pos}(\vec{x})$ quantity in Eq. 3.6 is minimized to extract $\vec{x}$, writing $\Omega_i(\vec{x})$ the solid angle seen by MPPC i at $\vec{x}$, $\sigma_{ph_i} = N_{ph_i}/\sqrt{N_{ph_i}}$. C is a fit parameter converting the solid angle to a number of photons.

$$\chi^2_{\text{pos}}\ (\vec{x}) = \sum_{i \in \text{nearby MPPCs}} \frac{\left(N_{\text{ph}_i} - C \times \Omega_i(\vec{x})\right)^2}{\sigma^2_{\text{ph}_i}} \tag{3.6}$$

The gamma conversion time is estimated with the scintillation light arrival time t_{pm_i} of surrounding MPPCs and PMTs with $N_{pe_i} > N_{\text{th}} = 50$. Writing t_{prop_i} the scintillation light propagation time between the conversion point and the photosensor i and $\sigma_{t,i}$ the time resolution, one can minimize $\chi^2_{time}(t_{conv})$ quantity in Eq. 3.7 and estimate the gamma conversion time t_{conv}.

$$\chi^2_{\text{time}}\ (t_{\text{conv}}) = \sum_{N_{\text{pe}_i} > N_{\text{th}}} \frac{\left(t_{\text{pm}_i} - t_{\text{prop}_i} - t_{\text{conv}}\right)^2}{\sigma^2_{t,i}} \tag{3.7}$$

A pile-up analysis was also developed based on advanced waveform analysis [73]. On-timing pile-up events, mostly due to positron annihilation in flight, are unlikely to be signal events and are discarded. Off-timing pile-up events due to two close-in-time muon decays are unfolded to reconstruct accurately the main gamma event.

The numbers of scintillation photon N_{ph_i} collected by each photosensor are then summed accounting for individual correction factors related to light collection efficiency and uniformity. It is finally converted to a gamma energy E_γ making use of a position and period-dependent energy scale. This energy scale is monitored periodically throughout the MEG-II data taking thanks to several complementary and redundant calibration methods.

Calibrations

Fig. 3.8 summarizes the extensive and regular calibration methods developed by the MEG-II collaboration to monitor precisely the XEC energy scale, uniformity, purity, alignment and sensor gains.

LED and α source The gain of each photosensor and its variation with time is estimated with a set of blue light LEDs placed on the lateral and outer faces of the calorimeter. The sensors are illuminated daily with various and reproducible

Process		Energy	Main Purpose	Frequency
Cosmic rays	$\mu^{\pm}$ from atmospheric showers	Wide spectrum O(GeV)	LXe–CDCH relative position LXe purity	Annually On demand
Charge exchange	$\pi^- p \to \pi^0 n$ $\pi^0 \to \gamma\gamma$	55, 83, 129 MeV photons	LXe energy scale/resolution	Annually
Radiative μ–decay	$\mu^+ \to e^+ \nu\bar{\nu}\gamma$	Photons >40 MeV, Positrons >45 MeV	LXe–pTC relative timing	Continuously
Proton accelerator	^{7}Li(p, γ)^{8}Be ^{11}B(p, γ)^{12}C	14.8, 17.6 MeV photons 4.4, 11.6, 16.1 MeV photons	LXe uniformity/purity LXe–pTC timing	Weekly Weekly
Neutron generator	^{58}Ni(n, γ)^{59}Ni	9 MeV photons	LXe energy scale	Weekly
Radioactive source	^{241}Am(α, γ)^{237}Np	5.5 MeV α's	LXe PMT/SiPM calibration LXe purity	Weekly
Radioactive source	^{9}Be($\alpha_{^{241}\mathrm{Am}}$, n)^{12}C* ^{12}C*($\gamma$)^{12}C	4.4 MeV photons	LXe energy scale	On demand
Radioactive source	^{57}Co(EC, γ)^{57}Fe	136 (11 %), 122 keV (86 %) X-rays	LXe–spectrometer alignment	Annually
LED		UV region	LXe PMT/SiPM calibration	Continuously

Figure 3.8: The MEG-II xenon calorimeter calibration tools.

.

light quantities to extract the gain from a linear fit of $\mu = G \times N_{ph}$ vs $\sigma^2 = G^2 \times N_{ph}$ at various LED intensities and monitor its variations. Moreover, 25 α-ray sources from ^{241}Am placed on five 100 μm wires are used to monitor the xenon purity by measuring the light attenuation between the periodically-spaced well-localized sources and the photosensors. With a 200 Bq activity, the rate is negligible compared to the gamma rate from the muon decays. The 5.5 MeV α's energy is also well below the expected 52.8 MeV signal gamma's energy.

17.6 MeV line from ^{7}Li, 4.4 MeV and 11.6 MeV lines from ^{11}B The MEG-II experiment makes use of its own Cockcroft-Walton accelerator, described in Sec. 4.1.1, providing protons with an energy up to 1.1 MeV and a current up to 100 μA. This beam, at a 500 keV proton energy and going in the opposite direction with respect to the muon beam, hits at a $Li_2B_4O_7$ attached to the proton beamline end and inserted at COBRA center. It produces monochromatic 17.6 MeV γ's from the ^{7}Li$(p,\gamma)^{8}$Be and monochromatic 4.4 MeV and 11.6 MeV γ's from the ^{11}B(p, $\gamma\gamma$)^{12}C which are ideal to follow the variation of the XEC energy scale with time. The insertion and extraction of the target and proton beamline is little time-consuming and is performed thrice a week.

Charge Exchange reaction and LH_2 target To determine the energy and time resolution of the calorimeter, a γ source close to the expected signal energy (52.8 MeV) is required. This is achieved by making use of the Charged EXchange reaction (CEX) $\pi^- p \to \pi^0 n$ reaction and the subsequent neutral pion decay $\pi^0 \to \gamma\gamma$. The γ's energy in the lab frame is largely dependent on the neutral pion direction and therefore on the opening angle between the two γ's $\Theta_{\gamma\gamma}$, following Eq. 3.8.

$$E_{\gamma} = \frac{E_{\pi^0}}{2} \pm \sqrt{\frac{E_{\pi^0}^2}{4} - \frac{m_{\pi^0}^2}{2\,(1 - \cos\Theta_{\gamma\gamma})}} \tag{3.8}$$

In particular, the back-to-back topology corresponds to a high energy gamma at ≈ 83 MeV and a low energy one at ≈ 55 MeV, close enough to the γ energy from the $\mu \to e\gamma$ decay. To achieve the CEX reaction with MEG-II, negative pions are sent through the πE5 beamline towards a liquid hydrogen (LH_2) specifically designed for the occasion: gaseous hydrogen is cooled with LHe in order to reach a liquid state below 20 K and fill a thin aluminum cell at COBRA center. Details on Fig. 3.9.

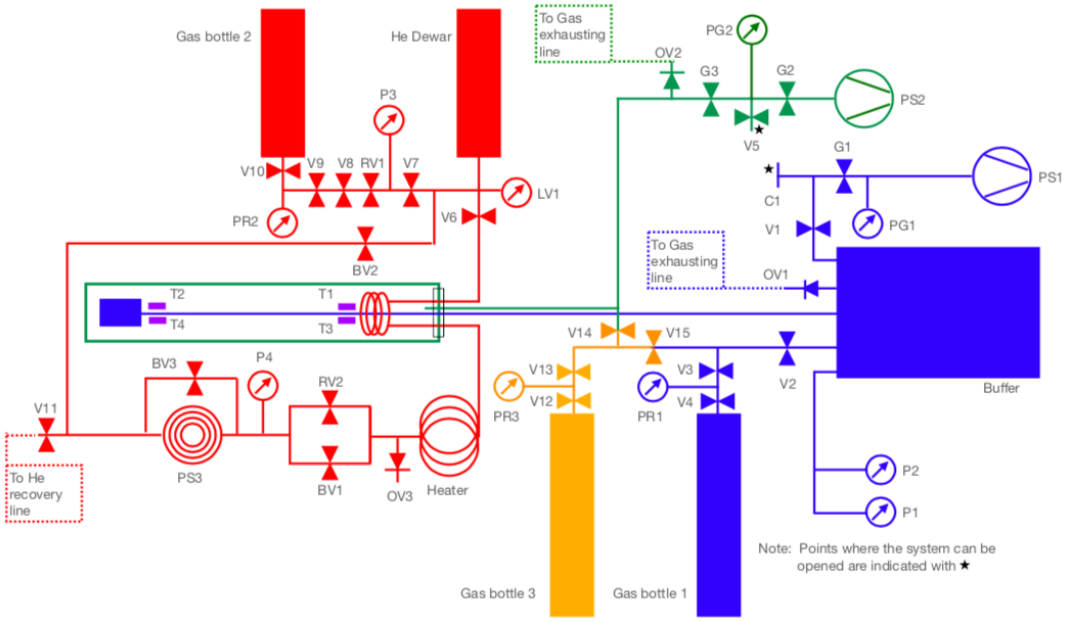

Figure 3.9: LH_2 target cooling circuit. The hydrogen system (buffer, exhausting line, vacuum pump, cell) is shown in blue, the helium one (bottle, dewar, copper rod, heater and recovery line) in red, the insulating vacuum one in green and the nitrogen flushing one in orange.

.

In order to select the back-to-back γ topology, an auxiliary detector is placed on the other side of the XEC with respect to the LH_2 target. This BGO calorimeter consists of a 4×4 array of bismuth germanate (BGO) crystals coupled to 16 PMTs and provides high energy resolution. A preshower, made of a pair of plastic scintillators, is placed in front of the BGO calorimeter in order to provide high-resolution timing information.

3.3.4 The Positron Spectrometer

The positron spectrometer aims at evaluating the positron direction, momentum and timing with high resolutions. After the muon decay, the positron trajectory is curved into the COBRA magnetic field and extracted making use of the hits produced on the Cylindrical Drift Chamber (CDCH) wires. Its direction and momentum at target can then be reconstructed with high resolutions. Being a slow detector, the CDCH is unable to provide timing information with the required accuracy. Two arrays of plastic scintillators called pixelated Timing Counters (pTC) located below the CDCH provide timing information with high resolution. Both detectors were designed in order to cope with a very large background positrons rate.

The COBRA magnet

The COnstant Bending RAdius magnet is a thin-wall superconducting magnet surrounding the positron spectrometer (see Fig. 3.10).

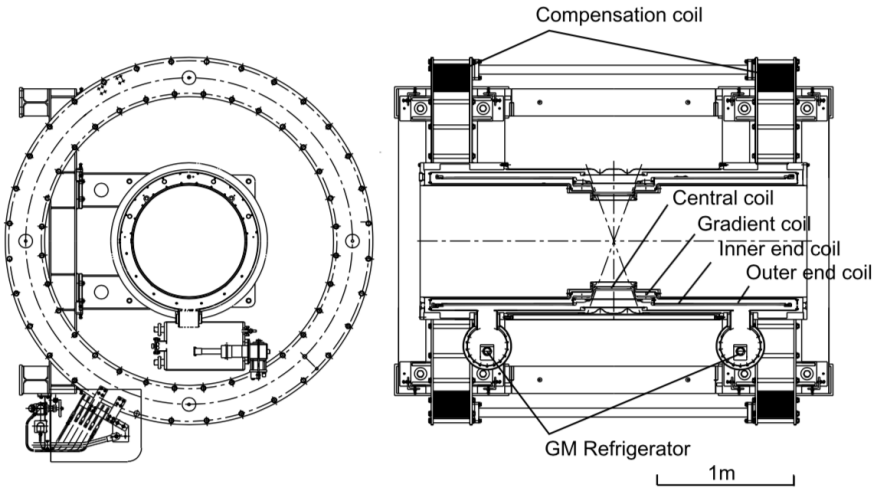

Figure 3.10: Technical drawing of the COBRA magnet.

.

It is designed with a small material budget (0.197 X_0) to enable γ's to pass through and reach the xenon calorimeter. Five coils at three different radii provide a gradient magnetic field from 1.27 T at the center to 0.49 T at both ends (see Fig. 3.11) and allow the positron bending radius to be almost independent from the emission angle. Such a gradient also sweeps away quickly the positrons emitted in the plane orthogonal to the muon beam in order to reduce the hit rate in the CDCH.

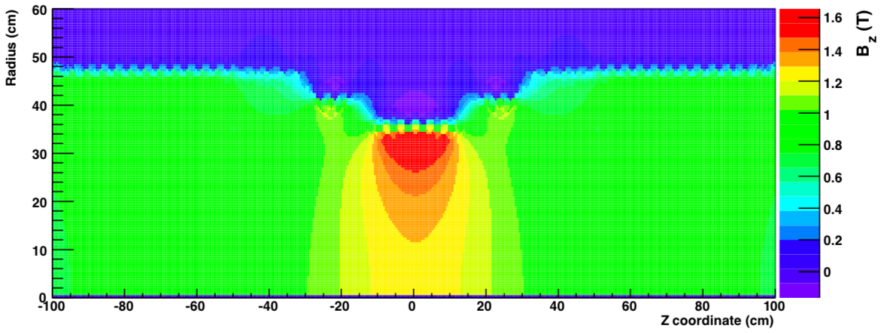

Figure 3.11: COBRA magnetic field map as function of the longitudinal and radial coordinates.

.

PMT gain is largely reduced within a strong magnetic field like COBRA's. Two compensation coils were added to cancel the stray field in the XEC region: the XEC PMTs and MPPCs see a field below 5 mT.

The Cylindrical Drift Chamber

The MEG-II Cylindrical Drift Chamber is a single volume tracking detector designed to minimize multiple scattering and to provide high transparency towards the pTC. The drift chamber has a cylindrical design to profit the positron curvature in COBRA. It is 191 cm long, has a 17 cm inner radius and a 29 cm outer radius. To know precisely the trajectory of the positron, the scattering of the particle has to be minimized and so does the amount of material crossed by the particle: this is the guideline for the CDCH design. The CDCH active volume is therefore filled with an ultralight He:iC_4H_{10}:O_2:2-propanol gas mixture with 88.5 %:9.8 %:0.5 %:1.2 % proportions. A positron turn through the chamber is equivalent to a 1.58×10^{-3} X_0. The CDCH volume is also separated from the muon-stopping target volume with a 20 μm-thick aluminised Kapton foil. The detector consists of 13056 wires set between the two end plates of the chamber (see Fig. 3.12).

The chamber is composed of 9 layers of 192 square drift cells, 5.8 to 8.7 mm wide based on the radial distance from the center. Each drift cell is composed of a central 20 μm diameter gold-plated tungsten anode surrounded by eight 40 or 50 μm silver-plated aluminum cathodes. The anode wires are mounted in a stereo configuration with a stereo angle between 6.0° for the innermost layer and 8.5° for the outermost layer. The stereo angle sign is alternated from one layer to the next, resulting in a hyperbolic profile of the chamber seen in Fig. 3.12. Two additional layers are placed in the inner and outer borders to equalize the electric field of the bordering cells.

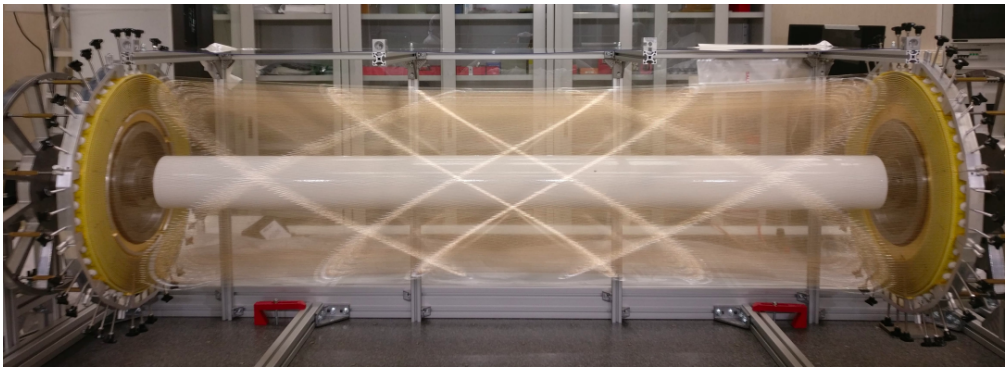

Figure 3.12: Picture of the CDCH with all mounted layers. The hyperbolic profile related to the stereo angles is observed.

.

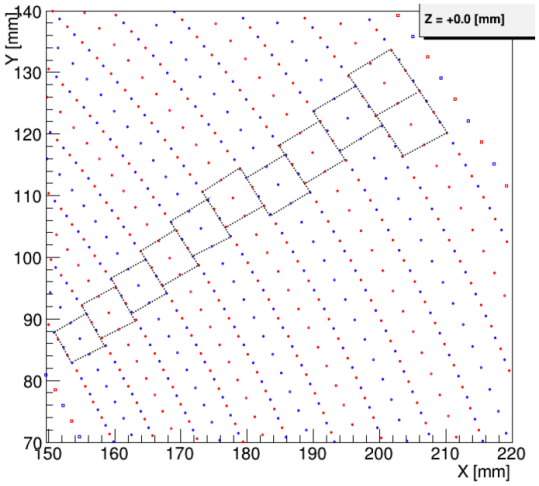

Figure 3.13: Drift cell configuration at the CDCH center ($z = 0$). The wires are in blue or red according to the alternating stereo angle sign.

.

A dedicated wiring strategy was performed to ensure the electrostatic stability of the drift cells, high precision on the wire positron, and tension into a huge wire density environment (≈ 6 wires/cm^2 at the endplates). The wires are read out on both sides making use of low-noise high-bandwidth front-end amplifier electronics. Two thirds of the anode wires are readout, the last third being outside of the acceptance defined by a back-to-back topology with respect to the C-shaped XEC. A charged particle going through the drift cells will lead to the creation of ion-electron pairs which will in turn lead to a signal in the anode wire (in the center of the drift cell). These induced signals or hits are used to reconstruct the positron

track (see Sec. 3.3.4). The CDCH performances are estimated:

- through a fit of the 52.8 MeV Michel decay ($\mu^+ \to e^+\nu_e\overline{\nu_\mu}$) spectrum edge.
- through Mott-scattered positrons: An e^+ beam is tuned to $\mathbf{p} = 52.8$ MeV/c and is sent towards the MEG-II target where it undergoes the well-known Mott scattering process.
- through straight cosmic rays μ tracks to perform the alignment of the CDCH.

A fit of the Michel positron spectrum shown in Fig. 3.14 is performed by multiplying the theoretical Michel spectrum by an acceptance error function and then convoluted with a resolution function, a sum of three Gaussians. Based on the offset between the fit and the spectrum, the energy scale of the positrons can be calibrated with a 0.01% precision. The positron energy resolution, extracted from the width of the main-contributing Gaussian, was estimated to be ≈ 90 keV.

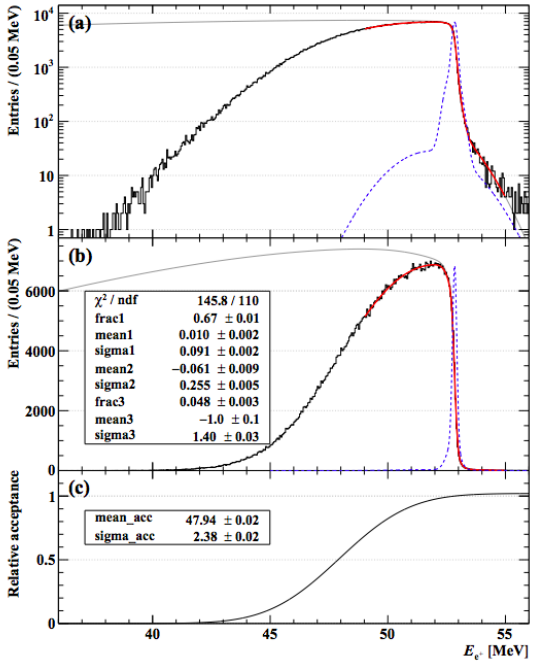

Figure 3.14: Michel positron spectrum (black) fitted with the function described in the text in logarithmic (top panel) and linear (middle panel) scales. The resolution function, a sum of three Gaussians, is shown with a dashed blue line. The fitted acceptance function is shown in the bottom panel.

.

The Pixelated Timing Counter

The CDCH is a slow detector, being unable to provide timing information with high resolution. A relative positron-γ timing resolution below 100 ps is mandatory for achieving the sensitivity MEG II aims for. The relative timing positron-γ is crucial to effectively reject the accidental background - the main background source. The timing information is also used to set the MEG-II trigger and for the reconstruction of the positron track through the CDCH. Two highly segmented plastic scintillator sections (see Fig. 3.15) are installed between the CDCH outer radius and the COBRA coils, one upstream (US) and one downstream (DS). The pTC volume is separated from the CDCH volume with a 2 mm-thick carbon fibre aiming at minimizing the multiple scattering between the two detectors and maximizing the matching efficiency between the CDCH track and the pTC hits. Composed of 256 tiles each, each counter section has a 45° orientation with respect to the beam axis to match in the best way possible the track of a signal positron. Their spatial arrangement also tends to maximize the number of positron hits in order to optimize the timing resolution.

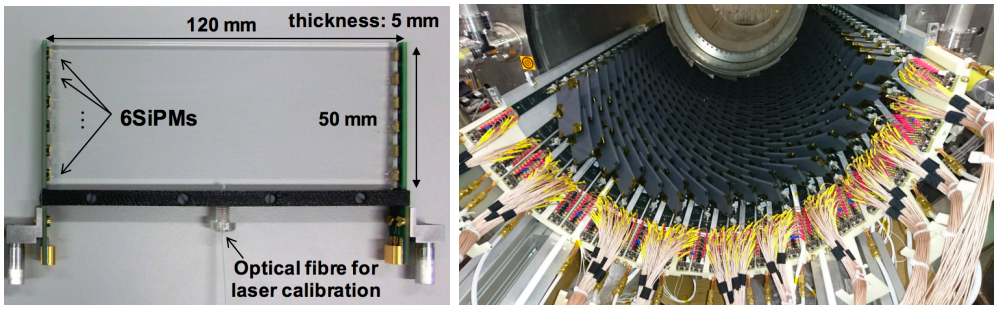

Figure 3.15: Picture of a single pTC tile (left) and of one of the two pTC sections (right).

.

Each BC422 scintillator tile, manufactured by Saint Gobain, is covered with a reflector aluminum foil and a 25 μm black sheet used for light insulation. Each 120 mm-wide, 5 mm-thick and 40 or 50 mm-high tile is read by 6 or 7 SiPMs, depending on the position of the tile, which collects the scintillating photons. A typical positron track goes through 10 tiles, leading to an average time resolution of 43 ps, according to the plot in Fig. 3.16.

Monitoring this timing detector with resolutions below 50 ps requires fast and precise calibration. The counters are connected to a picosecond laser source through optical fibres to check the detector stability and to calibrate the laser-counter and the inter-counter time offsets [74].

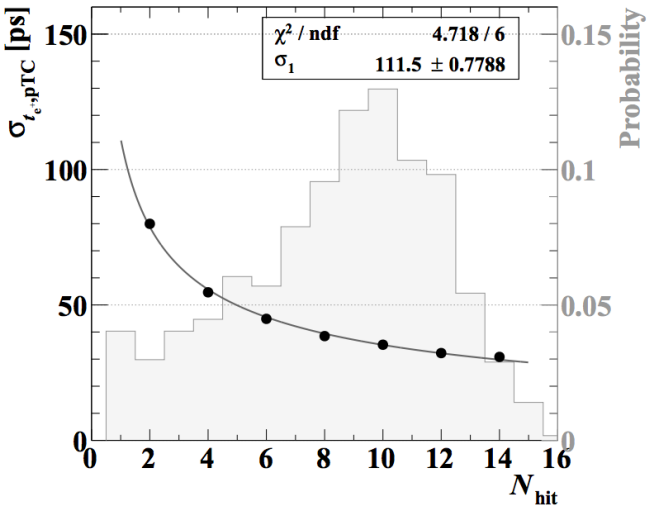

Figure 3.16: Positron timing resolution $\sigma_{t_{e^+},pTC}$ as a function of the number of positron hits in the pTC (black curve and dots). pTC positron hits number distribution for a signal positron (gray).

.

Positron track reconstruction

The positron track within the spectrometer is reconstructed following the steps introduced in Fig. 3.17. Details on the track reconstruction can be found in [75].

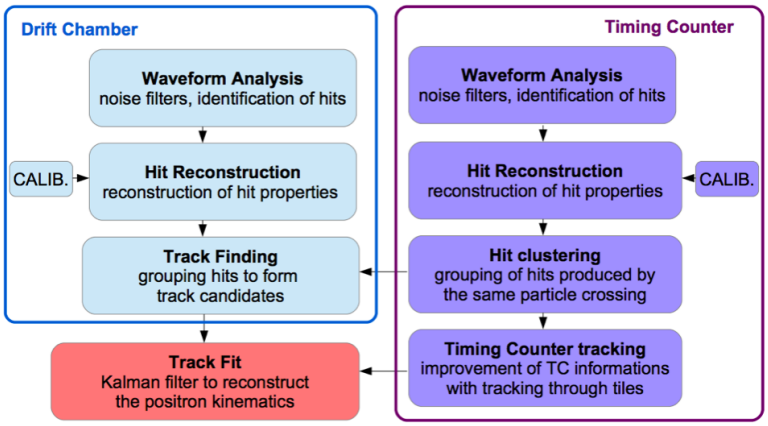

Figure 3.17: The different CDCH and pTC tasks performed in order to reconstruct the positron kinematics.

.

The track reconstruction is illustrated in Fig. 3.18: the positron track in the spectrometer (in red) is extrapolated from the combination of the CDCH and pTC

hits (in green) up to the target plane.

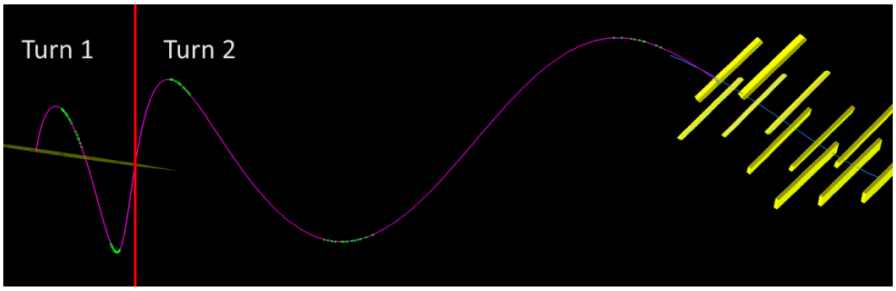

Figure 3.18: Track reconstruction illustration.

.

pTC hit reconstruction The pTC hits are reconstructed making use of the waveforms at both ends of each tile. After a pulse is found to pass over a threshold, the constant fraction method is applied to determine the arrival time of the scintillation light at each end of a tile, t_1 and t_2. Writing t_{tile} the time offset of the single tile, the time of the hit is extracted as $t_{hit} = \frac{t_1+t_2}{2} - t_{tile}$. Accounting for the scintillation light velocity within the tile and the time difference between t_1 and t_2, the coordinates of the hit on the tile are estimated. The hits are then clustered based on their timing and the hit tile position. The hits are ordered using their depth with respect to COBRA center.

CDCH hit reconstruction Pulses within a waveform are detected with a threshold crossing method. The waveforms then go through coherent noise subtraction. One front-end readout board delivers 16 waveforms from 16 adjacent wires. All pulseless ("noise") waveforms are averaged to obtain a proxy for the coherent noise. This noise is then subtracted from waveforms with a pulse. Waveforms at both ends of a wire, $f(t)$ and $g(t)$, are expected to be close in shape and are simultaneously fitted minimizing:

$$\int (f(t) - A \times g(t+\tau))^2 \, \mathrm{d}t \tag{3.9}$$

A and τ represent the amplitude and time difference between the two pulses. The hit time is extracted from $t_{1,2}$ the pulse time at each end of the wire: $t_{hit} = (t_1 + t_2)/2$. The hit coordinate along the wire is then estimated via two methods. The time difference method (T) estimates the longitudinal z_w coordinate along the wire thanks to the time difference between the two pulses:

$$z_{w,\mathrm{T}} = \frac{t_1 - t_2 - t_{\mathrm{ends}}}{2} \cdot v_{\mathrm{eff}} \tag{3.10}$$

t_{ends} represents the time offset between the two wire ends, v_{eff} the signal propagation speed along the wire.

The charge division method (Q) is estimated writing $Q_{1,2}$ the charge at each end of the wire, G_{diff} the gain difference between both ends, Z the input impedance of the amplifier, ρ the wire resistivity, L the wire length:

$$z_{w,\text{Q}} = \frac{G_{\text{diff}}\, Q_1 - Q_2}{G_{\text{diff}}\, Q_1 + Q_2} \left(\frac{Z}{\rho} + \frac{L}{2} \right) \tag{3.11}$$

z_w is then transformed into a z in the MEG-II global coordinate system accounting for the wire position and direction.

The particle's distance of closest approach (DOCA) to the anode wire is then estimated by converting the time of the first detected ionization cluster using the time–distance relationship. The latter was extracted from Garfield++ simulations [76] and the associated isochrones are shown in Fig. 3.19. The first ionization cluster time is approximated using the pTC cluster time t_{pTC} and the time-of-flight from the CDCH hit to the pTC t_{TOF}: $t_{hit} - t_{pTC} + t_{TOF}$.

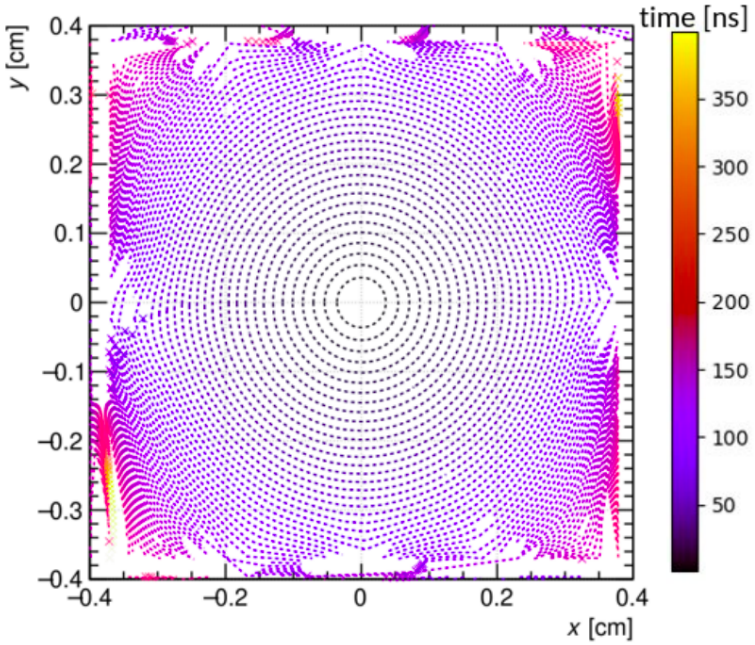

Figure 3.19: Garfield++ simulation of the isochrones connecting points with same drift time towards the sense anode wire.

.

Track finding The track finding is a pattern recognition algorithm which aims at combining reconstructed hits in order to form a track candidate.

The conversion from cluster time to drift distance doesn't provide the hit (x,y) position but a two-dimensional isochrone. To determine the actual hit position and the track direction, four hits must be combined: two hits from one layer and

two hits from the next. The external layers are preferably used for this track seeding because of their lower occupancy. A tracklet or track seed attempts to connect the various isochrones. Out of all the allowed tracklets, the combination of four hits provides the only viable one, as illustrated in Fig. 3.20. z coordinate compatibility between the hits and pTC cluster position compatibility with the track seed direction are imposed.

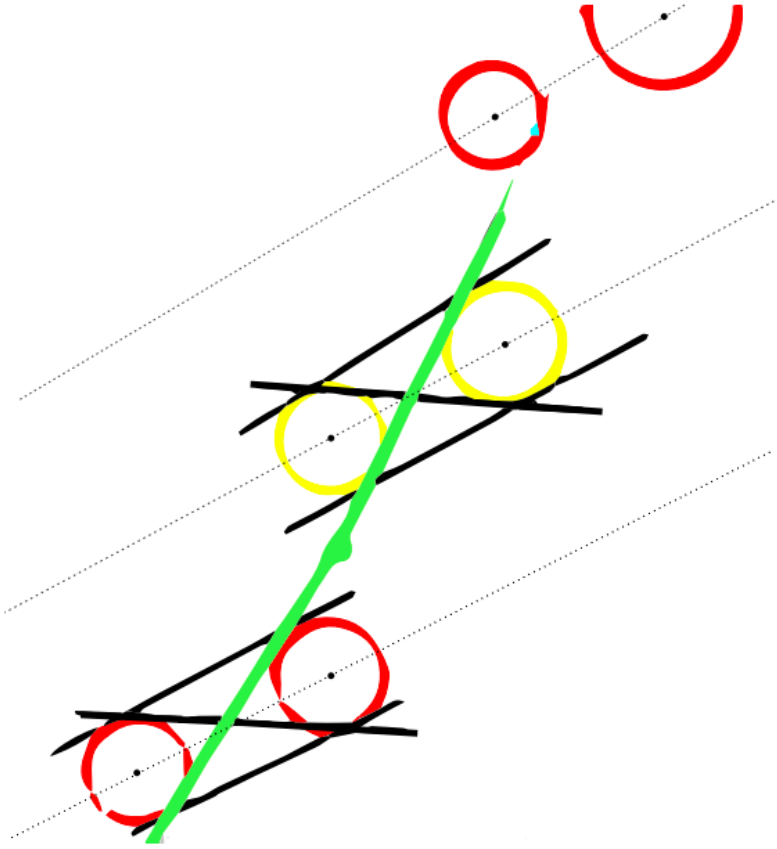

Figure 3.20: Track seeding example. Isochrones from pairs of hits in different layers are shown in red and yellow. Viable tracklets for pairs of hits are in black. The only tracklet allowed by the two pairs of hits is the green one.

.

The seed trajectory is then extended backward and forward to the adjacent layers aligning with the expected particle motion in the magnetic field and accounting for energy loss. If hits consistent with the expected trajectory are found, they are added to the track candidate, a list of hits supposedly induced by the same particle. The procedure is iterated and the trajectory estimate is refined until reaching the innermost layers.

Track fitting The track candidate can then be fitted via a Kalman filter [77] using the estimated drift distance of the hits and a weighted average of their time-difference and charge division z estimate. An additional deterministic annealing filter (DAF) [78], known for its good performance in a high noise and pileup environment, identifies and rejects background hits, not produced by the candidate particle. The track segments are fitted first. Afterwards, the turn-end of one segment propagated forward is compared to the turn-start of the next segment propagated backward. If a good match is found, the two segments are merged. Merging all possible segments leads to the full, multi-turn trajectory of the positron. The track is then extrapolated to each pTC hit and matched with a pTC cluster to extract the best estimate of the track time. With an updated track time and a first fitted track, hits missed in the first iteration can be recovered and the track is re-fitted to refine the trajectory estimate. The extrapolation to the target plane allows the precise extraction of the muon decay vertex (x,y,z) and the positron kinematics at vertex: magnitude of momentum, direction of momentum (including polar and azimuthal angles). The muon decay time is estimated by averaging the hit time on each pTC tile corrected by the TOF from the vertex to the tile: $t_{decay} = \frac{1}{n}\sum_{i=1}^{n}(t_{hit_i} - t_{TOF_i})$.

3.3.5 Radiative Decay Counter

A Radiative Muon Decay with E_γ close to the kinematic edge (> 48 MeV) emits a low-energy (1-5 MeV) positron. Such tracks are helices within the beamline volume and don't go through the spectrometer. Instead, they fly towards the endcap along the beam axis as seen in Fig. 3.21. The Radiative Decay Counter (RDC) aims at tagging such positrons with a 40% efficiency and reducing the γ background in the E_γ signal region. It was estimated to provide a 16% improvement to the $\mu^+ \to e^+\gamma$ sensitivity. The RDC tagging requires both timing and energy measurement.

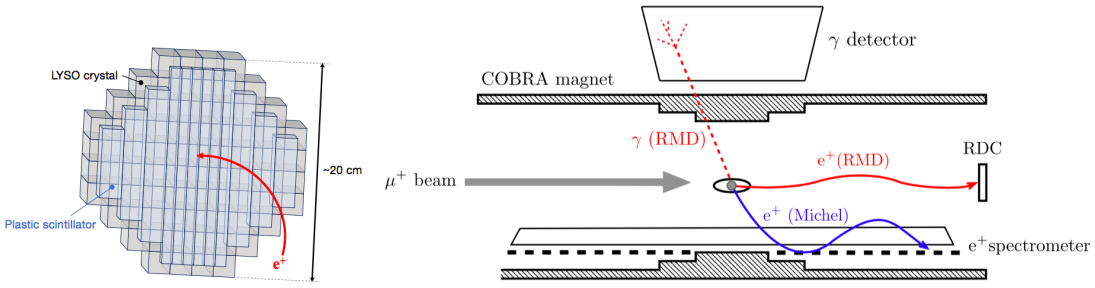

Figure 3.21: RDC design (left). RDC principle: low-energy positron from radiative muon decay can be tagged (right).

.

The detector consists of 76 ($2 \times 2 \times 2$ cm^3) LYSO crystals for energy measurement and 12 plastic scintillator bars for timing measurement. The crystals are arranged in an octagonal shape and are each coupled to one S12572-025P MPPC. The bars are arranged in front of the crystals in a plane covering the same octagonal area and coupled to two or three S13360-3050PE MPPCs in series.

3.3.6 Trigger and DAQ

The upgrade of the MEG experiment led to an increased segmentation of all detectors. A new trigger and data acquisition system, the WaveDAQ, was designed to cope with a total of $\approx$ 9000 channels while providing a 1.4 GHz digitization frequency. The WaveDAQ system consists of 35 crates, each containing 16 WaveDREAM (Waveform Domino REAdout Module) boards, a Data Concentrator Board for streaming and storage, and a Trigger Concentration Board for collecting trigger information. The WaveDREAM board, illustrated in Fig. 3.22, is a compact 16-channel platform containing two Domino Ring Sampler 4 (DRS4) chips.

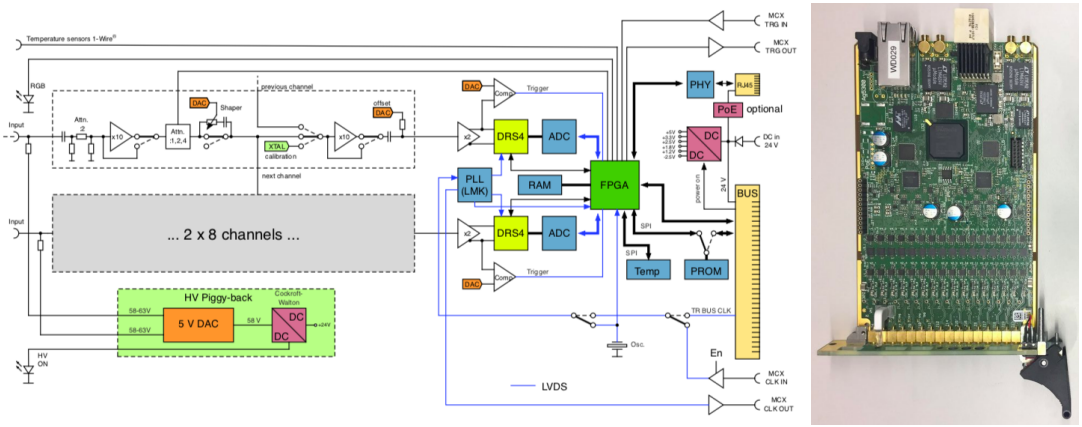

Figure 3.22: Simplified schematics (left) and picture (right) of a WaveDREAM board.

.

With a bandwidth of 1 GHz and a sampling speed of up to 5 GSPS, the DRS chips are 1024 sample-and-hold cells which sample and temporarily store the analogue signal from each channel. When the trigger is activated, the digitization of the signal is performed through an external analog-to-digital converter (ADC) at 80 MSPS. The outputs from the ADCs are sent to the FPGA which builds the trigger logic. The storage time of the DRS imposes a strong constraint on the trigger latency with a maximum allowed value of 731 ns. The CDCH information, due to drift times up to 300 ns, can therefore not be included in the trigger. The

latter only relies on XEC and pTC waveforms only and on the coincidence of three conditions:

- QSUM condition: energy deposit in the LXe calorimeter above a given threshold.
- Time condition: time coincidence between LXe energy deposit and pTC hit within a time window.
- Direction match condition: LXe energy deposit position and pTC hit location consistent with the back-to-back topology of the $\mu^+ \to e^+\gamma$ signal.

3.3.7 Simulation and software

A full simulation of the MEG-II detector was developed relying on Geant4 [79], measurements and dedicated simulations from Garfield++ for example. There are two main branches in the MEG-II software. One is dedicated to the data, the other to simulations but both go through the same reconstruction procedure. Therefore, these Monte-Carlo (MC) simulations are treated the same way as actual data. To do so, the software relies on three modules as illustrated in Fig. 3.23:

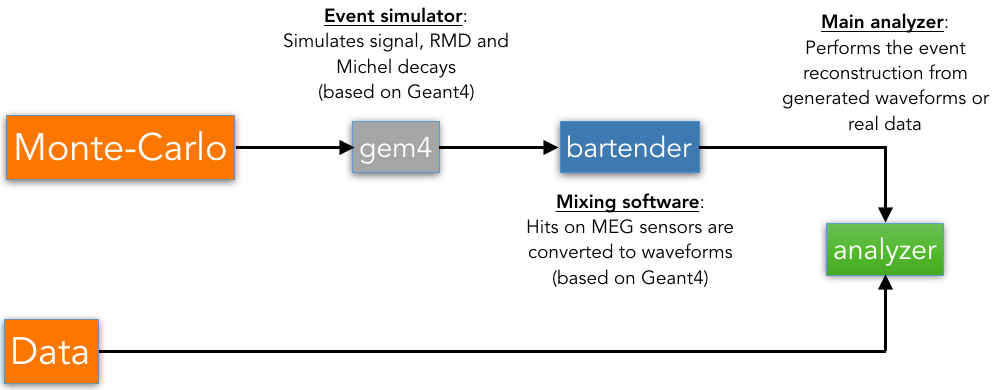

Figure 3.23: Structure of the MEG-II software allowing consistency between simulation and data.

- gem4 (event simulator): based on Geant4 simulation software, it simulates signal and background particles, the various materials in the experiment as well as their geometry, and the interactions between particles and matter
- bartender (mixing software): all hits on MEG-II sensors simulated at the gem4 level are converted into simulated electronic signals, thanks to actual

waveforms from collected data. Realistic waveforms are then reproduced. Different gem4 events are also mixed at this stage in order to simulate several muon decays within the same time window for example.

- analyzer: it analyses all waveforms (both from MC simulations and actual data), performs the event reconstruction and extracts the particles' kinematics

The analyzer module also relies on the MEG-II database which contains all information about the apparatus and the subdetectors, including position, rotation angles, the different materials and associated properties, the sensor gains, and the relevant timing windows.

Chapter 4

The apparatus and simulations for the X17 search

The MEG-II apparatus for the $\mu^+ \to e^+\gamma$ decay can be readily adapted to search for X17. With minor modifications, it allows for the study of the $^7\text{Li}(p, e^+e^-)^8\text{Be}$ reaction with enhanced resolution and broader angular acceptance than Atomki.

This chapter first outlines the necessary adaptations to the MEG-II apparatus and trigger for the X17 search, covering the proton beam, target, and magnetic field. The search requires excellent understanding of Internal and External Pair Conversion (IPC and EPC) backgrounds, which we address through specific simulations of detector, background processes and signal in the second part of the chapter.

4.1 Adapting MEG-II for the X17 search

The MEG-II apparatus is ideal to perform the X17 search. Its Cockcroft-Walton accelerator can be used as a proton source in order to shoot at a lithium target at the center of the apparatus. The lower energy particles can be tracked within the CDCH by tuning the magnetic field. Pairs of charged leptons can be selected with a specifically designed trigger based on both the CDCH and the pTC hits. The photon production, spectrum and rate can be followed with the BGO with minimal changes.

4.1.1 The Cockcroft-Walton Accelerator

The MEG-II XEC energy scale is estimated weekly making use of its own Cockcroft-Walton (CW) accelerator, a source of proton with currents up to 100 μA and energies up to 1100 keV [80]. For MEG-II purposes, the accelerator is ran at $E_p = 500$ keV. For the X17 search, the beam is required to be used at energies up to $E_p = 1080$ keV. The presence of several species within the beam also requires tuning in order to select a pure H^+ beam. We first describe the functioning of the

Cockcroft-Walton accelerator before presenting the three species produced by the accelerator. Finally, we introduce the beamline used to perform the H^+ selection and the tuning towards the target at COBRA center.

The MEG-II CW accelerator is a single-stage in-line singletron manufactured by HVEE. A general scheme of the accelerator is given in Fig. 4.1. A gas inlet is ionized and then directed towards a vacuum chamber by applying a terminal voltage. This high-voltage DC output is obtained from the conversion of a lower-voltage AC input through a cascade of voltage multipliers.

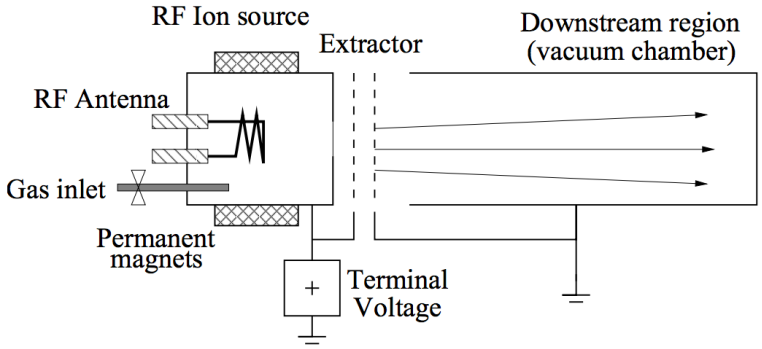

Figure 4.1: Scheme of the Cockcroft-Walton accelerator with the ion source, the downstream region at ground potential and the applied terminal voltage.

.

The RF ion source

An ion source is obtained by exciting a dihydrogen gas volume with an RF oscillator. The neutral gas collisions then lead to ionization. The resulting plasma, including H^+, H_2^+ and H_3^+ ions, is confined making use of an axial magnetic field. A DC high voltage is then applied to accelerate the ions. The scheme is detailed in Fig. 4.2 (left) while a picture of the source is shown in Fig. 4.2 (right).

The voltage multiplier cascade

The high voltage is obtained through the circuit schematized in Fig. 4.3 (left). It was first proposed by Cockcroft and Walton in 1932 [81] and allowed the production of the first man-made nuclear reaction. The base element of the circuit is surrounded by a dashed line and is called voltage multiplying stage. An alternative voltage U = U0 sin ωt is fed to two columns of capacitors (the pulsating column on the left and the static column on the right) connected with diodes. During the first negative half-cycle, C1 is charged at ΔV = U0. During the next positive

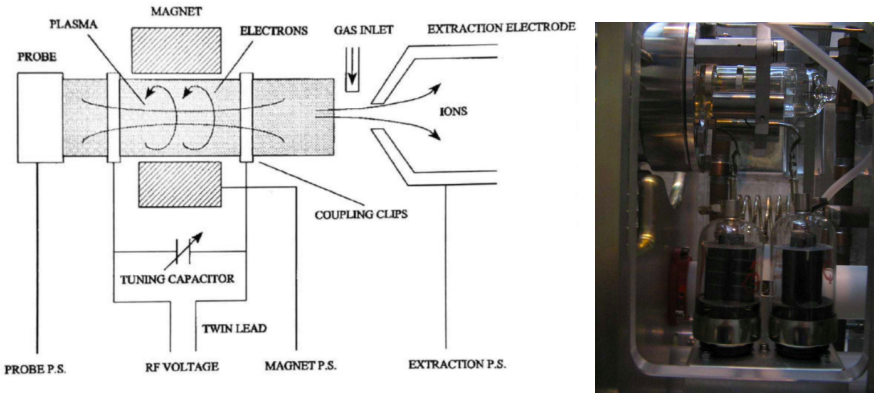

Figure 4.2: RF ion source scheme (left) and picture (right).

.

half-cycle, D1 is reverse-biased and blocks current while D2 is forward-biased. C2 will then be charged after a few cycles at $\Delta V = 2\text{U0}$. The process is repeated for each additional voltage multiplication stage. A potential difference of $\Delta V = 2N\text{U0}$ can be obtained using N stages. MEG-II's cascade has some specificities shown in Fig. 4.3 (bottom right). A set of capacitor coupling rings ensures the voltage transmission to the capacitors. The cascade is located within a pressure vessel filled with SF_6 insulating gas. Thanks to its high density and electronegativity, it is a good dielectric medium preventing electric arcs around the cascade. In case of arc, the SF_6 can break down but quickly reforms, leading to good stability. A picture of the CW accelerator, after SF_6 pumping and removal of the pressure vessel, is shown in Fig. 4.3 (top right).

The accelerator driver

The CW accelerator is controlled remotely through a dedicated industrial computer. After a good vacuum (10^{-6} mbar) is reached in the downstream volume, the gas inlet is opened and the plasma is stabilized within minutes. The probe voltage controls the extraction from the ion source and therefore the ion current. The extraction voltage controls the beam focusing. The terminal voltage selects the ion kinetic energy. The power is fed to a resonant circuit as an input for the voltage multiplication.

The proton beam line

A layout of the CW accelerator connected to the proton beamline as well as the elements along it is sketched in Fig. 4.4. The beamline is 10.5 m long from the CW accelerator to COBRA center. The CW area and the πE5 are separated by

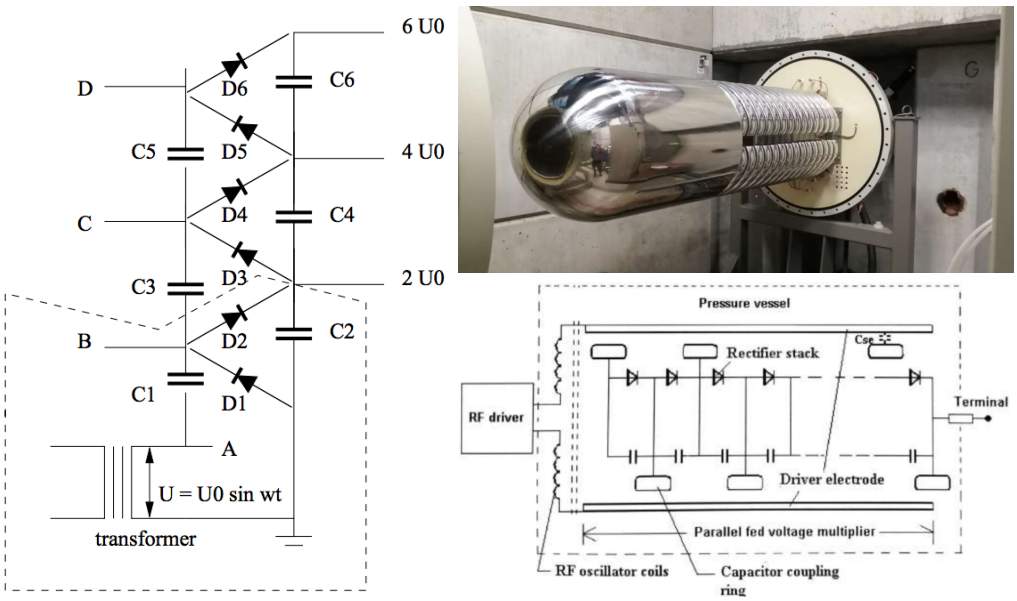

Figure 4.3: Standard CW voltage multiplier (left). MEG-II CW's voltage multiplier (right) picture (top) and scheme (bottom).

a concrete wall after which is located a beam blocker (BB) acting as a current probe. The vacuum along the beamline is performed by two pumping systems composed each of a primary scroll pump and a turbo-molecular pump. Together, a 10^{-6} mbar vacuum can be reached within the beamline, sufficient to open the gate valve connection to the accelerator. The beam trajectory is tuned making use of four dipolar fields, two for vertical deflections and two for horizontal deflections. The beam tuning is detailed in the next paragraph. The beam position can be monitored with a camera and a permanent movable proto-fluorescent quartz located after the magnets. The end of the beamline is connected to an extensible bellows system allowing the insertion and the extraction of the target to and from COBRA center, passing through the spectrometer volume. For the MEG-II search, a muon-stopping target is installed at COBRA center within a helium volume. For the X17 search, the muon target is extracted and the insertion system, responsible for moving the helium in and out for calibrations, is removed. The whole system is therefore immersed in air. The bellows system brings the target in at a speed of 4 mm/s. This allows safe operation and good complementarity between the MEG-II and the X17 operations. The longitudinal position of the target during and after insertion is obtained using an absolute encoder with a 1-mm precision.

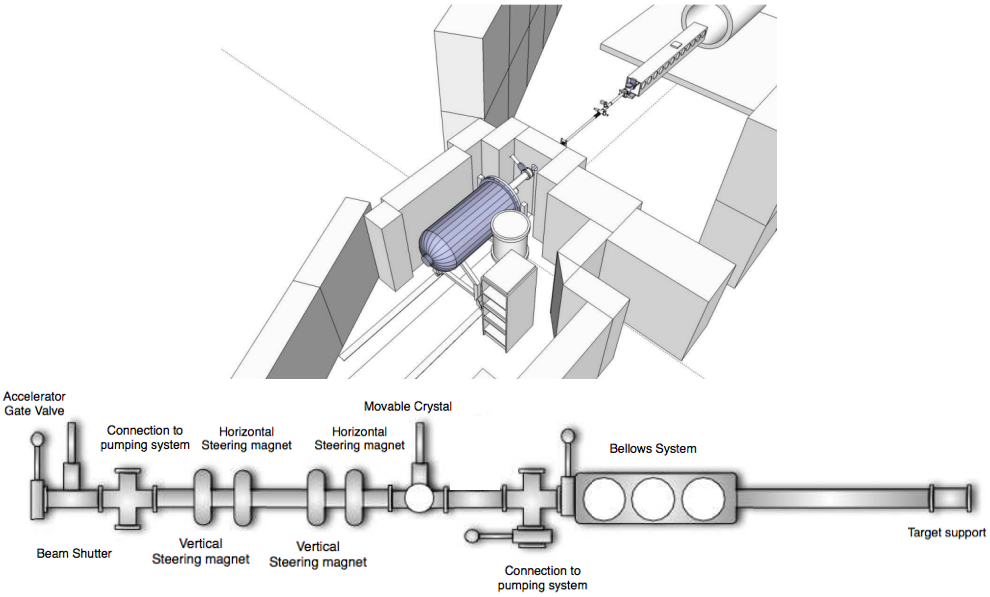

Figure 4.4: (Top) The CW area and the πE5 area layout: the CW accelerator is located before a separation wall after which the beamline is connected. (Bottom) Elements mounted along the beamline from the CW accelerator to the target.

.

Three species: H^+, H_2^+, H_3^+

After ionization of a dihydrogen gas, three species can be obtained: H^+, H_2^+, and H_3^+. It is crucial to understand their composition and optics in order to select the interesting one, H^+ in our case. Accelerated with the same terminal voltage, the three species have different momenta and are therefore deflected differently within a magnetic field. At the installation of the CW in 2007, a deflecting magnet along with a Faraday cup was used to select one of the three species and measure its associated current. The exercise was carried out by varying the overall current and the terminal voltage. The results are reported in Fig. 4.5 as a percentage of the total number of ions. The beam composition was found to be largely independent of the current and terminal voltage and to be dominated at almost 75% by the H^+ ion. H_2^+ represents 25% of the total while H_3^+ is almost negligible (2%).

More recently, in 2024, another study was carried out to better understand the beam composition. A proto-fluorescent quartz and a radiation-hard camera were used to observe the species and obtain the maximal separation, using two dipolar fields, one vertical and one horizontal located right after the wall, after BB. In Fig. 4.6 (left), the two fields' intensities were tuned to obtain such a separation between the H^+ and the H_2^+ spots, using their different momenta. The two spots

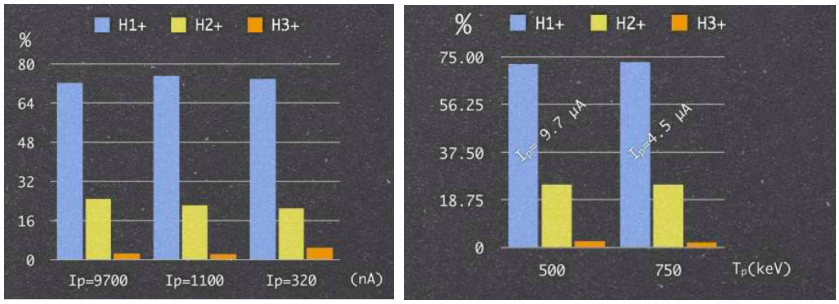

Figure 4.5: CW beam ion composition at various currents (left) and terminal voltages (right).

.

are represented by their blue light emission and are clearly observed. They can be identified knowing that the species with less momentum (H^+) should undergo the most deviation within our dipolar field. An additional test was performed to confirm the identification. A collimator, shown in Fig. 4.6 (middle), was designed and installed to block the H_2^+ species from the beam. It consists of a 100 μm half-circle copper film held between 2 C-shaped copper rings and is inserted within the beamline. It results in the isolation of the single H^+ beam spot as seen in Fig. 4.6 (right). The dipolar fields can also be tuned to have the H_2^+ beamspot pass the collimator while the H^+ spot would end up in the beam pipe in this configuration. The two species can then be selected without the contribution from the other.

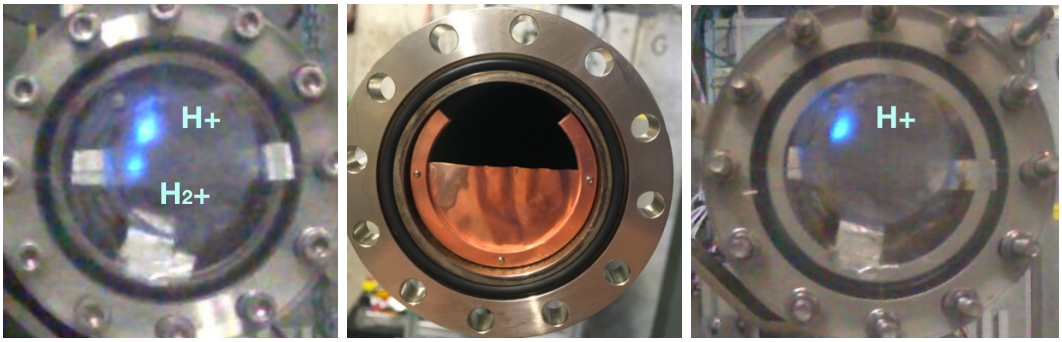

Figure 4.6: The beamspots observed with a camera on a proto-fluorescent quartz before (left) and after (right) installation of the copper collimator (middle).

.

A thin 1.9 μm LiPON target within a carbon fiber vacuum chamber, described in Sec. 4.1.2, was positioned right after the collimator in order to measure the photon rate of the $^7\mathrm{Li}(\mathrm{p},\gamma)^8\mathrm{Be}$ reaction for the two species using a 3"x3" Lanthanum Bromide (LaBr3(Ce)) scintillator installed in a configuration similar to

Fig. 4.7 (top). With a given terminal voltage of N kV, both H^+ and H_2^+ obtain the same kinetic energy of N keV. However, when arriving on target H_2^+ dissociates into two protons carrying each roughly half of the total kinetic energy, so roughly N/2 keV. Given the large difference of cross-section for the $^7Li(p,\gamma)^8Be$ at proton energies of 440 keV and 1000 keV (see Fig. 4.7 (bottom)), one should observe an order of magnitude difference in photon rate from both spots on target. The measured rates from both spots after tuning the detector threshold to be well above the detector's self-radiation background are given in Tab. 4.1. Based on the expected composition of the beam from Fig. 4.5, the difference in currents from both species should only result in a secondary effect on the measured photon rate. The background rate in this configuration, after the beam is turned off, was measured to be around 3 Hz and is mostly due to cosmic rays.

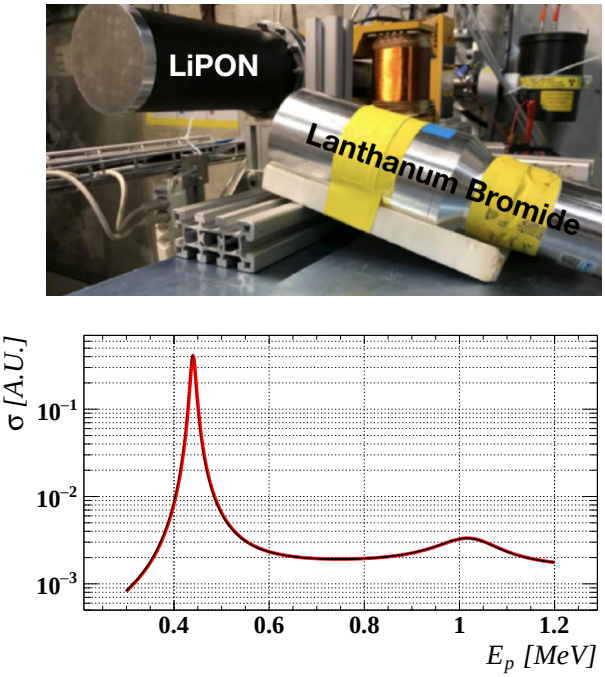

Figure 4.7: (Top) Beam spots identification setup making use of a LiPON target and a Lanthanum Bromide scintillator. (Bottom) Theoretical $^7Li(p,\gamma)^8Be$ cross-section as a function of the proton energy, computed from [7].

.

For the H^+ species, the rate should be an order of magnitude larger at 500 kV than at 800 kV or 1000 kV. For the H_2^+ species, the rate should be equal to the background rate at terminal voltages below 800 kV as the cross-section of the reaction is negligible for proton kinetic energies below $800/2 = 400$ keV. However,

Terminal voltage [kV]	**500**	**800**	**1000**
Beam spot on target	Top spot	Top spot	Top spot
Measured photon rate [Hz]	100	10	12
Beam spot on target	Bottom spot	Bottom spot	Bottom spot
Measured photon rate [Hz]	3	3	200

Table 4.1: Measured photon rates from the ^{7}Li(p, γ)^{8}Be for the two beam species at various terminal voltages.

at 1000 kV, the two protons from the H_2^+ species should scan the 440 keV resonance and yield a large photon rate. It is exactly what is observed from the measurements in Tab. 4.1. The top spot is confirmed to be H^+ while the bottom one corresponds to H_2^+.

After the identification was performed, the beam composition was re-measured with another method, making use of the collimator (C) between two Faraday cups, one upstream of the collimator, called BB and one downstream of the collimator, called FC. The setup pictures with the three elements are shown in Fig. 4.8. BB should measure the total current, all species included, while FC should measure the current after collimator.

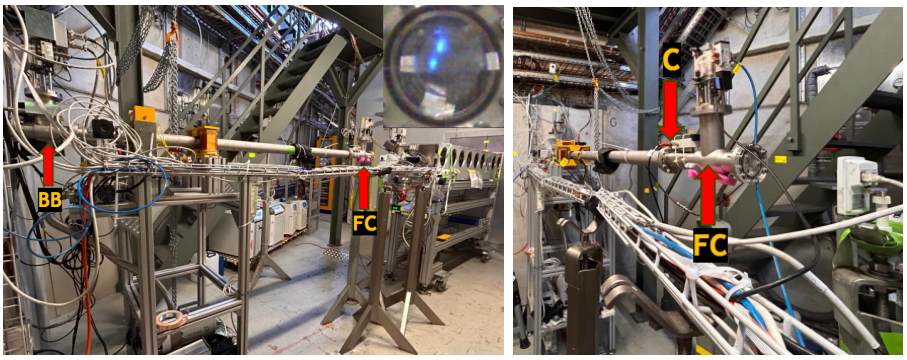

Figure 4.8: Beam composition measurement setup making use of two Faraday cups before (beam blocker, BB) and after (Faraday cup, FC). The collimator, when installed, is located at C.

.

The BB and FC currents were measured simultaneously and for total currents ranging between 0.5 μA and 30 μA. A set of measurements without collimator was performed in order to intercalibrate BB and FC and is reported in Fig. 4.9 (left). At large BB currents, one can see a deviation from the linear regime due to the shorter length of the BB with respect to the FC, leading to an enhanced electron escape and therefore an artificial additional current. The intercalibration and the linear

fit to the data are therefore performed for $I_{BB} < 10$ μA. Two types of data points were recorded in order to ensure consistency, the ones taken while increasing the total current and the ones taken while decreasing it. Measurements with collimator installed, selecting the H^+ species only, are shown in Fig. 4.9 (right).

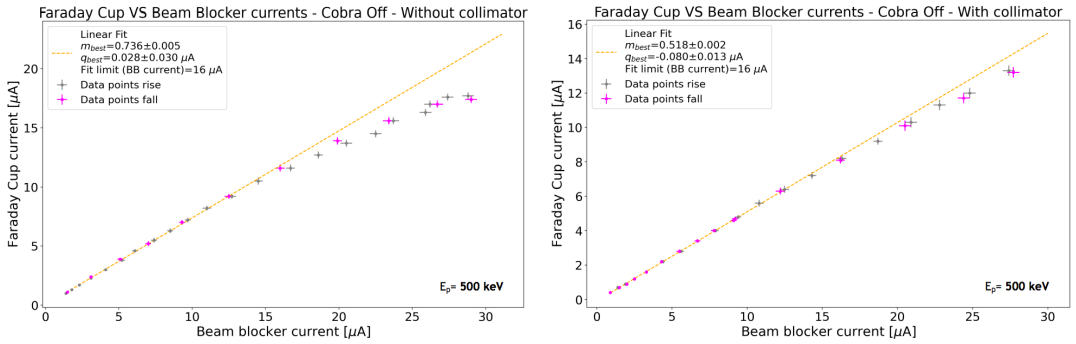

Figure 4.9: Measured Faraday cup current as a function of the measured beam blocker current at $E_p = 500$ keV without collimator (left) and with collimator (right) installed between BB and FC. Gray data points were recorded while increasing the total current and pink data points while decreasing it. A linear fit was performed on all points with $I_{BB} < 10\mu$A and its parameters are quoted.

.

The H^+ proportion is estimated from the ratio of the two slopes and the H_2^+ proportion is estimated as the complement. The H_3^+ proportion is neglected here.

$$P_{H^+} = (70 \pm 1)\% \tag{4.1}$$
$$P_{H_2^+} = (30 \pm 1)\% \tag{4.2}$$

These results are in line with those obtained in 2007 and presented in Fig. 4.5. After these tests, the beamline was re-connected to the bellows. While the first two dipoles, V1 and H1 (Fig. 4.10 (left)), were used to obtain the maximal separation between the two main species in the beam, two additional dipoles, V2 and H2 (Fig. 4.10 (right)), were added after the collimator to lead the remaining H^+ beam to the target placed at COBRA center. V and H stand for the vertical or horizontal orientation of the dipolar field.

The position of the species within the beam is expected to be independent from the current but has a strong dependence on the terminal voltage. The selection of H^+ at collimator and its tuning towards COBRA center should therefore be repeated at each interesting value of terminal voltage. A set of dipole voltages (V1, H1, V2, H2) was obtained for terminal voltages of 400 kV, 500 kV, 600 kV,

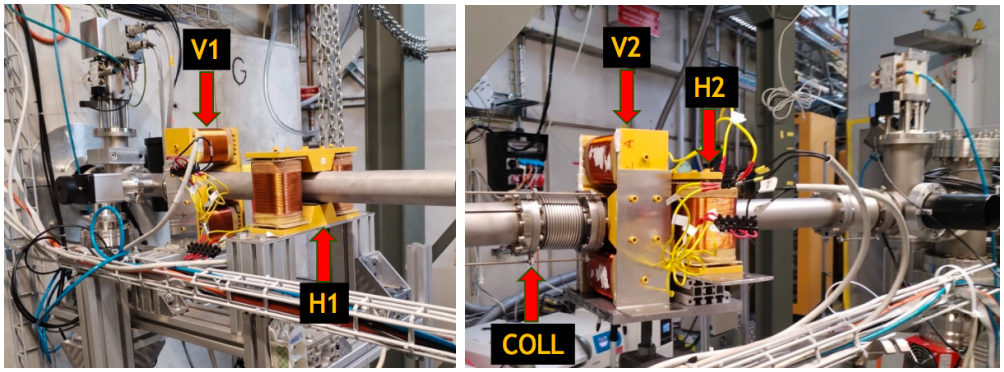

Figure 4.10: (Left) Vertical and horizontal dipoles placed right after the wall, V1 and H1. (Right) Vertical and horizontal dipoles placed right after the collimator (COLL), roughly two meters behind the wall, V2 and H2.

.

700 kV, 800 kV, 900 kV and 1000 kV. To do so, the separation was optimized with a proto-fluorescent quartz right after collimator and the beam was centered with another quartz at COBRA center. Pictures of the quartz at collimator and at COBRA center after tuning for terminal voltages of 500 kV and 1000 kV are shown in Fig. 4.11.

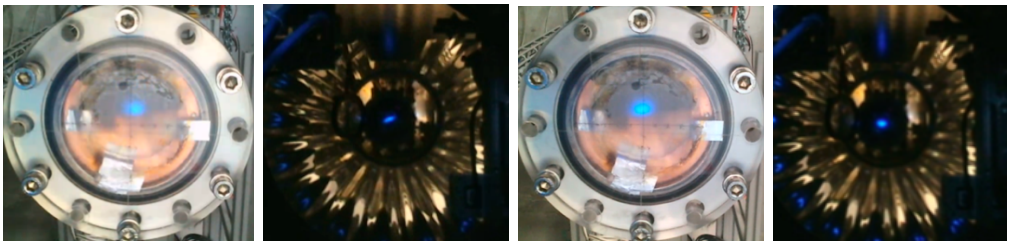

Figure 4.11: Pictures of pure H^+ beam impinging on proto-fluorescent quartz from left to right (a) at collimator, at 500 kV (b) at COBRA center, at 500 kV (c) at collimator, at 1000 kV (d) at COBRA center, at 1000 kV. The pictures are taken downstream of the beam.

.

4.1.2 New lithium target design

The target-supporting structure

In order to obtain reasonable resolutions on the angular variables of the reconstructed charged particle tracks, the target region needs to be redesigned. The

thick $Li_2B_4O_7$ target used for the XEC calibrations and the surrounding aluminum beam pipe is reasonable for photon reconstruction but leads to a large multiple scattering for electrons and positrons. All the elements from the beamline flange were revised and adapted to the X17 search. The amount of material was reduced to the bare minimum while ensuring thermal and mechanical stability. The new target region is shown in Fig. 4.12. A copper arm is attached to the proton beamline flange, copper being chosen for optimal heat dissipation capabilities. The end of the arm is made of a 45°-tilted thin copper ring to which the 25 μm-thick target substrate in copper is held. The structure is surrounded by a 400 μm-thick, 226 mm-long and 98 mm-diameter carbon fibre vacuum chamber, requiring a small material amount to ensure high-vacuum stability. The thickness values were chosen to be a balance between material reduction and thermal/mechanical stability. The chamber is internally supported by 4 plexiglass rings connected with 3 aluminum threaded rods.

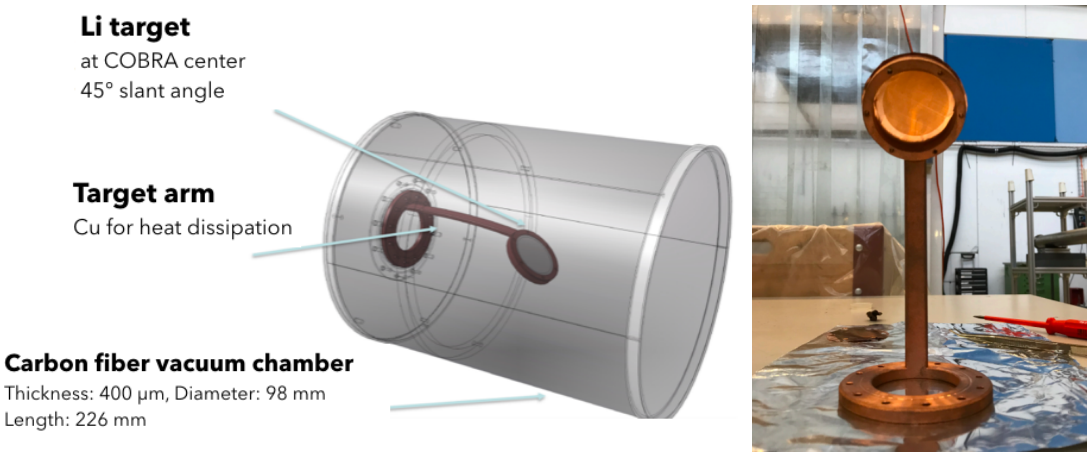

Figure 4.12: (Left) Layout of the target region with a copper target supporting arm, the target itself tilted with a 45° angle and the carbon fibre vacuum chamber. (Right) Picture of the target supporting arm (holding a LiF target).

.

A finite element analysis allows thermo-mechanical simulations of the setup as shown in Fig. 4.13. These simulations assume a 5 W beam power applied over a 1 cm-σ 2D Gaussian beamspot. This is equivalent to a 5 μA current from a 1 MeV proton beam. One can see the gradient of temperature starting from the beamspot on target permitted by the copper heat dissipation. The maximal temperature reached is 240°C which is well below the 1085°C copper fusion temperature. At this temperature, the maximal deformation is 0.52 mm. For a stable target choice such as LiPON, it should present little risk of mechanical damage. Tests with

currents up to 10 μA showed great mechanical stability of the target and substrate over a few weeks.

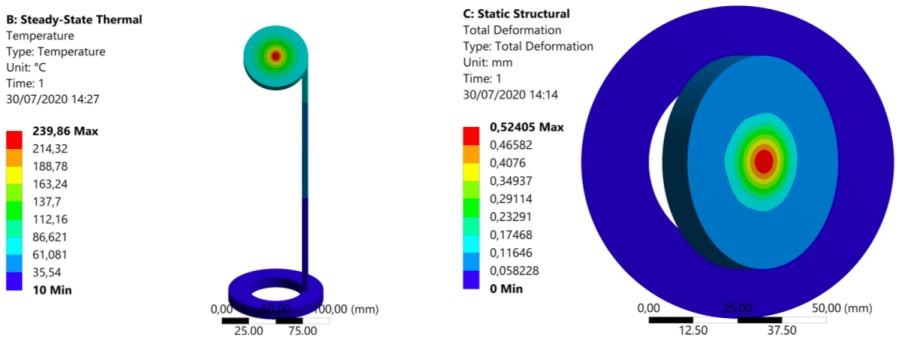

Figure 4.13: Thermal (left) and deformation (right) simulations of the final target region design for a 5 W beam power on a 25 μm copper substrate.

.

Using the same working principle as MEG-II, the tilt of the target is used to increase the target thickness as seen by the protons while minimizing the material crossed by electrons and positrons. A 45° tilt was found to optimize the invariant mass resolution, though this was estimated before the final reconstruction procedure was developed.

The target choice, production and studies

Lithium is a highly reactive and flammable element. Lithium deposits are often compounds such as LiF, $Li_2B_4O_7$, LiO_2, Li_3PO_4. LiF, with its great chemical stability, enters the composition of lithium-ion battery electrolytes [82, 83] and can be used as coolants for molten-salt nuclear reactors [84]. Solid solutions of Li_3PO_4 show high conductivity and stability and participated in the fast development of thin-film batteries [85]. The addition of nitrogen to the compound produces lithium phosphorus oxynitride (LiPON, $Li_{3-X}PO_{4-Y}N_{X+Y}$) and provides additional ionic conductivity and thermal stability [86]. We used both LiF and $Li_{3-X}PO_{4-Y}N_{X+Y}$ to carry out the X17 search taking advantage of the availability of the manufacturing groups.

Simulations of protons stopped within a thin lithium film with a 45° tilt give an energy loss of 60 keV per μm of deposited film. In order to scan the 1030 keV resonance of ^{8}Be, it was found a 2 μm-thick deposit was ideal, though thicknesses up to 5 μm are reasonable as they still prevent scanning the ^{8}Be lower energy resonance at 440 keV.

The LiF targets, produced at INFN Legnaro, are 5 μm-thick over a 10 μm-thick copper substrate. The LiPON targets were deposited over a 25 μm-thick copper

substrate at the Paul Scherrer Institute, making use of a sputtering deposition setup similar to the one presented in Fig. 4.14 (left). Two different batches of LiPON targets were made by two different groups, one in 2023 and one in 2024, and they will be referred to as LiPON23 and LiPON24 respectively. In Fig. 4.14 (right), one of the deposited LiPON23 targets is displayed while in Fig. 4.12 (right) a LiF target is shown. One can see the LiF deposit is visually uniform and well-defined. On the contrary, the LiPON deposit shows alternate bands of different darknesses, pointing at a high non-uniformity of the deposit.

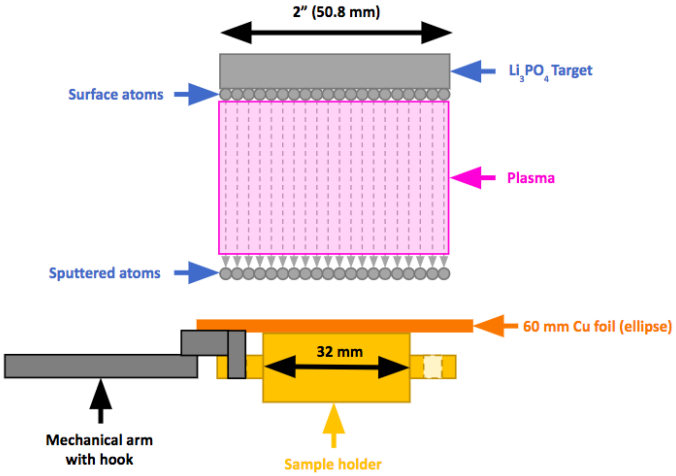

Figure 4.14: (Left) LiPON deposition setup. (Right) LiPON-deposited target on the copper arm (LiPON23).

.

Scanning Electron Microscopy (SEM) employs a highly focused electron beam to resolve images down to the nanometer scale. Energy-dispersive X-ray spectroscopy (EDX) determines the elemental composition of a sample with focused X-ray emission and detection making use of the typical electromagnetic emission spectrum of various elements. Both were applied to one of the LiPON23 samples and the results are shown in Fig. 4.15. The SEM image shows a largely non-uniform LiPON deposit with an average thickness of 7 μm and a peak-to-peak thickness of up to 10 μm, far from the 2 μm thickness request. Some delamination from the copper substrate is observed as well. A close-up picture shows pores within the lithium deposit. On the EDX image, Cu corresponds to the copper substrate but some copper is also present in the lower part of the deposit. The high temperatures during deposition (up to 300°C) could be responsible for some transfer between the substrate and the deposit. The LiPON is represented by phosphorus P. On the surface of the deposit, the thick and non-uniform presence of carbon can be interpreted by the formation of lithium carbonate (Li_2CO_3) from oxidation due to

contact with ambient air. It is important to transport and keep the target in a vacuum or in a non-reactive atmosphere like in argon. However, the installation of the target on the holder requires a brief transition through ambient air. Though the LiF showed a better deposition quality, a LiPON23 target was chosen for the main 2023 physics run because of the very high cross-section of $^{19}\mathrm{F}(\mathrm{p},\alpha\gamma)^{16}\mathrm{O}$ and a large contamination from its 6.05 MeV line. It was nonetheless used for calibrations. On the contrary, P, O and N only negligibly interact with protons at the energies of interest.

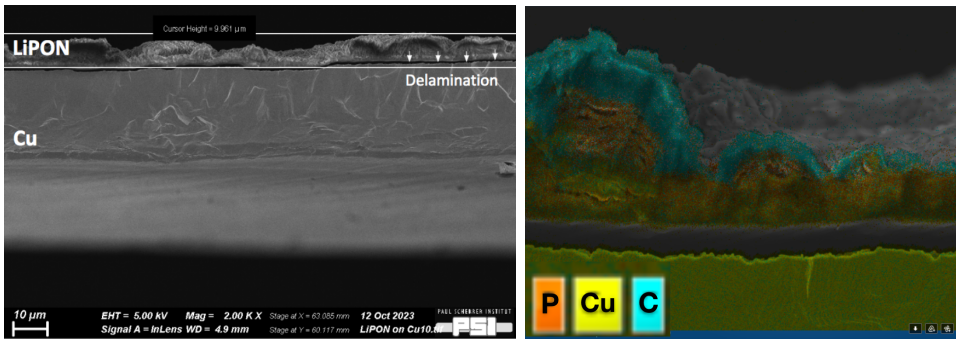

Figure 4.15: (Left) Scanning Electron Microscopy (SEM) image of a 2023 LiPON sample. (Right) Energy Dispersive X-ray (EDX) image of a 2023 LiPON sample surface.

.

Due to the poor quality of LiPON23, higher-quality LiPON targets were produced in 2024 thanks to the expertise of the PSI Chemistry Department. Fig. 4.16 shows SEM images of one of these with two different magnifications. Though slightly delaminated due to the sample preparation for the SEM itself, the deposit shows no pores and good thickness uniformity, close to 1.9 μm and the 2 μm objective.

Nonetheless, in Fig. 4.17, one can see some regular bump-like structures on the surface of the deposit both with an optical microscope and SEM. The EDX picture shows they are made of LiPON. They likely occur due to strain relaxation during large thicknesses deposition. Indeed such sputtering machines are designed for depositing thicknesses below 1 μm. The bumps' average thickness, below 0.5 μm, makes the total LiPON thickness non-uniform but still within requirements. This 1.9 μm LiPON24 was used for additional tests performed in 2024.

4.1.3 Reduced magnetic field

The MEG-II experiment relies on 52.8 MeV positrons' search using the default nominal COBRA magnetic field, with 1.27 T at COBRA center. For the X17

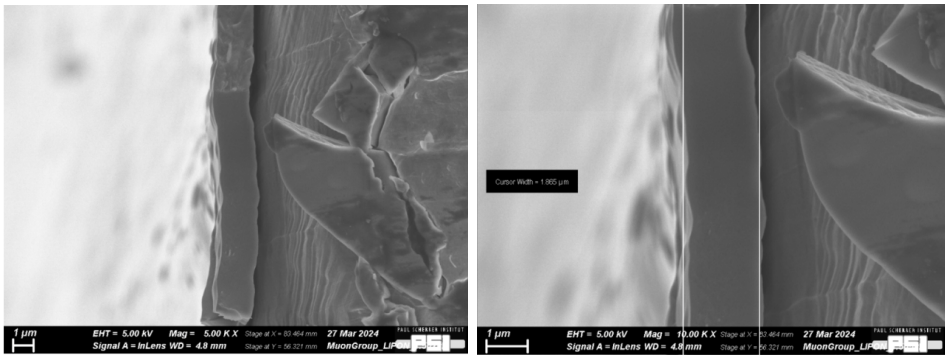

Figure 4.16: SEM image of the 2024 1.9 μm-thick LiPON deposit with 5 000 (left) and 10 000 (right) magnification factor.

.

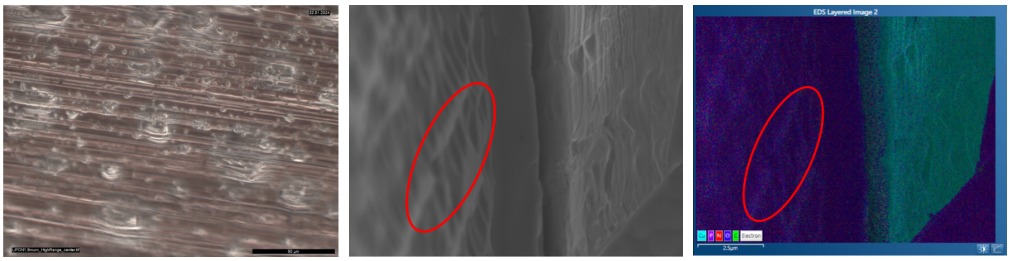

Figure 4.17: Optical microscope (left), SEM (middle) and EDX (right) images of the 2024 1.9 μm-thick LiPON surface. The red ellipse corresponds to the same region on the two right pictures and surrounds bump-like structures on the deposit surface.

.

search, the positrons' and electrons' momenta are roughly six times lower. In order to use the same spectrometer for such particles, the magnetic field strength has to be multiplied by a factor of roughly 1/6, without any change to the field map. To determine the optimal scaling factor, the X17 signal was simulated at three different scaling factors: 0.15, 0.16 and 0.174. Details on the simulation and the reconstruction can be found in Sec. 4.2 and Chap. 5 respectively. For now, we are only interested in choosing the optimal scaling factor for the magnetic field. Four criteria were estimated and compared for the three scaling values as displayed in Tab. 4.2.

- the signal reconstruction efficiency: how many X17 signal electron-positron pairs can be reconstructed given a set of simulated pairs? it is highly dependent on the scaling factor choice. It is equal to roughly 1% for 0.15 and 0.16 scaling while it falls down to 0.4% at 0.174 scaling. At such a scaling, low-momentum tracks are difficult to reconstruct.

- the signal invariant mass resolution: at 0.174 scaling, only pairs with a momentum asymmetry close to zero are reconstructed and therefore both tracks are well within the spectrometer acceptance, leading to a particularly good invariant mass resolution. The resolutions at 0.15 and 0.16 scaling are 25% worse but remain reasonable.

- available field map: even though the field can be considered to be directly scaled from the nominal field, having an available field map at reduced scaling can be used as a cross-check. A field map measurement was performed in 2018 at a 0.15 scaling, while none are available at 0.16 and 0.17. This measurement requiring large efforts, having such a map already available is an important advantage.

- low E_{sum} data availability. Before starting the main physics run, three small datasets impinging 1080 keV protons on a LiPON23 target with COBRA scaling of 0.15, 0.16 and 0.17 were written. The reconstruction procedure was applied and the E_{sum} spectra were built in Fig. 4.18. The X17 signal is expected to have $E_{sum} > 16$ MeV, a region which will be at least partially blinded (see Chapter 7). As expected, the decreasing COBRA scaling shifts the spectrometer acceptance towards lower E_{sum}. With a 0.15 scaling, a significant part of the dataset has $E_{sum} < 16$ MeV, which provides us with a background-only region to be used as a sideband for detailed analysis.

Given the high signal reconstruction efficiency, the reasonable invariant mass resolution and the availability of both a field map and a significant $E_{sum} < 16$ MeV region, a 0.15 COBRA magnetic field scaling was chosen for all the next runs.

COBRA magnetic field scaling	**0.15**	**0.16**	**0.174**
Signal rec. efficiency [%]	1.04	0.93	0.43
Signal inv. mass resolution [keV]	800	770	600
Available field map	Yes	No	No
Low E_{sum} can be used as a sideband?	Yes	No	No

Table 4.2: Signal reconstruction efficiency, signal invariant mass resolution, field map availability and low E_{sum} data availability for different COBRA magnetic field scaling values. Green and red values indicate pros and cons respectively.

4.1.4 Trigger description

The MEG-II trigger strategy cannot be applied to the X17 search. A specific trigger scheme was developed based on a coincidence between SPX (or pTC) hits

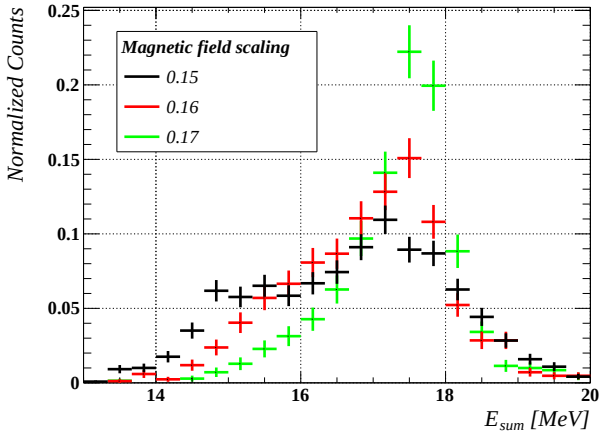

Figure 4.18: Samples of data taken with the spectrometer with a LiPON23 target for three different COBRA magnetic field scaling values: 0.15, 0.16, 0.17.

.

and CDCH hits. At least one SPX hit is required in each selected event as the track reconstruction is largely improved by using a time seed provided by an SPX hit. Fig. 4.19 (left) shows the distribution of waveform amplitudes from SPX hits. We see that no waveform from signal hits has an amplitude below 40 mV. The trigger threshold for the SPX waveform is therefore set at 40 mV on average. Based on noise variations between counters the thresholds were optimized around this value. The trigger requests one waveform on each of the two ends of at least one counter to be above this threshold. The SPX hit request is applied in the following.

The CDCH hit selection is more complex. In the signal region, at angles close to 140° and for E_{sum} close to 18 MeV, X17 pairs are indistinguishable from IPC pairs. There, the signal-to-background ratio is irreducible and fixed by physics processes. Therefore the TDAQ strategy to maximize the significance of the search relies on three complementary ideas:

- to reduce non-signal-like contamination: these are mostly EPC pairs, largely asymmetric momenta pairs and single tracks.
- to select signal-like events: these are pairs of tracks, with opening angle $>$ 120° and almost symmetric momenta.
- with the two items above, the proton current should be increased as much as possible, up to trigger capabilities

Selecting signal-like pairs is not straightforward because the CDCH, in its current state, provides no online access to the CDCH hit coordinates. The alternative is to use the online CDCH waveform amplitudes. Fig. 4.19 (right) shows the distributions of CDCH waveform amplitudes for all hits in black and only for good hits or hits on track in cyan. We see that a large noise structure peaks at around 20 mV. To select good hits, hits that are necessarily left by a track passing nearby, the trigger threshold on the CDCH waveforms was set to 60 mV on average. Again, wire-by-wire thresholds were optimized accounting for noise levels. A good hit is selected by requesting an upstream (US) and a downstream (DS) waveform to be both above this threshold.

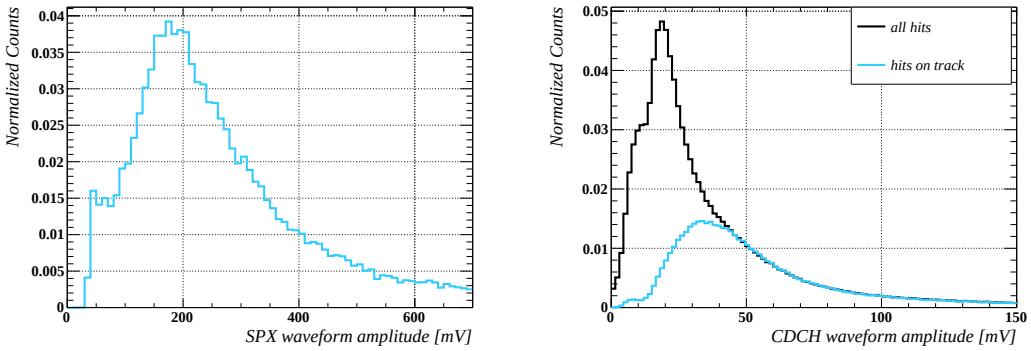

Figure 4.19: (Left) Waveform amplitudes for a timing counter (SPX) hit. (Right) Drift chamber (CDCH) waveform amplitudes for all hits (black) and for hits on track (cyan).

.

A request on the number of good hits above threshold, or multiplicity, can be performed to select signal-like pairs. In Fig. 4.20 (left), we see that the reconstructed positron momentum is largely dependent on the requested CDCH online multiplicity. In other words, one can reject tracks with momentum above 10 MeV by requiring an appropriate multiplicity. For an 18 MeV available energy, a positron at 12 MeV is associated with an electron of roughly 6 MeV. These are pairs with a large asymmetry that are not representative of signal pairs. Such high-momentum tracks should and can be rejected through a CDCH multiplicity request. For several types of events, single tracks, signal pairs and IPC pairs, we studied the distribution of multiplicities that allowed the reconstruction. The results are displayed in Fig. 4.20 (right). As expected, single tracks can be reconstructed with a multiplicity as small as 7 hits. These single tracks can contaminate the trigger and are unnecessary events. For pairs of tracks, signal-like or IPC pairs, the average multiplicity is larger, between 20 and 30 hits. By setting a multiplicity request of 18 hits, a large fraction of single tracks can be rejected while conserving

90% of the signal events. TDAQ tests showed that the total trigger rate is decreased by a factor of 5 going from a 10-hit to an 18-hit multiplicity request. The proton current can be increased by the same factor to increase the production of signal-like pairs. One can see that discriminating IPC pairs from signal pairs is not possible using the multiplicity method.

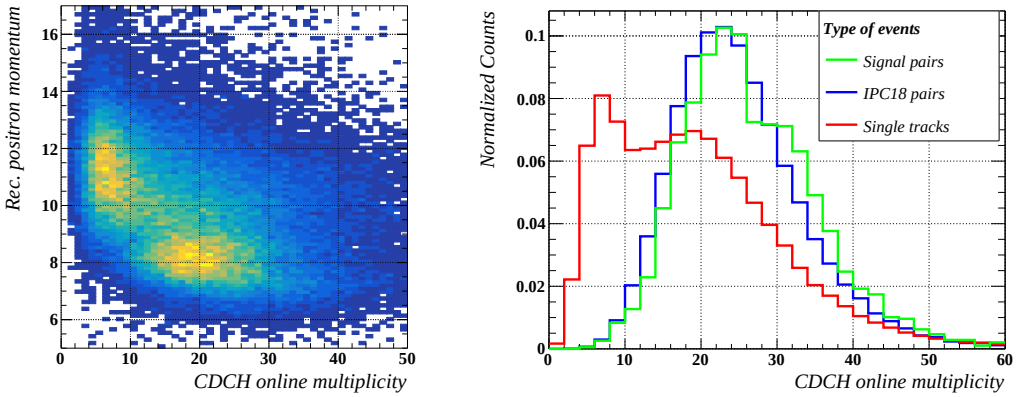

Figure 4.20: (Left) Distribution of reconstructed positron momentum as a function of the CDCH online multiplicity for single tracks. (Right) CDCH online multiplicity for three types of events signal-like pairs (green), IPC18-like pairs (blue), single tracks (red).

.

In summary, the trigger strategy was defined as follows:

- SPX: two waveforms on each end of at least 1 SPX counter above 40 mV: 1&1 above 40 mV
- CDCH: 18 waveforms above 60 mV both US and DS: 18&18 above 60 mV

This trigger strategy was also included within the MC simulation in order to reproduce the data acquisition conditions.

4.1.5 The X17 setup and the BGO calibration and operation

The full setup for the X17 search is schemed in Fig. 4.21. The BGO calorimeter, shown at the bottom right of the figure, is a 4×4 array of bismuth germanate (BGO) crystals coupled to 16 PMTs. The BGO is used as a XEC calibration tool through the Charge Exchange reaction but has a good energy resolution to perform photon analysis. While the charged particles are tracked within the spectrometer with reduced magnetic field the photon monitoring can be performed with the

XEC or the BGO. During a large part of the PSI muon beam shutdown period, in which the X17 DAQ is performed, the MEG-II apparatus is available but the XEC is not. Therefore, we mostly rely on the BGO, the main photon detector during the X17 data collection periods. Large energy deposits are not fully absorbed within a single BGO crystal. The array of crystals allows for the good containment of the photons and associated showers and improves energy resolution. A BGO operation, trigger, calibration and analysis scheme was developed specifically for the X17 search and is presented in the following.

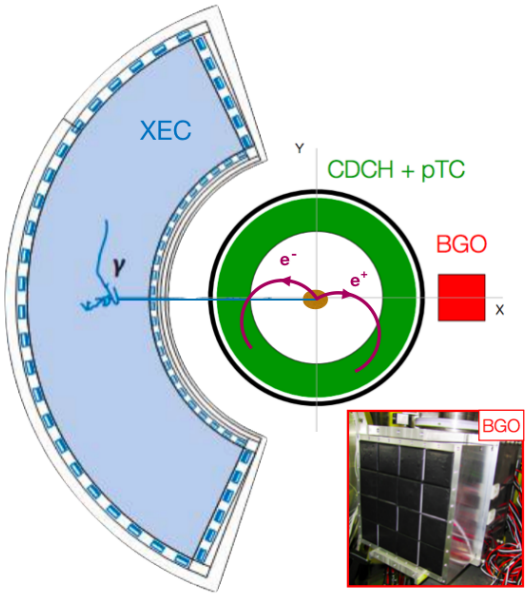

Figure 4.21: The full setup for the X17 search. The charged particles are tracked within the spectrometer while the photon spectrum can be monitored with the BGO and the XEC, when available. At the bottom right, is a picture of the BGO calorimeter, a 4×4 array of bismuth germanate (BGO) crystals.

For the Charge Exchange run, the energies deposited in the BGO are above 50 MeV while they are below 20 MeV for the X17 search. To maintain a good PMT signal quality, it is important to increase its gain and therefore its high voltage (HV) value. Each PMT has an independent high voltage value. Due to varying crystal qualities, the HVs should be adjusted with respect to one another: a given amount of energy deposited in any crystal should result in a similar PMT output charge. This prevents large offline corrections which could deteriorate the resolution. Such a tuning was performed making use of the 6.05 MeV photon from the $^{19}\mathrm{F}(\mathrm{p},\alpha\gamma)^{16}\mathrm{O}$ reaction and its high associated cross-section. $E_\mathrm{p} = 500$ keV photons were shot at a LiF target in order to excite the fluorine transition. The

integrated charge within each crystal is given in Fig. 4.22. The peak close to 6 MeV corresponds to such a photon impinging close to the center of the crystal entrance face. Smaller energy deposits correspond to residual showers from a hit in a neighbouring crystal. In this figure, the PMT HVs were tuned at first order to have the 6 MeV line well-defined and similar integrated charges for all PMTs.

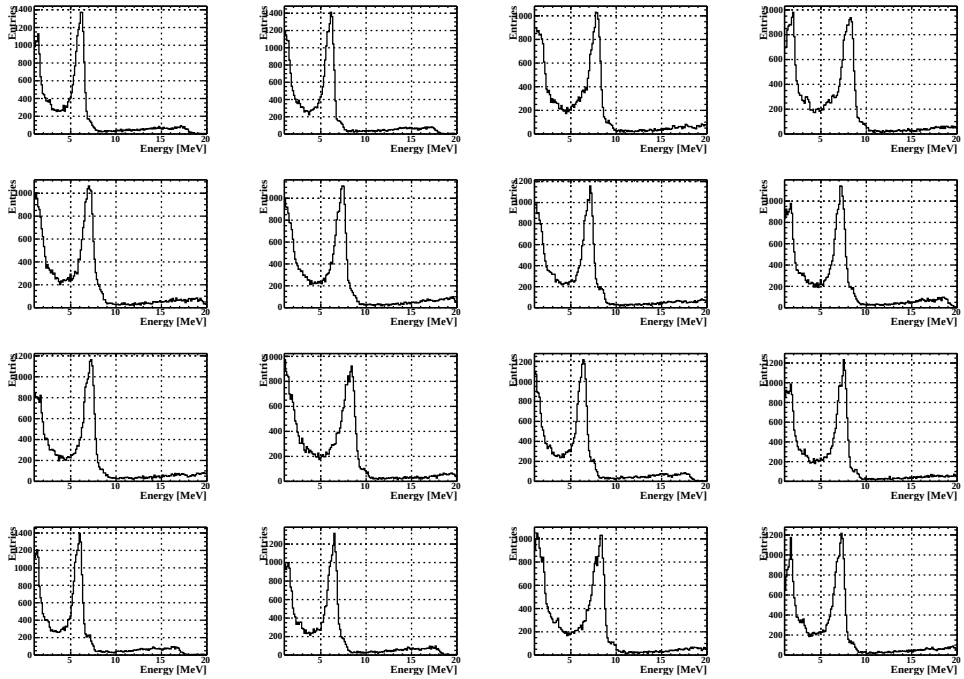

Figure 4.22: Photon energy deposit spectrum on each of the 16 crystals of the BGO calorimeter from protons at $E_p = 500$ keV impinging on a LiF target, after PMT HVs tuning. The sharp 6.05 MeV line from $^{19}F(p, \alpha\gamma)^{16}O$ is clearly visible.

After the HVs are set, precise weights are attributed to each crystal in order to tune the integrated charges exactly. Such weights are used so that the summed charge on all crystals is proportional to the deposited energy regardless of the hit position on the BGO entrance face. The weights are used both at the trigger level for the online event selection and at the offline level to reconstruct the photon spectrum with the highest resolution. For all BGO data shown, the trigger was set as a threshold on the weighted online summed charge. The threshold is adapted to the line of interest. The computation of such weights is called intercalibration. This is done by fitting the line of interest for each crystal and dividing the fitted position of the line by the known energy associated with the transition. In practice, the BGO response is not perfectly linear with energy. Therefore, the line chosen to

compute the weights should be as close as possible to the energies of interest. To do so, we have used the 17.6 MeV line from the ^{7}Li(p, γ)^{8}Be excited by shooting $E_p = 500$ keV photons at a LiPON23 target. The spectra are given in Fig. 4.23 and were fitted with a double Gaussian function in order to account for both the transition to ground state (17.6 MeV line) and the transition to first excited state (14.6 MeV line). The charge associated with the fitted 17.6 MeV line for each crystal is then used to compute the weights.

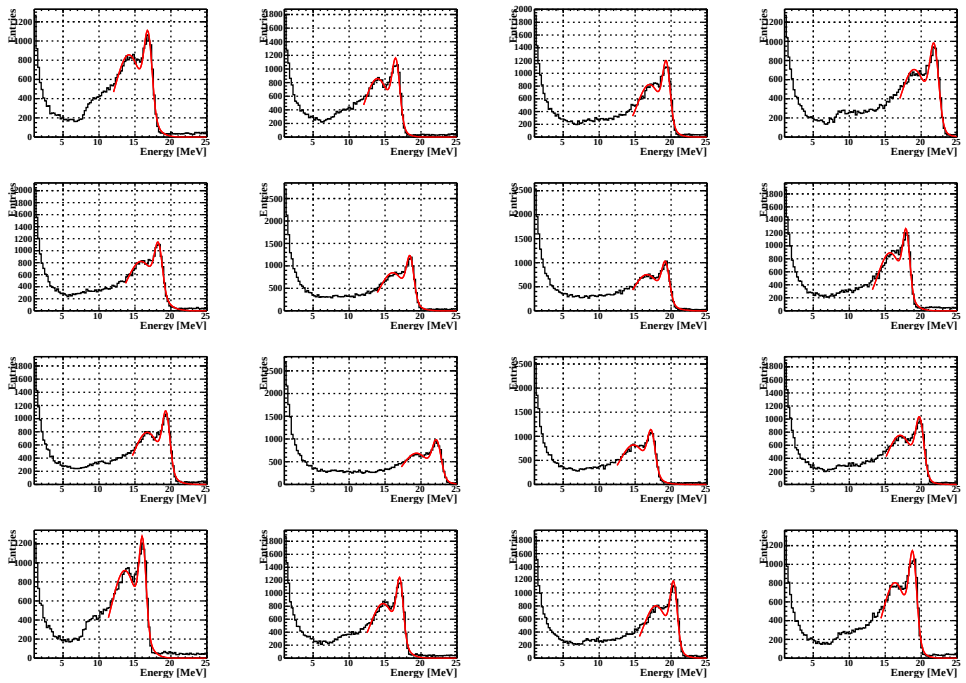

Figure 4.23: Photon energy deposit spectrum (in black) on each of the 16 crystals of the BGO calorimeter from protons at $E_p = 500$ keV impinging on a LiPON23 target. The two Be lines from ^{7}Li(p, γ)^{8}Be are fitted with a double Gaussian (in red).

For each event, the weighted summed charge on all 16 crystals is computed in order to build the energy spectrum shown in Fig. 4.24 (black). However, the resolution can be improved by selecting a subsample of events in which the maximal energy deposit is in one of the four central crystals (Fig. 4.24 (red)). For such events, the shower is indeed better contained than for a border crystal event. The BGO spectra appearing in the next chapters include this central-crystal selection. The fit of this summed spectrum gives a resolution of (640 ± 40) keV at 17.6 MeV, equivalent to $(3.6 \pm 0.2)\%$.

During the X17 data-taking periods, BGO prescaled trigger data are collected

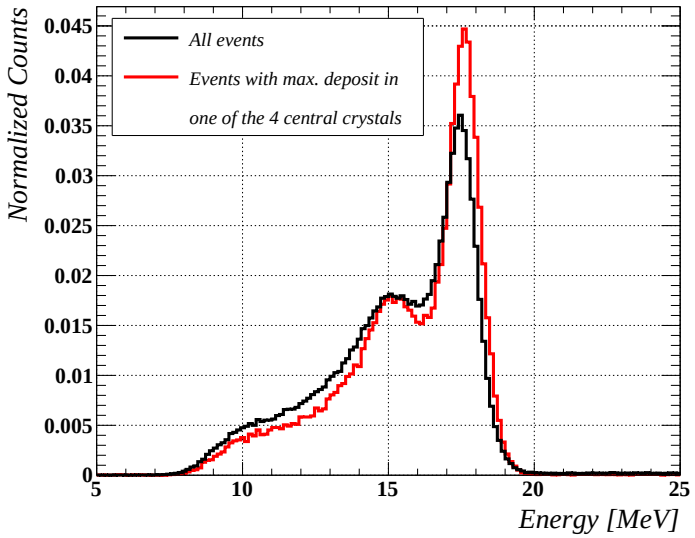

Figure 4.24: Total energy deposit within the BGO calorimeter from protons at $E_{\mathrm{p}} = 500$ keV impinging on a LiPON target. All events in black and events with the maximal energy deposit in one of the four central crystals in red.

continuously and dedicated BGO runs are performed daily to accumulate statistics.

4.2 Simulating the detectors and the X17 physics processes

In this section, we will describe the simulation of the detectors, the tuning of these simulations and the simulation of the physics processes relevant to the X17 search.

4.2.1 The detectors

The output of the detector simulation is a waveform set that reproduces the WaveDREAM data as best as possible. The aim is to ensure that the simulations are subjected to the same reconstruction process as the experimental data. The transportation, ionization and secondary physics processes are simulated after the primary particles are generated at the beamspot according to the physics process of interest. The trajectories' evaluation and energy deposits are simulated through the Monte-Carlo (MC) method based on Geant4 [79]. All relevant electromagnetic processes, such as pair creation and annihilation, bremsstrahlung, Compton scattering, photoelectric effect, ionization and multiple scattering are included. The detectors' response is also simulated. The BGO response relies on the scintillation

photon absorption, scattering, and reflection within the detector. The CDCH response uses Garfield++ [76] to simulate the gas ionization within the drift cells. The waveforms are generated from templates extracted from data (LXe, BGO, pTC) or from SPICE [87] (CDCH). Noise extracted from experimental data is then added to the waveforms before sampling and discretization are performed.

To ensure the best consistency between simulation and X17 data, the CDCH simulation requires some fine-tuning. The CDCH wires are distributed over the 2π azimuthal region. Due to the topology the $\mu^+ \to e^+\gamma$ decay and the arrangement of the sub-detectors, only two-third of the wires are readout as seen in the CDCH hit map in Fig. 4.25 (left). Before the X17 DAQ period, the readout of an additional sector of the CDCH was enabled. This can have a non-negligible effect on the acceptance of the detector, a crucial element for the X17 search. The simulation of this sector was therefore implemented as an updated list of active CDCH channels. A simulated hit map after the update is shown in Fig. 4.25 (right).

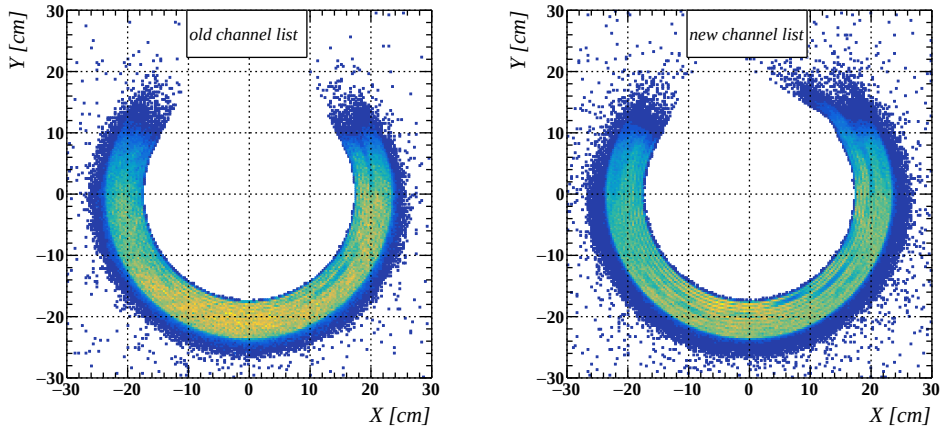

Figure 4.25: Simulated CDCH hit map before (left) and after (right) the alimentation of a new CDCH sector.

An accurate simulation of the waveform noise is crucial to ensure consistent hit efficiencies. For this purpose, a sample of CDCH data was taken in February 2023. The waveform RMS distribution is shown in Fig. 4.26 (left) in black for data and in red for the MC with the original noise template. This template is largely different from the data, with a fraction of waveform with zero-RMS and a wide structure peaking at 4 mV. The CDCH noise template had to be updated in the X17 simulation in order to match the noise observed in experimental data. The MC with the updated noise template is shown in green and matches well the experimental noise.

The same exercise was carried out to fine-tune the CDCH gas gain. The isopropyl alcohol content within the CDCH gas mixture is yearly adjusted to cope with some instabilities of the detector. This quantity has a large impact on the gas gain and therefore on the track reconstruction efficiency. The actual gas gain can be estimated based on the CDCH waveform amplitude distribution for hits on track. The data distribution is compared to MC distributions with different gas gains in Fig. 4.26 (right). It is clear a value of 350 000 leads to an excessive average waveform amplitude while 230 000 allows a good match with data.

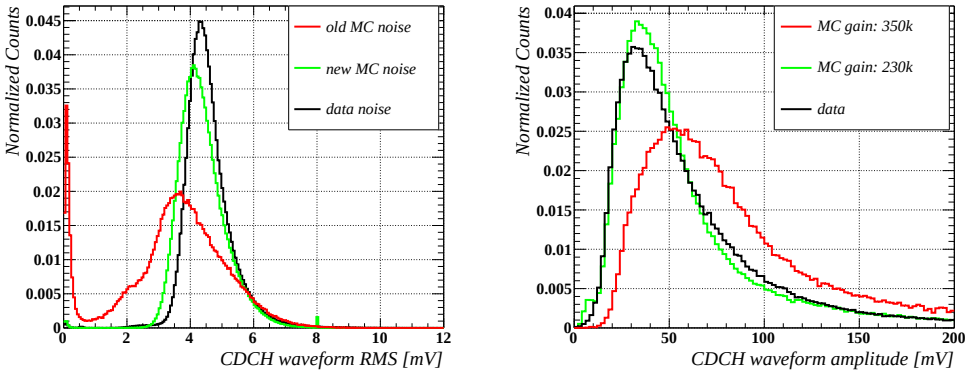

Figure 4.26: (Left) CDCH waveforms RMS distribution with the original noise template (red), the updated one (green) and the data (black). (Left) CDCH waveform amplitude of hits on track for simulations with a CDCH gas gain of 350 000 (red) and 230 000 (green) and for data (black).

A method described in Sec. 7 was developed to determine the exact position of the beamspot on the target. The width of the beamspot was also estimated. Both these information were implemented within the X17 simulation. The simulated beamspot in the XY and ZY planes is shown in Fig. 4.27.

Finally, all the target region's elements were added to the simulation. It includes the Li target deposited on a thin copper film, the heat-dissipating copper arm and ring, the six stainless steel screws holding the film, the carbon fibre vacuum chamber, its aluminum flange and rods and its plexiglass rings. The air outside the chamber is simulated as well. Fig. 4.28 shows the secondary particles' production points within the target region material. It allows us to understand the elements responsible for the most secondary particles but also to visualize some of the simulated elements. We clearly distinguish the carbon fibre chamber and its flange, the copper ring and arm and the six screws.

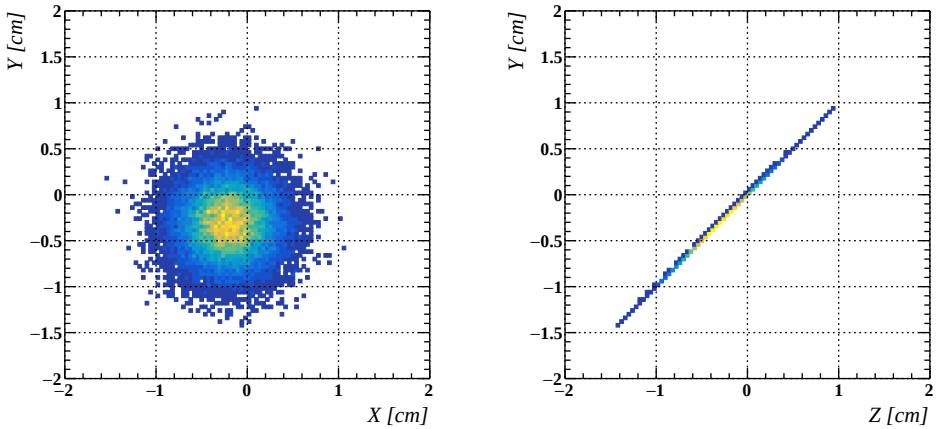

Figure 4.27: Simulated beamspot position with (x_0, y_0) = (-2 mm, -3 mm) and $\sigma = 3$ mm.

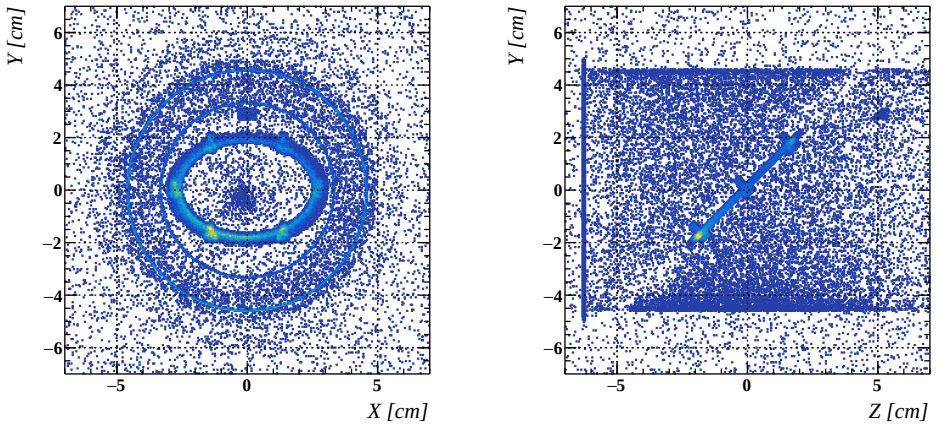

Figure 4.28: Simulated secondary particles' creation points within the target region's material. The main elements of the geometry can be seen.

4.2.2 Internal Pair Conversion background: Zhang-Miller model

One of the most important elements for the X17 search is to rely on accurate background simulations. The Zhang-Miller (ZM) photon and IPC models developed by Zhang and Miller in [7] are described in Sec. 2.1.1. Being one of the most comprehensive models to date and including all significant multipoles, anisotropy and interferences between multipoles, it was implemented within our simulation framework. The IPC electron-positron pair is simulated based on a 4D differential cross section $\mathrm{d}\sigma/\mathrm{dcos}\theta_{+-}\mathrm{dcos}\theta\mathrm{dE}_{+}\mathrm{d}\phi$, with θ and ϕ the polar and azimuthal direction of the virtual photon, E_{+} the positron energy and θ_{+-} the opening angle of the electron-positron pair. Fig. 4.29 shows the distributions of this quantity integrated over three of the four variables at $E_{\mathrm{p}} = 1030$ keV. The asymmetry over θ at this energy is clearly visible with the distorted $\sin\theta$ shape peaking at $\theta = 60°$. After a peak at $\theta_{+-} = 10°$, $\mathrm{d}\sigma/\mathrm{d}\theta_{+-}$ is monotonously decreasing, with a factor 10 difference in cross-section between 10° and 100°. The few % variations in ϕ are due to the fixed proton energy. In practice, with proton energy loss effects, the ϕ distribution is flat.

The IPC generator relies on the hit-or-miss algorithm following the differential cross-section. The ZM model cross-section can be written as:

$$\begin{aligned} &\mathrm{d}\sigma/\mathrm{d}\cos\theta_{+-}\mathrm{dE} + \mathrm{d}\cos\theta\mathrm{d}\phi \\ &\propto \quad T_{0,0} + T_{0,2}\cos 2\phi + T_{1,0}P_1 + T_{2,0}P_2 + T_{2,2}P_2\cos 2\phi \\ &\quad + T_{3,1}\sin\theta\cos\phi + T_{4,1}\sin 2\theta\cos\phi \end{aligned} \tag{4.3}$$

The first term represents a first-order approximation which should be equivalent to the Rose model while the next terms represent multipole interferences. In order to cross-check the ZM model, the ZM differential cross-section $T_{0,0}$ term was integrated over the full E_{+} and ϕ ranges and over the [70°,90°] range in θ. It corresponds to the integration ranges applied by Atomki to the Rose model in [21]. Fig. 4.30 compares Rose model and ZM $T_{0,0}$ term for both E1 and M1 multipoles. The agreement with Rose's work confirms the reliability of the ZM model. Though both E1 and M1 multipoles give monotonous shapes, it is important to notice the large steepness difference.

One can then add the interference terms provided by Zhang and Miller in order to see their effect on the cross-section shape. The proportions of E1 and M1 largely depend on the proton energy and so does the cross-section shape. Fig. 4.31 compares the full ZM model (all terms included) at the 1030 keV resonance with the Atomki's best background fit of their data at $E_{\mathrm{p}} = 1100$ keV. It is clear the background is underestimated by Rose at large angles. Though we already mentioned that this updated model cannot explain the anomaly, it can impact the significance of the excess. The ZM IPC model is used in the next chapters.

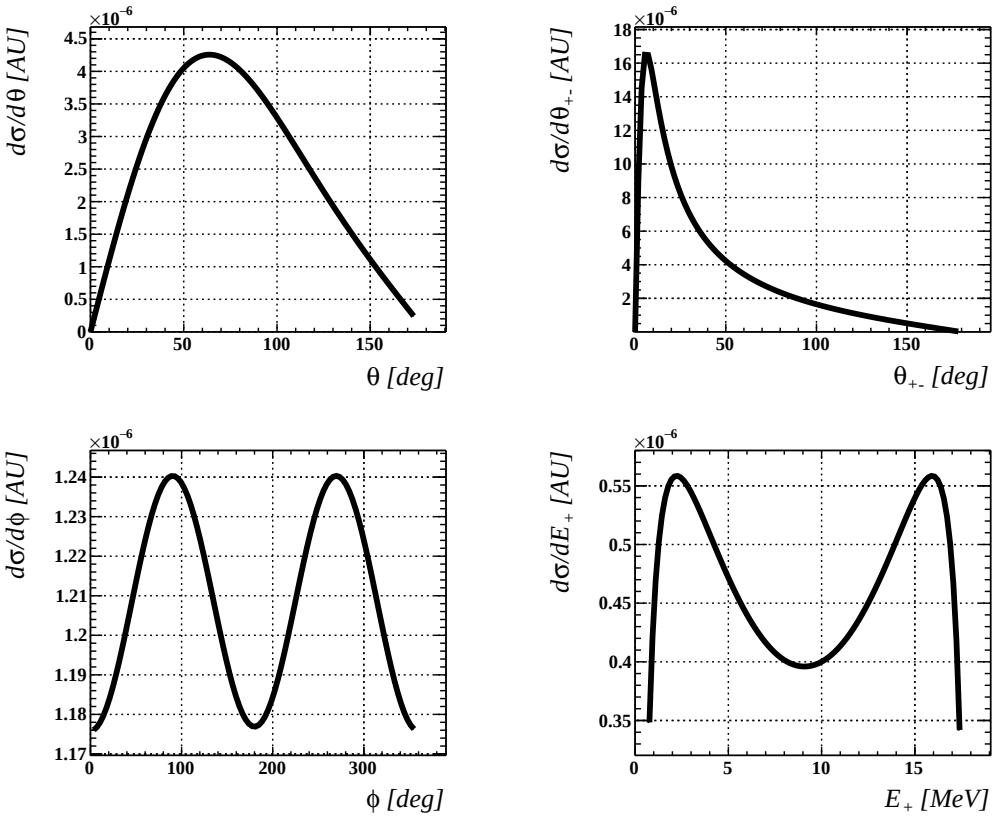

Figure 4.29: 1D differential cross sections from the IPC Zhang-Miller model after integration of 3 out of 4 variables at $E_{\mathrm{p}} = 1030$ keV.

Making use of the ZM model, one can observe the differences in IPC θ_{+-} shapes at three proton energies E_{p} in Fig. 4.32. The contributions of E1 and M1 multipoles vary a lot with E_{p} as observed in Fig. 2.2. The 440 keV resonant M1-dominated shape is much steeper than the 700 keV non-resonant E1-dominated one. At 1030 keV, E1 and M1 are mixed and the steepness is intermediary.

These critical differences will be used to understand and model the data in Sec. 6.2 and Chap. 7.

4.2.3 External Pair Conversion from gamma in matter

Extensive photon simulations were conducted based on the photon ZM model, incorporating all relevant electromagnetic processes, including pair creation and annihilation, bremsstrahlung, Compton scattering, the photoelectric effect, ionization, and multiple scattering. Two processes were found to be non-negligible: Compton scattering and pair creation. Though Compton scattering is roughly 50

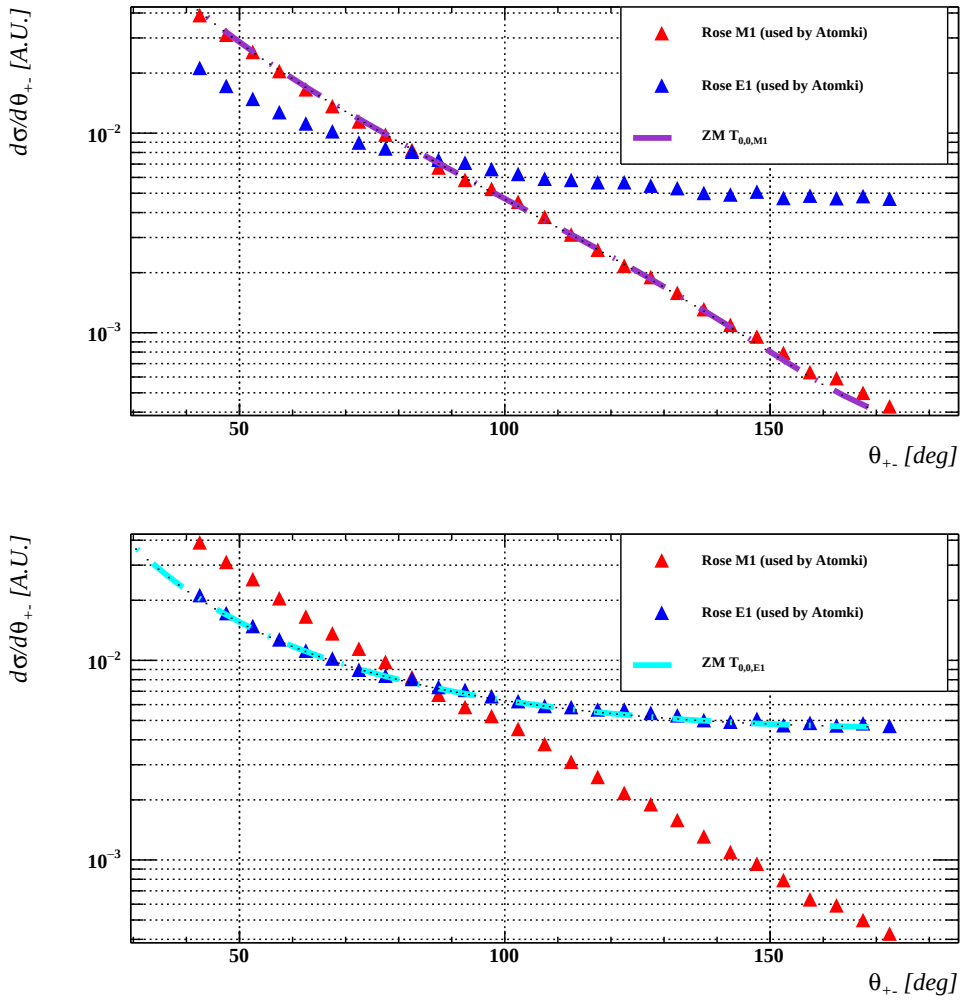

Figure 4.30: 1D θ_{+-} differential cross section developed by Rose and simulated by Atomki for M1 (red markers) and E1 (blue markers) multipoles. It is compared with the same quantity from the Zhang-Miller (ZM) model considering only the first term ($T_{0,0}$) for both M1 (dash-dotted magenta line, top) and E1 multipoles (dash-dotted magenta line, bottom).

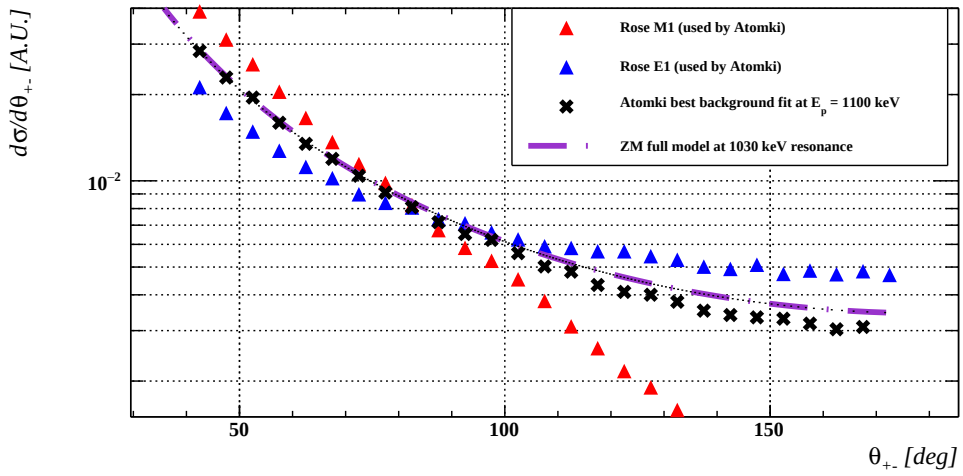

Figure 4.31: 1D θ_{+-} differential cross section developed by Rose and simulated by Atomki for M1 (red markers) and E1 (blue markers) multipoles. The best background fit obtained by Atomki fitting their data at $E_{\mathrm{p}} = 1100$ keV with a Rose E1/M1 mix is compared to the full Zhang-Miller model taken at the 1030 keV resonance (matched at 40°).

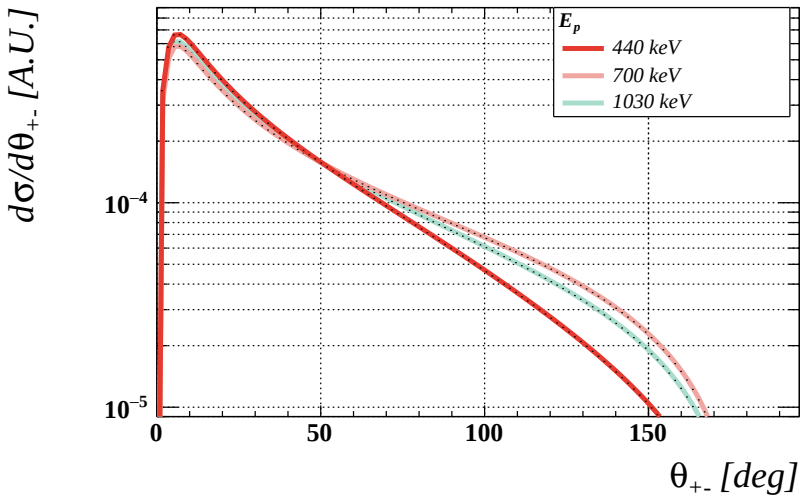

Figure 4.32: 1D θ_{+-} differential cross section from the full Zhang-Miller model taken at $E_{\mathrm{p}} = 440$, 700, 1030 keV and normalized to same area.

times more likely than pair creation for 18 MeV photons, most Compton electrons have energies below 5 MeV and are therefore not within our spectrometer acceptance. All in all, EPC and Compton from photons at 18 MeV lead to charged particles above 5 MeV with roughly the same probability in our apparatus. The Compton and EPC kinetic energy spectra are shown in Fig. 4.33. Two 9 MeV positron and electron from EPC are energetically indistinguishable from an IPC pair.

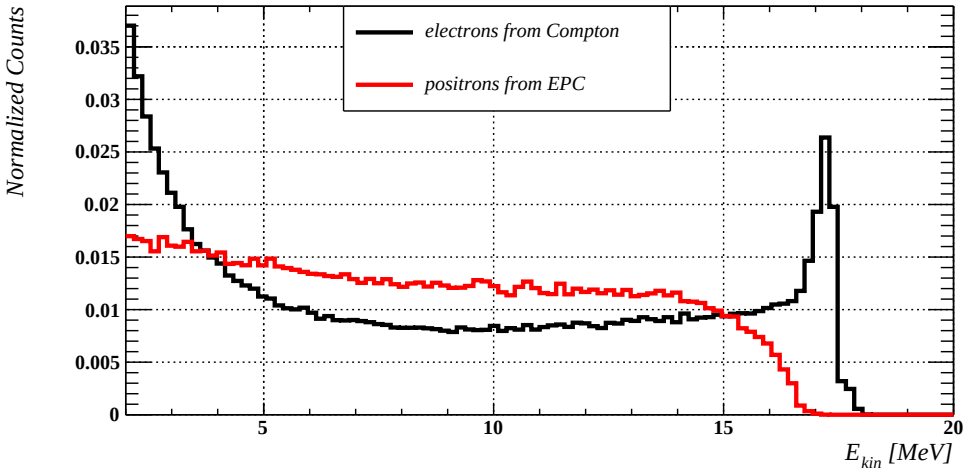

Figure 4.33: Kinetic energy spectra from Compton electrons and EPC positrons based on an 18 MeV photon simulation following ZM model at target.

These processes occur largely in the copper ring surrounding the target, as observed in Fig. 4.28. On top of the photon direction asymmetry at production, an additional asymmetry occurs in the EPC direction due to the target 45° tilt. The pTC being located at negative y, the pTC hit trigger requirement favours EPC produced with a negative y direction. EPC pairs produced with $\cos(\theta_\gamma) = \frac{(\vec{p}_{e^+}+\vec{p}_{e^-})\cdot\vec{z}}{|\vec{p}_{e^+}+\vec{p}_{e^-}||\vec{z}|} < 0$ are then more likely to be selected. All MC simulations presented in the remainder of the work are reconstructed through the same procedure as data, as described in Sec. 5. The trigger, described in Sec. 4.1.4, is simulated as well in order to best reproduce data conditions. Fig. 4.34 gives the reconstructed θ_γ distribution for both IPC pairs and EPC pairs. The (virtual) photon asymmetry dominates IPC direction asymmetry while the EPC one is dominated by the trigger selection effect associated with the ring tilt.

The reconstructed angular opening distributions for IPC and EPC pairs is shown in Fig. 4.35. The IPC distribution, monotonously decreasing for $\theta_{+-} > 10°$,

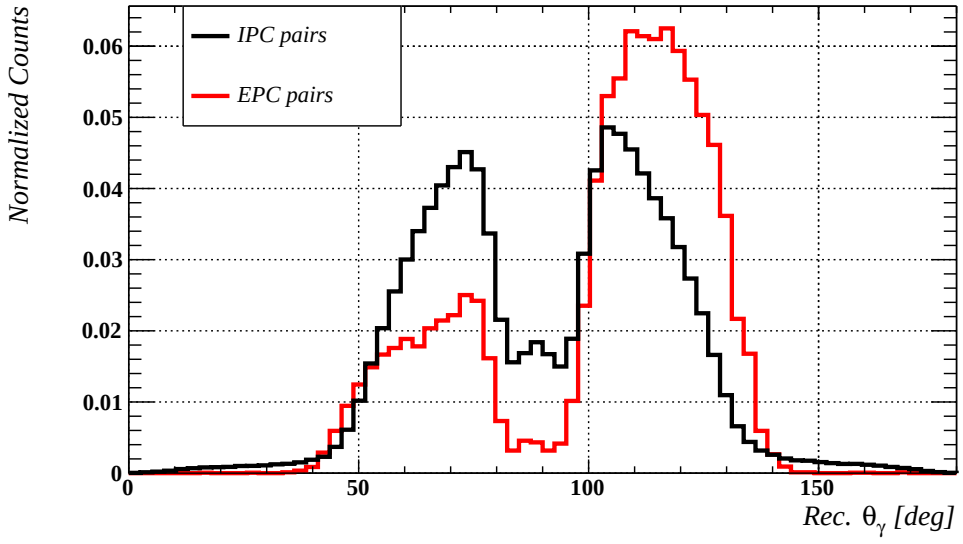

Figure 4.34: Reconstructed θ_γ from IPC and EPC simulations.

follows the cross-section shape previously studied. The EPC distribution peaks at $\theta_{+-} \approx 30°$ and is almost two orders of magnitude less likely than IPC at $\theta_{+-} \approx 100°$. At the photon conversion point, the pair is almost colinear. The subsequent multiple scattering of both electron and positron leads to an average angular opening close to 30° exiting the conversion material.

The EPC simulation corresponds to a photon simulation where all electromagnetic processes are allowed.

4.2.4 Transition to first excited state

The Zhang-Miller model was developed for the excited beryllium transition to the 0^+ ground state. Another relevant transition is the transition to the 3.05 2^+ first excited state, schematized in Fig. 4.36.

Both IPC and EPC processes occur from the transition to first excited state. These were simulated independently by applying the ZM model and adjusting the energy of the transition assuming a 1.2 MeV width to the first excited state. The IPC and EPC processes from this transition will be nicknamed IPC15 and EPC15 as the energies of this transition are close to 15 MeV. The respective processes from the transition to ground state will be referred to as IPC18 and EPC18.

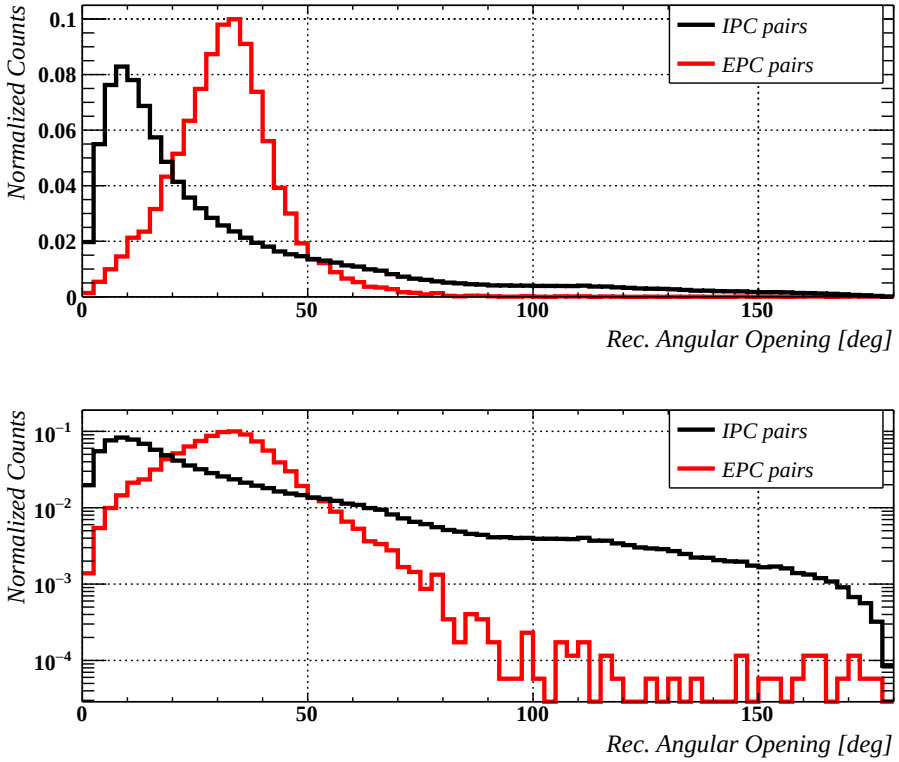

Figure 4.35: Reconstructed Angular Opening from IPC and EPC simulations in linear (top) and logarithmic (bottom) scale.

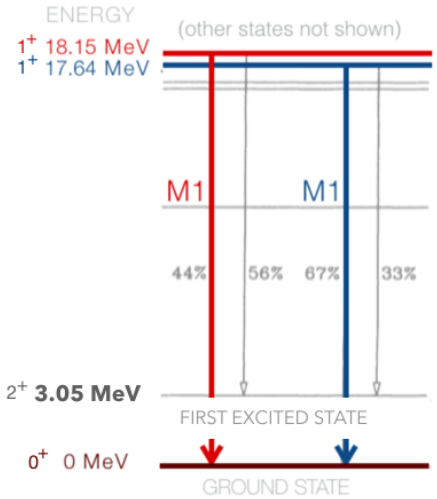

Figure 4.36: ^{8}Be energy states of interest and allowed transitions.

4.2.5 The X17 signal simulation

Due to the lack of information on the nature of the X17 particle, its simulation was kept as general as possible. An electron-positron pair emitted back-to-back and sharing the transition's available energy is boosted by the momentum of the X17 particle. The simulations were performed for X17 masses between 16.3 MeV/c^2 and 17.3 MeV/c^2. Two sets were simulated based on the proton energy, one assuming the particle is emitted from the 440 keV Be resonance (X17(17.6)) and one from the 1030 keV Be resonance (X17(18.1)). The X17 direction is considered to be isotropic. Fig. 4.37 gives the distribution of simulated electron-positron angular opening from the X17 decay assuming several masses hypotheses. The X17 boost is reduced for higher masses and the average angular opening is larger.

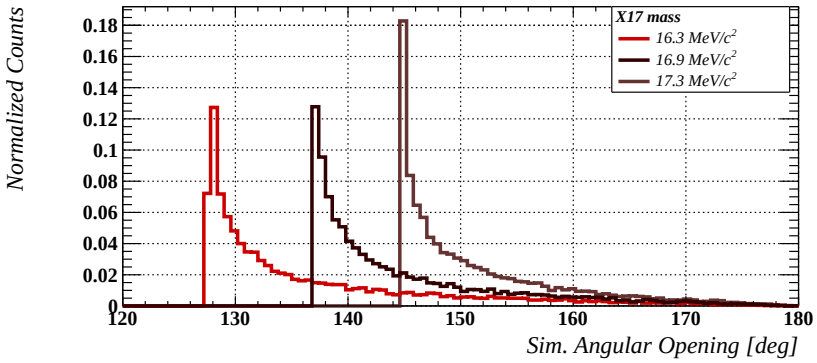

Figure 4.37: Simulated Angular Opening for X17 masses of 16.3, 16.9 and 17.3 MeV/c^2 emitted in the 1030 keV Be resonance.

The isotropic simulation of the X17 particle allows us to determine the range of X17 directions within our spectrometer's acceptance. The X17 direction, θ_{X17}, is defined as $\cos(\theta_{X17}) = \frac{(\vec{p}_{e+}+\vec{p}_{e-})\cdot\vec{z}}{|\vec{p}_{e+}+\vec{p}_{e-}||\vec{z}|}$ and is schematized in Fig. 4.38 (left). The relative number of reconstructed pairs from an X17 decay with respect to the X17 production is shown in Fig. 4.38 (right). The reconstruction procedure is detailed in Sec. 5. This figure shows our capabilities to reconstruct X17 not only emitted in the direction orthogonal to the beam, as for Atomki, but also in planes with angles between 30° and 150°. This clear advantage over Atomki can provide additional insights into the nature of the particle.

4.2.6 Mass production

Simulations with high statistics are required to have the best understanding of our data. To do so, several tricks were performed to fasten the MC production:

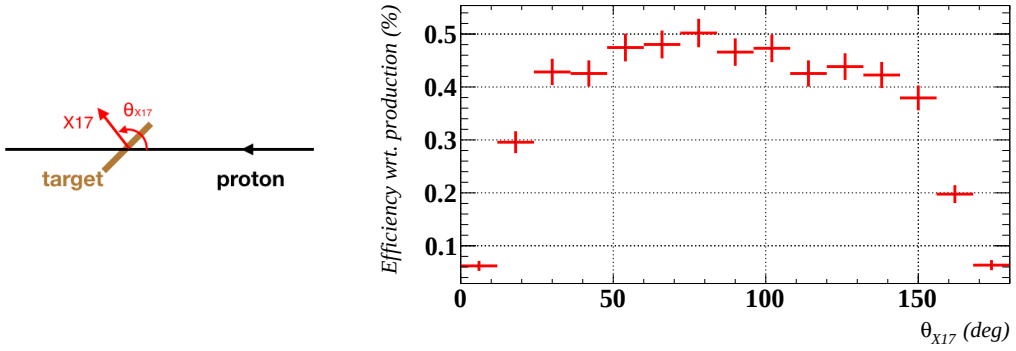

Figure 4.38: (Left) Definition of the X17 polar angle with respect to the beam direction. (Right) Acceptance for X17 signal events as a function of the polar angle of the X17 momentum, estimated from MC.

- Events were fully simulated only if at least one pTC tile was hit. Photons producing no charged particles are of no interest and likely won't deliver a hit signature within the pTC. These photon events are not simulated. IPC pairs outside of acceptance won't hit the pTC either. The trigger simulation would reject these events anyway.

- A charged particle with a momentum below 5 MeV/c, with $\theta < 30°$ or with $\theta > 150°$ is outside the spectrometer's acceptance. An IPC pair with at least one such particle is not simulated.

10 billion photons were simulated from both the transition to ground state and to first excited state. They constitute the EPC18 and EPC15 simulations. 100 million IPC pairs from each transition were simulated to constitute the IPC18 and IPC15 simulations. A summary of the various simulations including backgrounds and signals, along with the number of simulated events are shown in Tab. 4.3. The simulation of fake pairs or fakes is described in Sec. 5.

Simulation type	**Description**	**Number of simulated events**	**Proton energy [keV]**	**Transition**	
				To 1st excited state	To ground state
Backgrounds					
IPC	e^+e^- pair from Gaussian beamspot following ZM IPC model	1×10^8 /transition	[350, 1080]	**IPC15**	**IPC18**
EPC	photon from Gaussian beamspot following ZM photon model	1×10^{10} /transition	[350,1080]	**EPC15**	**EPC18**
fakes	single e^- from Gaussian beamspot following ZM IPC model	6×10^8	[350,1080]	/	**fakes**
Signal					
X17	back-to-back e^+e^-pair from Gaussian beamspot boosted in isotropic X17 frame. Masses from 16.3 MeV/c^2 to 17.3 MeV/c^2 in 0.2 MeV/c^2 steps	8×10^5 /X17 mass	441	/	**X17(17.6)**
		8×10^5 /X17 mass	1030	/	**X17(18.1)**

Table 4.3: Simulation type, event description, number of simulated events, proton energy and transition of interest for all 7 simulations used for the X17 search: IPC15, IPC18, EPC15, EPC18, fakes, X17(17.6), X17(18.1).

Chapter 5

Reconstruction of charged particles

The X17 search with MEG-II relies on the reconstruction of both electron and positron tracks within the spectrometer. The positron reconstruction was developed for the $\mu^+ \to e^+\gamma$ search. However, the reconstruction of electron tracks and the simultaneous reconstruction of an electron and a positron track require a procedure specific to the X17 search, introduced in this chapter. After presenting the peculiarities of electron tracks, we will introduce the reconstruction steps and justify the necessity of strong selections on the pair of tracks. We will then quote the estimated efficiencies and resolutions before describing a promising vertexing procedure.

5.1 Fine-tuning of time windows and offsets

The trigger for the X17 search requires the coincidence of a pTC hit and several CDCH hits, a trigger choice unused for the $\mu^+ \to e^+\gamma$ search. The waveform timing in each detector has an offset related to the trigger latency. These offsets must be well and precisely estimated to optimize the track reconstruction.

For the pTC, the latency is estimated from the distribution of pTC hit times, extracted from the fit of pTC waveforms and displayed in Fig. 5.1. A peak value of -610 ns is then set into the database and subtracted from the waveform timing before the hit reconstruction is performed.

The CDCH track reconstruction is the most critical aspect. It requires a fine-tuning of the time offsets at the nanosecond level in order to have the best estimate of the drift distance for each hit. The offset to tune is the one between the CDCH and the pTC. It corresponds to a difference in trigger latency between the two detectors, due in part to the difference between the signal cables length. A wrong offset between the pTC and the CDCH will bias the drift distance estimate and reduce the efficiency of the seeding. The distance of closest approach (DOCA) is first estimated for each hit as a departure point for the tracking and is written as d_{hit}. The DOCA estimate is refined after the tracking making use of the DOCA

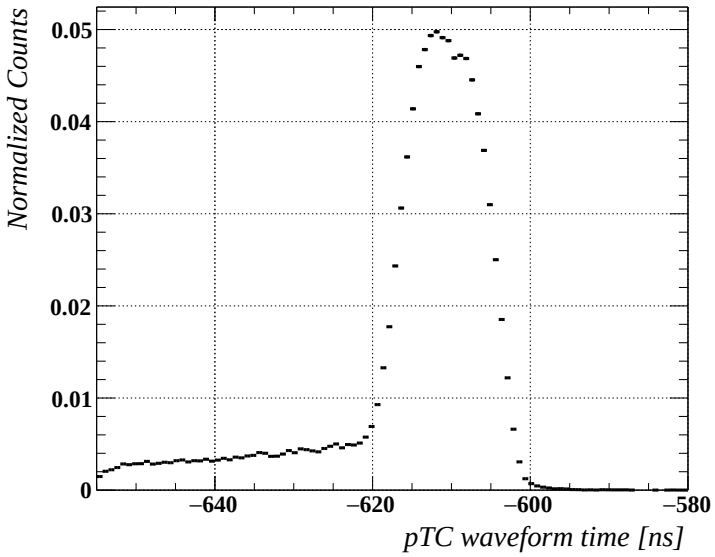

Figure 5.1: pTC waveforms time distribution.

.

estimated by the Kalman filter and is written d_{track}. The DOCA error is then expressed as $d_{hit} - d_{track}$ and their distribution should be zero-centered. An offset in the CDCH signal timing will show as an offset in the DOCA residuals distributions. The pTC-CDCH time offset is estimated from this distribution as shown in Fig. 5.2. The trigger timing offset between the two detectors is close to 13 ns, value for which the DOCA residuals distribution is best centered. This value is then set in the database.

The CDCH hit time distribution can then be studied. A finite time window has to be set to simultaneously maximize the number of in-time beam-related hits and the tracking efficiency and reduce pile-up. The optimized hit time selection window can be seen in Fig. 5.3. The first hits, where the ionization happens close to a wire, are detected at ≈ -610 ns, close to the pTC hits timing. The later ones, delayed due to drift time, occur in the next 200 ns.

5.2 Electron and positron track specificities

After the pTC and CDCH timing and offsets are estimated and set in the database, one needs to adapt the reconstruction procedure to electrons. An understanding of the electron track specificities in a positron-optimized apparatus is crucial.

A third of the CDCH wires, the 4 upper sections, are unread. This has negligible impact on the $\mu^+ \to e^+\gamma$ search which focuses on positrons with

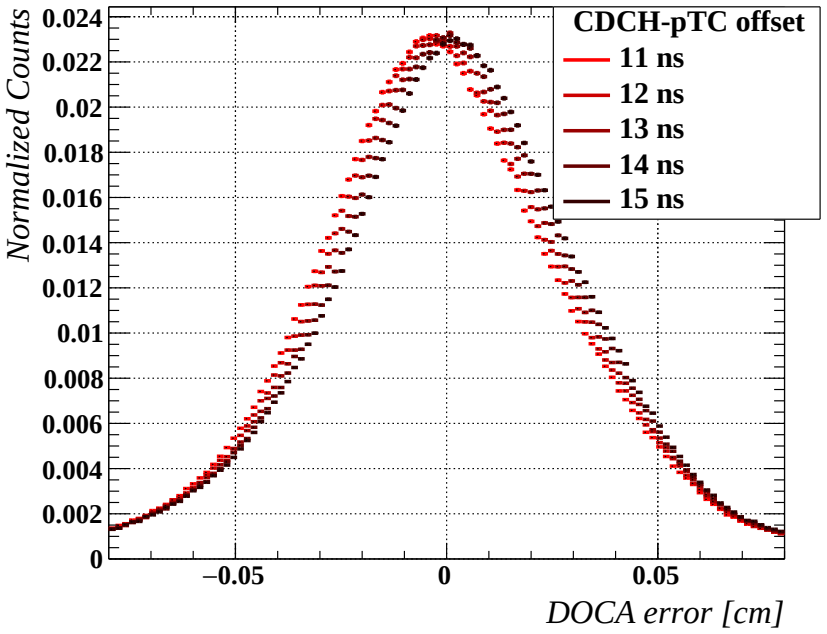

Figure 5.2: DOCA error $d_{hit} - d_{track}$ distribution for several values of the pTC-CDCH time offset. The DOCA error distribution is best centered for a 13 ns offset.

.

$-60° < \phi < 60°$ in accordance with the XEC acceptance. However, this strongly impacts the X17 search and positron and electron acceptance. In the COBRA magnetic field, both tracks turn in opposite directions. Fig. 5.4 represents simulated electron and positron tracks going through the chamber volume with different azimuthal emission angles. The x-axis direction has an azimuthal angle $\phi = 0°$.

The CDCH azimuthal acceptance is therefore different for electrons and positrons. It is clear for example that positron tracks with an angle at emission $\phi = 180°$ and electron tracks with an angle at emission $\phi = 0°$ are hard to reconstruct (in black in Fig. 5.4). The acceptance can be understood from Fig. 5.5 which shows the distribution of the reconstructed ϕ for electrons and positrons (reconstruction procedure is detailed in the next subsections). The unread section of the CDCH has a clear and strong impact on the shape of these distributions. The two distributions are also phase-shifted so a pair with both particles emitted in the same (azimuthal) direction will be hardly reconstructed.

A clear way to distinguish electron from positron hits is the ϕ vs $|z|$ space. From the target at COBRA center $z = 0$ the electrons and positrons are pushed away

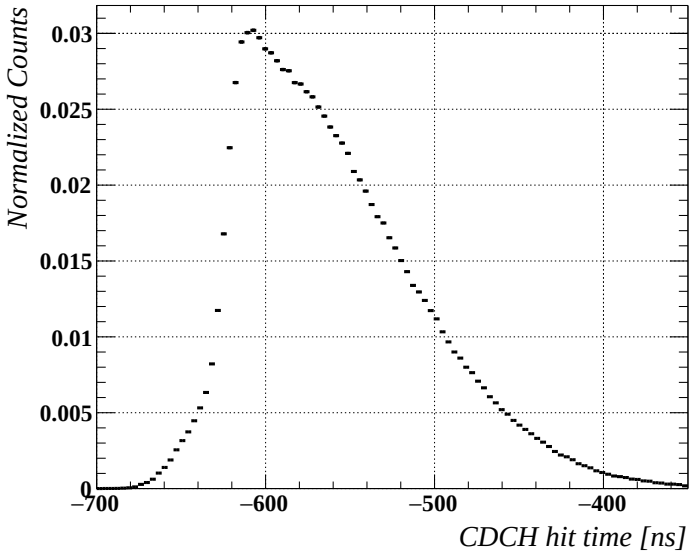

Figure 5.3: CDCH hit time distribution with optimized hit selection window.

.

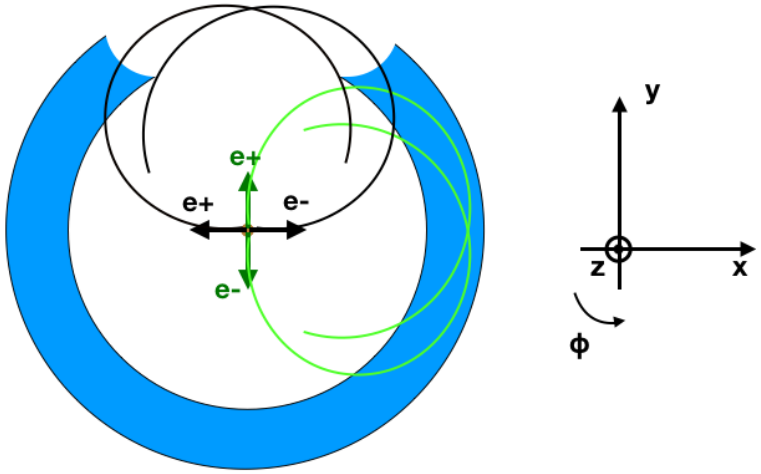

Figure 5.4: Sketch of electron and positron tracks going through the apparatus seen from the positive z. The particles are sketched with different azimuthal angles at emission. The drift chamber acceptance is represented in blue. The upper section of the CDCH, colourless, is not read.

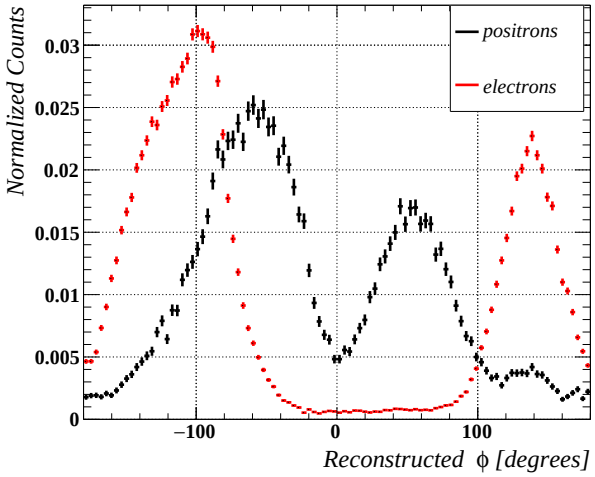

Figure 5.5: Azimuthal distribution of reconstructed positrons (black) and electrons (red)

towards increasing $|z|$. Their rotation directions are then translated in negative ϕ evolutions for positrons and in positive ϕ evolutions for electrons. The generated hit positions in the ϕ vs z plane for electron and positron simulated tracks are displayed in Fig. 5.6. Though at large $|z|$ the steepnesses are very different, it is harder to distinguish the ϕ vs $|z|$ sign at close to $z = 0$, where the tracks are both vertical in the plane.

As observed in Fig. 5.7, the pTC is ideal for positrons. Its tiles were designed so that a signal positron track, emitted opposite to the xenon calorimeter, hits them almost orthogonally. The energy loss in a tile is therefore minimized and the track can go through 10 tiles on average for a 52.8 MeV positron.

The typical electron and positron for the X17 search have momenta close to 8 MeV/c. Such low-energy positrons have fewer pTC hits than $\mu^+ \to e^+\gamma$ 52.8 MeV/c positrons because a pTC hit with an average 1 MeV energy deposit largely disrupts the trajectory of the former. Simulated 8 MeV/c positrons are compared with simulated 8 MeV/c electrons in Fig. 5.8. Both simulate an isotropic emission of charged particles at the target with a monochromatic momentum distribution for a 0.15-scaling COBRA field with respect to MEG-II's nominal field. The top left and top right plots show the number of pTC hits for all events and events with at least one hit. First, we can see that the positrons are more likely to hit the pTC (12%) than the electrons (8%). Then, for events with more than one hit in the pTC, there are fewer hits on average for electrons: more than 75% have 1 or 2 hits only. For positrons, $\approx 50\%$ of events have more than 2 hits. The bottom plot shows the simulated energy deposit distribution in a pTC tile. The

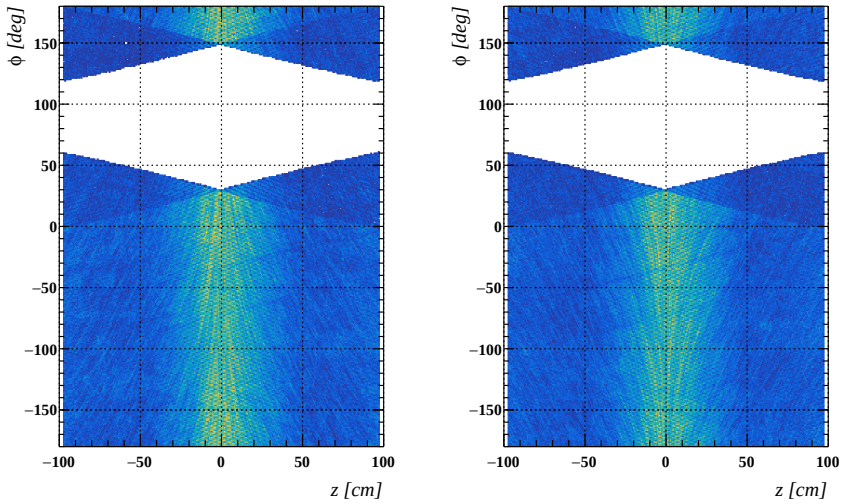

Figure 5.6: Generated CDCH hit position in ϕ vs z plane for positron (left) and electron (right) simulated tracks

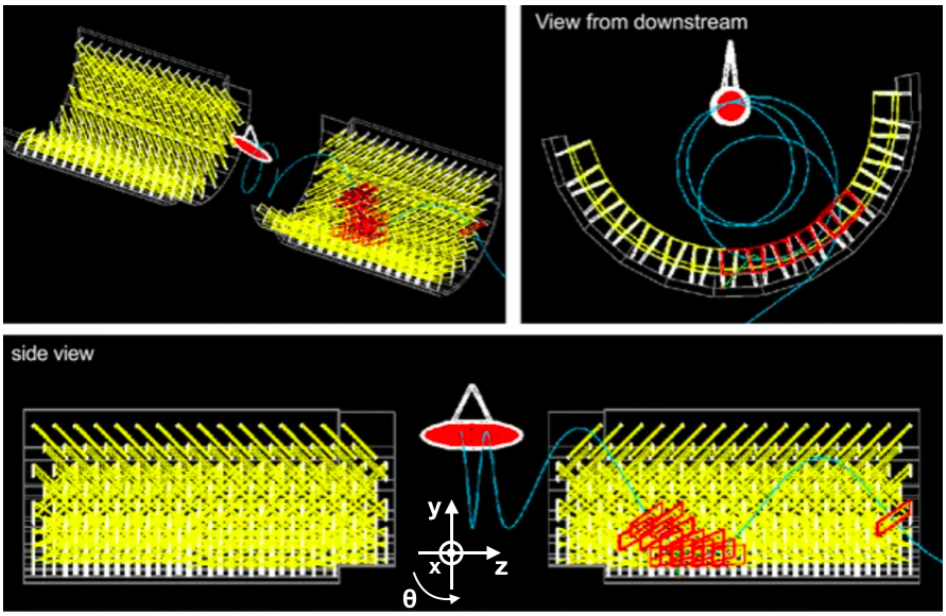

Figure 5.7: A simulated positron hitting the timing counter tiles. The CDCH is not represented. The coordinates system is indicated on the side view. θ corresponds to the angle between the initial momentum and the z-axis.

energy deposit is on average larger for electrons, which a non-orthogonal incoming angle of the electrons in the tiles can explain. It also implies a smaller number of hits in the pTC for electrons.

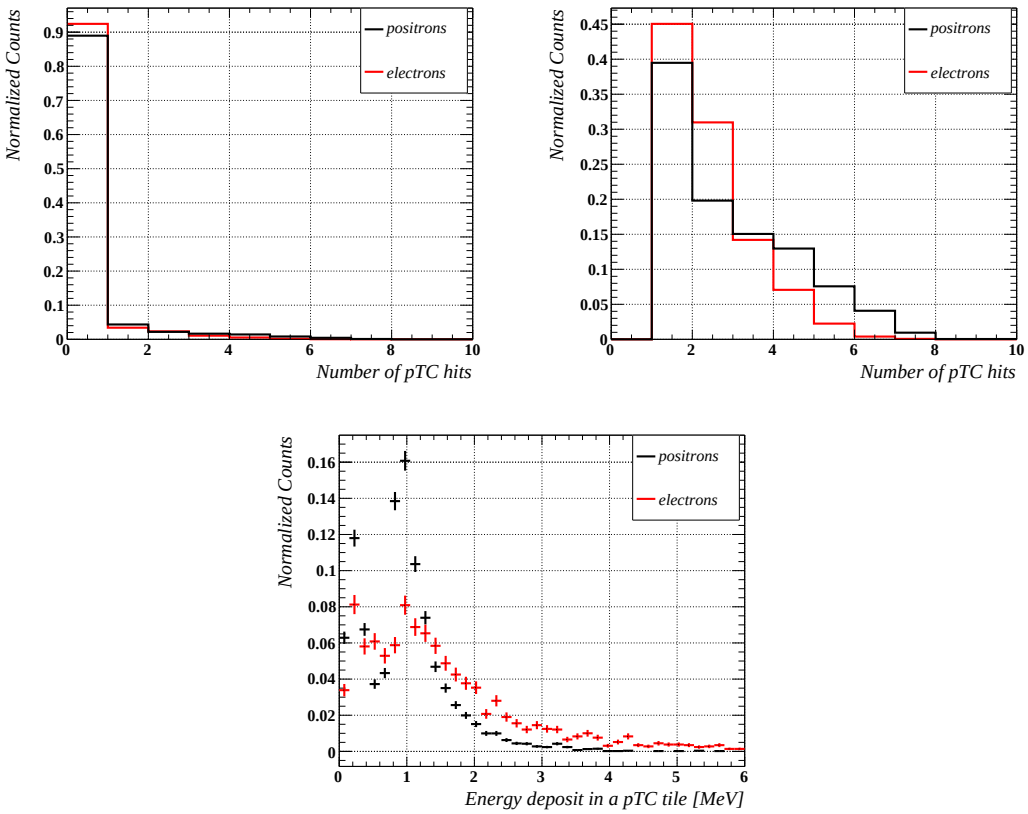

Figure 5.8: Number of pTC hits for all events (top left), for events with 1+ pTC hit (top right), energy deposit in a pTC tile (bottom) for monochromatic 8 MeV/c positrons and electrons simulated isotropically.

It shows that the pTC trigger condition is more likely fulfilled by a positron track (60% probability) than by an electron track (40% probability). The large energy deposit for electrons shows that a pTC waveform threshold passed by a positron hit will be likely passed by an electron hit. However, simulations have shown that both types of hits provide a good seed timing for track reconstruction. There is no need to distinguish electron- from positron-triggered events.

5.3 Reconstruction procedure

In order to confidently reconstruct a pair of charged particles, both an electron track and a positron track must be propagated back to a point close to the target where the kinematics can be extracted. When a track is found, it is propagated backwards from the first hit (lower $|z|$) in the CDCH to the target plane, where a state vector at target is computed including the position, momentum, polar, azimuthal angles, the associated errors and covariances matrices. Another state vector, called "at vertex", is estimated from the propagation of the track to the point of closest approach (POCA) to the z-axis. This point is used as our best estimate for the track origin and all the estimated observables for the particle at production are taken at this point.

The MEG-II track finder was optimized for positron tracks. To do so, it is requested that the sign of the transverse momentum difference from one hit to the next be compatible with a positron in accordance with the sign of the COBRA magnetic field. This was implemented for the $\mu^+ \to e^+\gamma$ search so that the number of track candidates and the computing time are reduced and that the positron tracking efficiency is improved. A simple and efficient way to find electron tracks is therefore to invert the assumption on the magnetic field sign. Indeed, an electron track in a given magnetic field is equivalent to a positron track in the sign-inverted magnetic field. For the pair reconstruction, the track finder is therefore run twice, once for the positron track search with the original COBRA field sign assumption, and once for the electron track search with the COBRA field sign assumption inverted. To estimate the capabilities of this method, the track finder with and without sign-inverted assumption was run on both electron-only and positron-only simulations. Fig. 5.9 shows the reconstructed vertices on target from an electron-only simulation reconstructed with the original COBRA field sign assumption (left) and with the inverted sign assumption (right).

As needed, the inverted-sign tracker is much more efficient at reconstructing electron tracks than the original-sign tracker. There are 100 times more reconstructed tracks when the field sign is inverted with respect to the original field sign. However, a fraction of tracks are reconstructed in the original field sign assumption, leading to them being incorrectly tagged by the finder as positrons. These are nicknamed fake positrons. An ideal finder should reconstruct zero tracks in such a configuration. It is crucial to characterize such fake tracks and to discriminate them as efficiently as possible. Fig. 5.10 shows the reconstructed polar angle θ distribution for both the electron tracks and such fake positron tracks. Though the reconstructed θ is spread between 30° and 150° for the real (electron) tracks, the fake positrons are reconstructed almost only at $\theta \approx 90°$. This behaviour can be understood from Fig. 5.6: the tracks emitted with $\theta \approx 90°$ are almost orthogonal to the beamline. In this configuration, ϕ vs z is mostly vertical for both electron

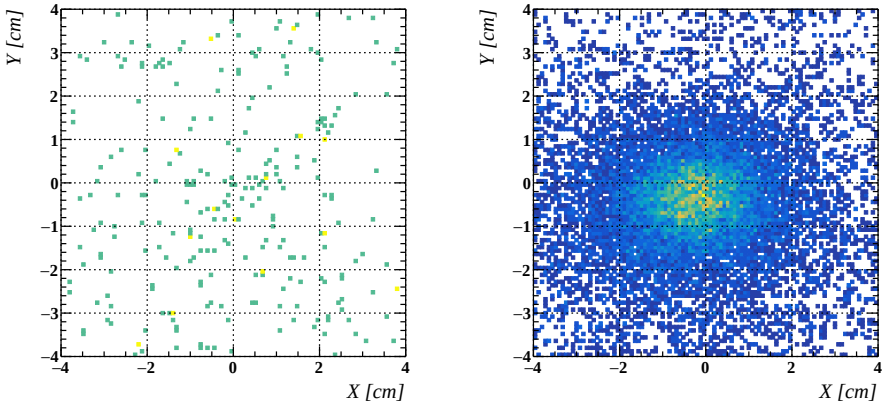

Figure 5.9: Reconstructed vertices on target from an electron-only simulation reconstructed with the original COBRA field sign assumption (left) and with the inverted sign assumption (right). 99% of the total number of reconstructed tracks has the correct sign (right) and the remaining 1% comes out as fake positrons (fake).

and positron tracks and it is therefore harder to distinguish both types of charged particles.

Because the CDCH is a slow detector, the hit timing cannot be used to distinguish the rotation direction of the tracks. The hit z is also hard to rely on due to a O(10 cm) error on the time difference or charge division methods. The track sign ambiguity is mitigated by combining the coordinates of all hits in a track and especially profiting from the stereo configuration of the CDCH. However, a fraction of tracks are still misreconstructed and assigned a wrong sign. Such tracks are particularly dangerous for the X17 search, they require a deep and precise characterization. Their rejection will be based on a trade-off between the fake track rejection and the good track acceptance.

5.3.1 Characterization of fake lepton tracks

In order to reject the fake tracks while accepting a maximal number of signal tracks, it is crucial to understand the specificities of such fake tracks. Several track observables for good and fake tracks were compared making use of an electron-only MC simulation described previously. The characterization presented here is not kinematic but aims at understanding how the lower-level information of the fitted tracks can be used to reject the fake tracks: it includes for example the number and density of fitted hits (or good hits), the vertex position, the propagation length to vertex, the distance between consecutive hits and several other variables.

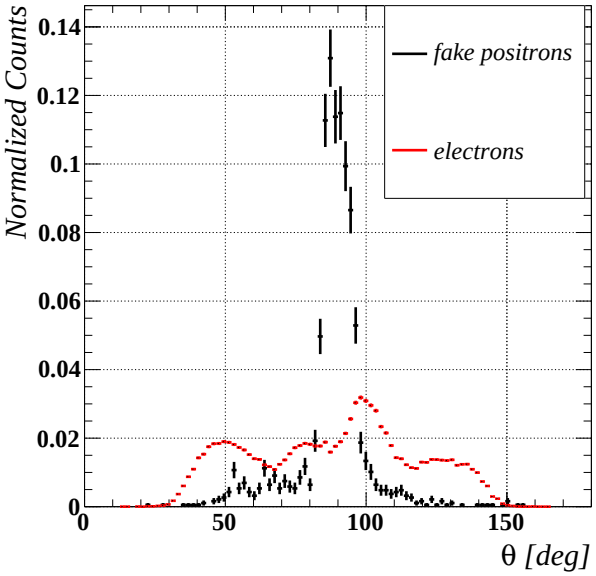

Figure 5.10: Reconstructed polar angle θ from an electron-only simulation reconstructed with the original COBRA field sign assumption (fake positrons, in black) and with the inverted sign assumption (electron, in red).

Fig. 5.11 and Fig. 5.12 compare relevant distributions extracted from both good tracks (in red) and fake tracks (in black). The former ones correspond to simulated electron tracks reconstructed with the inverted magnetic field sign assumption (true electron tracks) while the latter ones correspond to simulated electron tracks reconstructed in the original magnetic field sign assumption (fake positron tracks). Twelve observables are compared here and will be introduced and described from top left to bottom right. The tracks shown here include minimal selection: they are requested to propagate back to a z-axis point of closest approach (z-axis POCA or vertex) and within 8 cm from the true beam spot z-coordinate $z_{beamspot}$.

- $T0_{lasthit} - T0_{firsthit}$ represents the difference of time between the last fitted hit of the track and the first fitted hit. A time $T0$ is assigned to a CDCH hit starting from the precisely estimated pTC hit time and accounting for the time of flight between the estimated CDCH hit position and the pTC tile. The longer the $T0$ difference, the longer the track. The several-peak structure can be understood from different types of fitted tracks. Some enter the CDCH volume through the internal radius and exit it through the external radius. These are the shortest type of tracks and are called half-turn

tracks. Longer tracks or full-turn tracks enter the CDCH volume through the internal radius and exit it through the internal radius after exiting or not the CDCH volume externally. Tracks with one and a half turns or two full turns are rarer and correspond mostly to lower energy tracks turning several times through the CDCH before exiting the volume and hitting the pTC tiles. Comparing the distributions, it is clear the fake tracks are in average shorter than the good tracks and mostly consist of half-turn or one-turn tracks. It can also be observed that properly fitted tracks have an exclusively positive $T0$ difference as one expects a propagation direction from first to last hit. However, a small portion of fake tracks has a negative $T0$ difference due to problems with track fitting convergence. This quantity should be selected to be positive.

- Another observable of interest is $z_{lasthit} - z_{firsthit} \times sgn(z_{firsthit})$, the z difference between the last and first hit pondered by the sign of the first hit z. Because the particle is generated at the target, close to $z = 0$, almost all particles propagate towards increasing $|z|$. The fitted tracks corresponding to particles generated at target should therefore have a positive signed z difference. In Fig. 5.11, we observe indeed that most good tracks follow this condition. However, a majority of fake tracks have a negative signed z difference. This can be understood considering that electrons going away from the target have the same trajectory as positrons going toward the target. This quantity should be selected to be positive.

- $|z_{firsthit}|$ is the absolute value of the first hit z coordinate. It is largely dependent on the polar angle of emission. The particles emitted orthogonally to the beam axis ($\theta \approx 90°$) have a $|z_{firsthit}|$ close to 0 while smaller polar angles lead the particles to enter the CDCH volume at larger $|z|$. As already mentioned, the most sign-ambiguous tracks are the ones emitted almost orthogonally to the beam-axis where the ϕ vs $|z|$ evolution is also ambiguous. It is no surprise fake tracks have a majority of first hit $|z|$ in the first 5 cm while good tracks are more uniformly spread over the first 30 cm.

- The next observable requires clarification. It corresponds to the fraction of hits in a track with opposite z-coordinates. Writing n_+ or n_- the number of fitted hits with positive or negative z coordinate, this observable can be written: $\min(n_+, n_-)/(n_+ + n_-)$. The minimal value is 0.0 and occurs when all hits are on one side of the CDCH (all z being positive or all z being negative). The maximal value is 0.5 and occurs when half of the hits are in one part of the chamber and the other half is in the opposite part. Tracks with a non-zero observable are ambiguous as they have hits close to $z = 0$: either the particle actually went from a part of the CDCH to the opposite

part crossing the $z = 0$ plane (rare case), either the Kalman filter didn't correctly identify the track's path. In both cases, the track is ambiguous and should be discarded. In Fig. 5.11, we can see that 93% of the good tracks have hits strictly in one part of the CDCH, while for fake tracks this fraction goes down to only 65%. This can be used as an additional handle to reject fake tracks.

- $z_{vertex} - z_{beamspot}$ expresses the difference between the z coordinates of the track vertex (z-axis POCA of the propagated track) and the true beamspot center (or its best estimate). In the case of an ideal reconstruction, this quantity should follow the shape of the beamspot z, peak at 0 and fall like a Gaussian distribution. In a non-ideal case, the uncertainty from the reconstruction adds to the beamspot width but should still peak at 0 and be Gaussian-falling. It is what is observed for good tracks in Fig. 5.11 with the large majority of tracks reconstructed within 2.5 cm from the beamspot center z. However, the fake tracks are fitted with a large relative uncertainty on their direction leading to an almost flat $z_{vertex} - z_{beamspot}$ distribution in the first 4 cm.

- the propagation length in cm, computed as $(T0_{firsthit} - T0_{vertex}) \times c$, with c the speed of light, corresponds to the distance required to propagate back the track from the first hit to the z-axis POCA. In the case of a good track, it is equivalent to the distance flown by the particle between its emission and its first hit into the CDCH: the propagation length is then included between 15 cm and 40 cm depending on the polar emission angle. In the case of a fake track, the propagation direction is opposite with respect to a good track: instead of going straight back to the target, the propagation of fake tracks keeps on turning through the chamber volume before reaching the target. This leads to part of the fake tracks having a large propagation length, mostly between 35 cm and 60 cm.

- *ngoodhits* represent the number of fitted hits in a track. A three-peak structure is seen for good tracks in red in the top left plot of Fig. 5.12. It corresponds to tracks with a half turn, a full turn and one and a half turns. In MEG-II case, the signal is a monochromatic positron and the CDCH was designed so that such a positron goes through at least a full turn within the spectrometer volume. For the X17 search, the signal is an electron-positron with large momentum spreads. Low and high-momentum tracks going through the CDCH leave fewer hits and have therefore smaller *ngoodhits*. Moreover, the helium CDCH inner volume for MEG-II is replaced by air for the X17 search, leading to additional multiple scattering

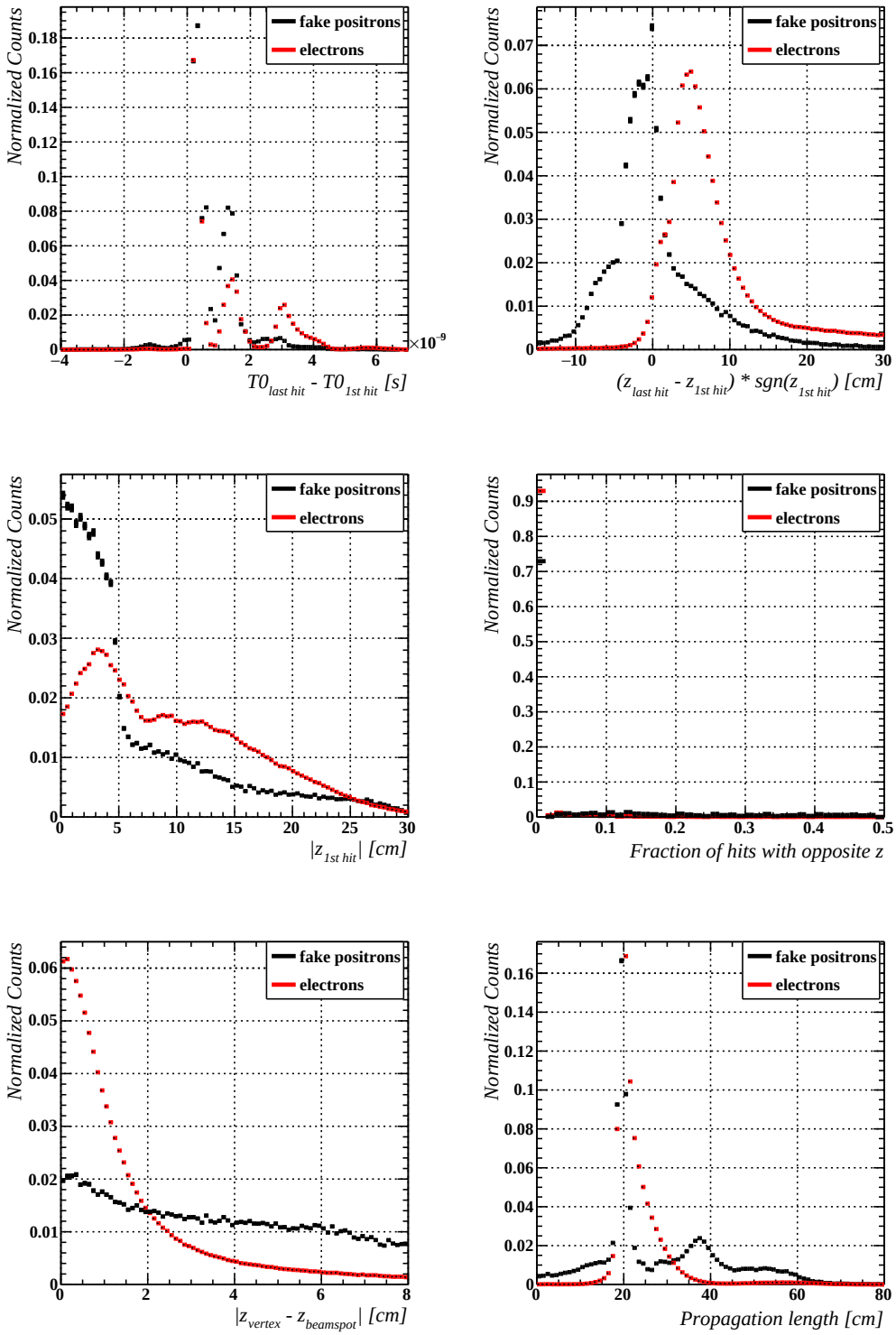

Figure 5.11: Observables comparison between good tracks (red) and fake tracks (black). (Top left) T0 difference between last and first fitted hit. (Top right) Signed z difference between last and first fitted hit. (Middle left) Absolute value of first hit z. (Middle right) Fraction of total number hits with opposite z. (Bottom left) Distance between the reconstructed vertex and the generated beam spot center z-coordinates. (Bottom right) Propagation length from first hit to vertex.

and increased complexity to reconstruct several-turn tracks. This explains how a majority of tracks are half-turns with $ngoodhits < 18$. Looking at the fake tracks, we can see there are no 1.5-turn tracks: such tracks are too long to be misfitted. One can also see that the half-turn and full-turn peaks have roughly 3 less good hits for fake tracks than for good tracks: it is more difficult to include good hits into a misfitted track as the quality of the track worsens. It leads to a half-turn left edge at 7 good hits for fake tracks, which can be easily discriminated. However there are more full turn fake tracks than full turn good tracks: fake tracks are more likely from lower momentum particles leading to more turns into the CDCH.

- the track hit density corresponds to the number of good hits per track cm. The top left plot of Fig. 5.12 shows the distribution of this quantity for tracks with $10 \leq ngoodhits \leq 16$. Most of the good tracks have on average between 0.8 and 2.0 hits/cm. A small fraction of good tracks have a hit density below 0.5 cm^{-1}. For fake tracks, one can see the fraction below 0.5 cm^{-1} is much larger. The fake tracks distribution also shows a shoulder between 0.5 cm^{-1} and 1.0 cm^{-1}. The wrong sign reconstruction making it harder to fit all hits, it leads to a smaller density of good hits.

- the track hit density is here plotted for half-turn tracks. As previously seen, for the X17 search most tracks go through only half a turn within the CDCH active volume. The various typologies of tracks can be understood from Fig. 5.13, presenting the hit density vs $ngoodhits$. Three types of tracks with increasing $ngoodhits$ and decreasing hit density are seen, corresponding to half-turn, full-turn and 1.5-turn tracks. Their decreasing density is due to the fact the last two types of tracks exit the CDCH active volume once and twice respectively, thus reducing the hit density. One can isolate the half-turn tracks requesting a hit density larger than $ngoodhits/12 - 2/3$. The hit density distribution for such tracks, both good and fake, is shown in Fig. 5.12 (middle left). For these short tracks, one can see the fake tracks are less dense on average than the good ones. In particular, a significant shoulder below 1.0 cm^{-1} can be observed for fake tracks. The red square in Fig. 5.13, with a low number of good hits and a low track hit density, is likely to include fake tracks and can be rejected with a minimal cost on good tracks.

- Fig. 5.12 (middle right) shows the track score distributions, defined as $ngoodhits + 10 \times$ hit density. The distributions are similar to Fig. 5.12 (middle left) but having an observable mixing both $ngoodhits$ and hit density allows further discrimination between good and fake tracks.

- the consecutive hits distance standard deviation is calculated for each track making use of the distance between one hit and the next. Because hits are less likely to be fitted in fake tracks, the distance between two consecutive fitted hits can be large. It is seen with this observable which is larger for fake tracks as seen in Fig. 5.12 (bottom left). Though the bulk of the distribution is at 0.4 cm for both good and fake tracks, the region above 0.9 cm mostly consists of fake tracks.

- $sgn(z_{mean} \times (\theta - 90°))$ compares the position of the track in the CDCH (positive or negative average z) with the direction of the track ($\theta < 90°$ or $\theta > 90°$). If emitted towards DS ($\theta < 90°$), the average z of the track hits should be positive. If emitted towards US ($\theta > 90°$), the average z of the track hits should be negative. $sgn(z_{mean} \times (\theta - 90°))$ should therefore be negative for good tracks. Only tracks emitted at $\theta = 90°$ can be an exception depending on the production point on the target: these only represent 3% of the good tracks. For fake tracks, however, the extrapolation from first hit to z-axis POCA (or target) often leads to an inversion of the reconstructed momentum as described in Fig. 5.14. $sgn(z_{mean} \times (\theta - 90°))$ is in practice positive for almost 60% of fake tracks.

5.3.2 Presentation of track and pair selection

Based on the previous characterization of fake tracks, a stringent track selection was developed based on a compromise between a high good track acceptance and a high fake track rejection. Track acceptance is the fraction of tracks passing the selection given a minimal preselection (z-axis POCA propagation and POCA within 8-cm from the true beam spot z-position $z_{beamspot}$). The track rejection is defined as (1 − acceptance). The list of selections is shown in Tab. 5.1 along with the good track acceptance and the fake track rejection. The last line gives the total good track acceptance and the total fake track rejection including all selections together. We see that with such a stringent selection almost 99% of the fake tracks are rejected while more than half of the good tracks are conserved.

In case several same-sign tracks are found, the best track in the event is chosen based on the smallest error on the momentum at z-axis POCA extracted from the Kalman fit. On top of this selection of single tracks, a selection on pair of tracks was developed in order to reject pairs for which one track is fake. To do so, this selection makes use of the track correlation defined as the number of hits in common between the selected electron and positron tracks. In theory, two different tracks should use two completely different sets of hits. If at least one hit is included in both tracks it is due to one of the two tracks being reconstructed with the wrong sign. Fake tracks can therefore be tagged by comparing all the fitted

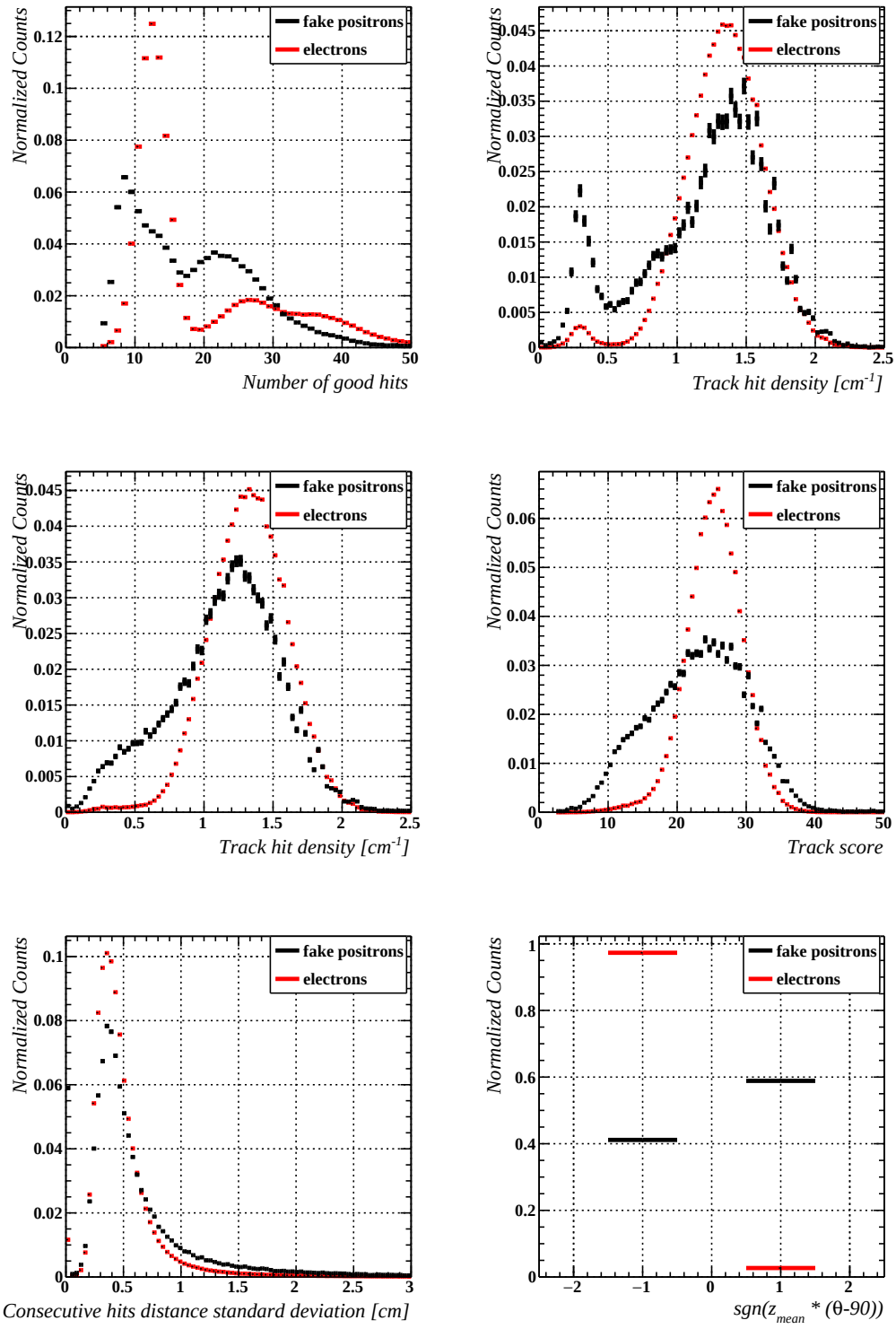

Figure 5.12: Observables comparison between good tracks (red) and fake tracks (black). (Top left) Number of good hits $ngoodhits$. (Top right) Track hit density for $10 \leq ngoodhits \leq 16$. (Middle left) Track hit density for half-turn tracks. (Middle right) Track score ($ngoodhits + 10 \times$ hit density) (Bottom left) Consecutive hits distance standard deviation. (Bottom right) Sign of the production of the average z of the track (z_{mean}) and its direction ($\theta - 90°$): $sgn(z_{mean} \times (\theta - 90°))$.

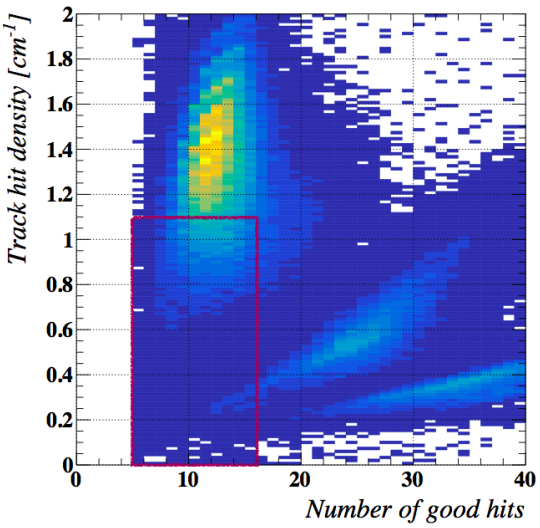

Figure 5.13: Track hit density vs ngoodhits from an IPC simulation. The red rectangle with a low number of good hits and a low track hit density is likely to include fake tracks and is therefore rejected.

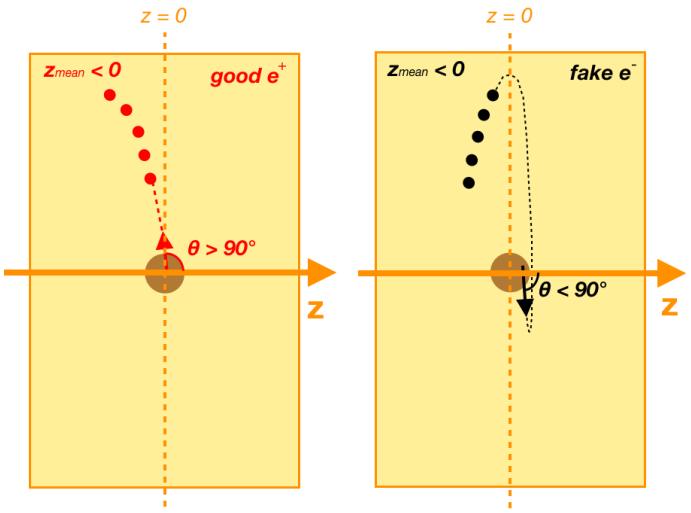

Figure 5.14: Scheme of extrapolation of momentum at target for a good track (left) and a fake track (right). The propagation of a fake track to target leads to a reconstructed track direction opposite to the expected track hit z position.

Condition	Good Track Acceptance (%)	Fake Tracks Rejection (%)
$ngoodhits \geq 10$	93	21
$\lvert z_{vertex} - z_{beamspot} \rvert \leq 2.5$ cm	80	58
$T0_{lasthit} - T0_{firsthit} \geq 0$	100	3
$(z_{lasthit} - z_{firsthit})$ $\times sgn(z_{firsthit}) \geq 0$ cm	97	58
propagation length ≥ 35 cm	97	29
if $10 \leq ngoodhits \leq 16$, hit density ≥ 1.1 hits/cm	86	25
if hit density $> ngoodhits/12 - 2/3$, hit density ≥ 0.8 hits/cm	98	11
if hit density $> ngoodhits/12 - 2/3$, track score ≥ 20	94	18
Consecutive hits distance std < 0.9 cm	90	26
$z_{firsthit} \geq 2.5$ cm	85	33
$z_{mean} \times (\theta - 90°) < 0$	97	59
Total	**50.4**	**98.8**

Table 5.1: List of selection on single tracks along with the good track acceptance and the fake tracks rejection

tracks with opposite signs and finding the ones with non-zero track correlation. Already applying the single track selection from Tab. 5.1, it is found that 60% of the selected fake tracks include at least one hit used by an opposite sign track. Two levels of selection are based on the track correlation:

- the track is rejected if it has a non-zero track correlation with at least one opposite sign track
- an event is rejected if it has at least two correlated tracks

The second selection is more stringent as seen in Tab. 5.2 and is applied in the final selection. One additional selection on the pair of tracks is the distance between the z-axis POCA vertices of the selected electron and positron tracks, requested to be below 3 cm. Already applying the single track selection, the additional pair selection rejects more than 90% of the fake pairs while accepting almost 85% of the good pairs.

Condition	Good Pairs Acceptance (%)	Fake Pairs Rejection (%)
Tracks not correlated (hits in common between e^+ and e^- tracks)	100	59
Event with no correlated tracks	100	64
Vertices distance $<$ 3 cm	84	61
Total	**84**	**91**

Table 5.2: Selection on pair of tracks after single track selection is already applied.

The application of the selection to a sample of reconstructed IPC pairs is illustrated in Fig. 5.15. The fake pairs correspond to two pieces of the same track extrapolated to the target region in two opposite directions. Therefore the opening angle of fake pairs is close to 180°, mostly above 150° leading to the structure peaking at 160° in the red distribution. However, when the final pair selection is applied the fakes' structure is rejected and the simulated monotonous IPC angular opening shape is recovered though acceptance variations are observed.

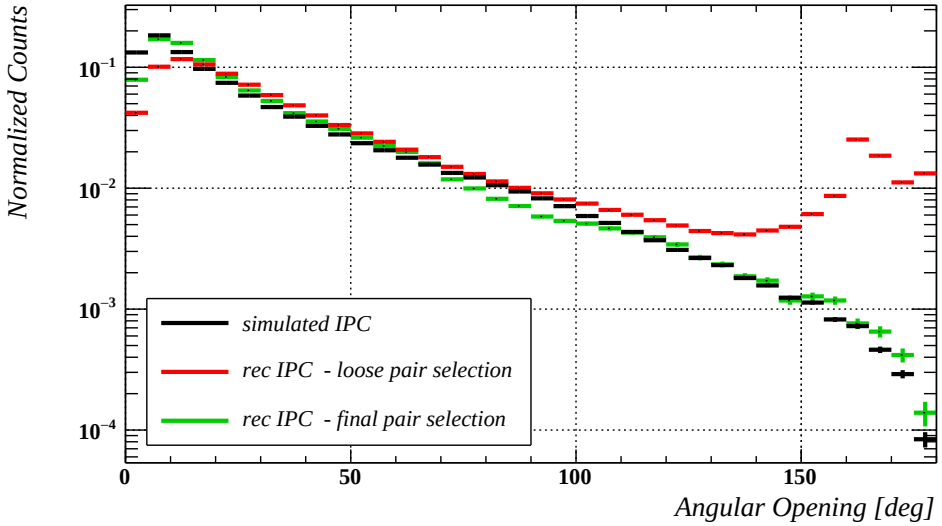

Figure 5.15: Angular opening distributions of the simulated IPC18 (green) and reconstructed IPC18 before (red) and after (black) applying the selection described in the text.

5.4 Efficiencies and resolutions

Tab. 5.3 shows the trigger, positron (wrt trigger) and pair selection efficiency for the X17 signal and the different IPC/EPC backgrounds on MC and for a set of data taken with the trigger described in Sec. 4.1.4: an event is considered to pass the trigger condition if it simultaneously passes the 18&18 CDCH waveforms condition and the pTC hit requirement. A positron track event is selected if it passes the selection described in Sec. 5.3.2. A pair event is selected if both an electron and a positron track pass the single track selection and both tracks pass the pair selection. The trigger selection efficiency is normalized with respect to the total number of produced events. The positron track and pair selection efficiencies are normalized with respect to the total number of triggered events. IPC pairs have large momentum asymmetry and the particles' momentum distribution is almost flat between 2 MeV/c and 16 MeV/c. X17 signal pairs have a smaller asymmetry and the particle's momentum ranges between 6 MeV/c and 12 MeV/c. The trigger selection efficiency is 4 times higher for X17 than for IPC because the trigger choice more likely selects tracks within the detector's acceptance, with momenta between 7 MeV/c and 10 MeV/c. The EPC trigger efficiency is low because it is given with respect to the photon production and therefore includes the photon conversion probability. The signal and IPC tracks are better reconstructed than EPC tracks due to the off-beam production and the large multiple scattering that the latter tracks undergo. The reconstruction efficiency is also improved for higher energy production (IPC18 vs IPC15 and EPC18 vs EPC15) again due to the detector's acceptance favouring signal-like tracks. The large inefficiency in data with respect to MC is commented in Sec. 6.1. The pair energy sum

	X17 MC	**IPC18 MC**	**IPC15 MC**	**EPC18 MC**	**EPC15 MC**	**data**
trigger selection eff.	16%	4.7%	3.9%	0.026%	0.020%	100%
e^+ selection eff. (wrt trg)	39%	42%	35%	21%	17%	8.3%
e^+e^- selection eff. (wrt trg)	6.5%	6.0%	2.8%	1.5%	0.6%	0.7%

Table 5.3: Trigger, positron and pair selection efficiency (wrt trigger) for the X17 signal MC with $m_0 = 16.9$ MeV/c^2, the four MC backgrounds and the actual data

is defined as $E_{sum} = E_+ + E_-$, the sum of positron and electron energies and calculated based on the reconstructed momenta at z-axis POCA vertex. The

Angular Opening corresponds to the angle between the two momenta. Pair energy sum E_{sum} and Angular Opening resolution were determined using the 16.9 MeV/c^2 X17 MC production. The true and reconstructed variables are subtracted and fitted with a two-gaussian function where the main Gaussian fraction is fixed to 75% as seen in Fig. 5.16. The resolutions are extracted as $\sigma_{1,\text{AngularOpening},X17} = (5.0 \pm 0.2)^\circ$ ($\sigma_{2,\text{AngularOpening},X17} = (7.3 \pm 0.4)^\circ$) and $\sigma_{1,E_{sum},X17} = (0.43 \pm 0.01)$ MeV ($\sigma_{2,E_{sum},X17} = (1.04 \pm 0.02)$ MeV).

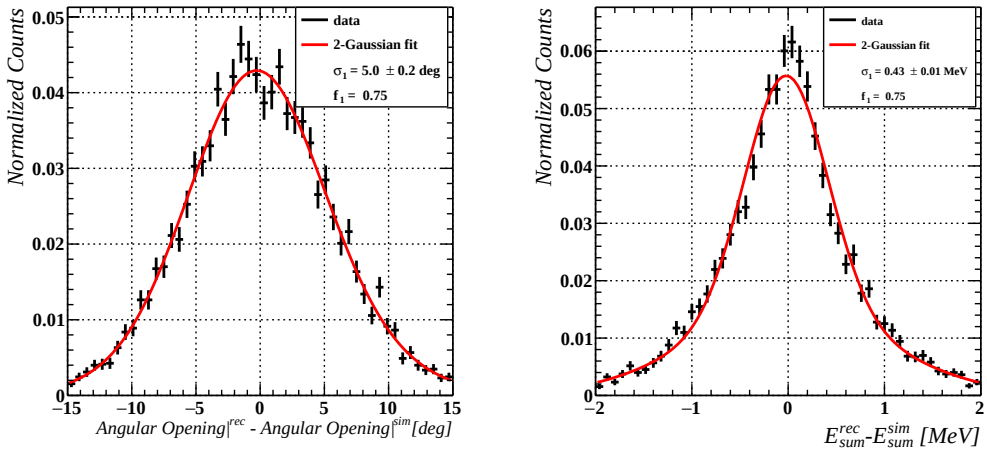

Figure 5.16: Reconstructed - simulated distributions for the Angular Opening (left) and the energy sum E_{sum} (right) for a 16.9 MeV/c^2 X17. The distributions are fitted with a two-gaussian function (in red) where the fraction of the main one is fixed to 75%. The width of the core Gaussian is quoted.

5.5 Vertexing

For the X17 search, the helium inner volume of CDCH is replaced with air. It leads to a larger average multiple scattering of the electron and positron tracks before entering the CDCH. For the $\mu^+ \to e^+\gamma$ search, the polar and azimuthal resolutions on signal positron reconstructed momenta are below 10 mrad (or below 0.5°). The electron and positron X17 signal tracks have angular resolutions in the order of O(5°) roughly an order of magnitude larger. Due to this worsened resolution, the propagation of the track is not done to target but to z-axis POCA, which can be O(cm) away from the target. In the previous procedure, the tracks are also fitted individually.

An alternative is to use a vertexing method: it is introduced and applied here in order to improve the angular resolutions of the fitted tracks. The idea is to make use of the information from both the electron and the positron tracks and the best estimate of the beam spot position on target in order to find a common vertex for the tracks. The RAVE (Reconstruction (of vertices) in abstract versatile environments) vertexing tool [88] includes both vertex finding and vertex fitting. Its robust reconstruction algorithms are built on an adaptive filter called AdaptiveVertexFitter (AVF).

The inputs and outputs of the vertexing tool are presented in Tab. 5.4. It requires information from the fitted tracks: a 6-vector $(\mathbf{p}_i(\vec{x_i}, \vec{p_i}))$ for each fitted track i at a given point including position and momentum 3-vectors and an associated covariance matrix. The beamspot information can be optionally added as a beamspot center coordinates 3-vector $\mathbf{b}$ and an associated covariance matrix giving its profile. The beamspot constraint is then included as a Bayesian a priori information of the vertex position. After vertex finding and fitting, the outputs are the vertex coordinates $\mathbf{v}$ and the momentum 3-vector $\mathbf{q}_i$ of each track at $\mathbf{v}$.

	Symbol	Information
Inputs		**Fitted tracks**
	$\mathbf{p}_i(\vec{x_i}, \vec{p_i})$	6-vector of track parameters
	cov($\mathbf{p}_i$,$\mathbf{p}_i$)	symmetric 6x6 matrices
		Beamspot
	$\mathbf{b}$	3-vector of beamspot center
	cov($\mathbf{b}$,$\mathbf{b}$)	symmetric 3x3 matrix of beamspot profile
Outputs		**Vertex**
	$\mathbf{v}$	3-vector of vertex coordinates
	cov($\mathbf{v}$,$\mathbf{v}$)	symmetric 3x3 matrix of vertex
		Tracks at vertex
	$\mathbf{q}_i$	3-vector of track momentum at vertex
	cov($\mathbf{q}_i$,$\mathbf{q}_i$)	symmetric 3x3 matrices

Table 5.4: Inputs and outputs of the vertexing procedure.

In practice, we provide $\mathbf{p}_{e^+}$ and $\mathbf{p}_{e^-}$ extrapolated at z-axis POCA. The beamspot center and profile are taken to be the ones generated in case of simulation and the ones resulting from the best estimate (see Sec. 7.2) in case of the data. It corresponds to a 2D-Gaussian beamspot on the target plane. A simplified scheme showing the principle of the vertexing on one track is shown in Fig. 5.17. From a $\vec{p}_{rec}$ at z-axis POCA (here z_{rec}), we obtain $\vec{p}_{vertexing}$ within the beamspot constraint on the target place. The angular variable estimate, here of θ, is then improved.

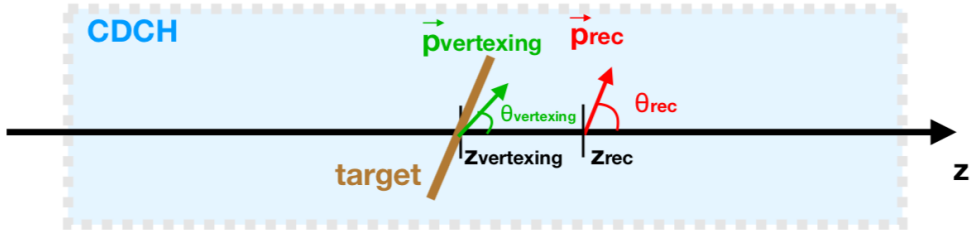

Figure 5.17: Scheme of vertexing correction of momentum.

The application of the RAVE tool to IPC tracks passing the selection from Sec. 5.3.2 is shown in the following figures. First of all, it should be highlighted that $> 99.9\%$ of events successfully undergo the vertex finding and fitting. Fig. 5.18 gives the reduced χ^2 distribution of the built IPC positron vertices. It evaluates the compatibility and likelihood that the electron and positron tracks originate from a common vertex located within a Gaussian beamspot on the target plane. The quality of the vertexing is supported by the distribution peaking at 1 and the majority of the vertices having $\chi^2_{red} < 3$. A tail is present at larger χ^2_{red} indicating a fraction of poorly fitted vertices. Fig. 5.19 gives the XY and ZY distributions of the positron vertices before vertexing and after vertexing. Before vertexing we see all the vertices close to z-axis as the request is an extrapolation to the z-axis POCA. After vertexing, the vertices are all located on the tilted (45°) target plane and within a Gaussian beamspot.

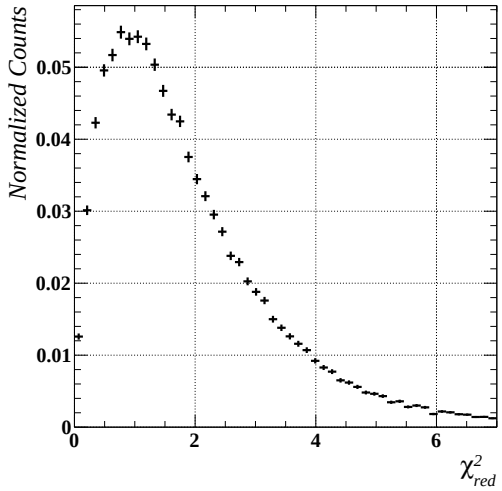

Figure 5.18: Reduced χ^2 distribution of the built IPC positron vertices.

The θ and ϕ resolutions before and after vertexing for IPC positrons are given

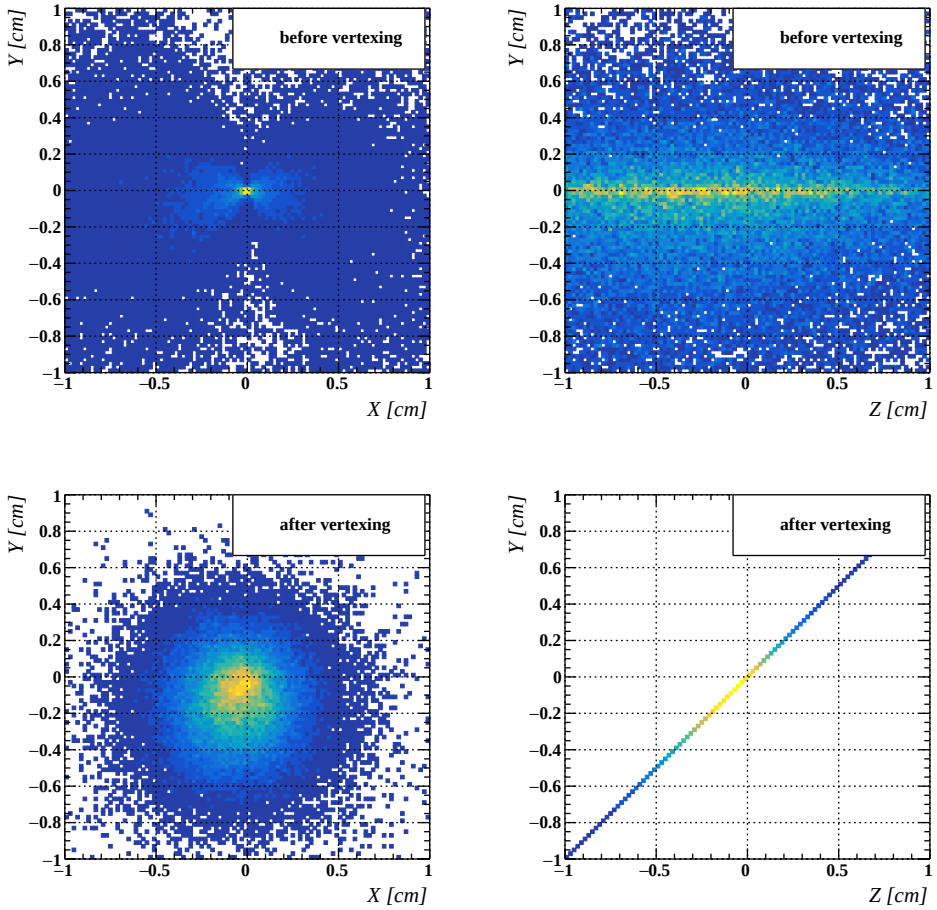

Figure 5.19: XY and ZY distributions of the IPC positron vertices before vertexing (z-axis POCA) (top) and after vertexing (on the target plane) (bottom).

in Fig. 5.20 based on a fit to the (reconstructed - simulated) distributions. Both resolutions are improved by over 20%. The IPC Angular Opening distribution, in Fig. 5.21 is improved as well, as a result of all angular variables being improved. We go from $\sigma_{1,\text{AngularOpening},IPC} = (4.9 \pm 0.1)^\circ$ to $\sigma_{1,\text{AngularOpening},IPC} = (3.7 \pm 0.1)^\circ$, a 25% improvement.

The vertexing procedure was also applied to the 16.9 MeV/c^2 X17 signal, the θ, ϕ and Angular Opening distributions being shown in Fig. 5.22 and Fig. 5.23. All angular variables improve. The X17 Angular Opening distribution is improved by 15%, going from $\sigma_{1,\text{AngularOpening},X17} = (5.0 \pm 0.1)^\circ$ to $\sigma_{1,\text{AngularOpening},X17} = (4.3 \pm 0.1)^\circ$.

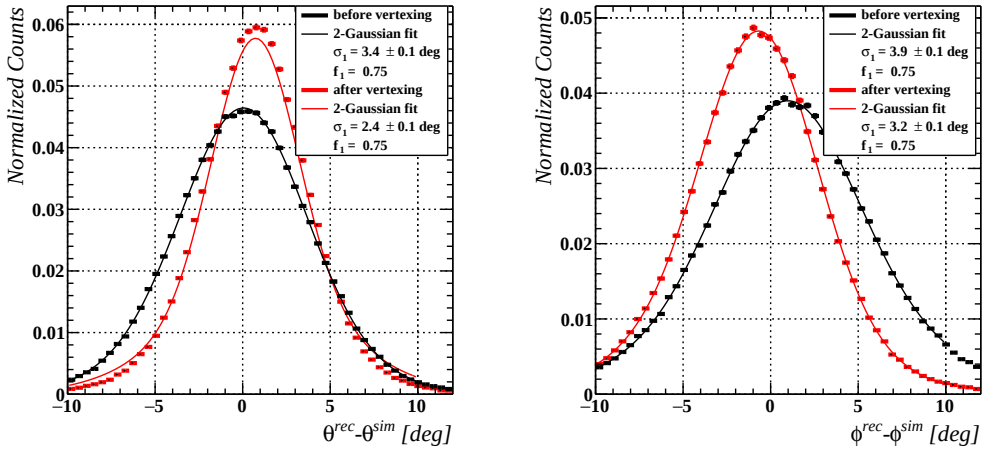

Figure 5.20: Reconstructed - simulated IPC positron tracks distributions for the polar angle θ (left) and the azimuthal angle ϕ (right) before (black) and after vertexing (red). The two-Gaussian fit of the distributions is shown as well as the width of the core Gaussian, representing 75% of the events.

Further improvement could be obtained by selecting events with a good vertexing quality (small χ^2_{red}). Moreover, the vertexing is only applied here to improve angular resolutions but it could be a priori applied to improve the momentum resolution of the tracks. Finally, the application of vertexing to a real dataset should be done with care. Indeed:

- The precise knowledge of the beamspot position and profile is crucial. An error in its estimate could bias the angular variables.
- Here the vertexing was applied to tracks generated at the beamspot. The behaviour of vertexing applied to EPC tracks, generated in the material around the target, is more complex to estimate.
- The application of vertexing to fake pairs passing the selection is also difficult to estimate precisely. The exercise is shown in Fig. 5.24. With vertexing, the fake pairs' shape is smeared out and its typical monotonous shape is lost. Instead, a peak is observed. In these conditions and due to its closeness to the signal region, it is dangerous to apply the vertexing to a dataset with fake pairs. It will not be used in the remainder of the analysis though further rejection of the fake tracks could allow the introduction of vertexing into the analysis in the future.

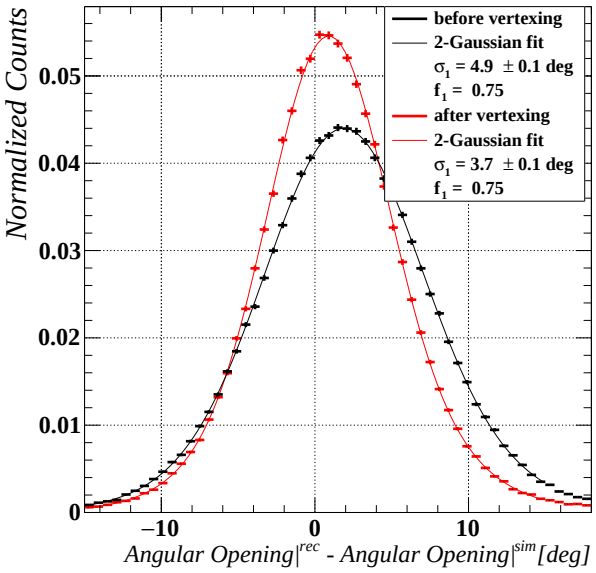

Figure 5.21: Reconstructed - simulated IPC distributions for the Angular Opening before (black) and after vertexing (red). The two-Gaussian fit of the distributions is shown as well as the width of the core Gaussian, representing 75% of the events.

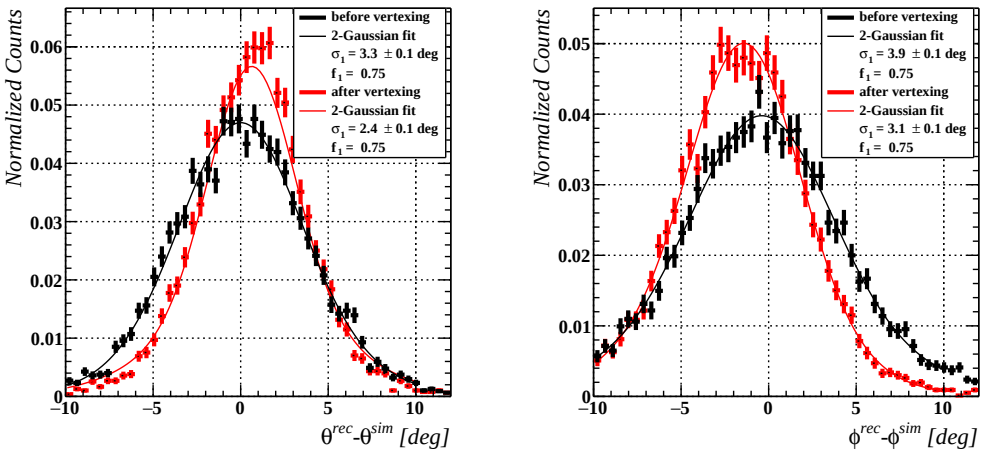

Figure 5.22: Reconstructed - simulated 16.9 MeV/c^2 X17 positron tracks distributions for the polar angle θ (left) and the azimuthal angle ϕ (right) before (black) and after vertexing (red). The two-Gaussian fit of the distributions is shown as well as the width of the core Gaussian, representing 75% of the events.

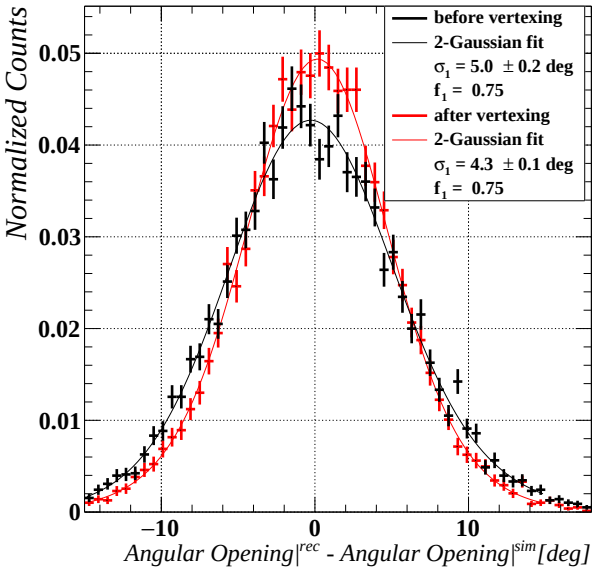

Figure 5.23: Reconstructed - simulated 16.9 MeV/c^2 X17 distributions for the Angular Opening before (black) and after vertexing (red). The two-Gaussian fit of the distributions is shown as well as the width of the core Gaussian, representing 75% of the events.

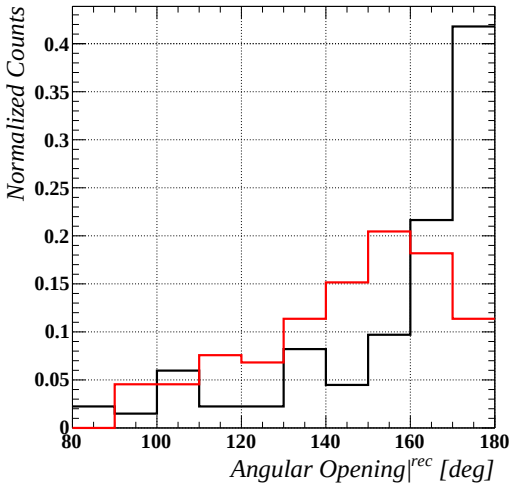

Figure 5.24: Reconstructed distribution for the Angular Opening of fake pairs before (black) and after vertexing (red).

Chapter 6

A first look at the 2023 dataset

In February 2023, a four-week data acquisition period was performed for the X17 search, collecting 75 M spectrometer-triggered events. In this chapter, we make use of the Monte-Carlo simulations introduced in Sec. 4.2 and the reconstruction procedure described in Chap. 5 in order to get a first understanding of the 2023 dataset content. After studying the main differences between data and Monte-Carlo simulations, we will investigate the resonances excited during the 2023 DAQ period. We will see that both 440 keV and 1030 keV resonances were excited due to the neglection of the H_2^+ species within the Cockcroft-Walton beam. Finally, we will present the results from a pure H^+ beam onto a thin 2 μm LiPON target, which provides the baseline for future measurements at the 1030 keV resonance.

6.1 Data and Monte Carlo comparisons

6.1.1 The 2023 dataset

The 2023 DAQ period used a 7 μm-thick LiPON23 target (see Fig. 4.15) onto a 25 μm copper substrate. It lasted for about 4 weeks, with an integrated live time of 15 days. The CW terminal voltage was set at $E_{\mathrm{p}} = 1080$ keV. The dataset will be referred to as 1080 keV dataset, though we will see that protons with various energies reached the target. The CW beam current was set at $I_{\mathrm{p}} = 10$ μA though 10% variations were observed. Fig. 6.1 presents the CW current (top) and the BGO rate divided by the CW current (bottom) over the full DAQ period. Good stability of both the accelerator and the target were observed though the slight decrease of the plotted quantity can be interpreted as some degradation of the LiPON target. The few outliers are due to CW operators' mistakes. The dataset consists of 25 000 runs with each 3000 triggered events. The reconstruction procedure from Chap. 5 was applied to the full 2023 dataset. About 500 000 electron/positron pairs were reconstructed. They are shown in Fig. 6.2 in the E_{sum} vs Angular Opening plane. The CDCH acceptance forces all reconstructed pairs to have a low

energy asymmetry: $|y| = |\frac{E_{e^-} - E_{e^+}}{E_{e^-} + E_{e^+}}| < 0.3$ and therefore all pairs have an energy asymmetry compatible with a signal pair. 11M events have at least one electron track while 4M have at least one positron track.

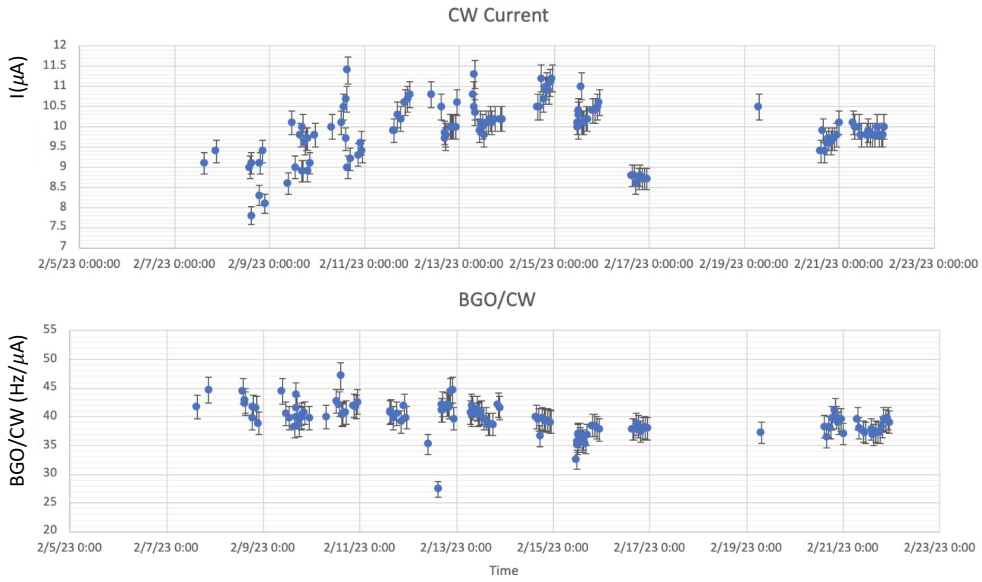

Figure 6.1: CW current (upper plot) and the ratio of BGO rate over CW current (lower plot) as a function of time during the DAQ period run.

We first study the electron/positron asymmetry. We then perform the normalization of the data based on the BGO photons. Afterwards, we put forward a pair reconstruction inefficiency in data compared to MC and finally investigate possible reasons for it.

6.1.2 Electron excess

Based on the reconstruction procedure applied to the 2023 dataset, the number of events with reconstructed electron tracks was found to be larger than the number of events with reconstructed positron tracks by a factor of 2.8. Fig. 6.3 (left) shows the momentum distribution of single positron track (from events with no electron tracks), single electron tracks (from events with no positron tracks) and pair positron and electron tracks (from events where both types of tracks were reconstructed). As positrons are uniquely produced in pair production events, single positrons and pair positrons distributions are close in shape though small discrepancies are present due to acceptance effects. It is also clear that pair positrons and pair electrons have similar distributions. However, single electrons have a momentum distribution shape largely different from the other distributions, putting

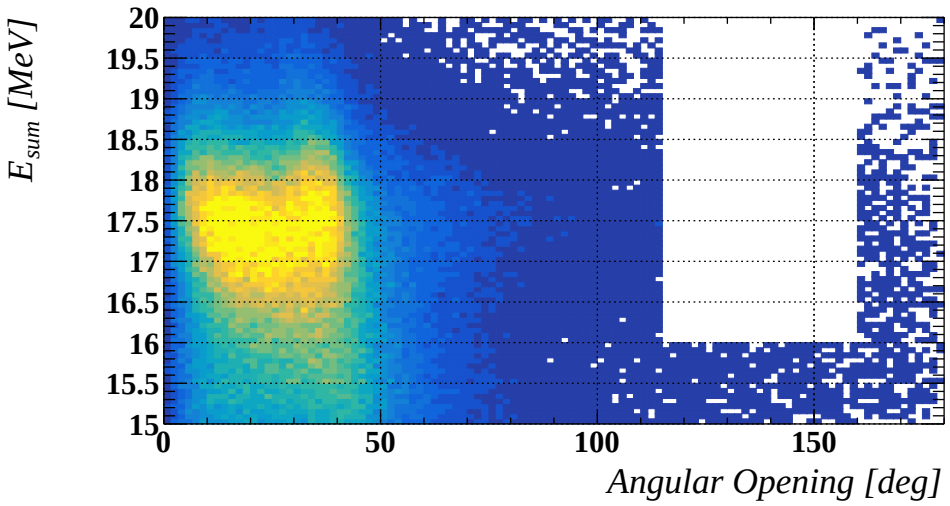

Figure 6.2: Feb 2023 dataset E_{sum} vs Angular Opening plane with blinded signal region.

forward the fact that such single electrons are in majority not produced from the pair conversion process. The reconstructed electron momentum distribution from this additional source was estimated by subtracting the pair electrons distribution from the single electrons distributions and is shown in Fig. 6.3 (right). With an average momentum of 8 MeV/c, these electrons can only be produced from a transition between nuclear states. The Compton scattering process was quantified based on photon simulations. The electrons reconstructed from this process represent at most 30% of the reconstructed pair conversion electrons and therefore cannot account for the 180% excess. Another explanation for this electron excess would be a positron reconstruction inefficiency not properly accounted for in the MC simulations. The next sections further investigate the reasons for inefficiencies in data with respect to MC.

6.1.3 Photon normalization

Fig. 6.4 gives the number of BGO-triggered photons per run and integrated as a function of the livetime. In total, 500 million photons above 9 MeV were stopped in the BGO detector which represents less than 1% of the full solid angle. The decreasing trend in the differential curve can be explained by both the decrease of the CW current and the degradation of the LiPON target. The integrated curve is used to connect the number of triggered photons with the number of reconstructed photons at different periods.

Let's write $\mathcal{N}_{\text{IPC}}/\mathcal{N}_{\text{photons}}$ the ratio between the number of IPC pairs produced

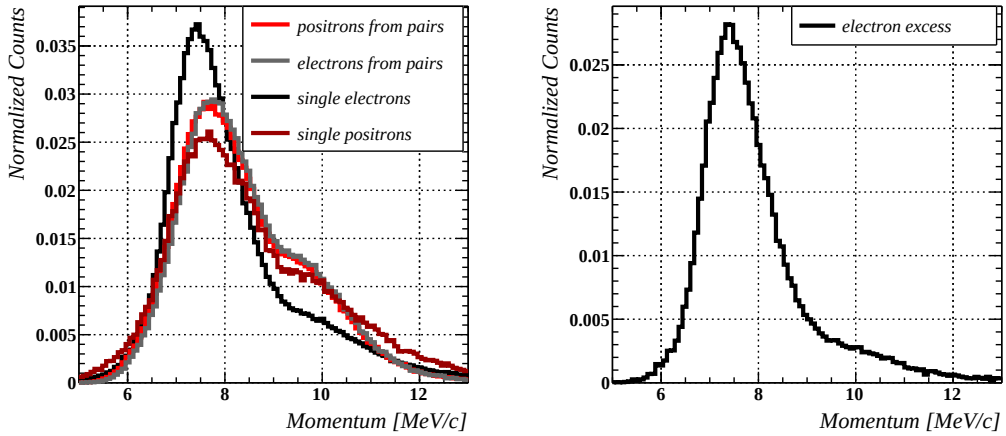

Figure 6.3: (Left) Single electrons (black), single positrons (dark red), pair electrons (gray), pair positrons (red) momentum distributions. (Right) Approximate excess electrons momentum distribution obtained by subtracting the pair electrons distribution from the single electron distribution with the appropriate normalization.

and the number of photons produced (over the full solid angle). The point of this section is to compare this ratio for both data and MC and put forward possible charged track reconstruction inefficiency. $\mathcal{N}_{\text{IPC}}$ is computed as $\mathcal{N}_{\text{IPC}} = \frac{\mathcal{N}_{\text{IPC,rec}}}{\epsilon_{\text{IPC,rec}}}$ with $\mathcal{N}_{\text{IPC,rec}}$ the number of reconstructed IPC pairs and $\epsilon_{IPC,rec}$ the reconstruction efficiency of IPC based on MC. $\mathcal{N}_{\text{photons}}$ for both the 18 MeV transition and 15 MeV transition will be expressed as $\mathcal{N}_{\text{photons,18}}$ and $\mathcal{N}_{\text{photons,15}}$.

$$\begin{aligned}\mathcal{N}_{\text{photons},j} &= \mathcal{N}_{\text{photons,BGOrec},j}\frac{1}{\epsilon_{\text{BGOrec},j}} \\ &= \mathcal{N}_{\text{photons,BGOrec},j}\frac{\mathcal{N}_{\text{photons,MC},j}}{\mathcal{N}_{\text{photons,BGOrec,MC},j}} \\ &= \mathcal{N}_{\text{photons,BGOrec},j}\frac{\mathcal{N}_{\text{photons,restricted,MC},j}}{\mathcal{N}_{\text{photons,BGOrec,MC},j}A_{\text{restricted}}}\end{aligned} \tag{6.1}$$

$\epsilon_{\text{BGOrec},j}$ refers to the reconstruction efficiency of the BGO for line j, $\mathcal{N}_{\text{photons,BGOrec}}$ to the numbers of photons reconstructed in the BGO. The MC index indicates Monte-Carlo simulations and restricted alludes to the restricted photon production solid angle in which the simulations were performed. $A_{\text{restricted}}$ represents the fraction of solid angle covered by the simulation range and is equal to $(1.7 \pm 0.1)\%$. $\mathcal{N}_{\text{photons,BGOrec}}$ are obtained from a two-Gaussian fit to the MC

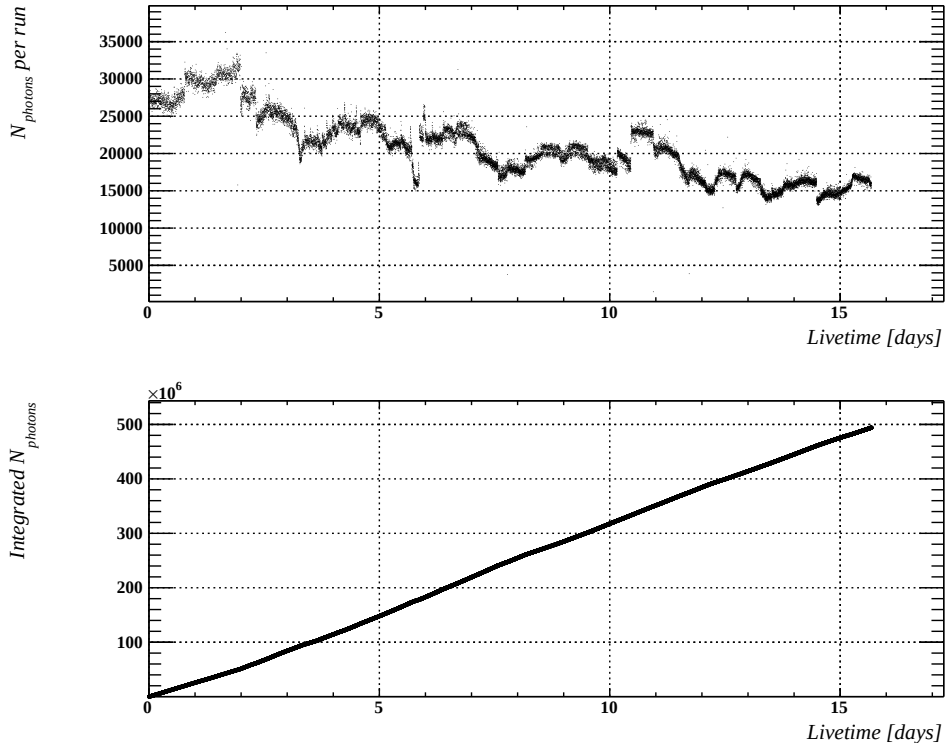

Figure 6.4: Number of BGO-triggered photons per run (top) and integrated (bottom) as a function of livetime.

and data distributions. All the numbers were extracted from BGO/photons simulations and are reported in Tab. 6.1. It was estimated that the total number of photons produced during the 2023 DAQ period is $(51 \pm 4) \times 10^9$ and $(37 \pm 3) \times 10^9$ for the transitions to first excited and ground state respectively.

Tab. 6.2 then compares $\mathcal{N}_{\text{photons}}$ to $\mathcal{N}_{\text{IPC}}$. The latter is obtained based on the charged particles analysis of the 2023 dataset performed in Chapter. 7. We obtain an IPC/photon ratio which can be compared to the theoretical branching ratio extracted from [7]. The inconsistency between the measured and theoretical ratios points at a factor 2.6 inefficiency of the pair reconstruction in data with respect to MC. The source of inefficiency is investigated in the next subsection.

6.1.4 Track reconstruction inefficiency

One source of track reconstruction inconsistency between data and MC can be the noise and signal hits rate within the CDCH. In Fig. 6.5, comparing the CDCH hit time distributions in data and MC gives access to the noise/signal rate ratio.

	BGO MC	Full 2023 DAQ
$\mathcal{N}_{\text{photons,BGOrec}}$	15 MeV: (10.7 ± 0.4) k 18 MeV: (10.5 ± 0.4) k	15 MeV: (59 ± 2) M 18 MeV: (42 ± 1) M
$\mathcal{N}_{\text{photons,restricted}}$ (generated in restricted range)	15 MeV: 158 k 18 MeV: 158 k	/
$\mathcal{N}_{\text{photons}}$ (generated on 4π)	15 MeV: (9.3 ± 0.5) M 18 MeV: (9.3 ± 0.5) M	15 MeV: (51 ± 4) G 18 MeV: (37 ± 3) G

Table 6.1: Number of photons reconstructed in the BGO, number of photons simulated in an arbitrary restricted range and number of photons generated on the full solid angle from a dedicated BGO simulation and from the 2023 DAQ period. Directly measured numbers are in green while extrapolated ones are in red.

	18 MeV	15 MeV
$\mathcal{N}_{\text{IPC}}$	(45 ± 9) M	(73 ± 15) M
$\mathcal{N}_{\text{photons}}$	(37 ± 3) G	(51 ± 4) G
Measured IPC/photon ratio	$(1.2 \pm 0.3) \times 10^{-3}$	$(1.4 \pm 0.3) \times 10^{-3}$
Theoretical IPC/photon BR from [7]	$(3.1 \pm 0.2) \times 10^{-3}$	/

Table 6.2: Number of IPC and photons from each line produced during the 2023 DAQ period. The ratio of both quantity and the theoretical branching ratio from [7] are also quoted.

Indeed, noise hits have a flat time distribution while signal hits have a triangular time distribution. The figure shows similar noise/signal area for data and MC, meaning noise rates and hit reconstruction efficiency are not responsible for the observed inconsistency.

Another observable of interest is the number of fitted hits per track or *ngoodhits*. Fig. 6.6 gives its distribution for data tracks and IPC18 MC, IPC15 MC, EPC18 MC and EPC15 MC tracks. These distributions largely depend on the momentum of the tracked particle as higher momentum particles are less likely to form tracks with more than half a turn ($\approx$ 12 hits). IPC15 MC therefore has a larger proportion of full turn tracks ($\approx$ 30 hits) than IPC18 MC for example. However, the common point between all MC distributions is the peak number of hits for half-turn and full-turn tracks, respectively at 12 and 26 good hits. For data, however, the distribution has fewer good hits per track, with peaks at 9 and 22 good hits. No combination of MC species can explain it. Therefore, despite the data/MC consistency of the CDCH gas gain, noise rate and shape and hit

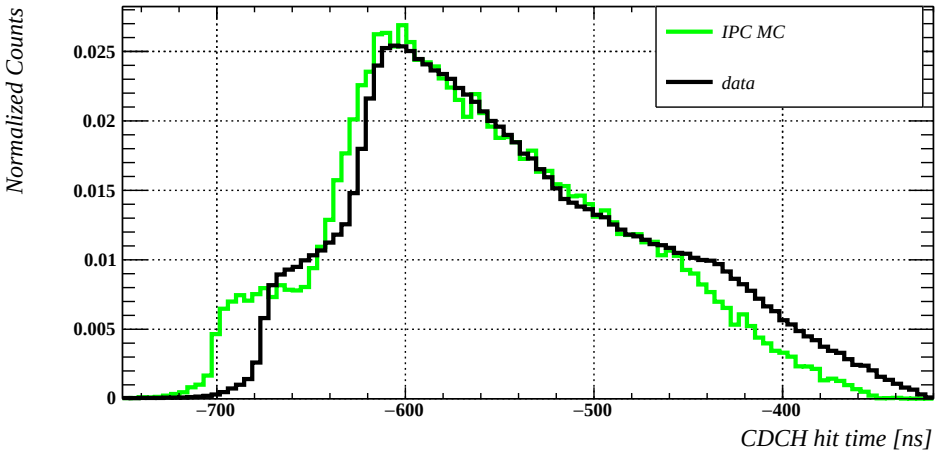

Figure 6.5: CDCH hit time distribution for both data (black) and IPC MC (green).

efficiency, the CDCH track in data has a lower quality on average than in MC.

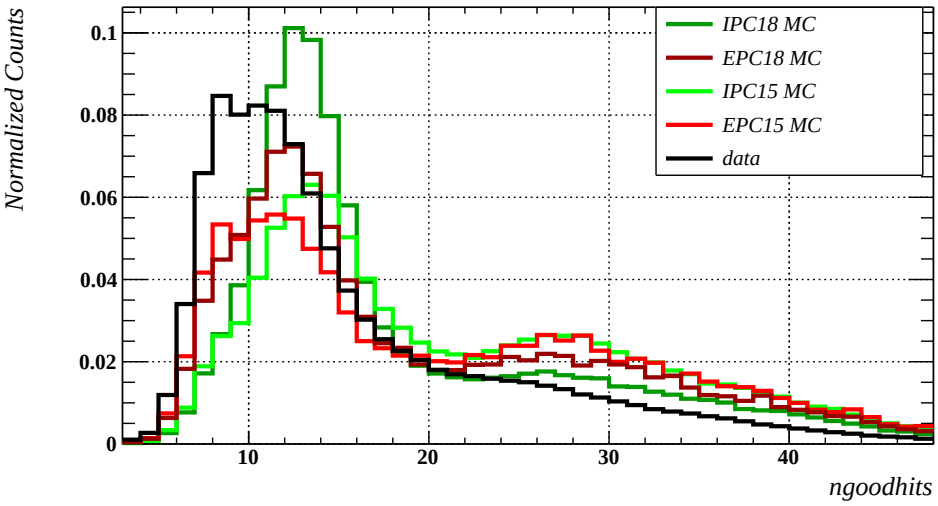

Figure 6.6: *ngoodhits* distribution for IPC18 MC, EPC18 MC, IPC15 MC, EPC15 MC and data, without the stringent track selection described in Chap. 5.

Tab. 6.3 compares the quality of the IPC18 MC, EPC18 MC and data tracks based on several observables regarding the fraction of events:

- with at least 1 track candidate

- with at least 1 track successfully propagated to the z-axis POCA
- with at least 1 track successfully propagated to the z-axis POCA and with $ngoodhits \geq 10$
- with at least 1 track successfully propagated to the z-axis POCA, with $ngoodhits \geq 10$ and with $|z_{vertex}| = |\text{POCA z}| \leq 7$ cm

The two first observables are in line in MC and data within 10%. When the *ngoodhits* selection is added, a larger (15%) discrepancy is observed which can be understood due to the lower number of good hits in data and therefore to a larger fraction of data tracks which doesn't pass the selection. Because the same track selection is applied in MC and data, the difference in number of good hits per track explains part of the inefficiency in data. Moreover, a substantial difference, close to 40%, occurs when requesting tracks to have $|z_{vertex}| \leq 7$ cm. z_{vertex} is the z-coordinate of the z-axis POCA of the track, it is used as our best estimate of its z-origin (see Chap. 5). It means that, on top of their lower number of good hits, data tracks have significantly worse quality than in MC, leading to a large fraction of them being propagated far from their original beam spot. Because the selection requires track with $|z_{vertex}| \leq 2.5$ cm, many tracks from data, more than in MC, are rejected. The single track inefficiency in data gets squared when it comes to a pair of tracks, overall leading to a factor 2.6 ratio of efficiency between data and MC. The spectrometer simulation is currently being assessed to better understand the differences between data and MC tracks.

wrt to #triggered events	**% track candidate**	**% to z-POCA**	**% to z-POCA + ngoodhits** ≥ 10	**% to z-POCA + ngoodhits** ≥ 10 **+** $\lvert z_{vertex} \rvert \leq 7$ cm
IPC18 MC	99%	98%	82%	71%
EPC18 MC	99%	94%	89%	77%
data	93%	84%	73%	48%

Table 6.3: Fraction of events wrt. trigger with at least one track passing the selections mentioned in the table and described in the text.

6.2 2023: evidence for the domination of the 440 keV resonance

After having put forward significant pair reconstruction inefficiency in data with respect to MC, we can have a further look at the dataset by normalizing both MC

and data distributions in order to correct for the inefficiency. In this section, we try and understand which resonances were excited during the 2023 DAQ period, which will set the baseline for the fitting model presented in Chap. 7. We will see that the dataset is dominated at 80% by the 440 keV resonance and its 17.6 MeV associated state while the remaining contribution comes from the 1030 keV resonance and its 18.1 MeV associated state.

6.2.1 Photon spectra from BGO calorimeter

First of all, BGO photon data at $E_{\mathrm{p}} = 500\ keV$ and $E_{\mathrm{p}} = 1080\ keV$ were acquired during the 2023 X17 DAQ period. The dataset were taken back-to-back in time in order to neglect PMT gain variations. The spectra after calibration (see Sec. 4.1.5) are shown in Fig. 6.7 (top) along with a two-Gaussian fit to model both the transition to ground state and to first excited state. In the case of a pure proton beam, one would expect to see a 500 keV shift between the two fitted 18 MeV lines. However, here, the two Gaussian fit yields a O(100 keV) shift between the two lines pointing at a domination of the 440 keV resonance in the 1080 keV dataset. The ratio between the amplitudes between the 15 MeV and the 18 MeV lines is also expected to be larger by a factor of 2 at the 1030 keV resonance than at the 440 keV resonance. The similar 15/18 ratios observed in these spectra are also in line with the 440 keV domination.

A preliminary estimate of the 18.1 MeV proportion within the 1080 keV dataset can be obtained through a three-Gaussian fit assuming that the dataset is equivalent to the 500 keV dataset plus a contribution from the 18.1 MeV line. The 17.6 MeV Gaussian mean and width are fixed from the 500 keV data fit. The 15 MeV Gaussian can fit both 14.6 MeV and 15.1 MeV lines simultaneously due to their large natural width. Its parameters remain free. The 18.1 MeV line mean is fixed and its width is taken identical to the 17.6 MeV line's. All amplitudes are free and fitted to extract the 17.6 and 18.1 lines' relative proportions as shown in Fig. 6.7 (bottom). The best-fit results in a $\approx 10\%$ proportion of the 18.1 MeV line, confirming the 17.6 MeV line domination.

6.2.2 E_{sum} spectra

A similar analysis can be performed by making use of the $E_{sum} = E_+ + E_-$ instead of the photon spectrum. Indeed, the sum of the electron and positron energies should reproduce the excited states' transitions. To do so, it is crucial to calibrate precisely the energy scale of the reconstructed tracks, to account for uncertainties in the exact value magnetic field (BField) scaling ($\approx 15\%$ of MEG-II nominal scaling). A small sample of CDCH+pTC data at $E_{\mathrm{p}} = 500$ keV was acquired where only the 17.6 MeV line is present. The e^+e^- pairs were reconstructed and the

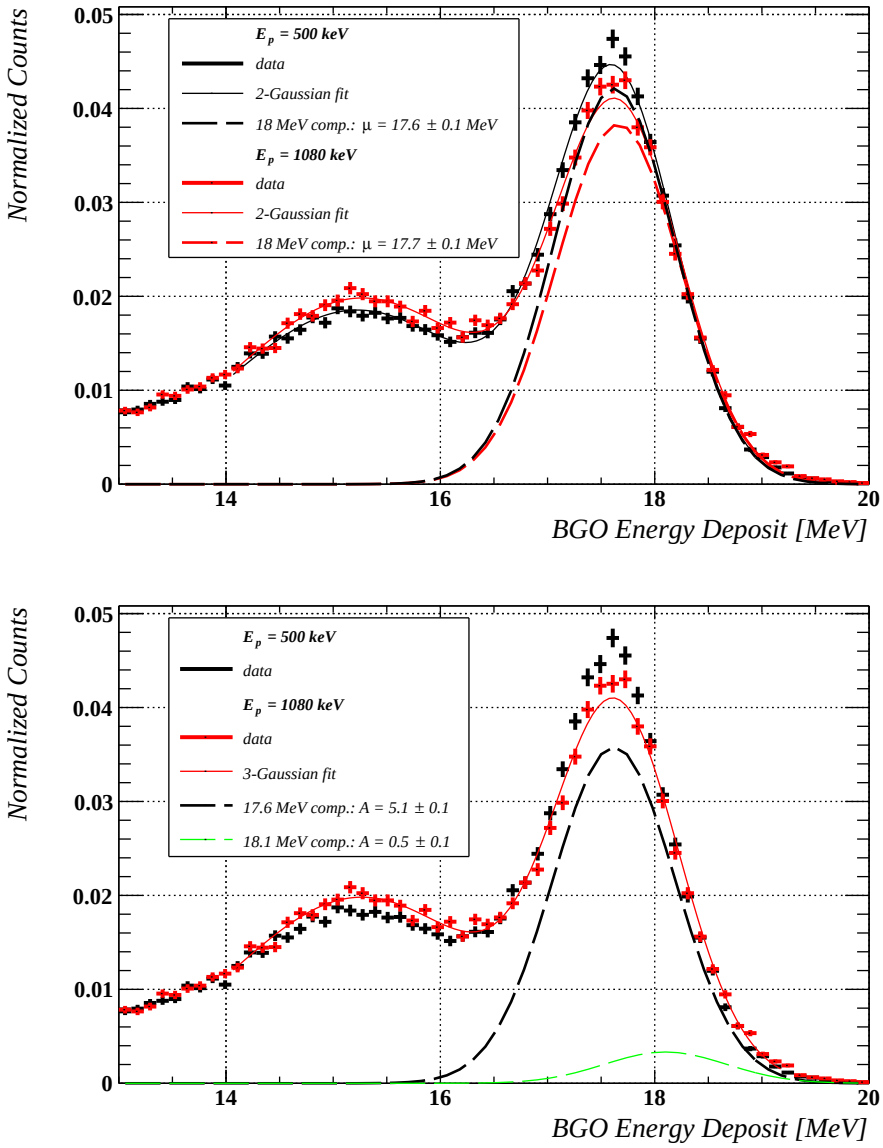

Figure 6.7: BGO energy deposit distribution from two datasets with $E_{\mathrm{p}} = 1080$ keV (red) and $E_{\mathrm{p}} = 500$ keV (black). (Top) The two-Gaussian fit, the "18 MeV" component (transition to ground state) and its mean μ for each distribution are displayed as a full and a dashed line respectively. (Bottom) The three-Gaussian fit, the 17.6 MeV and the 18.1 MeV components are displayed as a red full, a black dashed and a green dashed line respectively. The amplitude of each of the two components is quoted in arbitrary units.

Angular Opening and raw E_{sum} were computed. Such a dataset, at angular openings below 115°, should consist of four backgrounds, IPC17.6, IPC14.6, EPC17.6 and EPC14.6 to account for both processes and both transitions. The raw E_{sum} spectrum from data is corrected, after reconstruction, by applying a factor BField scaling/0.150, 0.150 being the BField scaling applied in MC. A simultaneous fit of E_{sum} and Angular Opening was performed varying the BField scaling value applied to data in a range between 0.150 and 0.155. The best fit was found for a BField scaling of 0.1537 ± 0.002 and is shown in Fig. 6.8. Data and MC agree well both in E_{sum} and Angular Opening. Moreover, the IPC/EPC mix explains well the two-peak structure and the subsequent steepness observed in the Angular Opening distribution.

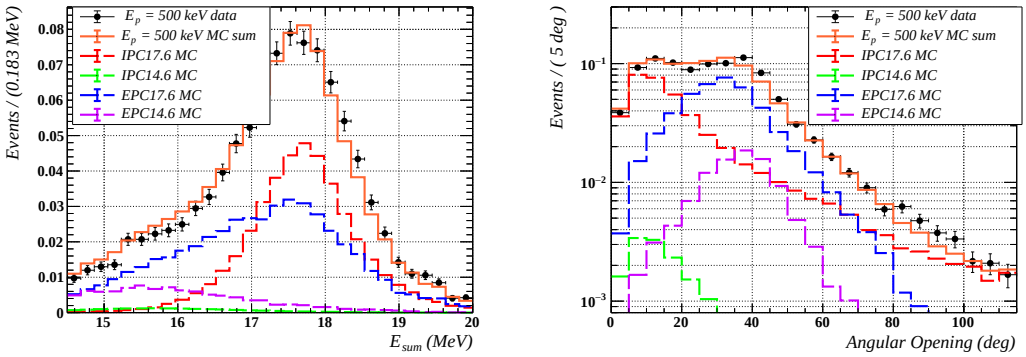

Figure 6.8: 500 keV data E_{sum} (left) and Angular Opening (right) distributions fitted with a sum of IPC18 MC (red), IPC15 MC (green), EPC18 MC (blue) and EPC15 MC (purple). The MC sum is shown in orange. The data is fitted for $\theta_\gamma \geq 100°$ and the BField scaling applied to data is 0.1537.

Fig. 6.9 gives the obtained χ^2 as a function of the BField scaling applied as a correction to data. The best fit is obtained at 0.1537 and yields a $\chi^2/dof = 1.2$.

E_{sum} from data is corrected by this factor in the remainder of the thesis. The same energy scale correction factor was applied to the 1080 keV data presented in Fig. 6.10. It is compared to the 500 keV MC distribution expected if the beam for the 2023 DAQ period had been set at $E_{\mathrm{p}} = 500$ keV. Simulations have shown that large differences in 18/15 ratio can occur when the beamspot position varies, explaining the difference between the MC E_{sum} spectrum in Fig. 6.8 and Fig. 6.10. Nonetheless, it is clear from the latter figure that there is no significant shift between the two distributions, though a 500 keV shift would be expected if the 1030 keV resonance only had been excited. Again, it points at a domination of the 440 keV resonance in the $E_{\mathrm{p}} = 1080$ keV data.

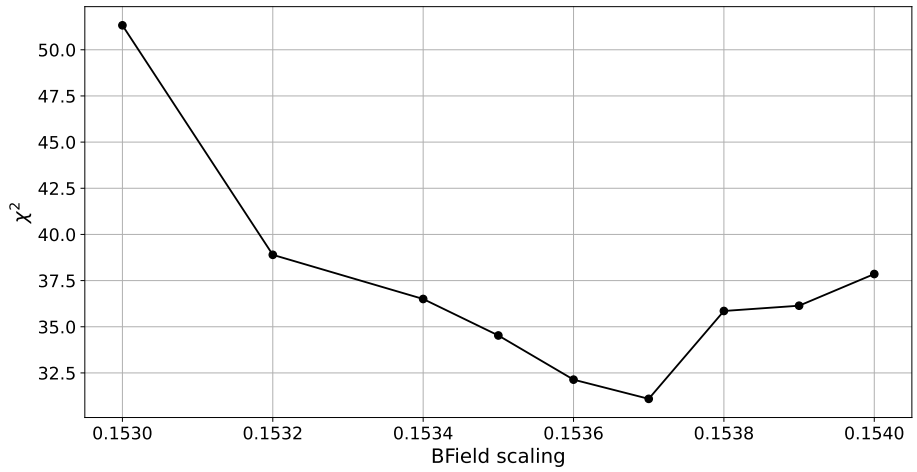

Figure 6.9: 500 keV data 2D fit χ^2 as a function of the magnetic field (BField) scaling.

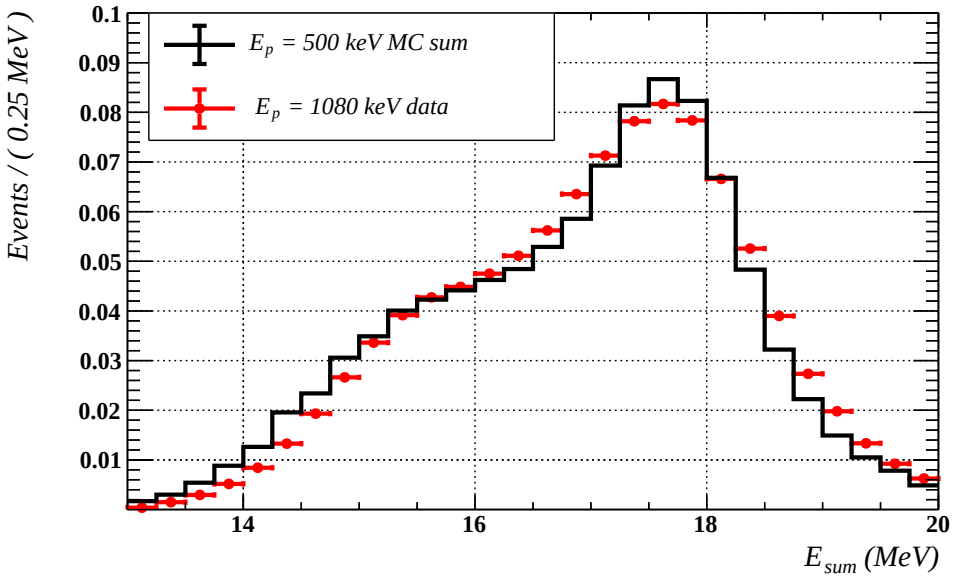

Figure 6.10: E_{sum} distribution from $E_p = 1080$ keV 2023 dataset (red) compared to an expected $E_p = 500$ keV MC simulation (black).

6.2.3 Angular Opening spectra

In Sec. 4.2.2, we compared the shapes of IPC angular opening distributions at 440 keV (17.6 MeV line) and 1030 keV (18.1 MeV line). The resonant M1 contribution is steeper than the non-resonant E1 component. The E1-enriched 18.1 MeV line therefore yields a flatter IPC shape than the M1-dominated 17.6 MeV line. One can compare the Angular Opening spectra from the $E_{\mathrm{p}} = 500$ keV and the $E_{\mathrm{p}} = 1080$ keV datasets in Fig. 6.11. Though in agreement up to 115°, the 1080 keV dataset is flatter at larger angles. It supports the presence of a minority proportion of the 18.1 MeV line within the 1080 keV dataset.

On the same figure, the 500 keV dataset is fitted by the sum of an EPC MC and IPC17.6 MC. The agreement, up to 160°, is good. This fit represents an excellent probe of the Zhang-Miller IPC model onto a dataset: it can be considered a reliable model in the upcoming analysis.

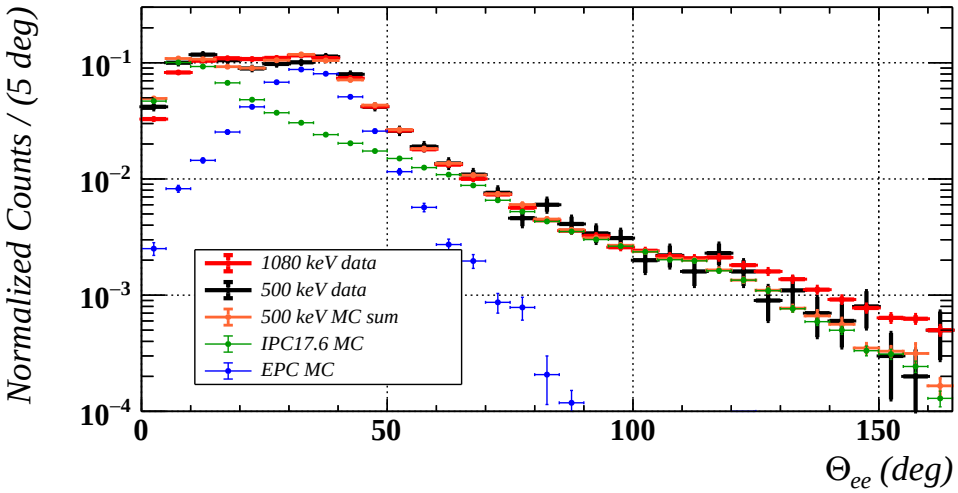

Figure 6.11: Angular opening distribution from $E_{\mathrm{p}} = 1080$ keV 2023 dataset (red) and from a small $E_{\mathrm{p}} = 500$ keV dataset (black) for 16 MeV $\leq \mathrm{E}_{sum} \leq$ 20 MeV. The 500 keV data are fitted with a 500 keV MC sum (orange) of EPC MC (blue) and IPC17.6 (brown).

Given the IPC17.6 MC and IPC18.1 MC shapes, one can fit the Angular Opening distribution from the 1080 keV dataset. The fit is performed at angles above 80° in order to neglect the EPC contributions. As displayed in Fig. 6.12, the data are in good agreement with the sum of the two IPCs. IPC18.1 becomes the dominant IPC above 120°. Based on this fit, the proportion of the 18.1 MeV line can be extrapolated to the full range. It was found to be $\approx 20\%$.

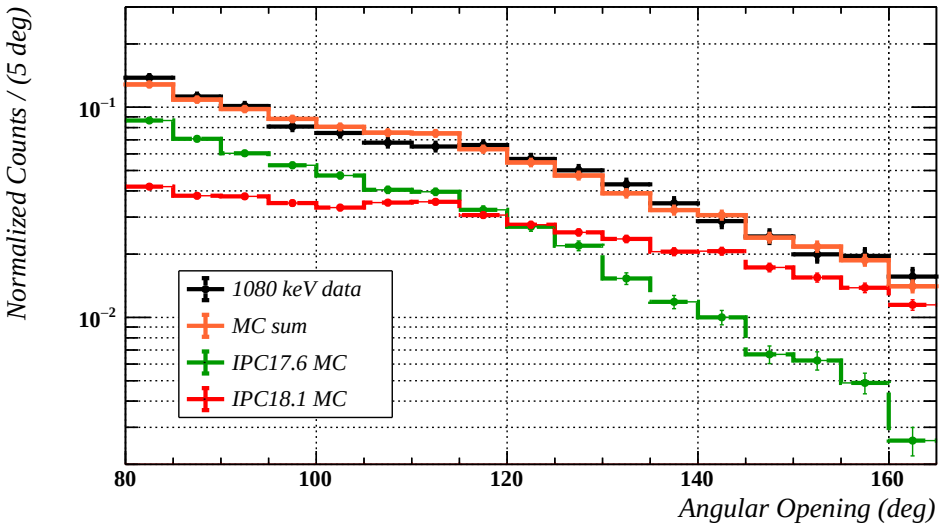

Figure 6.12: Angular opening distribution from $E_p = 1080$ keV 2023 dataset (black) fitted with an MC sum (orange) composed of both IPC17.6 (brown) and IPC18.1 (red).

The exact proportion of this line will be extracted from the maximum likelihood fit described in Sec. 7.6.

6.2.4 Both H^+ and H_2^+ on target

The presence of both 440 keV and 1030 keV resonances and the domination of the former within the $E_p = 1080$ keV dataset can be understood through the following paragraph. In 2023, the H^+ and H_2^+ species were not properly separated and the beam getting to the LiPON target therefore contained both species. Due to their identical charge, both H^+ and H_2^+ were accelerated to the same kinetic energy but the twice larger mass of H_2^+ means that each proton in H_2^+ carries half of the total kinetic energy:

$$E_{\text{p in } H_2^+} = \frac{1}{2} E_{\text{p in } H^+} \tag{6.2}$$

Based on a 75%/25% H^+/H_2^+ proportion within the beam, it means the beam contains 60% of protons with $E_p = 1080$ keV and 40% of protons with $E_p = 540$ keV. With an estimated 7 μm average target thickness, the 540 keV protons then trigger the 440 keV resonance. Assuming from the Zhang-Miller model a 10 times higher cross-section integral at 440 keV than at 1030 keV, it results that $\approx 15\%$ of the protons trigger the 1030 keV resonance, in line with BGO photon

and Angular Opening results.

6.3 2024: a pure H^+ dataset in the BGO calorimeter

In 2024, through the protocol described in Sec. 4.1.1, a pure H^+ beam was obtained. A better quality LiPON target with uniform 1.9 μm thickness (see Fig. 4.16) was used to test the beam and study the photon emission.

6.3.1 E_p scan and BGO rate

The BGO trigger rate was measured by making use of a pure proton beam impinging on a 1.9 μm-thick LiPON target. The rate was measured at varying kinetic energies of the proton beam. A cosmic-ray rate of 20 Hz was obtained with the beam off. The cosmic-subtracted BGO trigger rate is plotted in Fig. 6.13 (left) as a function of the proton energy. Error bars account for CW current instabilities. The theoretical ^{7}Li(p,γ)^{8}Be cross-section, computed from [7], is shown in Fig. 6.13 (right). The target thickness corresponds to a 200 keV proton energy loss. Going from 400 keV to 500 keV, the BGO rate increases by a factor of 20 as expected from exciting the 440 keV resonance. At 600 keV, the rate is comparable to 500 keV as the proton energy loss leads to exciting the 440 keV resonance in both cases. At 700 keV and 800 keV, the rate decreases as we are getting further away from the resonance and enter the non-resonant or direct proton capture region. At 900 keV and 1000 keV, we approach the weak 1030 keV resonance leading to a slight increase of the rate. The behaviour is perfectly explained by the theoretical cross-section and evidences the absence of H_2^+ within the beam.

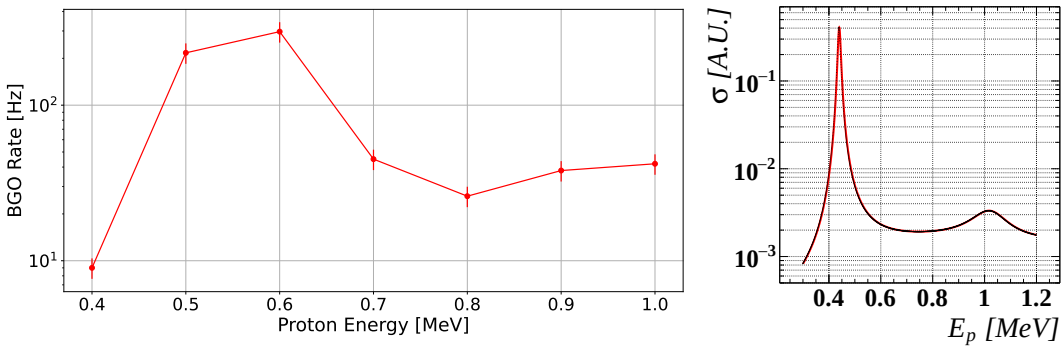

Figure 6.13: (Left) BGO cosmic-subtracted trigger rate (Hz) vs proton energy E_p (keV) using a 1.9 μm-thick LiPON24 target. (Right) Theoretical ^{7}Li(p,γ)^{8}Be cross-section as a function of the proton energy, computed from [7].

6.3.2 BGO spectra

A small dataset was taken with the BGO at each of the aforementioned proton energies. Fig. 6.14 presents the calibrated BGO spectra fitted with 2-Gaussian fit to account for the transitions to ground state and first excited state. First, the 500 keV and 600 keV spectra are very similar as they are both dominated by the 440 keV resonance and have the same mean, $\mu_{500} = (17.64 \pm 0.01)$ MeV and $\mu_{600} = (17.65 \pm 0.01)$ MeV. Then, increasing the proton energy, we see two effects: the 15/18 amplitude ratio increases and both lines shift towards higher energy. Both outcomes are expected from the literature. The probability of the transition to the ground state is lower when the energy increases and the additional proton energy is transferred to the emitted photon. For an infinitesimally thin target and a flat cross-section curve, a 100 keV increase in proton energy yields an 88 keV increase in photon energy due to the small $^8Be^*$ boost. The exact computation is more convoluted but one can expect such an order of magnitude at proton energies far from the intense 440 keV resonance. From 600 keV to 1000 keV in steps of 100 keV of proton energy, the observed "18 MeV line" shift is 70, 90, 90 and 100 keV. At $E_p = 1000$ keV and considering an average energy loss of 200 keV, the average interacting proton energy is close to 900 keV. At this energy, the average photon energy should be 18.04 MeV close to the fitted mean $\mu_{1000} = (18.00 \pm 0.01)$ MeV. The small discrepancy may arise from the simplified energy loss model or some slight BGO PMTs gain drift, neglected here.

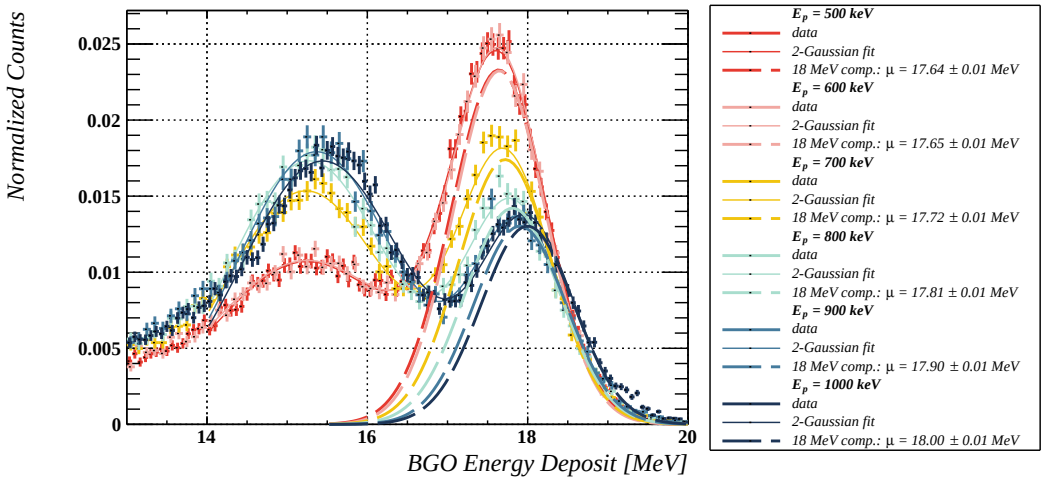

Figure 6.14: BGO energy deposit distribution from datasets with proton energy $E_p = 500$, 600, 700, 800, 900, 1000 keV. The two-Gaussian fit, the 18 MeV component and its mean for each distribution are displayed as a full and a dashed line respectively.

Altogether, these spectra evidence the quality of the proton beam, the absence of H_2^+ in it, the control of the target thickness and the readiness for future measurements focused on the 1030 keV resonance.

Chapter 7

The X17 search in the 2023 dataset

In this chapter, we present and perform the X17 search within the 2023 dataset previously introduced. We first estimate the significance of a potential X17 excess in our dataset based on Atomki's results from both ^{8}Be*(18.1) and ^{8}Be*(17.6) de-excitations. After extracting the beamspot position with O(mm) precision and studying some sources of systematic errors, we introduce the analysis strategy, relying on a blinded signal region. We then detail a weighting analysis procedure which accounts for the presence of H_2^+ within the beam and proton energy loss within the target thickness. Afterwards, a two-dimensional E_{sum} vs Angular Opening maximum likelihood fit is performed, resulting in no significant signal excess. The 1D projections of this fit in Angular Opening, Energy Sum, and Invariant Mass are then displayed: they all show a good agreement between data and Monte Carlo background in the signal region. Finally, 90% C.L. exclusion limits are set on the X17 particle based on its mass and branching ratio with respect to photon emission from both ^{8}Be*(18.1) and ^{8}Be*(17.6) de-excitations. The compatibility between our best fit and Atomki's X17 hypothesis is finally tested.

7.1 X17 production

An estimate of the significance of an X17 excess within the 2023 dataset was preliminarily performed. As evidenced in Sec. 6.2, this dataset includes e^+e^- pairs from both ^{8}Be*(17.6) and ^{8}Be*(18.1) resonances. Atomki [1] has provided strong claims for the ^{8}Be*(18.1) X17 production but controversial results from the ^{8}Be*(17.6) were also reported. Moreover, Feng [4] has highlighted the possibility of an X17 production from the ^{8}Be*(17.6) state. Though dynamically allowed, the X17 production from this resonance is kinematically suppressed by a factor of 2.2, the particle mass being close to the 17.6 MeV available energy. The X17 search will be simultaneously performed on both resonances.

The number of X17 expected from each resonance can be computed from the

number of IPC pairs in our dataset and from the X17 branching ratio with respect to IPC. The latter are written $R_{\mathrm{X17/IPC,18.1},Atomki}$ and $R_{\mathrm{X17/IPC,17.6},Feng}$. They are calculated from $R_{\mathrm{X17}/\gamma,18.1,Atomki}$ based on Atomki [1],$R_{\mathrm{X17}/\gamma,17.6,Feng}$ based on Atomki+Feng [4], $R_{\mathrm{IPC}/\gamma,18.1,Rose}$ based on Rose [10] and $R_{\mathrm{IPC}/\gamma,17.6,Rose}$ based on Rose+Zhang-Miller [7]. $R_{\mathrm{A/B},Q,name}$ represents the ratio of branching ratios of A and B processes for the reaction with Q-value Q computed first by *name*. The number of IPC generated and reconstructed during the DAQ period, $\mathcal{N}_{\mathrm{IPC}}$ and $\mathcal{N}_{\mathrm{IPC,rec}}$ respectively, are obtained from the best fit from Sec. 7.6 and the MC-based data-corrected efficiencies. All the numerical values are given in Tab. 7.1 and lead to an estimate of (114 ± 23) X17 events from ^{8}Be*(18.1) and (293 ± 60) X17 events from ^{8}Be*(17.6). Neglecting the various uncertainties, a preliminary $\frac{S}{\sqrt{S+B}}$ excess significance estimate leads to 2.2σ and 5.4σ respectively. This results from an estimate of the IPC background in an Angular Opening signal region window between 115° and 160°.

7.2 Beam spot position estimate

A beam spot position estimate from Feb2023 dataset with mm precision is required to perform the track selection and to generate accurate MC simulations. Fig. 7.1 displays the distributions of reconstructed vertices at the target plane for positrons and electrons from pairs in data, focusing on tracks that propagate back to the target plane. The vertices are offset from the center by about 7 mm, with the positron and electron distributions x-shifted relatively to one another. In MC, both electron and positron IPC vertices are accurately reconstructed (within 1 mm of the generated position), while EPC vertices exhibit such electron/positron x-offset and a systematic shift toward negative y with respect to the simulated beam spot. EPC pairs are not produced in the target plane but rather in the surrounding material, mostly in the 3-cm radius heat-dissipating copper ring. EPC tracks propagated back to the target plane result in a systematic x-shift between the electron and positron vertices. A y-shift can be explained by considering the trigger selection. Due to the 45° copper ring tilt and the negative y-position of the pTC, most EPC-triggered events correspond to conversions in the negative y region of the copper ring, leading to an observed systematic 5 mm negative y-shift of the reconstructed vertices compared to the true beam spot position.

The beam spot position in the data was determined using the following:

- **x-coordinate**: This was obtained from an IPC-enriched subsample of the data by selecting events with low opening angles. Indeed, simulations indicated that IPC events peak around 10°, whereas EPC events are more prominent at larger angles, closer to 40°. The average between the x-coordinates

	Atomki results + Theory
$R_{\mathrm{X17}/\gamma,18.1,Atomki}$	$(1.5 \pm 0.3) \times 10^{-3}$
$R_{\mathrm{X17}/\gamma,17.6,Feng}$	$(7.9 \pm 1.4) \times 10^{-4}$
	Feb2023 1080 keV dataset
$\mathcal{N}_{\mathrm{IPC,rec}}$	18.1 MeV: (28 ± 3) k 17.6 MeV: (100 ± 11) k
$\mathcal{N}_{\mathrm{IPC}}$ (generated on 4π)	18.1 MeV: (25 ± 5) M 17.6 MeV: (94 ± 20) M
Expected $\mathcal{N}_{\mathrm{X17}}$ (generated on 4π)	18.1 MeV: (39 ± 8) k 17.6 MeV: (74 ± 15) k
Expected $\mathcal{N}_{\mathrm{X17,rec}}$	18.1 MeV: 114 ± 23 17.6 MeV: 293 ± 60
X17 significance estimate $\frac{S}{\sqrt{S+B}}$	18.1 MeV: 2.2 σ 17.6 MeV: 5.4 σ

Table 7.1: (Top) For both 18.1 MeV and 17.6 MeV lines, X17 branching ratio wrt. to IPC production based on Atomki results and Rose [10], Zhang-Miller [7] and Feng [4]. (Bottom) For both 18.1 MeV and 17.6 MeV lines, estimated number of IPC generated on the full solid angle ($\mathcal{N}_{\mathrm{IPC}}$) and reconstructed during the Feb2023 DAQ period ($\mathcal{N}_{\mathrm{IPC,rec}}$). The corresponding numbers for the X17 production are also given as $\mathcal{N}_{\mathrm{X17}}$ and $\mathcal{N}_{\mathrm{X17,rec}}$ along with a simplified $\frac{S}{\sqrt{S+B}}$ significance estimate in case of observation. The background is estimated in a [115°,160°] Angular Opening window where the X17 signal is expected. The table uses MC-based data-corrected efficiencies in order to account for the inefficiency observed in data with respect to MC (see Sec. 6.1.4).

of the electron and positron reconstructed vertices from this subsample was taken to be the proton beam spot best estimate: $x_{beam} = (-2 \pm 1)$ mm

- **y-coordinate**: This was determined by fitting the data y-distribution to an EPC MC/IPC MC mix. The MC beam spot was assumed to be Gaussian and was generated at (x,y)=(0,0). 60%/40% EPC/IPC proportions were estimated from MC and fixed in the fit. The fit gives freedom to the absolute position of the EPC and IPC distributions but fixes their offset to 5 mm to account for the EPC reconstruction bias. The result of the fit is shown in Fig. 7.2. The beam spot y-coordinate is taken as the IPC mean, known to be accurately reconstructed: $y_{beam} = (-3 \pm 1)$ mm

Some deviations between the beam spot shape and the Gaussian-assumed MC fit are observed. Based on images of the beam on scintillating quartz, the beam

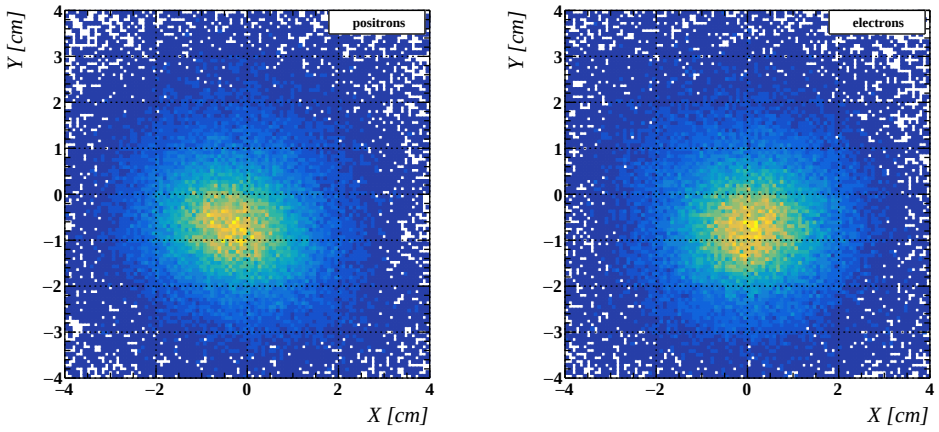

Figure 7.1: Distribution of the reconstructed vertices at the target plane for positrons (left) and electrons (right) in Feb23 data.

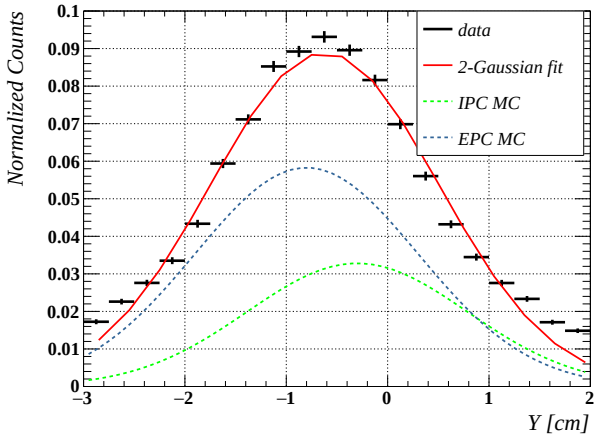

Figure 7.2: Distribution of the y-vertices distribution on data fitted by EPC and IPC MC distribution where a 60%-40% proportion has been assumed for EPC/IPC.

spot shape is more intricate. Additionally, the coexistence of H^+ and H_2^+ adds another layer of complexity to the beam spot shape. It was eventually simulated as a 3 mm σ 2D Gaussian beam spot.

7.3 Systematic studies

On top of the BField scaling factor (introduced in Sec. 6.2.2), two additional sources of systematic errors were studied: the beam spot position and the ^{8}Be nucleus boost. Their impact on both the Angular Opening and E_{sum} distributions are described in the following.

7.3.1 Beam spot position

In order to study the effect of a beam spot position misestimate on the observables, an IPC18 simulation was generated uniformly over a 4-cm diameter circle on the target. The simulated vertex on target of the reconstructed pairs is shown in Fig. 7.3 (top left). A lower reconstruction efficiency is observed at positive y, mostly due to the +y unread sector of the CDCH and the -y position of the pTC. The generated circle was divided into 4 square regions A, B, C and D, each separated on average by almost 2 cm, one order of magnitude above the error on the beam spot estimate from Sec. 7.2. A 20 keV shift was observed at most between the reconstructed E_{sum} distributions from each region shown in Fig. 7.3 (top right). This error is included as an additional error on the BField scaling factor estimated in Sec. 6.2.2. The Angular Opening distributions are shown in Fig. 7.3 (bottom). The 4 distributions are close in shape though 5% discrepancies at large angles are observed despite low statistics. It is included by increasing the error on the IPC templates used in the maximum likelihood (see Sec. 7.6).

7.3.2 ^{8}Be boost and doppler effect

The ^{8}Be nucleus resulting from the proton capture of ^{7}Li is slightly boosted with respect to the laboratory frame. The boost was neglected within the MC simulations but it leads to a dependence of the photon energy on its emission angle:

$$E_\gamma = \frac{E_{\gamma,CM}}{\gamma_{CM}(1+\beta_{CM}\cos\theta_\gamma)} \tag{7.1}$$

with $E_{\gamma,CM}$, β_{CM} and γ_{CM} the photon energy, the ^{8}Be velocity and Lorentz factor in the ^{8}Be center-of-momentum frame and E_γ and θ_γ the photon energy and polar angle in MEG-II's rest frame and coordinate system. Fig. 7.4 illustrates this O(100 keV) dependence on θ_γ. The distribution of θ_γ, the polar angle of $\vec{p}_+ + \vec{p}_-$ for all pairs in Feb2023 dataset is overlaid. A 40 keV difference is expected between

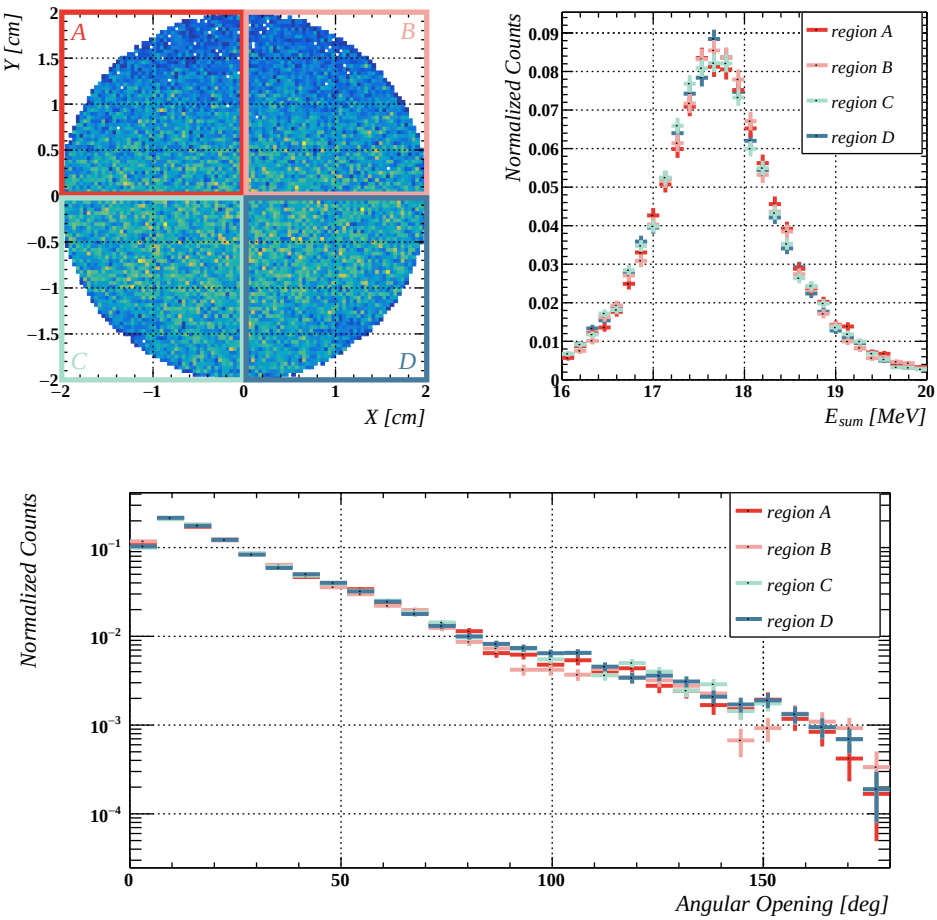

Figure 7.3: (Top left) Generated vertices of reconstructed pairs from a uniform 2 cm-radius simulation. It was arbitrarily divided into four regions A, B, C and D. Reconstructed E_{sum} (top right) and Angular Opening (bottom) distributions from each of the four regions.

the pairs emitted DS ($\theta_\gamma < 90°$) and US ($\theta_\gamma > 90°$), which is well below the E_{sum} resolution and therefore cannot be resolved. Moreover, a pondered average of the θ_γ distribution and the $E_\gamma(\theta_\gamma)$ curve gives an average of 17.63 MeV for the (virtual) photons in the Feb2023 dataset. It is 10 keV away from the MC simulation energy, fixed at 17.64 MeV. This 0.1% effect is accounted for in the BField scaling factor (see Sec. 6.2.2).

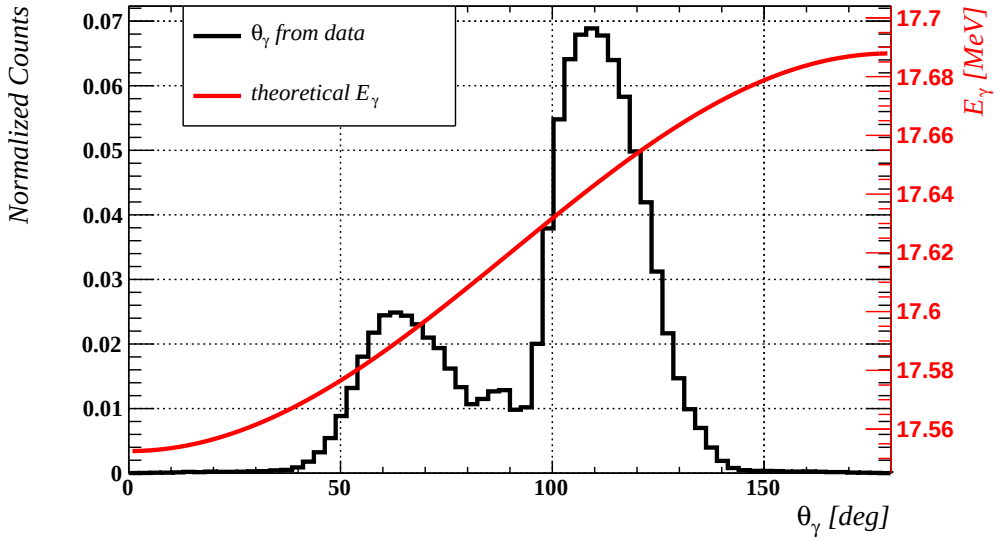

Figure 7.4: θ_γ distribution from Feb 2023 data (black) and E_γ dependence on θ_γ (red).

7.4 Analysis strategy

The analysis of the Feb2023 dataset and the extraction of the X17 yields is entirely carried out in the E_{sum} vs Angular Opening plane. While the Angular Opening is crucial to observe any significant deviation from the IPC background, the E_{sum} observable provides good discrimination between 18 MeV (transition to ground state) and 15 MeV (transition to first excited state) processes and further EPC/IPC discrimination. Moreover, a low E_{sum} region, where X17 is kinematically forbidden, is used to cross-check our background model. Finally, a blinded signal region was defined to prevent biasing. The plane was therefore divided into three regions illustrated in Fig. 7.5:

- a blinded Signal region for $E_{sum} \in [16\text{ MeV}, 20\text{ MeV}]$ and Angular Opening $\in [115°, 160°]$: based on MC simulations presented in Sec. 4.2.5, this region covers the range of X17 masses of interest from both ^{8}Be*(17.6) and ^{8}Be*(18.1) transitions; outside this region, excesses from X17 decay were estimated negligible.

- the Angular Opening sideband for $E_{sum} \in [16\text{ MeV}, 20\text{ MeV}]$ and Angular Opening $\in [0°, 115°[\cup]160°, 180°]$: here, the model at angles lower and higher than the Signal region but at same E_{sum} can be tested.

- the E_{sum} sideband for $E_{sum} \in [15\ \text{MeV}, 16\ \text{MeV}[$ and Angular Opening $\in [0°, 180°]$: this region where no X17 signal is expected is used to test the acceptance of our apparatus in the same Angular Opening region as the Signal region.

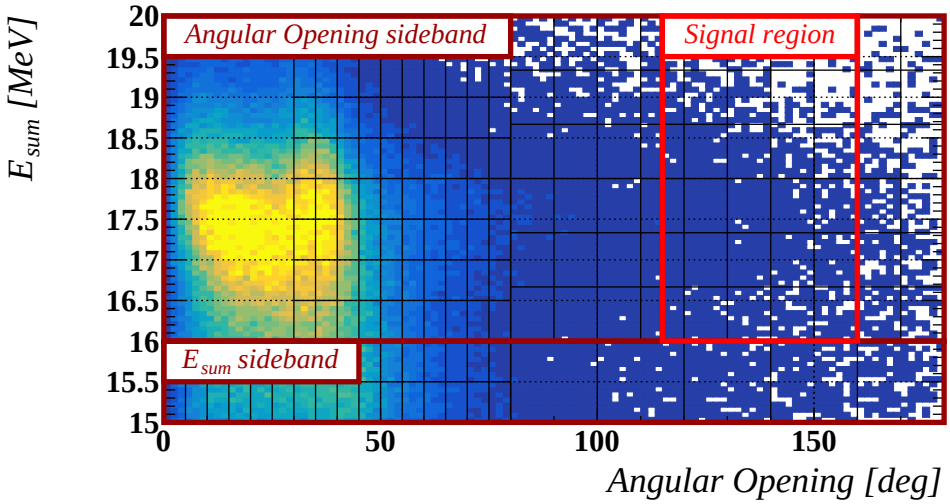

Figure 7.5: Feb 2023 dataset E_{sum} vs Angular Opening plane. The Angular Opening and E_{sum} sidebands are shown in purple. The signal region after unblinding is shown in red here. The fitting range and associated bins are overlaid in black.

Our background model was first used to model the data in the two sidebands. After a good understanding was obtained, the Signal region was unblinded and the model was applied to this region in order to extract the X17 yield. Over these three regions, a fitting range and associated binning was chosen in the plane and is schematized in black in Fig. 7.5. The fitting range choice can be understood based on a difference in track quality between data and MC. Below 50°, the quick variations in Angular Opening shape due to IPC and EPC peaks are difficult to model with higher quality tracks from MC (wrt. data), likely due to differences in resolutions. The Angular Opening spectrum of Feb2023 dataset for $\theta_\gamma < 80°$ and $\theta_\gamma > 100°$ is shown in Fig. 7.6. Due to the copper ring tilt towards the US pTC, the $\theta_\gamma > 100°$ region is richer in EPC. For $\theta_\gamma < 80°$, the IPC/EPC ratio is larger and the quick variations make it harder to model. Overall, it was chosen to fit the following regions:

- for $\theta_\gamma \geq 80°$ and $E_{sum} \in [16\ \text{MeV}, 20\ \text{MeV}]$, Angular Opening $\in [30°, 180°]$

- for $\theta_\gamma \geq 80°$ and $E_{sum} \in [15\text{ MeV}, 16\text{ MeV}]$, Angular Opening $\in [0°, 180°]$: this region is included to better discriminate the 15 MeV from the 18 MeV background
- for $\theta_\gamma < 80°$, Angular Opening $\in [50°, 180°]$

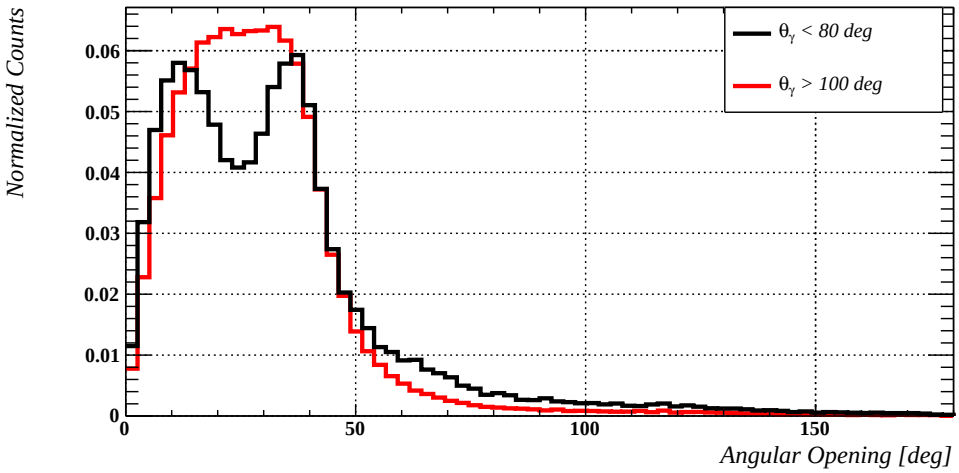

Figure 7.6: Angular Opening distribution from Feb 2023 data (black) for $\theta_\gamma < 80°$ (black) and $\theta_\gamma > 100°$ (red).

7.5 Weighting procedure

Sec. 6.2 put forward the evidence for both ^{8}Be*(17.6) and ^{8}Be*(18.1) transitions within the Feb2023 dataset. Sec. 4.1.2 pointed out a large (7 μm) target thickness which could lead to the excitation of the non-resonant region of the p+^{7}Li reaction, between the two resonances. Due to large uncertainties on the respective proportions of the two resonances and of the non-resonant region within the dataset, three IPC templates were used, each corresponding to a slice in proton energy as illustrated in Fig. 7.7 (left). The following slices were chosen in order to focus on the resonant part of the 440 keV and 1030 keV resonances and the non-resonant flat region around 700 keV and to minimize the correlations between the IPC shapes from each slice:

- "17.6" MeV resonant slice with 420 keV $\leq E_\mathrm{p} \leq$ 460 keV: M1-dominated region exciting the ^{8}Be*(17.6) state

- "17.9" MeV non-resonant slice with 593 keV $\leq E_{\mathrm{p}} \leq$ 836 keV: E1-dominated region leading to direct proton capture process with average energy 17.9 MeV
- "18.1" MeV resonant slice: 980 keV $\leq E_{\mathrm{p}} \leq$ 1060 keV: M1/E1 mixed region exciting the ^{8}Be*(18.1) state

The reconstructed IPC shapes from each slice is shown in Fig. 7.7 (right). As expected, the M1-dominated IPC17.6 has a much steeper shape than the E1-dominated IPC17.9 and the E1-enriched IPC18.1. Three additional IPC templates, nicknamed IPC14.6, IPC14.9 and IPC15.1, use the same proton energy slices, are equivalent to IPC17.6, IPC17.9 and IPC18.1 but apply to transitions to first excited state. The proportions of each population are constrained and fitted in Sec. 7.6.

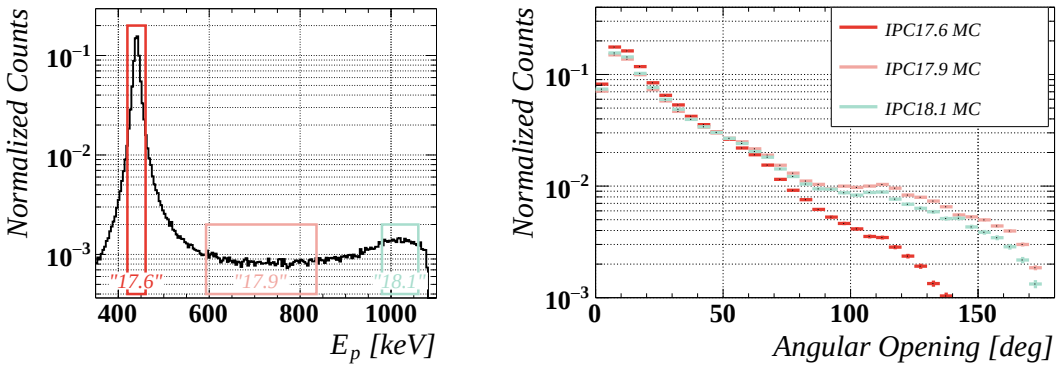

Figure 7.7: (Left) Proton energy distribution from IPC generation and the three chosen slices, corresponding to the 17.6 MeV resonant (red), 17.9 MeV non-resonant (orange) and 18.1 MeV resonant states (blue). (Right) Reconstructed MC Angular Opening distribution from IPC generated in each of the three proton energy slices.

Concerning EPC, no significant differences between EPC17.6, EPC17.9 and EPC18.1 templates were resolved. Therefore, one only EPC template from 18 MeV transitions, making use of the whole proton energy range, enters the final fit: it is nicknamed EPC18. Same for 15 MeV transitions, the EPC template being nicknamed EPC15.

Moreover, the X17 $e^{+}e^{-}$ decay was simulated from both 17.6 MeV and 18.1 MeV resonances, leading to two X17 templates: X17,17.6 and X17,18.1. The X17 search is carried out in both resonances simultaneously.

Finally, a template for fake pairs passing the selection was generated in Sec. 5 and is referred to as fake pairs.

In summary, the Feb2023 dataset will be fitted in the E_{sum} vs Angular Opening plane making use of 11 different templates generated from MC. They account for two types of physical backgrounds, EPC and IPC, one non-physical background, fake pairs, and two X17 signals from ^{8}Be*(17.6) and ^{8}Be*(18.1). A summary is presented in Tab. 7.2.

Template type	**Proton energy slice [keV]**	**Transition**	
		To 1st excited state	To ground state
Backgrounds			
IPC	[420,460], H_2^+ on target [593,836], H^+ energy loss [980,1060], H^+ on target	**IPC14.6** **IPC14.9** **IPC15.1**	**IPC17.6** **IPC17.9** **IPC18.1**
EPC	[350, 1080]	**EPC15**	**EPC18**
fakes	[350, 1080]	**fakes**	
Signal			
		^{8}Be*(17.6) to ground	^{8}Be*(18.1) to ground
X17	/	**X17(17.6)**	**X17(18.1)**

Table 7.2: Description of the 9 background and 2 signal templates used in the fit of the Feb2023 data

7.6 Maximum likelihood fit

The X17 search relies on a two-dimensional maximum likelihood fit of the 1080 keV Feb2023 data in the E_{sum} vs Angular Opening plane. It uses a binned likelihood function and template histograms representing both the backgrounds and the signal. Template histograms, instead of PDFs, introduce a two-fold advantage. There is no need to define a PDF parametrization, enabling a quicker transition from Monte Carlo production to fitting. Additionally, the templates can be constructed two-dimensionally, allowing for direct incorporation of any expected correlations. These templates are generated using Monte Carlo simulations introduced in Sec. 4.2 and are validated in the sidebands before unblinding. The simulated templates have limited statistics. Generating them requires substantial computational resources (around 200 CPUs) and extended processing time (several weeks) due to the low reconstruction efficiencies of both IPC and EPC events. EPC generation is especially inefficient, beginning from the photon production and selecting rare e^+e^- pair events. As a result, the number of reconstructed IPC

events in the MC templates compares to the one observed in the data while the EPC sample has 20 times fewer events than the data. The lack of statistics in the Monte Carlo templates introduces systematic effects which are accounted for by the simplified Beeston-Barlow approach described in [89].

The X17 signal search is performed in the two resonances. The number of signal events from each resonance, $\mathcal{N}_{\mathrm{X17}(Q)}$ is obtained from the branching ratio $\mathcal{BR}(^8\mathrm{Be}^*(Q) \to {}^8\mathrm{Be}+\mathrm{X17})$, with $Q = 17.6\,\mathrm{MeV}$ or $18.1\,\mathrm{MeV}$ and from the number of corresponding IPC, $\mathcal{N}_{\mathrm{IPC}(Q)}$:

$$\mathcal{N}_{\mathrm{X17}(Q)} \;=\; \mathcal{N}_{\mathrm{IPC}(Q)} \times R_{\mathrm{X17/IPC},Q} \times k(m_{\mathrm{X17}}) \tag{7.2}$$

where $R_{\mathrm{X17/IPC},Q}$ is the ratio between the X17 signal and IPC branching ratios for the excited state Q:

$$R_{\mathrm{X17/IPC},Q} \;=\; \frac{\mathcal{BR}(^8\mathrm{Be}^*(Q) \to {}^8\mathrm{Be} + \mathrm{X17})}{\mathcal{BR}(^8\mathrm{Be}^*(Q) \to {}^8\mathrm{Be} + \mathrm{e}^+\mathrm{e}^-)} \tag{7.3}$$

and:

$$k(m_{\mathrm{X17}}) = \frac{\epsilon_{\mathrm{X17}}(m_{\mathrm{X17}})}{\epsilon_{\mathrm{IPC}}} \tag{7.4}$$

is the ratio between the X17 signal and IPC reconstruction efficiencies.

The likelihood function is explicitly parametrized in terms of the branching ratios relative to the γ emission:

$$R_{\mathrm{X17}/\gamma,Q} = \frac{\mathcal{B}(^8\mathrm{Be}^*(Q) \to {}^8\mathrm{Be} + \mathrm{X17})}{\mathcal{B}(^8\mathrm{Be}^*(Q) \to {}^8\mathrm{Be} + \gamma)}\,. \tag{7.5}$$

which are computed from $R_{\mathrm{X17}/\gamma,Q} = R_{\mathrm{X17/IPC},Q} \times R_{\mathrm{IPC}/\gamma,Q}$, with:

$$R_{\mathrm{IPC}/\gamma,Q} = \frac{\mathcal{B}(^8\mathrm{Be}^*(Q) \to {}^8\mathrm{Be} + \mathrm{e}^+\mathrm{e}^-)}{\mathcal{B}(^8\mathrm{Be}^*(Q) \to {}^8\mathrm{Be} + \gamma)}\,. \tag{7.6}$$

To allow for direct comparison with the ATOMKI results and to accommodate potential rescalings based on new theoretical models, we use the same value as reported in [1]: $R_{\mathrm{IPC}/\gamma,18.1} = 3.9 \times 10^{-3}$. $R_{\mathrm{IPC}/\gamma,17.6} = 3.4 \times 10^{-3}$ is obtained by applying Zhang-Miller's [7] proton energy dependence to $R_{\mathrm{IPC}/\gamma,18.1}$. This approach neglects theoretical uncertainties on $R_{\mathrm{IPC}/\gamma,Q}$, considered small with respect to $R_{\mathrm{X17}/\gamma,Q}$'s.

The full MC template is obtained by summing all templates with their relative proportions, fitting a total of 15 parameters. The total number of events $\mathcal{N}_{\mathrm{total}}$ in the dataset can be expressed as:

$$
\begin{aligned}
\mathcal{N}_{\text{total}} &= \mathcal{N}_{\text{EPC18}} + \mathcal{N}_{\text{EPC15}} + \mathcal{N}_{\text{fakes}} \\
&\quad + \mathcal{N}_{\text{IPC17.6}} + \mathcal{N}_{\text{IPC14.6}} \\
&\quad + \mathcal{N}_{\text{IPC17.9}} + \mathcal{N}_{\text{IPC14.9}} \\
&\quad + \mathcal{N}_{\text{IPC18.1}} + \mathcal{N}_{\text{IPC15.1}} \\
&\quad + \mathcal{N}_{\text{X17(17.6)}} + \mathcal{N}_{\text{X17(18.1)}} \\
&= \sum_{t=15,18} \mathcal{N}_{\text{EPCt}} + \mathcal{N}_{\text{fakes}} \\
&\quad + \sum_{j=440,700,1030} \mathcal{N}_{\text{IPC18,j}} + \mathcal{N}_{\text{IPC15,j}} \\
&\quad + R_{\text{X17/IPC,17.6}} \cdot \mathcal{N}_{\text{IPC17.6}} \cdot k(m_{\text{X17}}) \cdot n + R_{\text{X17/IPC,18.1}} \cdot \mathcal{N}_{\text{IPC18.1}} \cdot k(m_{\text{X17}}) \cdot n \\
&= \sum_{t=15,18} \mathcal{N}_{\text{EPCt}} + \mathcal{N}_{\text{fakes}} \\
&\quad + \sum_{j=440,700,1030} \mathcal{N}_{\text{IPCj}} \cdot (p_{\text{IPC18,j}} + (1 - p_{\text{IPC18,j}}) \cdot \mathcal{F}_{\text{beamspot}}) \\
&\quad + \frac{R_{\text{X17}/\gamma,17.6}}{R_{\text{IPC}/\gamma,17.6}} \cdot \mathcal{N}_{\text{IPC17.6}} \cdot k(m_{\text{X17}}) \cdot n + \frac{R_{\text{X17}/\gamma,18.1}}{R_{\text{IPC}/\gamma,18.1}} \cdot \mathcal{N}_{\text{IPC18.1}} \cdot k(m_{\text{X17}}) \cdot n \\
&= \sum_{t=15,18} \mathcal{N}_{\text{EPCt}} + \mathcal{N}_{\text{fakes}} \\
&\quad + \sum_{j=440,700,1030} \mathcal{N}_{\text{IPCj}} \cdot (p_{\text{IPC18,j}} + (1 - p_{\text{IPC18,j}}) \cdot \mathcal{F}_{\text{beamspot}}) \\
&\quad + \left(\frac{R_{\text{X17}/\gamma,17.6}}{R_{\text{IPC}/\gamma,17.6}} \cdot \mathcal{N}_{\text{IPC440}} \cdot p_{\text{IPC17.6}} + \frac{R_{\text{X17}/\gamma,18.1}}{R_{\text{IPC}/\gamma,18.1}} \cdot \mathcal{N}_{\text{IPC1030}} \cdot p_{\text{IPC18.1}} \right) \\
&\quad \cdot k(m_{\text{X17}}) \cdot n
\end{aligned}
\tag{7.7}
$$

The 14 parameters quoted in Eq. 7.7 plus the energy scale factor α_{field} are described in Tab. 7.3.

A finite number of X17 masses were simulated: the dependence of the X17 templates on the mass of the particle is introduced through vertical morphing [90]. The energy scale factor, α_{field} scales the E_{sum} templates to account for the uncertainty put forward in Sec. 6.2.2. It is also introduced through vertical morphing. Constraints are applied on the proportion of IPC18,j with respect to the total

Parameter	Description	Formula	Constraint
$\mathcal{N}_{\text{EPC18}}$	number of EPC18 events	/	∅
$\mathcal{N}_{\text{EPC15}}$	number of EPC15 events	/	∅
$\mathcal{N}_{\text{fakes}}$	number of fake pairs	/	∅
$\mathcal{N}_{\text{IPC440}}$	number of IPC events from the [420 keV, 460 keV] slice	$\mathcal{N}_{\text{IPC440}} = \mathcal{N}_{\text{IPC17.6}} + \frac{\mathcal{N}_{\text{IPC14.6}}}{\mathcal{F}_{\text{beamspot}}}$	∅
$\mathcal{N}_{\text{IPC700}}$	number of IPC events from the [593 keV, 836 keV] slice	$\mathcal{N}_{\text{IPC700}} = \mathcal{N}_{\text{IPC17.9}} + \frac{\mathcal{N}_{\text{IPC14.9}}}{\mathcal{F}_{\text{beamspot}}}$	∅
$\mathcal{N}_{\text{IPC1030}}$	number of IPC events from the [930 keV, 1060 keV] slice	$\mathcal{N}_{\text{IPC1030}} = \mathcal{N}_{\text{IPC18.1}} + \frac{\mathcal{N}_{\text{IPC15.1}}}{\mathcal{F}_{\text{beamspot}}}$	∅
$p_{\text{IPC17.6}}$	proportion of IPC17.6 in [420 keV, 460 keV] slice	$\mathcal{N}_{\text{IPC17.6}} = p_{\text{IPC17.6}} \cdot \mathcal{N}_{\text{IPC440}}$	from BGO at 500 keV (Fig. 6.14): 79.3(12)%
$p_{\text{IPC17.9}}$	proportion of IPC17.9 in [593 keV, 836 keV] slice	$\mathcal{N}_{\text{IPC17.9}} = p_{\text{IPC17.9}} \cdot \mathcal{N}_{\text{IPC700}}$	from BGO at 800 keV (Fig. 6.14): 48.2(19)%
$p_{\text{IPC18.1}}$	proportion of IPC18.1 in [980 keV, 1060 keV] slice	$\mathcal{N}_{\text{IPC18.1}} = p_{\text{IPC18.1}} \cdot \mathcal{N}_{\text{IPC1030}}$	from BGO at 1000 keV (Fig. 6.14): 42(2)%
$\mathcal{F}_{\text{beamspot}}$	ratio IPC15/IPC18 acceptance compared to MC	$\mathcal{N}_{\text{IPC15,j}} = (1 - p_{\text{IPC18,j}}) \cdot \mathcal{N}_{\text{IPCj}} \cdot \mathcal{F}_{\text{beamspot}}$	∅
m_{X17}	X17 mass	/	[16.5 MeV/c^2, 17.1 MeV/c^2]
$R_{\text{X17}/\gamma,17.6}$	see Eq. 7.5		∅
$R_{\text{X17}/\gamma,18.1}$	see Eq. 7.5		∅
α_{field}	energy scale factor	/	$0.1537^{+0.002}_{-0.002}$
n	normalization factor centered at 1, account for 20% uncertainty on acceptance	/	Gaussian constraint with 20% uncertainty

Table 7.3: The 15 parameters used in the maximum likelihood fit of the Feb2023 data

number of IPC in the proton energy slice j. Their values depend on two elements:

- the 18/15 decay probability: it is fixed by physics processes and is extracted from the BGO spectra obtained in Fig. 6.14
- the 18/15 IPC pairs acceptance: it is dependent on the apparatus and was extracted from MC simulations

To account for differences between data and MC on the 18/15 acceptance, $\mathcal{F}_{\text{beamspot}}$, independent from the proton energy slice, was introduced. For an ideal MC, exactly reproducing the data conditions, we have $\mathcal{F}_{\text{beamspot}} = 1$. Due to some uncertainty on the beamspot position, the 18/15 acceptance of the apparatus can vary: $\mathcal{F}_{\text{beamspot}}$ accounts for it.

A 20% uncertainty on $k(m_{X17})$, due to relative geometrical acceptance, was estimated based on the 500 keV data best fit displayed in Fig. 6.11. n, a normalization factor centered at 1 accounts for this uncertainty. $R_{\text{X17}/\gamma,Q}$ are bound to be positive and the X17 mass is constrained between 16.5 MeV/c^2 and 17.1 MeV/c^2. A larger mass is kinematically forbidden to explain the Atomki results on ^{12}C. The lower limit is 2.5 σ away from the best mass estimate. The latter was computed as an average of Atomki's best result on ^{8}Be [37] (17.01 MeV/c^2), ^{4}He [19] (16.84 MeV/c^2) and ^{12}C [21] (17.03 MeV/c^2) pondered by their uncertainties. The ^{8}Be estimate results itself from an average between an updated analysis of 2016 results [1] and 2018 results [26], as discussed in Sec. 1.3.2. It results in a best estimate: $m_{X17} = 16.97(22)$ MeV/c^2.

The constraint terms are incorporated into the likelihood using Gaussian functions. The likelihood is expressed as the product of three terms:

$$\mathcal{L} = \mathcal{L}_{\text{D}} \times \mathcal{L}_{\text{S}} \times \mathcal{L}_{\text{C}} \tag{7.8}$$

where $\mathcal{L}_{\text{D}}$ represents the Poisson probability density function (PDF) multiplied over the bins, $\mathcal{L}_{\text{S}}$ accounts for the limited statistics of the Monte Carlo templates as described in [89], and $\mathcal{L}_{\text{C}}$ is the constraint term. For a given set of parameters $\Omega = (R_{\text{X17}/\gamma,17.6}, R_{\text{X17}/\gamma,18.1}, m_{\text{X17}}, \mathcal{N}_{\text{IPC}}, \mathcal{N}_{\text{EPC}}, \mathcal{N}_{\text{fakes}})$, the Beeston-Barlow coefficients β_i, and the nuisance parameters $\alpha_m = (p_{\text{IPC17.6}}, p_{\text{IPC17.9}}, p_{\text{IPC18.1}}, \alpha_{\text{field}}, k(m_{\text{X17}}))$, the likelihood terms are given by:

$$\mathcal{L}_{\mathrm{D}}(\Omega, \alpha_m, \beta_i) = \prod_i \frac{f_i(\Omega, \alpha_m, \beta_i)^{D_i} e^{-f_i(\Omega, \alpha_m, \beta_i)}}{D_i!} \tag{7.9}$$

$$\mathcal{L}_{\mathrm{S}}(\Omega, \alpha_m, \beta_i) = \prod_i \frac{(\beta_i \mu_{\mathrm{eff},i}(\Omega, \alpha_m))^{\mu_{\mathrm{eff},i}} e^{-\beta_i \mu_{\mathrm{eff},i}(\Omega, \alpha_m)}}{\mu_{\mathrm{eff},i}(\Omega, \alpha_m)!} \tag{7.10}$$

$$\mathcal{L}_{\mathrm{C}}(\alpha_m) = \prod_m \frac{1}{\sqrt{2\pi}\sigma_{\alpha_m}} e^{-\frac{(\alpha_m - \alpha_{m,0})^2}{2\sigma_{\alpha_m}^2}} \tag{7.11}$$

Here, D_i denotes the observed count in the i-th bin, and f_i is the estimated count. m loops over the nuisance parameters. β_i scales the bin population estimate to account for the limited MC statistics. The statistical uncertainty σ_{β_i} is used to compute $\mu_{\mathrm{eff},i} = 1/\sigma_{\beta_i}^2$. The sideband data were first fitted maximizing this likelihood. It revealed some discrepancies between data and fit model. To account for this, the statistical uncertainty of the IPC template was inflated by a factor of $\sqrt{3}$. This increased uncertainty also accounts for the beam spot uncertainty discussed in Sec. 7.3.1.

Making use of the binning grid illustrated in Fig. 7.5, the result of the likelihood maximization in the sideband is shown in Fig. 7.8. It is a 1D projection of the 2D fit in several ranges of E_{sum}. The normalized residuals for each bin are shown below. A goodness-of-fit test, using the Poisson log-likelihood chi-square statistics as defined in [91], yields a p-value of 12.2% from a set of randomly generated pseudo-experiments. This result indicates no significant deviation from the underlying model. Data agrees with the best fit model within 2σ for all bins, except for those below 30°. More than 90% of the bins exhibit agreement within 1σ. The residuals are evenly distributed around zero, with no significant patterns observed. Additionally, the four bins preceding the signal region and the two bins following it demonstrate good agreement between the data and the model. The poor agreement below 30° is most likely due to poorer track quality in data with respect to MC, as discussed in Sec. 6.1. Overall, the IPC/EPC mix can explain the two-peak structure below 40°. Above 60°, the IPC is the dominating contribution and the steepness is well modelled by a sum of steeper IPC17.6 and flatter IPC18.1. Above 160°, a small contribution of fake pairs explains the flattening of the data. Overall, the good agreement between data and model led to the unblinding of the signal region.

The likelihood maximization was repeated for the unblinded data and the fit result along with the normalized residuals is shown in Fig. 7.9. The best fit is well in line with the blinded fit and results in a p-value of 10.5%. The values of the parameters obtained from this best fit are compiled in Tab. 7.4. The sum of

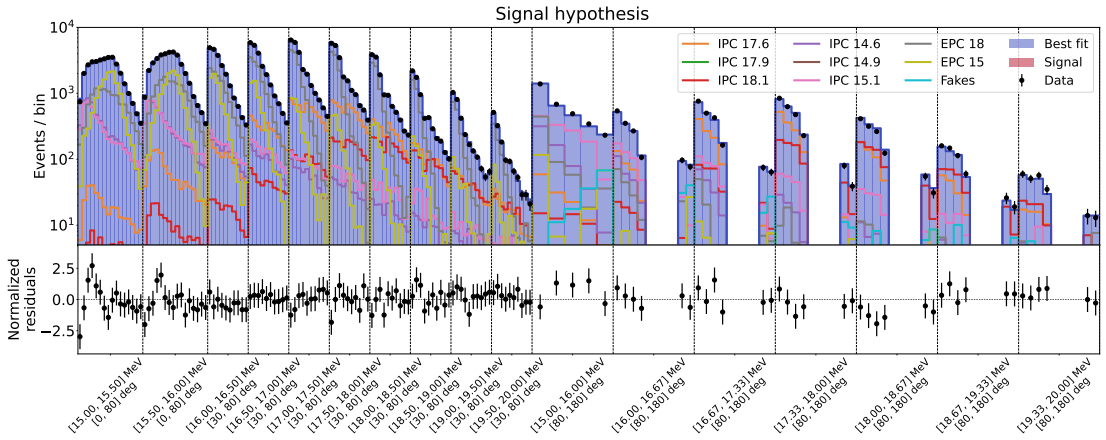

Figure 7.8: Before unblinding: (Top) Comparison between the Feb2023 data Angular Opening spectrum (black dots) and the best fit (blue) for different E_{sum} bins. The IPC populations from the de-excitation to ground state are shown in orange and red (IPC 17.6, IPC18.1), the IPC populations from the de-excitation to the first excited state are shown in purple and pink (IPC 14.6, IPC15.1), the EPC populations (EPC18, EPC15) are shown in gray and olive and the population of fake events (see Sec. 5) is shown in cyan. (Bottom) Residuals normalized to the statistical uncertainty on the data points.

the background contributions well describes the data, with the best fit estimating (10 ± 94) (16.5 ± 0.6) MeV/c^2 X17 signal events, compatible with zero but little-compatible with the (114 ± 23) (16.97 ± 0.22) MeV/c^2 expected events based on Atomki's prediction. No significant excess was observed. The compatibility between the best fit and the X17 hypotheses is computed and discussed in Sec. 7.8. In the signal region, no significant trend is observed in the residuals and all bins show a below 1.5σ agreement. The following quoted numbers extrapolate the best fit to $E_{sum} \in [10\text{ MeV}, 20\text{ MeV}]$ and Angular Opening $\in [0°, 180°]$ in order to understand the content of the full dataset. EPC and IPC represent 59% and 41% of the total number of events. Among all IPC18 events, 21.5 % come from the 18.1 MeV IPC, 78.5 % from the 17.6 MeV IPC and 0.0 % from the 17.9 MeV IPC. The $p_{\text{IPC18,j}}$ fitted values are close to the values extracted from the BGO spectra and therefore confirm the method. $\mathcal{F}_{\text{beamspot}} = 1.04 \pm 0.08$ is consistent with 1.00 and therefore supports the goodness of the MC simulation and the associated fit model. $\alpha_{\text{field}} = 0.15342(8)$ is within the uncertainty of the estimate from Sec. 6.2.2: 0.1537(2). The total number of pairs in the dataset is 482297 while the number of estimated events from the MC model is (533000 ± 35000). This 10% overestimate is largely due to the mismodelling of the data below 30°, outside the fit region.

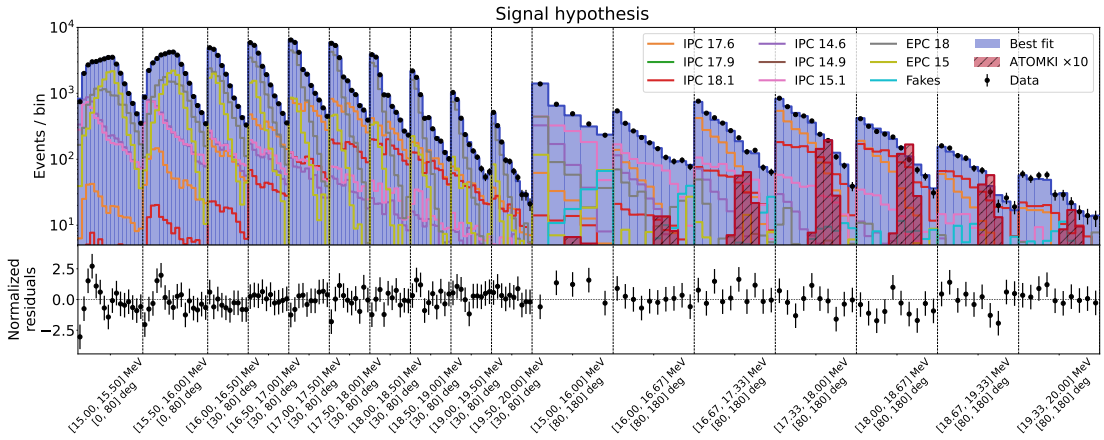

Figure 7.9: After unblinding: (Top) Comparison between the Feb2023 data Angular Opening spectrum (black dots) and the best fit (blue) for different E_{sum} bins. The IPC populations from the de-excitation to ground state are shown in orange and red (IPC 17.6, IPC18.1), the IPC populations from the de-excitation to the first excited state are shown in purple and pink (IPC 14.6, IPC15.1), the EPC populations (EPC18, EPC15) are shown in gray and olive and the population of fake events (see Sec. 5) is shown in cyan. For comparison, the signal template is shown (hatched red) for a branching ratio 10 times larger than that measured at ATOMKI. (Bottom) Residuals normalized to the statistical uncertainty on the data points.

Sec. 7.7 projects this best fit onto several 1D quantities in order to better understand and visualize the data/model agreement. Sec. 7.8 extracts from this best fit the exclusion limits that one can set on the X17 particle, its mass and branching ratios. It also tests the compatibility between our best fit and Atomki's X17 predictions.

7.7 Best fit projections

The best fit extracted from the likelihood maximization in the E_{sum} vs Angular Opening plane can be projected to one-dimensional observables to better probe the data/model agreement, especially in the signal region. The value of each fitted parameter were extrapolated to the region where $E_{sum} \in [15\ \text{MeV}, 20\ \text{MeV}]$ and Angular Opening $\in [30°, 180°]$. The following plots are projected from this region to the Angular Opening between 30° and 180°, the E_{sum} between 15 MeV and 20 MeV, the Invariant Mass between 5 MeV/c^2 and 20 MeV/c^2 and θ_γ between 30° and 150° in Figs. 7.10, 7.11, 7.12 and 7.13 respectively. It should be noted

Parameter	Best fit value
$\mathcal{N}_{\text{EPC18}}$	204400 ± 4800
$\mathcal{N}_{\text{EPC15}}$	108300 ± 4200
$\mathcal{N}_{\text{fakes}}$	1270 ± 360
$\mathcal{N}_{\text{IPC440}}$	145300 ± 7700
$\mathcal{N}_{\text{IPC700}}$	0 ± 950
$\mathcal{N}_{\text{IPC1030}}$	70300 ± 7400
$p_{\text{IPC17.6}}$	0.691 ± 0.018
$p_{\text{IPC17.9}}$	0.482 ± 0.019
$p_{\text{IPC18.1}}$	0.392 ± 0.020
$\mathcal{F}_{\text{beamspot}}$	1.04 ± 0.08
m_{X17}	16.5 ± 0.6 MeV/c^2
$R_{\text{X17}/\gamma,17.6}$	$(0.00 \pm 1.64) \times 10^{-4}$ $\Leftrightarrow (0.0 \pm 60.5)$ events
$R_{\text{X17}/\gamma,18.1}$	$1.62 \times 10^{-4} \pm 1.27 \times 10^{-3}$ $\Leftrightarrow (9.9 \pm 92)$ events
α_{field}	0.15342(8)
n	1.0 ± 0.2

Table 7.4: The best fit value for the 15 parameters from the maximum likelihood fit of the Feb2023 data

that the region with Angular Opening $\in [30°, 50°]$ and $\theta_\gamma < 80°$, though not a part of the fitting region, is part of the projections. No signal events is used in these projections, as the fitted number of events is considered negligible here. The residuals, normalized to the error on both data and MC are displayed below each projection.

The mismodelling at low angles and the overestimate of the number of events in MC with respect to data leads to some discrepancies in Angular Opening at low angles (below 70°) and Invariant Mass at low masses (below 10 MeV/c^2). The E_{sum} model is normalized to the data integral to compensate for the overestimate and compare the shapes.

In Fig. 7.10, the Angular Opening projection agrees well with the Feb2023 dataset. Above 70°, no significant underestimate or overestimate is observed and the residuals are evenly distributed around zero. The change of steepness in the data at 90° is well understood as we pass from an EPC-dominated to an IPC-dominated region. Though the steeper IPC17.6 is the dominating IPC contribution up to 130°, the flatter IPC18.1 dominates above and flattens out the data. Above 165°, the small fake pairs contribution dominates. However, some oscillating trend is observed in the residuals: it is at least in part due to the lack of statistics in

the IPC18 MC populations but some mismodelling intrinsic to the IPC theory developed by Zhang-Miller cannot be rejected.

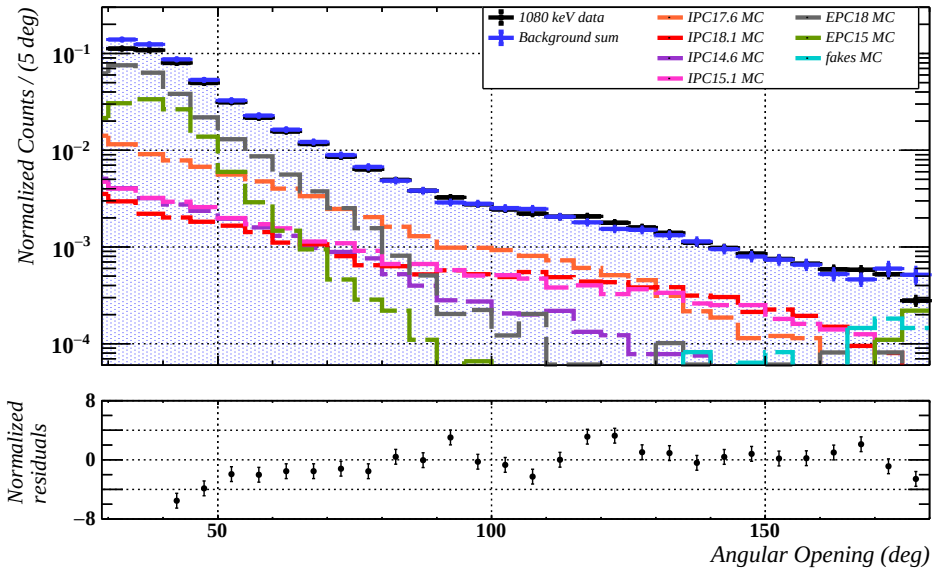

Figure 7.10: (Top) 1D Angular Opening projection of the Feb2023 1080 keV data best fit. The fit procedure is described in Sec. 7.6. Data points are in black, all simulated backgrounds are shown and the sum of backgrounds is in blue. (Bottom) Residuals normalized to the statistical uncertainty on both data and MC.

In Fig. 7.11, the E_{sum} model shape is in good agreement with the data. EPC pairs dominate the dataset. The two-peak structure reproduces the two main transitions of the ^{8}Be excited states, to ground state and to first excited state. The high-energy peak, at 17.6 MeV, points at the domination the 440 keV resonance in the dataset. The 18.1 MeV contribution in both IPC and EPC explains in part the high-energy tail. The energy loss experienced by the EPC pairs is highlighted by the left tail of the EPC18 MC template, which causes a broadening of the two-peak structure. Outliers in the residuals can be attributed to the limited statistics of the EPC templates, as evidenced by the strong fluctuations of EPC18 MC around 17 MeV.

In Fig. 7.12, the Invariant Mass projection is in excellent agreement with the data above 10 MeV/c^2. The mismodelling at low angular openings translates into a discrepancy at small invariant masses. At 10 MeV/c^2, we pass from an EPC to an IPC-dominated regime, explaining the steepness change. Above 16 MeV/c^2, all templates are negligible compared to IPC18.1, which alone explains the smoother drop of the data. In Invariant Mass, the X17 particle should translate into an

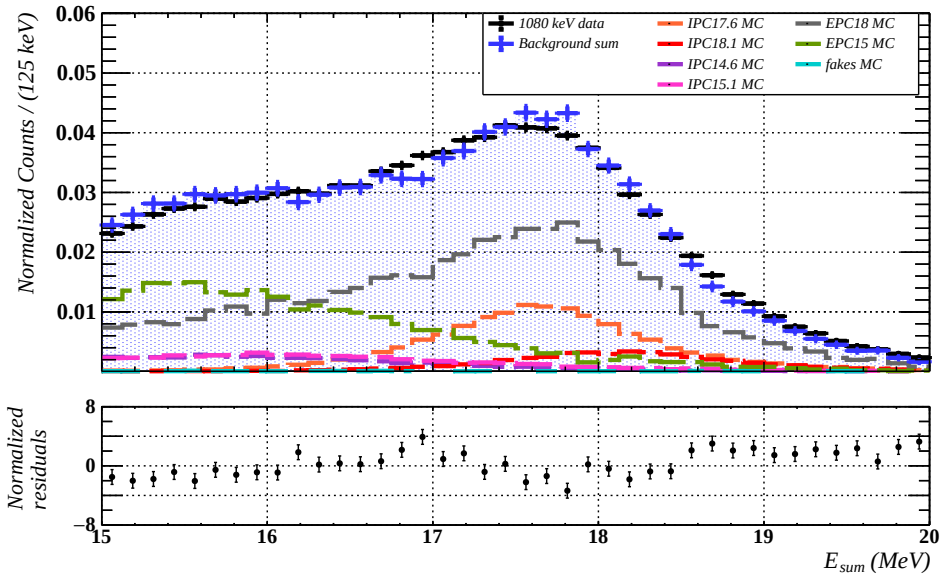

Figure 7.11: (Top) 1D E_{sum} projection of the Feb2023 1080 keV data best fit. The fit procedure is described in Sec. 7.6. Data points are in black, all simulated backgrounds are shown and the sum of backgrounds is in blue. (Bottom) Residuals normalized to the statistical uncertainty on both data and MC.

excess at the corresponding mass. The excellent data/model agreement confirms the absence of a significant X17 signal in the dataset, both from ^{8}Be*(17.6) and ^{8}Be*(18.1) transitions.

In Fig. 7.13, the sum of backgrounds poorly agrees with the dataset in θ_γ. Three regions can be distinguished in both data and MC, peaking respectively at 110°, 85° and 70°. The upstream/downstream asymmetry is also observed in both data and model with a larger number of pairs upstream ($\theta_\gamma > 100°$), mostly EPC. However, the asymmetry is more pronounced in data. The lack of pairs in data for $\theta_\gamma < 80°$ could be explained by two factors:

- the asymmetry in the photon and IPC spectra is not well modelled by Zhang-Miller
- the material budget of the apparatus in the downstream region ($\theta_\gamma < 80°$) is underestimated in the simulations and the track reconstruction efficiency is therefore overestimated; the impact of the CW beamline inserted within the CDCH, and the aluminum flanges along it, could be for example underestimated.

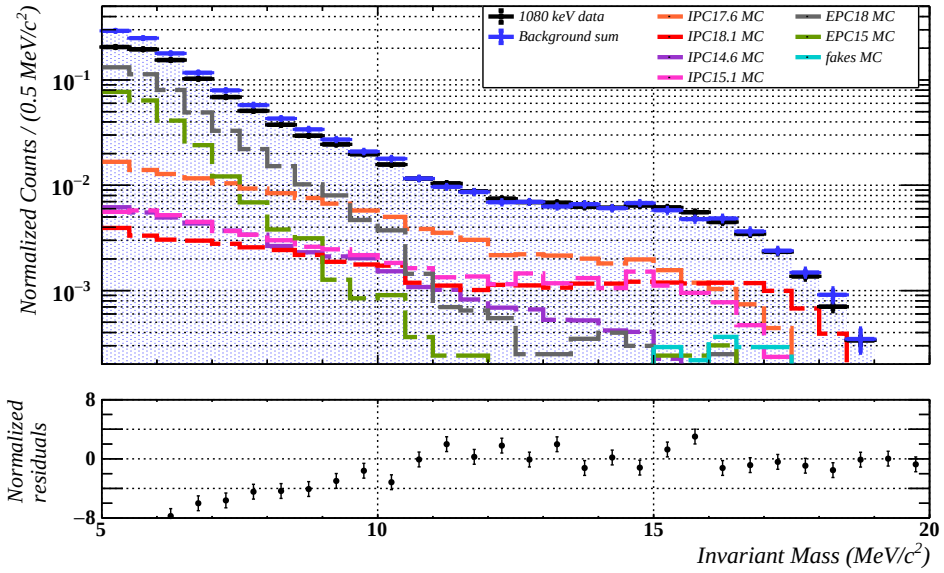

Figure 7.12: (Top) 1D Invariant Mass projection of the Feb2023 1080 keV data best fit. The fit procedure is described in Sec. 7.6. Data points are in black, all simulated backgrounds are shown and the sum of backgrounds is in blue. (Bottom) Residuals normalized to the statistical uncertainty on both data and MC.

7.8 Branching ratio results

Based on the maximum likelihood fit presented in Sec. 7.6 and due to the absence of significant signal excess in the Feb2023 dataset, a confidence level was determined to exclude certain assumptions about the mass and production rate of the X17 particle. Confidence regions are constructed in the three-dimensional parameter space ($R_{\mathrm{X17}/\gamma,17.6}$, $R_{\mathrm{X17}/\gamma,18.1}$, m_{X17}), using the Feldman-Cousins method [92], with an ordering defined by the profiled likelihood ratio:

$$\lambda_p(R_{\mathrm{X17}/\gamma,17.6}, R_{\mathrm{X17}/\gamma,18.1}, m_{\mathrm{X17}}) = \frac{\mathcal{L}(R_{\mathrm{X17}/\gamma,17.6}, R_{\mathrm{X17}/\gamma,18.1}, m_{\mathrm{X17}}, \hat{\hat{\eta}})}{\mathcal{L}(\hat{R}_{\mathrm{X17}/\gamma,17.6}, \hat{R}_{\mathrm{X17}/\gamma,18.1}, \hat{m}_{\mathrm{X17}}, \hat{\eta})} \tag{7.12}$$

with $\eta = (\mathcal{N}_{\mathrm{IPC}}, \mathcal{N}_{\mathrm{EPC}}, \mathcal{N}_{\mathrm{fakes}}, \alpha_m, \beta_i)$. The hats and double hats indicate the variables with respect to which the likelihood is maximized following notation from Eq. 40.49 in [93]. The upper limits on $R_{\mathrm{X17}/\gamma,Q}$ are conservatively quoted as the maximum extension of the confidence regions. Fig. 7.14 displays the 3D limits on $R_{\mathrm{X17}/\gamma,17.6}$, $R_{\mathrm{X17}/\gamma,18.1}$ and m_{X17} at 90 % confidence levels (C.L.). Fig. 7.15 projects

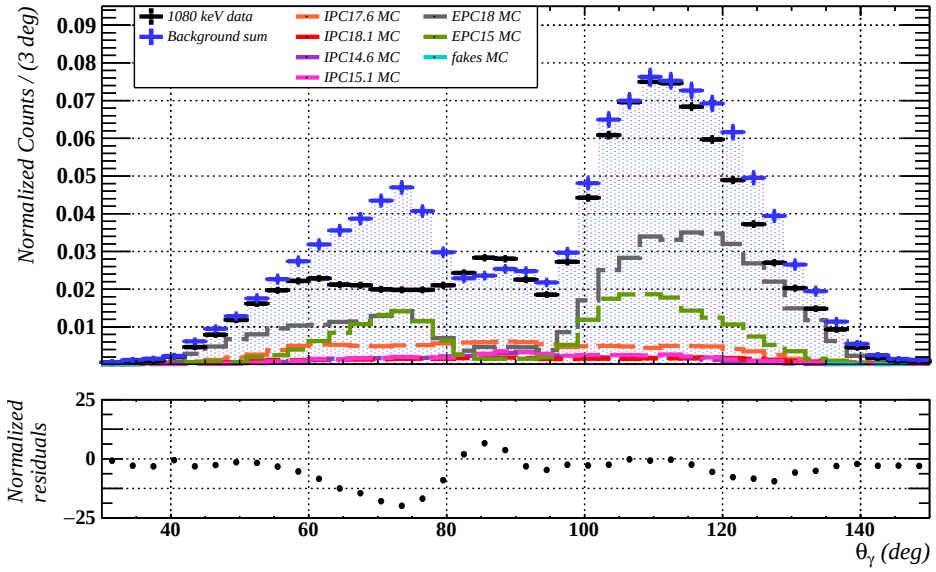

Figure 7.13: (Top) 1D θ_γ projection of the Feb2023 1080 keV data best fit. The fit procedure is described in Sec. 7.6. Data points are in black, all simulated backgrounds are shown and the sum of backgrounds is in blue. (Bottom) Residuals normalized to the statistical uncertainty on both data and MC.

these 3D limits over 2D planes, $R_{\mathrm{X17}/\gamma,17.6}$ vs $R_{\mathrm{X17}/\gamma,18.1}$ (top) and $R_{\mathrm{X17}/\gamma,Q}$ vs m_{X17} (bottom). For the 90% C.L. region, we get $R_{\mathrm{X17}/\gamma,18.1} < 1.2 \times 10^{-5}$ and $R_{\mathrm{X17}/\gamma,17.6} < 1.8 \times 10^{-6}$, which correspond to approximate upper limits of 230 and 200 on the total number of signal events respectively. A 16.97(22) MeV/c^2 X17 signal from the 18.1 MeV state decay, as suggested by Atomki, is excluded at roughly 90% C.L. (see Fig. 7.15 (bottom)).

Specific hypotheses about the mass and branching ratios can be tested by randomly generating values in pseudo-experiments, based on Gaussian distributions with mean and standard deviation derived from Atomki's results. In this approach, a Gaussian constraint on the mass is incorporated into the likelihood ratio, defined as:

$$\lambda_{pH} = \frac{\mathcal{L}(\overline{R_{\mathrm{X17}/\gamma,17.6}}, \overline{R_{\mathrm{X17}/\gamma,18.1}}, \overline{m_{\mathrm{X17}}}, \hat{\hat{\eta}})\, G(\overline{m_{\mathrm{X17}}})}{\mathcal{L}(\hat{R}_{\mathrm{X17}/\gamma,17.6}, \hat{R}_{\mathrm{X17}/\gamma,18.1}, \hat{m}_{\mathrm{X17}}, \hat{\eta})\, G(\hat{m}_{\mathrm{X17}})} \,. \tag{7.13}$$

Here, the bar denotes the mean value of the assumed Gaussian distribution. This likelihood ratio is computed for each pseudo-experiment and the p-value for the tested hypothesis is determined as the fraction of pseudo-experiments yielding a smaller λ_{pH} value than the one observed in the actual data.

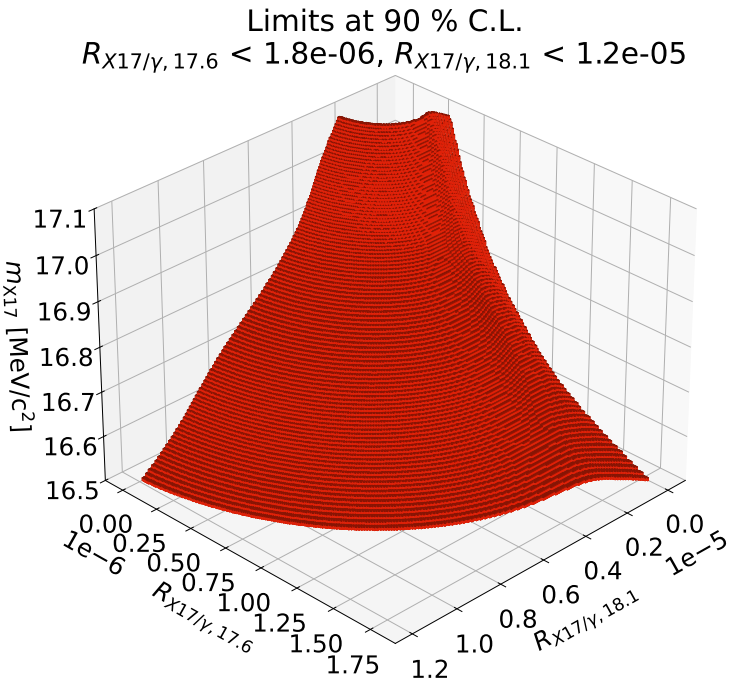

Figure 7.14: 3D limits on $R_{\mathrm{X17}/\gamma,17.6}$, $R_{\mathrm{X17}/\gamma,18.1}$ and m_{X17} at 90 % C.L..

We consider two hypotheses:

- **ATOMKI hypothesis**: In this scenario, X17 is produced only from ^{8}Be*(18.1) decay and $R_{\mathrm{X17}/\gamma,17.6}$ is set to zero, based on the claim that no evidence for X17 production was found from the 17.6 MeV state decay. The X17 mass and $R_{\mathrm{X17}/\gamma,18.1}$ are generated from Gaussian distributions, with mean and standard deviation derived from a pondered average of Atomki's published result on the three nuclei: $m_{\mathrm{X17},Atomki} = 16.97(22)\,\mathrm{MeV/c^2}$ and $R_{\mathrm{X17}/\gamma,18.1,Atomki} = 6(1) \times 10^{-6}$.
- **Feng et al. [4] hypothesis**: In this scenario, X17 is produced from both ^{8}Be*(17.6) and ^{8}Be*(18.1) decays. The X17 mass and $R_{\mathrm{X17}/\gamma,18.1}$ are generated similarly to the previous hypothesis. $R_{\mathrm{X17}/\gamma,17.6,Feng}$ is based on Feng's estimate: $2.7(5) \times 10^{-6}$.

The p-values for these two hypotheses are found to be 6.2 % (1.5σ) and 1.8 % (2.1σ), respectively. Therefore, the Atomki hypothesis is incompatible at 94% confidence with our best fit while the Feng hypothesis is incompatible at 98%.

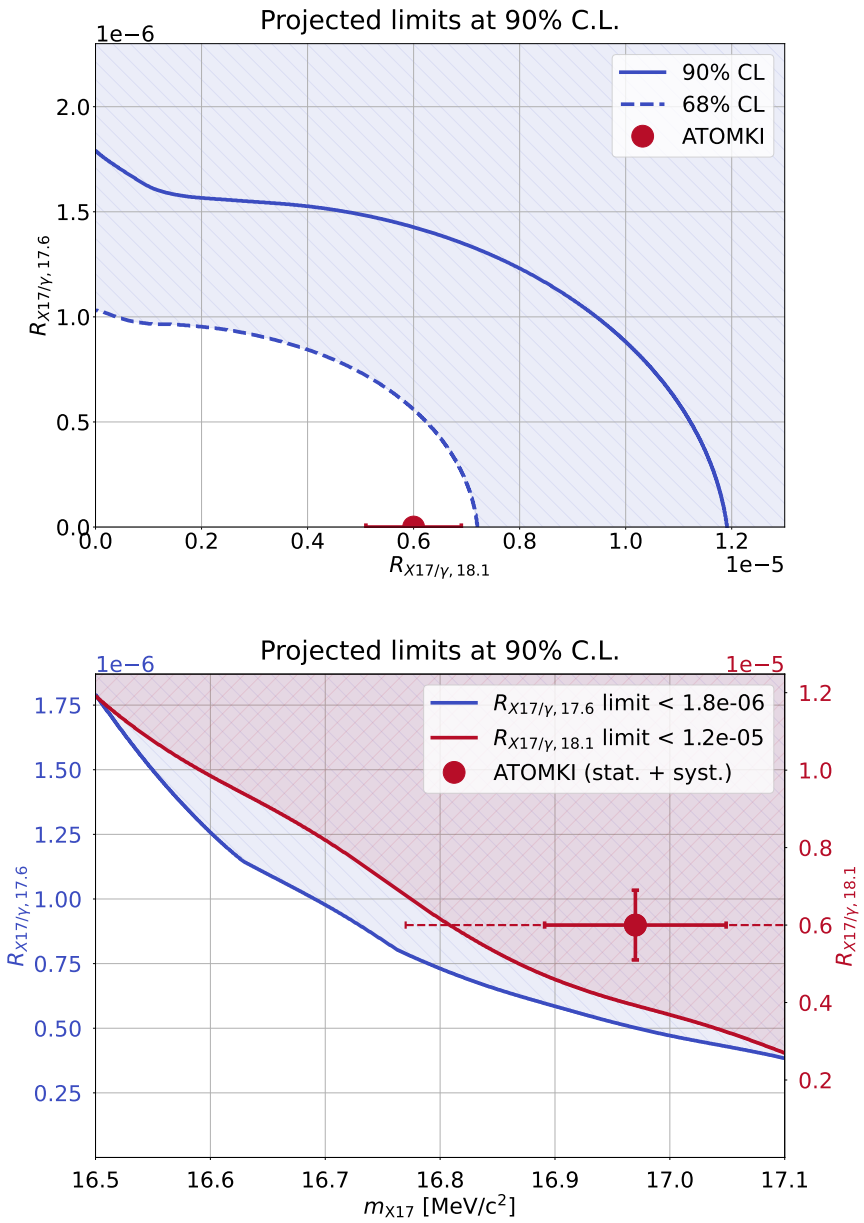

Figure 7.15: (Top) 90 % and 68 % C.L. limit projections on $R_{\mathrm{X17}/\gamma,17.6}$ vs $R_{\mathrm{X17}/\gamma,18.1}$ plane within the allowed mass range. (Bottom) 90 % C.L. limit projections on $R_{\mathrm{X17}/\gamma,17.6}$ vs m_{X17} plane (blue) and $R_{\mathrm{X17}/\gamma,18.1}$ vs m_{X17} plane (red) within the allowed mass range. The hatched areas represent the excluded regions. The red point represents the measured branching ratio at ATOMKI. The full and dashed error bars represent the statistic and systematic errors on the X17 mass respectively.

7.9 Discussion and prospects

The analysis of the Feb2023 dataset required a careful and comprehensive analysis in order to cope with the H_2^+ contamination within the proton beam, the different excited states, a large number of backgrounds, the limited Monte-Carlo and data statistics, the uncertainties on the apparatus acceptance, the beamspot position, the IPC Zhang-Miller model and the energy scale. They all impact the sensitivity of the X17 search. Below is some discussion about future prospects which could improve the sensitivity to the search:

- Beam The H_2^+ contamination within the proton beam was extensively discussed. The number of IPC templates was doubled to account for it and additional free parameters were incorporated into the fit to account for the unknown proportions of the various excited states. The pure proton beam evidenced in Sec. 6.3 can largely reduce the number of required MC templates. A 7 μm-thick target leads to a non-negligible energy loss which had to be accounted for. With a pure H^+ beam on a 2 μm-thick LiPON target (already delivered and tested), the dataset could be modelled with 2 IPC templates only (transition to ground and first excited states). Improved knowledge of the beamspot on target through regular proto-fluorescent quartz checks would also be useful. Indeed, the uncertainty on the beamspot position and shape is thought to be the main reason for EPC mismodelling and data/model disagreement at low angular openings.

- Apparatus The heat-dissipating copper ring holding the target was found to be the main source of photon conversion. Tests at beam currents up to 20 μA showed no significant deterioration of the target and therefore a good heat dissipation at high temperatures. The copper ring thickness could be reduced, almost proportionally reducing the number of EPC pairs, the dominant background of the Feb2023 dataset. A reduced proportion of EPC would lead to a better understanding of the IPC model at low angles, the dominant background in the signal region. EPC pairs also dominating the trigger rate, a thinner copper ring would give room for a proton current increase and therefore reduced DAQ time. The carbon fiber chamber holds the target in vacuum. Its thickness is a compromise between good mechanical stability and minimized multiple scattering for charged particles. However, it has a small diameter and therefore doesn't cover the full CDCH inner diameter. All tracks are significantly scattered before reaching the CDCH diameter, going through 15 cm of air on average. A larger diameter vacuum chamber requires a larger wall thickness to be mechanically stable but could be optimized to prevent particle propagation through air. The improvement

in angular resolution could then yield an improved sensitivity to the X17 production. Additionally, it was found that an increase in the CDCH gas gain by decreasing the isopropyl alcohol content can lead to an improvement in hit and track reconstruction. Such a configuration with higher gain was tested and no instability of the CDCH was observed.

- Simulation The knowledge of the IPC background in the signal region is a strong limiting factor. The uncertainties coming with the Zhang-Miller IPC model were accounted for in the previous analysis and turned out to be the dominating uncertainty on the extracted confidence limit. Though this model is the most comprehensive IPC model to date, it was not extensively and successfully confronted with experimental data. In this work, a small dataset at $E_{\mathrm{p}} = 500$ keV supported the model. Large statistics at such a proton energy would provide an excellent probe for the model in order to better understand its actual limitations and the room for improvement. The EPC MC model suffers a lack of statistics due to an inefficient generation process, starting from the photon production and relying on a rare conversion in the apparatus material. The implementation of a cross-section bias for the photon pair conversion process in the simulation could solve the issue.

- Reconstruction software The charged track reconstruction and selection was developed to reject fake tracks which can contaminate the signal region. The cost of the rejection is a 50% loss on good tracks and therefore a 75% loss on good pairs. Further understanding of fake tracks, based on their reconstructed vertices distribution for example, could yield further acceptance for good tracks and therefore increase the number of pairs in the signal region in order to improve the sensitivity. More intricate, a new track finder for electrons and positrons, focused on the evolution of the transverse momentum direction to discriminate the track sign. Preliminary attempts at a track finder based on neural networks showed encouraging results.

- TDAQ Overall, acquiring as many signal-like tracks as possible is needed. The X17 DAQ period occurs during the yearly shutdown of the PSI proton accelerator, when the MEG-II apparatus is available. The restricted DAQ time requires strategies to optimize the signal-like DAQ rate. The proton current should be increased within DAQ rate limits. Reducing the EPC trigger rate and the material amount is crucial. The trigger choice could also be optimized by selecting signal-like CDCH hits based on the wire position. Moreover, we saw that 1/3 of the CDCH wires are not readout, unnecessary for the $\mu^+ \to \mathrm{e}^+\gamma$ search. However, it has a large impact on the acceptance of large angular opening signal-like pairs. Instrumenting this region could lead to a factor of 2 increase in signal acceptance.

Conclusion

An excess in the electron-positron angular opening of the ^{7}Li(p, e$^+$e$^-$)^{8}Be reaction suggested the existence of a new neutral boson with a mass close to 17 MeV/c^2, nicknames X17. In this work, we performed the X17 search with the MEG-II apparatus. We demonstrated that MEG-II's setup, sub-detectors and trigger could be adapted to study the ^{7}Li(p, e$^+$e$^-$)^{8}Be reaction with good efficiency, improved resolutions and broader angular acceptance with respect to Atomki. We developed and implemented comprehensive background simulations for the Internal and External Pair Conversion (IPC and EPC) processes from ^{8}Be* decay. We established an efficient and reliable e$^+$e$^-$ pair reconstruction procedure. A 1080 keV proton beam impinging onto a 7 μm-thick LiPON target was used to acquire a four-week dataset with about 500 000 e$^+$e$^-$ pairs. Both ^{8}Be*(18.1 MeV) and ^{8}Be*(17.6 MeV) states were simultaneously excited within this dataset due to the presence of both H^+ and H_2^+ within the beam. Dedicated weighting procedure and blinded analysis were developed to model the various background contributions in the dataset. A maximum likelihood fit yielded no significant X17 signal excess over the known backgrounds. Limits at 90% C.L. were set on the X17 branching ratios relative to γ emission from the two resonances: $R_{\mathrm{X17}/\gamma,17.6} < 1.8 \times 10^{-6}$ and $R_{\mathrm{X17}/\gamma,17.6} < 1.2 \times 10^{-5}$. The X17 hypothesis, based on Atomki results, is incompatible at 94% confidence with our best fit. Additional data taking, exciting the 1030 keV Li resonance, is foreseen to further explore the existence of the anomaly and the viability of its X17 interpretation.

Acknowledgements

First, I need to thank my supervisor **Angela Papa** for the wonderful opportunity to join her research group and for sharing with me her boundless passion.

Bastiano Vitali, I hope you know how much I have needed you for the kindness and friendship but also for the long days and sleepless nights at PSI.

Giovanni Dal Maso, thank you for the endless discussions and misunderstandings, for the stimulation and passion and for sharing your indomitable faith in X17's existence. We would have never found it without you.

I would like to thank **Stergiani Vogiatzi** and **Giuseppe Lospalluto** for all the time spent during and outside office hours and for memorable ski slopes.

Luca G., **Antoine Venturini**, **Elia Grandoni**, **Marco Chiappini**, **Marco Francesconi**, I have never looked so much forward to lunches before you. Thanks for letting me become a capo, I will hold tightly to the title.

I want to express my gratitude to **Alessandro Baldini** for making me learn Italian so fast, to **Fabrizio Cei**, **Donato Nicoló** and **Marco Grassi** for the countless pieces of advice.

Thanks to **Francesco Renga**, **Luca C.** and the MEG-II collaboration: I have learnt so much!

Leon Andre, your constance was key.

Dimitri, I need to thank you for putting the effort into trying to understand what I was doing, for the shoulder and for all the rest.

Marie, merci merci merci.

Finally, I am deeply grateful for my friends and family's support: it fills me with serenity and allows me to go forward.

Bibliography

[1] A. J. Krasznahorkay, M. Csatlós, L. Csige, Z. Gácsi, J. Gulyás, M. Hunyadi, I. Kuti, B. M. Nyakó, L. Stuhl, J. Timár, T. G. Tornyi, Z. Vajta, T. J. Ketel, and A. Krasznahorkay, "Observation of Anomalous Internal Pair Creation in ^{8}Be: A Possible Indication of a Light, Neutral Boson," Physical Review Letters, vol. 116, p. 042501, Jan 2016.

[2] D. Tilley, J. Kelley, J. Godwin, D. Millener, J. Purcell, C. Sheu, and H. Weller, "Energy levels of light nuclei A=8,9,10," Nuclear Physics A, vol. 745, no. 3, pp. 155–362, 2004.

[3] J. L. Feng, B. Fornal, I. Galon, S. Gardner, J. Smolinsky, T. M. P. Tait, and P. Tanedo, "Particle physics models for the 17 MeV anomaly in beryllium nuclear decays," Physical Review D, vol. 95, p. 035017, Feb 2017.

[4] J. L. Feng, B. Fornal, I. Galon, S. Gardner, J. Smolinsky, T. M. P. Tait, and P. Tanedo, "Protophobic Fifth-Force Interpretation of the Observed Anomaly in ^{8}Be Nuclear Transitions," Physical Review Letters, vol. 117, p. 071803, Aug 2016.

[5] D. Zahnow, C. Angulo, C. Rolfs, S. Schmidt, W. H. Schulte, and E. Somorjai, "The S(E) factor of ^{7}Li(p,γ)^{8}Be and consequences for S(E) extrapolation in ^{7}Be(p, γ_0)^{8}B," Zeitschrift für Physik A Hadrons and Nuclei, vol. 351, pp. 229–236, Jun 1995.

[6] C. Rolfs, "Spectroscopic factors from radiative capture reactions," Nuclear Physics A, vol. 217, no. 1, pp. 29–70, 1973.

[7] X. Zhang and G. A. Miller, "Can nuclear physics explain the anomaly observed in the internal pair production in the Beryllium-8 nucleus?," Physics Letters B, vol. 773, pp. 159–165, 2017.

[8] P. Gysbers, P. Navrátil, K. Kravvaris, G. Hupin, and S. Quaglioni, "*Ab initio* investigation of the ^{7}Li$(\mathrm{p}, \mathrm{e}^{+}\mathrm{e}^{-})^{8}$Be process and the X17 boson," Physical Review C, vol. 110, p. 015503, Jul 2024.

[9] M. E. Rose, "Chapter II - Internal Conversion Theory," in Internal Conversion Processes (J. H. Hamilton, ed.), pp. 15–33, Academic Press, 1966.

[10] M. E. Rose, "Internal Pair Formation," Physical Review, vol. 76, pp. 678–681, Sep 1949.

[11] M. E. Rose, G. H. Goertzel, B. I. Spinrad, J. Harr, and P. Strong, "The Internal Conversion Coefficients. I: The K-Shell," Physical Review, vol. 83, pp. 79–87, Jul 1951.

[12] J. C. Jaeger and H. R. Hulme, "On the Production of Electron Pairs," Proceedings of the Royal Society of London. Series A, Mathematical and Physical Sciences, vol. 153, no. 879, pp. 443–447, 1936.

[13] "A pair spectrometer for measuring multipolarities of energetic nuclear transitions," Nuclear Instruments and Methods in Physics Research Section A: Accelerators, Spectrometers, Detectors and Associated Equipment, vol. 808, pp. 21–28, 2016.

[14] F. W. N. de Boer, O. Fröhlich, K. Stiebing, K. Bethge, H. Bokemeyer, A. Balanda, A. Buda, R. van Dantzig, T. Elze, H. Folger, J. van Klinken, K. Müller, K. Stelzer, P. Thee, and M. Waldschmidt, "A deviation in internal pair conversion," Physics Letters B, vol. 388, no. 2, pp. 235–240, 1996.

[15] F. W. N. de Boer, R. van Dantzig, J. van Klinken, K. Bethge, H. Bokemeyer, A. Buda, K. A. Müller, and K. E. Stiebing, "Excess in nuclear e^+e^- pairs near 9 MeV/c^2 invariant mass," Journal of Physics G: Nuclear and Particle Physics, vol. 23, p. L85, Nov 1997.

[16] F. W. N. de Boer, K. Bethge, H. Bokemeyer, R. van Dantzig, J. van Klinken, V. Mironov, K. A. Müller, and K. E. Stiebing, "Further search for a neutral boson with a mass around 9 MeV/c^2," Journal of Physics G: Nuclear and Particle Physics, vol. 27, p. L29, Apr 2001.

[17] A. Vitez, A. Krasznahorkay, J. Gulyas, M. Csatlos, L. Csige, Z. Gacsi, A. Krasznahorkay, B. Nyako, F. De Boer, T. Ketel, and J. Van Klinken, "Anomalous internal pair creation in Be-8 as a signature of the decay of a new particle," Acta Physica Polonica B, vol. 39, pp. 483–487, Feb 2008.

[18] A. Krasznahorkay, J. Gulyás, M. Csatlós, A. Vitéz, T. Tornyi, L. Stuhl, L. Csige, Z. Gácsi, J. A. Krasznahorkay, and M. Hunyadi, "Searching for a Light Neutral Axial-Vector Boson in Isoscalar Nuclear Transitions," in Frascati Physics Series, vol. 56, p. 86, Dark Forces at Accelerators, 2012.

[19] A. J. Krasznahorkay, M. Csatlos, L. Csige, J. Gulyas, M. Koszta, B. Szihalmi, J. Timar, D. S. Firak, A. Nagy, N. J. Sas, and A. Krasznahorkay, "New evidence supporting the existence of the hypothetic X17 particle," 2019. arXiv:1910.10459.

[20] A. J. Krasznahorkay, M. Csatlós, L. Csige, J. Gulyás, A. Krasznahorkay, B. M. Nyakó, I. Rajta, J. Timár, I. Vajda, and N. J. Sas, "New anomaly observed in ^{4}He supports the existence of the hypothetical X17 particle," Physical Review C, vol. 104, p. 044003, Oct 2021.

[21] A. J. Krasznahorkay, A. Krasznahorkay, M. Begala, M. Csatlós, L. Csige, J. Gulyás, A. Krakó, J. Timár, I. Rajta, I. Vajda, and N. J. Sas, "New anomaly observed in ^{12}C supports the existence and the vector character of the hypothetical X17 boson," Physical Review C, vol. 106, p. L061601, Dec 2022.

[22] K. E. Stiebing, F. W. N. de Boer, O. Fröhlich, H. Bokemeyer, K. A. Müller, K. Bethge, and J. van Klinken, "A multi-detector array for high energy nuclear e^+e^- pair spectroscopy," Journal of Physics G: Nuclear and Particle Physics, vol. 30, p. 165, Jan 2004.

[23] G. Charpak and F. Sauli, "Multiwire proportional chambers and drift chambers," Nuclear Instruments and Methods, vol. 162, no. 1, pp. 405–428, 1979.

[24] S. Ravan, P. Pujahari, S. Prasad, and C. A. Pruneau, "Correcting correlation function measurements," Physical Review C, vol. 89, p. 024906, Feb 2014.

[25] A. J. Krasznahorkay, M. Csatlós, L. Csige, J. Gulyás, T. J. Ketel, A. Krasznahorkay, I. Kuti, A. Nagy, B. M. Nyakó, N. Sas, and J. Timár, "On the creation of the 17 MeV X boson in the 17.6 MeV M1 transition of ^{8}Be," EPJ Web Conf., vol. 142, p. 01019, 2017.

[26] A. J. Krasznahorkay, M. Csatlós, L. Csige, Z. Gácsi, J. Gulyás, A. Nagy, N. Sas, J. Timár, T. G. Tornyi, I. Vajda, and A. J. Krasznahorkay, "New results on the ^{8}Be anomaly," Journal of Physics: Conference Series, vol. 1056, p. 012028, Jul 2018.

[27] D. Tilley, H. Weller, and G. Hale, "Energy levels of light nuclei A = 4," Nuclear Physics A, vol. 541, no. 1, pp. 1–104, 1992.

[28] M. Viviani, E. Filandri, L. Girlanda, C. Gustavino, A. Kievsky, L. E. Marcucci, and R. Schiavilla, "$X17$ boson and the $^3\mathrm{H}(\mathrm{p}, \mathrm{e}^+\mathrm{e}^-)^4\mathrm{He}$ and $^3\mathrm{He}(\mathrm{n}, \mathrm{e}^+\mathrm{e}^-)^4\mathrm{He}$ processes: A theoretical analysis," Physical Review C, vol. 105, p. 014001, Jan 2022.

[29] J. Kelley, J. Purcell, and C. Sheu, "Energy levels of light nuclei A=12," Nuclear Physics A, vol. 968, pp. 71–253, 2017.

[30] A. Aleksejevs, S. Barkanova, Y. G. Kolomensky, and B. Sheff, "A Standard Model Explanation for the "ATOMKI Anomaly"," 2021. arXiv:2102.01127.

[31] B. Koch, "X17: A new force, or evidence for a hard $\gamma + \gamma$ process?," Nuclear Physics A, vol. 1008, p. 122143, 2021.

[32] M. Meucci, "Search for the X(17) particle in the ^{7}Li(p, e$^+$e$^-$)^{8}Be reaction with the MEG II detector." PhD thesis, Sapienza Università di Roma, 2022.

[33] H.-W. Hammer, C. Ji, and D. R. Phillips, "Effective field theory description of halo nuclei," Journal of Physics G: Nuclear and Particle Physics, vol. 44, p. 103002, Sep 2017.

[34] B. Mainsbridge, "The angular distributions of the gamma radiation from the ^{7}Li(p,γ)^{8}Be reaction from $E_p = 200$ keV," Nuclear Physics, vol. 21, pp. 1–14, 1960.

[35] D. J. Schlueter, R. W. Krone, and F. W. Prosser, "Measurements and analysis of angular distribution interference effects in the ^{7}Li(p,γ)^{8}Be reaction," Nuclear Physics, vol. 58, pp. 254–272, 1964.

[36] S. Baroni, P. Navrátil, and S. Quaglioni, "Unified ab initio approach to bound and unbound states: No-core shell model with continuum and its application to ^{7}He," Physical Review C, vol. 87, p. 034326, Mar 2013.

[37] A. J. Krasznahorkay, M. Csatlós, L. Csige, D. Firak, J. Gulyás, A. Nagy, N. Sas, J. Timár, T. G. Tornyi, and A. Krasznahorkay, "On the X(17) Light-particle Candidate Observed in Nuclear Transitions," in Proceedings of the Zakopane Conference on Nuclear Physics: Extremes of the Nuclear Landscapes, vol. 50, (Zakopane, Poland), p. 675, 2019.

[38] P. B. Denton and J. Gehrlein, "Neutrino constraints and the ATOMKI X17 anomaly," Physical Review D, vol. 108, p. 015009, Jul 2023.

[39] J. L. Feng, T. M. P. Tait, and C. B. Verhaaren, "Dynamical evidence for a fifth force explanation of the ATOMKI nuclear anomalies," Physical Review D, vol. 102, p. 036016, Aug 2020.

[40] U. Ellwanger and S. Moretti, "Possible explanation of the electron positron anomaly at 17 MeV in ^{8}Be transitions through a light pseudoscalar," Journal of High Energy Physics, vol. 2016, p. 39, Nov 2016.

[41] J. R. Batley et al. (NA48/2 Collaboration), "Search for the dark photon in π^0 decays," Physics Letters B, vol. 746, pp. 178–185, 2015.

[42] A. Anastasi et al. (KLOE Collaboration), "Limit on the production of a low-mass vector boson in $e^+e^- \to U\gamma, U \to e^+e^-$ with the KLOE experiment," Physics Letters B, vol. 750, pp. 633–637, 2015.

[43] D. Banerjee et al. (NA64 Collaboration), "Improved limits on a hypothetical $X(16.7)$ boson and a dark photon decaying into e^+e^- pairs," Physical Review D, vol. 101, p. 071101, Apr 2020.

[44] X. Zhang and G. A. Miller, "Can a protophobic vector boson explain the ATOMKI anomaly?," Physics Letters B, vol. 813, p. 136061, 2021.

[45] D. Barducci and C. Toni, "An updated view on the ATOMKI nuclear anomalies," Journal of High Energy Physics, vol. 2023, p. 154, Feb 2023.

[46] Y. Kahn, G. Krnjaic, S. Mishra-Sharma, and T. M. P. Tait, "Light weakly coupled axial forces: models, constraints, and projections," Journal of High Energy Physics, vol. 2017, p. 2, May 2017.

[47] J. Kozaczuk, D. E. Morrissey, and S. R. Stroberg, "Light axial vector bosons, nuclear transitions, and the ^{8}Be anomaly," Physical Review D, vol. 95, p. 115024, Jun 2017.

[48] E. Abouzaid et al. (KTeV Collaboration), "Measurement of the rare decay $\pi^0 \to e^+e^-$," Physical Review D, vol. 75, p. 012004, Jan 2007.

[49] T. T. Anh, T. Dinh Trong, A. J. Krasznahorkay, A. Krasznahorkay, J. Molnár, Z. Pintye, N. A. Viet, N. T. Nghia, D. T. Khanh Linh, B. T. Hoa, L. X. Chung, and N. T. Anh, "Checking the ^{8}Be Anomaly with a Two-Arm Electron Positron Pair Spectrometer," Universe, vol. 10, no. 4, 2024.

[50] K. U. Abraamyan, C. Austin, M. I. Baznat, K. K. Gudima, M. A. Kozhin, S. G. Reznikov, and A. S. Sorin, "Observation of Structures at ˜17 and ˜38 MeV/c2 in the $\gamma\gamma$ Invariant Mass Spectrum in dCu Collisions at a Momentum of 3.8 GeV/c per Nucleon," Physics of Particles and Nuclei, vol. 55, pp. 868–873, Aug 2024.

[51] H. Abreu et al. (FASER Collaboration), "Search for dark photons with the FASER detector at the LHC," Physics Letters B, vol. 848, p. 138378, 2024.

[52] K. Ban, Y. Jho, Y. Kwon, S. C. Park, S. Park, and P.-Y. Tseng, "Search for new light vector boson using J/Ψ at BESIII and Belle II," Journal of High Energy Physics, vol. 2021, p. 91, Apr 2021.

[53] L. Darmé, M. Mancini, E. Nardi, and M. Raggi, "Resonant search for the X17 boson at PADME," Physical Review D, vol. 106, p. 115036, Dec 2022.

[54] R. Corliss et al. (DarkLight Collaboration), "Searching for a dark photon with DarkLight," Nuclear Instruments and Methods in Physics Research Section A: Accelerators, Spectrometers, Detectors and Associated Equipment, vol. 865, pp. 125–127, 2017.

[55] B. Echenard, R. Essig, and Y.-M. Zhong, "Projections for dark photon searches at Mu3e," Journal of High Energy Physics, vol. 2015, p. 113, Jan 2015.

[56] P. Ilten, J. Thaler, M. Williams, and W. Xue, "Dark photons from charm mesons at LHCb," Physical Review D, vol. 92, p. 115017, Dec 2015.

[57] B. Wojtsekhowski, G. Baranov, M. Blinov, E. Levichev, S. Mishnev, D. Nikolenko, I. Rachek, Y. Shestakov, Y. Tikhonov, D. Toporkov, J. Alexander, M. Battaglieri, A. Celentano, R. D. Vita, L. Marsicano, M. Bondì, M. D. Napoli, A. Italiano, E. Leonora, and N. Randazzo, "Searching for a dark photon: project of the experiment at VEPP-3," Journal of Instrumentation, vol. 13, p. P02021, Feb 2018.

[58] F. Hug, K. Aulenbacher, R. Heine, B. Ledroit, and D. Simon, "MESA - an ERL Project for Particle Physics Experiments," in Proc. of Linear Accelerator Conference (LINAC'16), East Lansing, MI, USA, 25-30 September 2016, no. 28 in Linear Accelerator Conference, (Geneva, Switzerland), pp. 313–315, JACoW, May 2017.

[59] O. Moreno, "The Heavy Photon Search Experiment at Jefferson Lab," 2013. arXiv:1310.2060.

[60] A. Ahmidouch et al. (PRad/X17 Collaboration), "A Direct Detection Search for Hidden Sector New Particles in the 3-60 MeV Mass Range," 2022. axXiv:2108.13276.

[61] "INFN National Laboratory of Legnaro." https://www.lnl.infn.it/en/.

[62] B. Bastin et al. (New JEDI Collaboration), "Investigation of a light Dark Boson existence: The New JEDI project," EPJ Web Conf., vol. 275, p. 01012, 2023.

[63] D. S. M. Alves, D. Barducci, G. Cavoto, L. Darmé, L. Delle Rose, L. Doria, J. L. Feng, A. Frankenthal, A. Gasparian, E. Goudzovski, C. Gustavino, S. Khalil, V. Kozhuharov, A. J. Krasznahorkay, T. Marchi, M. Meucci, G. A.

Miller, S. Moretti, M. Nardecchia, E. Nardi, H. Natal da Luz, G. Organtini, A. Papa, A.-K. Perrevoort, V. Petousis, G. Piperno, M. Raggi, F. Renga, P. Schwendimann, R. Sýkora, C. Toni, P. Valente, C. Voena, C.-Y. Wong, and X. Zhang, "Shedding light on X17: community report," The European Physical Journal C, vol. 83, p. 230, Mar 2023.

[64] G. Azuelos, D. Bryman, W. Chen, H. de Luz, L. Doria, A. Gupta, L.-A. Hamel, M. Laurin, K. Leach, G. Lefebvre, J.-P. Martin, A. Robinson, N. Starinski, R. Sykora, D. Tiwari, U. Wichoski, and V. Zacek, "Status of the X17 search in Montreal," Journal of Physics: Conference Series, vol. 2391, p. 012008, Dec 2022.

[65] M. Sabaté-Gilarté et al. (n_TOF Collaboration), "High-accuracy determination of the neutron flux in the new experimental area n_TOF-EAR2 at CERN," The European Physical Journal A, vol. 53, p. 210, Oct 2017.

[66] "Laboratory for Underground Nuclear Astrophysics." https://luna.lngs.infn.it/.

[67] M. Sevior, M. Baker, L. Bignell, C. Curceanu, J. T. H. Dowie, T. Kibedi, D. Jamieson, A. Stuchbery, A. Thamm, and M. White, "A Time Projection Chamber to Search for Feebly Interacting Bosons via Proton Induced Nuclear Reactions," 2023. arXiv:2302.13281.

[68] A. M. Baldini et al. (MEG-II Collaboration), "The design of the MEG II experiment," The European Physical Journal C, vol. 78, May 2018.

[69] B. W. Lee and R. E. Shrock, "Natural suppression of symmetry violation in gauge theories: Muon- and electron-lepton-number nonconservation," Physical Review D, vol. 16, pp. 1444–1473, Sep 1977.

[70] D. P. Aguillard et al. (Muon $g-2$ Collaboration), "Measurement of the Positive Muon Anomalous Magnetic Moment to 0.20 ppm," Physical Review Letters, vol. 131, p. 161802, Oct 2023.

[71] A. M. Baldini et al. (MEG Collaboration), "Search for the lepton flavor violating decay $\mu^+ \to e^+\gamma$ with the full dataset of the MEG experiment," The European Physical Journal C, vol. 76, p. 434, 2016.

[72] K. Afanaciev et al. (MEG-II Collaboration), "Operation and performance of the MEG II detector," The European Physical Journal C, vol. 84, p. 190, Feb 2024.

[73] S. Kobayashi, "Full Commissioning of Liquid Xenon Scintillation Detector to Search for $\mu^+ \to e^+\gamma$ with the Highest Sensitivity in MEG II Experiment." PhD thesis, The University of Tokyo, 2022.

[74] G. Boca, P. Cattaneo, M. De Gerone, M. Francesconi, L. Galli, F. Gatti, J. Koga, M. Nakao, M. Nishimura, W. Ootani, M. Rossella, Y. Uchiyama, M. Usami, K. Yanai, and K. Yoshida, "The laser-based time calibration system for the MEG II pixelated Timing Counter," Nuclear Instruments and Methods in Physics Research Section A: Accelerators, Spectrometers, Detectors and Associated Equipment, vol. 947, p. 162672, 2019.

[75] A. M. Baldini, H. Benmansour, G. Boca, G. Cavoto, F. Cei, M. Chiappini, G. Chiarello, A. Corvaglia, F. Cuna, M. Francesconi, L. Galli, F. Grancagnolo, E. G. Grandoni, M. Grassi, M. Hildebrandt, F. Ignatov, M. Meucci, W. Molzon, D. Nicolò, A. Oya, D. Palo, M. Panareo, A. Papa, F. Raffaelli, F. Renga, G. Signorelli, G. F. Tassielli, Y. Uchiyama, A. Venturini, B. Vitali, and C. Voena, "Performances of a new generation tracking detector: the MEG II cylindrical drift chamber," The European Physical Journal C, vol. 84, p. 473, May 2024.

[76] H. Schindler, Garfield++ User Guide (Version 2023.1), 2023.

[77] R. Frühwirth, "Application of Kalman filtering to track and vertex fitting," Nuclear Instruments and Methods in Physics Research Section A: Accelerators, Spectrometers, Detectors and Associated Equipment, vol. 262, no. 2, pp. 444–450, 1987.

[78] R. Frühwirth and A. Strandlie, "Track fitting with ambiguities and noise: A study of elastic tracking and nonlinear filters," Computer Physics Communications, vol. 120, no. 2, pp. 197–214, 1999.

[79] S. Agostinelli et al. (GEANT4 Collaboration), "GEANT4–a simulation toolkit," Nuclear Instruments and Methods in Physics Research Section A: Accelerators, Spectrometers, Detectors and Associated Equipment, vol. 506, pp. 250–303, 2003. RD44.

[80] J. Adam et al (MEG Collaboration), "Calibration and monitoring of the MEG experiment by a proton beam from a Cockcroft–Walton accelerator," Nuclear Instruments and Methods in Physics Research Section A: Accelerators, Spectrometers, Detectors and Associated Equipment, vol. 641, no. 1, pp. 19–32, 2011.

[81] J. D. Cockcroft and E. T. S. Walton, "Experiments with High Velocity Positive Ions. (I) Further Developments in the Method of Obtaining High Velocity Positive Ions," Proceedings of the Royal Society of London. Series A, Containing Papers of a Mathematical and Physical Character, vol. 136, no. 830, pp. 619–630, 1932.

[82] C. Wang, X. Sun, X. Zhang, and H. Li, "Introducing nanodiamonds in electrolyte and SEI for highly improving performances of lithium-ion batteries," Applied Surface Science, vol. 600, p. 154178, 2022.

[83] M. Finas, H. A. Girard, and J.-C. Arnault, "How to efficiently isolate multiple size ranges of oxidized or hydrogenated milled nanodiamonds," Nanoscale Adv., vol. 6, pp. 5375–5387, 2024.

[84] C. N. A. Bahri, W. M. Al-Areqi, M. Ruf, and A. A. Majid, "Characteristic of molten fluoride salt system LiF-BeF2 (Flibe) and LiF-NaF-KF (Flinak) as coolant and fuel carrier in molten salt reactor (MSR)," in AIP Conference Proceedings, vol. 1799, (Melville, NY), p. 040008, AIP Publishing, January 2017.

[85] A. Machín, C. Morant, and F. Márquez, "Advancements and Challenges in Solid-State Battery Technology: An In-Depth Review of Solid Electrolytes and Anode Innovations," Batteries, vol. 10, no. 1, 2024.

[86] C. Nimisha, K. Y. Rao, G. Venkatesh, G. M. Rao, and N. Munichandraiah, "Sputter deposited LiPON thin films from powder target as electrolyte for thin film battery applications," Thin Solid Films, vol. 519, no. 10, pp. 3401–3406, 2011.

[87] University of California, Berkeley, "SPICE (Simulation Program with Integrated Circuit Emphasis)." https://ptolemy.berkeley.edu/projects/embedded/pubs/downloads/spice/, 2024.

[88] W. Waltenberger, W. Mitaroff, and F. Moser, "RAVE—a Detector-independent vertex reconstruction toolkit," Nuclear Instruments and Methods in Physics Research Section A: Accelerators, Spectrometers, Detectors and Associated Equipment, vol. 581, no. 1, pp. 549–552, 2007. VCI 2007.

[89] H. Dembinski and A. Abdelmotteleb, "A new maximum-likelihood method for template fits," The European Physical Journal C, vol. 82, p. 1043, Nov 2022.

[90] M. Baak, S. Gadatsch, R. Harrington, and W. Verkerke, "Interpolation between multi-dimensional histograms using a new non-linear moment morphing

method," Nuclear Instruments and Methods in Physics Research Section A: Accelerators, Spectrometers, Detectors and Associated Equipment, vol. 771, pp. 39–48, 2015.

[91] S. Baker and R. D. Cousins, "Clarification of the use of CHI-square and likelihood functions in fits to histograms," Nuclear Instruments and Methods in Physics Research, vol. 221, no. 2, pp. 437–442, 1984.

[92] G. J. Feldman and R. D. Cousins, "A Unified approach to the classical statistical analysis of small signals," Physical Review D, vol. 57, pp. 3873–3889, 1998.

[93] S. Navas et al. (Particle Data Group), "Review of particle physics," Physical Review D, vol. 110, p. 030001, Aug 2024.